

**ULTRA LOW RANGE SIDELobe LEVEL PULSE
COMPRESSION WAVEFORM DESIGN FOR
SPACEBORNE METEOROLOGICAL RADARS**

by

Lluís Vinagre i Solans

A thesis submitted to the University of London for the Degree of
Doctor of Philosophy in Electronic Engineering

Department of Electronic and Electrical Engineering
University College London

June 1997

ProQuest Number: 10017765

All rights reserved

INFORMATION TO ALL USERS

The quality of this reproduction is dependent upon the quality of the copy submitted.

In the unlikely event that the author did not send a complete manuscript and there are missing pages, these will be noted. Also, if material had to be removed, a note will indicate the deletion.



ProQuest 10017765

Published by ProQuest LLC(2016). Copyright of the Dissertation is held by the Author.

All rights reserved.

This work is protected against unauthorized copying under Title 17, United States Code.
Microform Edition © ProQuest LLC.

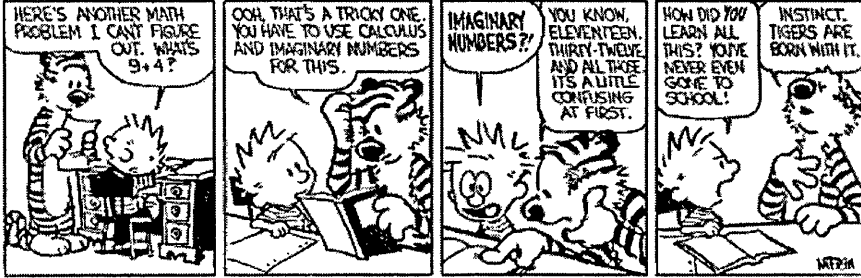
ProQuest LLC
789 East Eisenhower Parkway
P.O. Box 1346
Ann Arbor, MI 48106-1346

ABSTRACT

Meteorological measurements from spaceborne radars present several advantages over current passive techniques, due to the radar capability to discriminate backscattered energy in range. However, the system configuration imposes stringent design requirements in order to guarantee cloud and rain detectability, in particular on the radar waveform. Since power is severely restricted on board a satellite, it is necessary to achieve an efficient range resolution with low transmitted power requirements. Pulse compression theory solves the previous conflicting demand, but the transmitted signal needs to be carefully designed in order to allow the significantly large dynamic range (between 60 and 80 dB depending on the type of meteorological target) needed to carry out the measurements.

Several pulse compression range sidelobe reduction techniques of differing natures have been investigated and reported in the literature during the past 50 years. A detailed survey of the most relevant range sidelobe suppression procedures has been carried out in order to identify the most suitable frequency modulation candidates which are potentially capable of meeting the stringent specifications of spaceborne radar meteorology.

Novel pulse compression waveform design techniques have also been developed, employing linear FM predistortion functions and asymmetric frequency modulation laws, which provide excellent performance in terms of range sidelobe level (below -60 dB) and Doppler tolerance. Different options for the provision of a rain mode for the RA-2 Radar Altimeter (due to fly on European Space Agency ENVISAT satellite) are described, based on altimetry linear FM full-deramp technique concepts. Finally, amplitude modulated pulse compression waveform design alternatives are analysed for the MACSIM radar (Millimetre wave Active Cloud Structure Imaging Mission, European Space Agency Pre Phase A Study), which allow to measure different type of clouds within the Mission required radiometric resolution accuracy.



Calvin and Hobbes © Watterson. Reprinted with permission of Universal Press Syndicate. All rights reserved.

To Montserrat, Gonzalo and David

ACKNOWLEDGEMENTS

Without the supervision, help and friendship of Professor H.D. Griffiths, this research would have not been possible. I am in debt for his scientific expertise and continuous support during the course of this work. I would also like to thank Professor K. Milne and Professor R. Benjamin for their advice and lengthy discussions throughout their countless visits to UCL.

Thanks are also due to Dr C. Zelli and F. Provvedi from Alenia Spazio, Italy, to Dr P. Mancini from ESTEC, Holland, R. Girard from MPBT, Canada, and H.R Schulte from Dornier, Germany, for their comments and technical contributions during the Radar Altimeter-2 and the MACSIM research studies.

Finally, I would like to express my gratitude to all the students and members of staff of the Antennas and Radar Group at University College London, and in particular to O. Andreu, R. Arroyo, R.J. Bullock, J.M. Butler, S. Caufapé, E. Chiva, J.W. Eades, M. Fernández-Pola, F. Giné, R.J. Maunder, X. Perramon, V. Rasche, H.A. Read (who proof-read this thesis at The Albion), N. Rudolf, J.M. Solà, S.L. Twohig and X. Viladegut for their encouragement, and for sharing a few pints and equations during the long and never-ending postgraduate years.

ULTRA LOW RANGE SIDELobe LEVEL PULSE COMPRESSION WAVEFORM DESIGN FOR SPACEBORNE METEOROLOGICAL RADARS

Index of Contents

Title Page	
Abstract.....	2
Acknowledgements	4
Index of Contents	5
List of Figures	8
List of Tables	13
List of Principal Symbols and Acronyms	14
1 INTRODUCTION	
1.1 Historical Background.....	20
1.2 Objectives and Thesis Layout.....	21
2 SPACEBORNE METEOROLOGICAL RADAR	
2.1 Introduction.....	24
2.1.1 Need for Spaceborne Meteorological Radars	24
2.1.2 Spaceborne Rain Radar Requirements (TRMM and BEST Missions).....	26
2.2 Meteorological Radar Equation	27
2.3 Signal-to-Noise Ratio	29
2.4 Earth Surface Clutter Interference	32
2.4.1 Earth Surface Radar Equation.....	32
2.4.2 Interference through Range Sidelobe.....	33
2.4.3 Interference through Antenna Sidelobe	34
2.5 Signal Doppler Spectrum.....	35
2.6 References	39
3 LINEAR FM PULSE COMPRESSION	
3.1 Historical Background.....	41
3.2 The Matched Filter	42
3.3 Linear Frequency Modulation.....	44
3.3.1 Linear FM Signal Formulation	45
3.3.2 Linear FM Signal Spectrum.....	47
3.3.3 Linear FM Compressed Pulse	49
3.4 Linear FM Signal Ambiguity Function.....	51
3.5 References	54
4 PULSE COMPRESSION RANGE SIDELobe REDUCTION THEORY	
4.1 Frequency and Amplitude Weighting	55
4.2 Nonlinear FM Range Sidelobe Reduction	62
4.2.1 Nonlinear FM Theory	63
4.2.2 Design of Nonlinear FM Signals.....	64
4.3 Influence of Doppler Frequency Shifts on Range Sidelobe Reduction.....	66
4.4 References	70
5 PREDISTORTED LINEAR FM SIGNAL DESIGN	
5.1 Linear FM Predistortion	72
5.1.1 Theory and Design.....	72
5.1.2 Practical Application: BEST Radar Waveform.....	74

5.2	Predistorted Linear FM Compressed Pulse Analysis	76
5.2.1	Crosscorrelation Function	77
5.2.2	Compressed Pulse Analytical Expression	79
5.3	Predistortion Function Range Sidelobe Matching Design Method	84
5.4	Predistorted Linear FM Ambiguity Function	89
5.5	References	91

6 ASYMMETRIC FM SIGNAL DESIGN

6.1	Introduction	92
6.2	Asymmetric Nonlinear FM Pulse Compression	93
6.3	Symmetric Nonlinear FM Pulse Compression	98
6.4	Waveform Generation Considerations	103
6.5	References	106

7 RAIN OBSERVATION BY RADAR ALTIMETER

7.1	Introduction	107
7.1.1	RA-2 Instrument and Rain Mode Objectives	107
7.1.2	Rain Mode for SEASAT Altimeter	109
7.1.3	RA-2 Rain Mode Design Options	110
7.2	RA-2 Rain Mode: Full Deramp Alternative	112
7.2.1	Range Window Configuration	112
7.2.2	Rain and Surface Return Power Levels	115
7.2.3	Signal-to-Noise Ratio Analysis	117
7.2.4	Rain Mode Doppler Frequency Offset Analysis	118
7.3	Full Deramp of Nonlinear FM Waveforms	119
7.3.1	Predistorted Linear FM signals	119
7.3.2	Nonlinear FM Signals	120
7.4	RA-2 Rain Mode: Full Deramp Formulation	122
7.4.1	Full Deramp Formulation of Signals of Different Lengths	123
7.4.2	Ground Clutter Range Sidelobe Interference	124
7.5	Range Sidelobe Reduction Techniques	126
7.5.1	Amplitude Weighting	126
7.5.2	AGC Gain-Varying Functions	129
7.5.3	Combined Amplitude and Phase Weighting Schemes	133
7.5.4	Ground Clutter Echo Cancellation	137
7.6	References	138

8 MACSIM: CLOUD PROFILING RADAR

8.1	Introduction	140
8.2	MACSIM Waveform Design Alternatives	142
8.2.1	Unmodulated Pulse Alternative	142
8.2.2	Pulse Compression Alternative	144
8.3	High Time-Bandwidth Amplitude Modulated Pulse Compression	147
8.3.1	ARMAR Mission	147
8.3.2	ARMAR Amplitude Modulation Scheme	148
8.3.3	Pulse Volume Multiple Look Averaging	150
8.4	Amplitude Modulated Linear FM Signal Loss Factors	153
8.4.1	Multiple Look Averaging Gain and Effective Compression Ratio	153
8.4.2	Signal Decorrelation Loss	154
8.4.3	Finite Bandwidth Loss	160
8.4.4	ARMAR Single Pulse Sensitivity Balance	161
8.5	Radiometric Resolution	163
8.6	References	167

9 CONCLUSIONS

9.1	Summary	169
-----	---------------	-----

9.2 Novel Predistorted Linear FM Waveform Design Technique	171
9.3 Novel Asymmetric FM Waveform Design Technique	172
9.4 RA-2 Rain Mode Design Discussion	174
9.5 MACSIM Design Discussion	178

APPENDIX A

Doppler Frequency Due to Satellite Motion Formulation	182
---	-----

APPENDIX B

B.1 Linear FM Compressed Pulse Calculation	184
B.2 Linear FM Ambiguity Function Calculation	186
B.3 Linear FM Ambiguity Function Calculation (Amplitude Mismatch)	188

APPENDIX C

Predistorted linear FM Crosscorrelation Formulation	193
---	-----

APPENDIX D

D.1 Full-Deramp Formulation of Linear FM Signals of Equal Lengths	200
D.2 Full-Deramp Formulation of Linear FM Signals of Different Lengths	205
D.3 Full-Deramp Formulation of Weighted Linear FM Signals	207

List of Figures

Figure 2.1. METEOSAT optical image (source: University of Nottingham).....	25
Figure 2.2. Predicted signal-to-noise ratio for: (a) TRMM rain radar (5-km rain cloud height and nadir incidence). Reproduced from [Li et al., 1988]; (b) BEST rain radar (power measurement at the bottom of a 5 km depth rain layer with uniform rainfall rate). Reproduced from [Marzoug et al., 1988].	31
Figure 2.3. Spaceborne meteorological radar target scenario and geometry.....	33
Figure 2.4. Pr/Ps ratio contour maps (in dB) for sea clutter through range sidelobe at 13.8 GHz: (a) Scan angle $\theta = 0^\circ$; (b) Scan angle $\theta = 15^\circ$. Reproduced from [Manabe et al., 1988].	34
Figure 2.5. Pr/Ps ratio contour maps (in dB) for sea clutter through antenna sidelobe at 13.8 GHz. (a) Scan angle $\theta = 0^\circ$; (b) Scan angle $\theta = 15^\circ$. Reproduced from [Manabe et al., 1988].....	35
Figure 2.6. Doppler frequency offset map as a function of ground coordinates.....	37
Figure 2.7. Range sidelobe level specification as a function of: (a) Rainfall rate and Doppler frequency; (b) Doppler frequency and minimum detectable rainfall rate.....	38
Figure 3.1. Linear FM signal: (a) Instantaneous frequency; (b) Complex envelope, in-phase component; (c) Complex envelope, quadrature component.	46
Figure 3.2. Fresnel integral, C(x) and S(x) components.....	48
Figure 3.3. Linear FM signal spectrum: (a) $TB = 25$; (b) $TB = 100$; (c) $TB = 500$; (d) $TB = 1000$	49
Figure 3.4. Diagram of Linear FM signal autocorrelation integration limits.	50
Figure 3.5. Linear FM signal: (a) Compressed pulse diagram; (b) Compressed pulse $TB = 250$	50
Figure 3.6. Ambiguity functions of: (a) Unmodulated pulse; (b) Linear FM signal.....	52
Figure 3.7. Ambiguity function constant amplitude level contour plots relative to $ \chi(0,0) $ for: (a) Unmodulated pulse; (b) Linear FM signal. Reproduced from [Cook and Bernfeld, 1967].....	53
Figure 4.1. Hamming, Dolph-Chebyshev, Kaiser-Bessel and minimum 3-term Blackman-Harris weighting functions.....	59
Figure 4.2. Fourier transforms of: (a) Hamming function; (b) Dolph-Chebyshev function; (c) Kaiser-Bessel function; (d) Minimum 3-term Blackman-Harris function.	60
Figure 4.3. Compressed pulses for different linear FM matched filter amplitude mismatching functions: (a) Hamming window; (b) Dolph-Chebyshev window; (c) Kaiser-Bessel window; (d) Minimum 3-term Blackman-Harris window.	61
Figure 4.4. Linear FM range sidelobe level as a function of time-bandwidth product for different matched filter amplitude mismatching functions.	61
Figure 4.5. Frequency modulation for a Hamming function compressed pulse spectrum as a function of: (a) Frequency; (b) Time (after iteration and fitting into a Chebyshev polynomial). Reproduced from [Johnston, 1983].....	65
Figure 4.6. Design of nonlinear FM signals with a Hamming function compressed pulse spectrum: (a) Nonlinear FM signal spectrum ($TB = 100$); (b) Nonlinear FM compressed pulse ($TB = 100$), range sidelobe level -32 dB; (c) Nonlinear FM signal spectrum ($TB = 1000$); (d) Nonlinear FM compressed pulse ($TB = 1000$), range sidelobe level -41 dB. Reproduced from [Johnston, 1983]. ..	65
Figure 4.7. Ambiguity function (Blackman-Harris amplitude mismatch): (a) Linear FM; (b) Linear FM, $TB = 300$,	68
Figure 4.8. Range sidelobe level as a function of Doppler frequency for a linear FM matched filter mismatched in amplitude with a minimum 3-term Blackman-Harris function ($TB = 300$).	68
Figure 4.9. Ambiguity functions of: (a) Barker code of length 13; (b) Frank code of length 16.	69
Figure 5.1. Predistorted linear FM instantaneous frequency characteristic versus time. Reproduced from [Cook and Paolillo, 1964].	73
Figure 5.2. Modulation scheme employed for the BEST radar.	74
Figure 5.3. Signal spectra ($B = 4.5$ MHz): (a) Linear FM; (b) Predistorted linear FM.....	76
Figure 5.4. Predistorted linear FM compressed pulse ($BT = 270$, $\delta\Delta f = 0.54$)	77
Figure 5.5. Compressed pulse spectra ($B = 4.5$ MHz), minimum 3-term Blackman-Harris amplitude mismatching function: (a) Linear FM; (b) Predistorted linear FM.	78

Figure 5.6. Compressed pulses ($B = 4.5$ MHz), minimum 3-term Blackman-Harris amplitude mismatching function: (a) Linear FM; (b) Predistorted linear FM.	78
Figure 5.7. Predistorted linear FM crosscorrelation function constituent terms diagram.	80
Figure 5.8. Predistorted linear FM signal crosscorrelation function (real and imaginary components): (a) $\text{Re}(R_1(\tau))$; (b) $\text{Im}(R_1(\tau))$; (c) $\text{Re}(R_3(\tau))$; (d) $\text{Im}(R_3(\tau))$; (e) $\text{Re}(R_{\bar{r},\bar{r}w}(\tau))$; (f) $\text{Im}(R_{\bar{r},\bar{r}w}(\tau))$...	82
Figure 5.9. Predistorted linear FM compressed pulse: (a) FFT signal processing; (b) Analytical calculation.	83
Figure 5.10. (1) Linear FM (amplitude weighted) compressed pulse $R_1(t)$, time-bandwidth product = 270, sidelobe level -50.4 dB; (2) Crosscorrelation between the predistortion function and the linear FM signal (amplitude weighted); (3) Predistorted linear FM (amplitude weighted) compressed pulse, sidelobe level -62.8 dB.	85
Figure 5.11. Comparison between predistortion function design procedures as function of pulse width for a constant time-bandwidth product of 270, (1) indicates the Cook and Paolillo method ($\delta\Delta f = 0.75$) and (2) the range sidelobe matching method (mismatching: minimum 3-term Blackman-Harris function). (a) Range sidelobe levels; (b) Compressed pulses for the range sidelobe matching method; (c) Predistorted function parameters for the range sidelobe matching method.....	85
Figure 5.12. Comparison between predistortion function design procedures as function of pulse width for a constant time-bandwidth product of 270 ($B = 4.5$ MHz), (1) indicates the Cook and Paolillo method ($\delta\Delta f = 0.75$) and (2) the range sidelobe matching method (mismatching: minimum 3-term Blackman-Harris function). (a) Range sidelobe levels; (b) Compressed pulses for the range sidelobe matching method; (c) Predistorted function parameters for the range sidelobe matching method. ...	86
Figure 5.13. Minimum 4-term Blackman-Harris function Fourier transform.....	87
Figure 5.14. Comparison between predistortion function design procedures as function of pulse width for a constant time-bandwidth product of 270, (1) indicates the Cook and Paolillo method ($\delta\Delta f = 0.75$) and (2) the range sidelobe matching method (mismatching: minimum 4-term Blackman-Harris function). (a) Range sidelobe levels; (b) Compressed pulses for the range sidelobe matching method; (c) Predistorted function parameters for the range sidelobe matching method.....	88
Figure 5.15. Predistorted linear FM ambiguity functions ($BT = 270$): (a) Minimum 3-term Blackman-Harris mismatching function; (b) Minimum 4-term Blackman-Harris mismatching function.....	89
Figure 5.16. Range sidelobe level degradation as a function of Doppler frequency for linear and predistorted linear FM signals ($BT = 270$): (a) minimum 3-term Blackman-Harris amplitude mismatching function; (b) minimum 4-term Blackman-Harris amplitude mismatching function. ...	90
Figure 6.1. Linear period-modulated ($TB = 100$): (a) spectrum; (b) compressed pulse. Reproduced from [Kroszczynski, 1969].	92
Figure 6.2. Asymmetric FM compressed pulse range sidelobe level as a function of phase polynomial order for instantaneous frequencies of $0.75 B$, $1.0 B$ and $1.5 B$ at $f_i(+T/2)$ with respect to a linear FM nominal TB of 300.....	95
Figure 6.3. Asymmetric FM signal (33^{rd} order phase polynomial giving an instantaneous frequency of $1.5 B$ at $f_i(+T/2)$ with respect to a linear FM TB of 300): (a) Instantaneous frequency; (b) Compressed pulse, $RSL = -43.3$ dB; (c) Spectrum; (d) Spectrum (phase polynomial of 501 order). ...	96
Figure 6.4. Asymmetric FM compressed pulse range sidelobe level (minimum 3-term Blackman-Harris weighting) as a function of phase polynomial order for instantaneous frequencies of $0.75 B$, $1.0 B$ and $1.5 B$ at $f_i(+T/2)$ with respect to a linear FM nominal TB of 300.	97
Figure 6.5. Asymmetric FM for a 33^{rd} order phase polynomial giving different instantaneous frequency increases with respect to a linear FM nominal TB of 300: (a) Instantaneous frequency (b) Compressed pulse (minimum 3-term Blackman-Harris mismatching function).	97
Figure 6.6. Asymmetric FM compressed pulse range sidelobe level as a function of time-bandwidth product, for a 33^{rd} order phase polynomial giving different maximum instantaneous frequencies with respect to a linear FM nominal TB of 300 (minimum 3-term Blackman-Harris mismatching function).	98
Figure 6.7. Asymmetric FM signal ambiguity function for a 33^{rd} order phase polynomial giving an instantaneous frequency of $1.5 B$ at $f_i(+T/2)$ with respect to a linear FM nominal TB of 300 (minimum 3-term Blackman-Harris mismatching function).	98

Figure 6.8. Nonlinear FM compressed pulse range sidelobe level as a function of phase polynomial order giving instantaneous frequencies of $\pm 0.75 B$, $\pm 1.0 B$ and $\pm 1.5 B$ at $f_i(\pm T/2)$ with respect to a linear FM nominal TB of 300.	100
Figure 6.9. Nonlinear FM signal (10^{th} order phase polynomial giving an instantaneous frequency of $\pm 1.5 B$ at $f_i(\pm T/2)$ with respect to a linear FM TB of 300): (a) Instantaneous frequency; (b) Compressed pulse, $RSL = -35.5$ dB; (c) Ambiguity function.	101
Figure 6.10. Nonlinear FM signal (phase polynomial of order 1042 giving an instantaneous frequency of $\pm 1.5 B$ at $f_i(\pm T/2)$ with respect to a linear FM TB of 300, minimum 3-term Blackman-Harris mismatching function): (a) instantaneous frequency; (b) compressed pulse, $RSL = -64.5$ dB; (c) Ambiguity function; (d) Range sidelobe level as a function of Doppler frequency.	102
Figure 6.11. Block diagram of pulse generation and compression system, showing adaptive scheme for compensation of phase and amplitude errors. Reproduced from [Griffiths, 1993].	104
Figure 6.12. Pair-echo amplitude [Klauder et al., 1960] for: (a) amplitude distortion; (b) phase distortion	104
Figure 7.1. Echo power returned to altimeter from various distances below the top of rain versus rain rate. Reproduced from [Goldhirsh and Walsh, 1982].	109
Figure 7.2. Full deramp mode of operation diagram.	113
Figure 7.3. Full deramp: (a) Delay between received chirp and LO reference signal; (b) Power spectrum, ($T_p = 20 \mu\text{s}$, $B = 500$ kHz, $t_d = 4 \mu\text{s}$).	113
Figure 7.4. Full deramp power spectrum: (a) Power loss as a function of deramped pulse width; (b) Mainlobe broadening (-3 dB and between nulls) as a function of deramped pulse width.	114
Figure 7.5. RA-2 range window configuration options: (a) Multiple LO pulse; (b) Single LO pulse.	114
Figure 7.6. RA-2 rain mode range window baseline solution.	115
Figure 7.7. RA-2 predicted power levels: (a) Rain power level for different precipitation rates as a function of depth below the storm top; (b) Ground clutter power level for different backscattering coefficients as a function of precipitation rate (storm top 4 km above the ground).	116
Figure 7.8. Rain to ground clutter power ratio for different precipitation rates as a function of depth below the storm top ($\sigma^0 = 10$ dB).	117
Figure 7.9. RA-2 signal-to-noise ratio: (a) SNR from various distances below the storm top as a function of rain rate (Ku Band, $f_0 = 13.575$ GHz, $\sigma^0 = 10$ dB); (b) SNR as a function of rain rate and depth from storm top (Ku Band, $f_0 = 13.575$ GHz, $\sigma^0 = 10$ dB).	118
Figure 7.10. Doppler frequency: (a) Offset at the edges of the antenna footprint; (b) Spectrum spread.	118
Figure 7.11. Predistorted linear FM ($TB = 10$): (a) Instantaneous frequency; (b) Compressed pulse, $RSL = -34.5$ dB; (c) Full deramp power spectrum, $RSL = -11$ dB.	120
Figure 7.12. Nonlinear FM ($TB = 10$): (a) Instantaneous frequency (after [Johnston, 1983]); (b) Compressed pulse, $RSL = -20.7$ dB; (c) Full deramp power spectrum, $RSL = -10.5$ dB.	121
Figure 7.13. Diagram of nonlinear FM waveform full deramp.	122
Figure 7.14. Diagram of RA-2 rain mode full deramp of signals of different length.	123
Figure 7.15. Precipitation model: (a) Radar reflectivity as a function of altitude; (b) Altitude variation of rainfall rate. Reproduced from [Amayenc et al., 1994].	124
Figure 7.16. Ground clutter range sidelobe interference (4 km precipitation field) for low, medium and high rainfall rates: (a) 5 mm/h; (b) 20 mm/h; (c) 50 mm/h; (d) Minimum detectable height as a function of rain rate.	125
Figure 7.17. Hamming weighting: (a) Comparison between RA-2 rain mode unweighted and weighted power spectrums; (b) Power spectrum relative power loss as a function of position in the range window.	127
Figure 7.18. Ground clutter range sidelobe interference after Hamming weighting over the range window (4 km precipitation field) for low, medium and high rainfall rates: (a) 5 mm/h; (b) 20 mm/h; (c) 50 mm/h; (d) Minimum detectable height as a function of rain rate.	128
Figure 7.19. Weighting schemes: (a) FM pulse compression; (b) Full deramp technique.	129
Figure 7.20. Ground clutter sidelobe interference width.	129
Figure 7.21. Hamming gain-varying function: (a) Diagram; (b) Power spectrum.	130
Figure 7.22. Ground clutter range sidelobe interference after an AGC Hamming gain-varying function (4 km precipitation field) for low, medium and high rainfall rates: (a) 5 mm/h; (b) 20 mm/h; (c) 50 mm/h; (d) Minimum detectable height as a function of rain rate.	131
Figure 7.23. Linear gain-varying function: (a) Diagram; (b) Power spectrum.	131

Figure 7.24. Exponential gain-varying function: (a) Diagram; (b) Power Spectrum.....	132
Figure 7.25. Ground clutter range sidelobe interference after an AGC exponential gain-varying function (4 km precipitation field): (a) 20 mm/h; (b) Minimum detectable height as a function of rain rate.	132
Figure 7.26. RA-2 rain mode: 20 μ s (100%) point target response (dashed line); 10 μ s (50%) point target response (plain line).....	133
Figure 7.27. Combined amplitude and phase weighting scheme: (a) Diagram (plain line: Hamming and Kaiser amplitude functions, dashed line: phase function); (b) Power spectrum relative power loss as a function of position in the range window.....	134
Figure 7.28. Combined amplitude (Hamming and Kaiser) and phase weighting scheme: (a) Point target distortion as a function of position in the range window; (b) Surface return power spectrum.....	134
Figure 7.29. Combined amplitude and phase weighting scheme: (a) Diagram (plain line: Hamming amplitude function, dashed line: phase function); (b) Power spectrum relative power loss as a function of position in the range window.	135
Figure 7.30. Combined amplitude (Hamming) and phase weighting scheme: (a) Point target distortion as a function of position in the range window; (b) Surface return power spectrum.....	135
Figure 7.31. Ground clutter range sidelobe interference after amplitude (Hamming) and phase weighting schemes (4 km precipitation field) for low, medium and high rainfall rates: (a) 5 mm/h; (b) 20 mm/h; (c) 50 mm/h; (d) Minimum detectable height as a function of rain rate.	136
Figure 7.32. Ground echo cancellation: (a) Diagram; (b) Simulated surface full deramped signal.	137
Figure 8.1. Penetration depth as a function of minimum detectable reflectivity and cloud type (solid 95 GHz, dashed 79 GHz). Reproduced from [Riegger et al., 1996].	141
Figure 8.2. Linear FM compressed pulse ($BT = 33.6$) for different mismatching functions: (a) matched filter, $RSL = -13.6$ dB; (b) Hamming, $RSL = -33.0$ dB; (c) Dolph-Chebyshev, $RSL = -33.1$ dB; (d) minimum 3-term Blackman-Harris, $RSL = -32.3$ dB.....	144
Figure 8.3. Nonlinear FM compressed pulse ($BT = 33.6$) for: (a) matched filter (after [Johnston, 1983]), $RSL = -25.0$ dB; (b) Hybrid (after [Johnston, 1983] and [Judd, 1973]), Hamming mismatching function, $RSL = -33.9$ dB.	145
Figure 8.4. Predistorted linear FM compressed pulse ($BT = 33.6$) for: (a) Dolph-Chebyshev mismatching function, $RSL = -41.5$ dB; (b) Minimum 3-term Blackman-Harris mismatching function, $RSL = -45.0$ dB.	145
Figure 8.5. Asymmetric FM compressed pulse ($BT = 33.6$) for: (a) linear FM matched filter, $RSL = -29.2$ dB; (b) linear FM matched filter, minimum 3-term Blackman-Harris mismatching function, $RSL = -43.6$ dB.	146
Figure 8.6. ARMAR point target response (average of 6000 compressed pulses from airborne measurements, $T = 20$ μ s). reproduced from [Durdan et al., 1994]).	148
Figure 8.7. ARMAR signal: (a) Amplitude modulation scheme; (b) Comparison between linear FM and ARMAR compressed pulses ($TB = 33$).....	149
Figure 8.8. Predistorted linear FM compressed pulse ($TB = 1200$).....	151
Figure 8.9. Multiple look averaging over the user range resolution cell diagram.	151
Figure 8.10. ARMAR compressed pulse average range sidelobe level over the first user resolution cell (500 m), for bandwidths of: (a) 3 MHz; (b) 8 MHz.	152
Figure 8.11. ARMAR compressed pulse: (a) Average range sidelobe level over a range of 500 m as a function of signal bandwidth; (b) $TB = 1200$, $ARSL = -80$ dB.....	152
Figure 8.12. Multiple look averaging: (a) Compressed pulse -3dB width range resolution ($T = 150$ μ s) for linear FM, ARMAR and decorrelated ARMAR signals as a function of bandwidth; (b) Available number of looks over a range of 500 m for linear FM, ARMAR and decorrelated ARMAR signals as a function of bandwidth.	154
Figure 8.13. Ensemble average of linear FM compressed pulse instantaneous power ($B = 300$ kHz, $\tau_d = 150$ μ s) for pulse widths of: (a) $T = 75$ μ s; (b) $T = 150$ μ s; (c) $T = 300$ μ s.....	158
Figure 8.14. Decorrelation losses L_{pd} and L_{ad} as a function of pulse width (decorrelation time τ_d of 150 μ s) for: (a) linear FM signal; (b) ARMAR amplitude modulated linear FM signal.....	159
Figure 8.15. Ensemble average of ARMAR amplitude modulated linear FM compressed pulses instantaneous power ($\tau_d = 150$ μ s): (a) $TB = 1200$; (b) $TB = 1200$, detail (dashed line shows the non decorrelated compressed pulse).....	159
Figure 8.16. ARMAR amplitude modulation range weighting function.	160

Figure 8.17. Correlation width τ_w for the ARMAR amplitude modulated linear FM signal as a function of: (a) bandwidth; (b) signal-to-noise ratio.	164
Figure 8.18. ΔZ_{\min} for pulse compression and unmodulated pulse alternatives as a function of signal width ($SNR = 1$)	165
Figure 8.19. ΔK_p for pulse compression and unmodulated pulse alternatives as a function of signal width for different cloud volume reflectivities.	166
Figure 8.20. Radiometric resolution K_p for the ARMAR amplitude modulated linear FM signal as a function of signal width for different cloud volumetric reflectivities.	166
Figure 9.1. Predistorted linear FM ($TB = 270$): (a) instantaneous frequency; (b) compressed pulse.	172
Figure 9.2. Asymmetric FM ($TB = 300$): (a) instantaneous frequency; (b) compressed pulse.	173
Figure 9.3. Minimum detectable height as a function of rain rate for different sidelobe suppression techniques.	177
Figure A.1. Spaceborne rain radar system geometry.	182
Figure C.1. Predistorted linear FM instantaneous frequency.	193
Figure D.1. Time vs. frequency characteristic: (a) Point target return; (b) Point target deramped return.	200
Figure D.2. Altimeter receiver diagram.	201

List of Tables

Table 2.I: Comparison between TRMM and BEST Mission configurations.....	27
Table 4.I: Weighting Function Fourier Transform characteristics.....	59
Table 4.II: Mismatched linear FM (amplitude weighted) compressed pulse characteristics	60
Table 4.III: Nonlinear FM (after [Johnston, 1983]) compressed pulse characteristics	66
Table 4.IV: Range sidelobe level of Doppler shifted nonlinear FM signals ($B = 5$ MHz)	68
Table 5.I: BEST radar waveform parameters	75
Table 5.II: Linear and predistorted linear FM compressed pulse characteristics	78
Table 5.III: Predistorted linear FM signal crosscorrelation function term widths	80
Table 5.IV: Range sidelobe matching method, predistorted linear FM average parameter values	88
Table 6.I: Asymmetric FM compressed pulse characteristics ($TB = 300$).....	95
Table 6.II: Asymmetric FM (mismatched) compressed pulse characteristics	97
Table 6.III: Symmetric nonlinear FM compressed pulse characteristics	101
Table 6.IV: ‘Continuous’ predistorted linear FM compressed pulse characteristics	102
Table 7.I: RA-2 system parameters	108
Table 7.II: SEASAT and RA-2 configuration comparison.....	111
Table 7.III: RA-2 rain mode signal characteristics	115
Table 8.I: MACSIM system requirements	141
Table 8.II: Range sidelobe level reduction techniques characteristics.....	147
Table 8.III: ARMAR system parameters	148
Table 8.IV: Linear FM and ARMAR compressed pulse characteristics	150
Table 8.V: Linear FM decorrelation losses ($\tau_d = 150 \mu\text{s}$).....	158
Table 8.VI: ARMAR amplitude modulated linear FM decorrelation losses ($\tau_d = 150 \mu\text{s}$)	159
Table 8.VII: ARMAR pulse compression and unmodulated alternative single pulse sensitivities	162
Table 8.VIII: Optimum ΔK_p pulse compression signal width selection.....	166
Table 9.I: Detection constraints for different range sidelobe reduction techniques	176
Table 9.II: Sidelobe reduction techniques performance comparison	177

List of Principal Symbols and Acronyms

<i>Symbol</i>	<i>Definition</i>	<i>Units</i>
ARMAR	Airborne Rain Mapping Radar	
ARSL	FM signal compressed pulse average range sidelobe level	dB
A_{eff}	antenna effective area	m ²
BEST	Bilan Energétique du Système Tropical	
B	radar signal bandwidth	Hz
B_n	equivalent noise bandwidth	Hz
CNES	Centre National d'Etudes Spatiales (France)	
CNET	Centre National d'Etudes de Télécommunication (France)	
CNRS	Centre National de Recherche Scientifique (France)	
c	speed of light in vacuum	m/s
$C(x)$	Fresnel integral real component	
D	rain drop diameter	cm
D_0	median volume drop diameter	cm
ENVISAT	Environmental Satellite	
ERS	Earth Resources Satellite	
ESA	European Space Agency	
ESTEC	European Space Technology Centre	
$e(t)$	radar signal envelope	V
$e_{dt}(t)$	amplitude distortion term	V
E	radar signal energy	J
E	electric field intensity	V/m
FM	frequency modulation/modulated	
FFT	fast Fourier transform	
f	frequency	Hz
Δf	linear FM signal predistortion function bandwidth	Hz
Δf	radar signal frequency step	Hz
f_d	Doppler frequency	Hz
Δf_d	Doppler frequency spread over the antenna footprint	Hz
$f_i(t)$	radar signal instantaneous frequency	Hz
f_s	sampling frequency	Hz
f_T	inverse radar signal time width	Hz
f_0	radar signal carrier frequency	Hz
F	receiver noise figure	dB

$F(x)$	Fresnel integral	
G	antenna power gain	dB
h	altitude	m
h_{st}	storm top altitude	m
Δh_r	precipitation field altitude	m
Δh_s	storm top altitude	m
$h(t)$	reception filter impulse response	V
$h_{opt}(t)$	matched filter impulse response	V
$\tilde{h}_{opt}(t)$	matched filter complex envelope impulse response	V
$H(f)$	reception filter impulse response spectrum	
$H_{opt}(f)$	matched filter impulse response spectrum	
$\tilde{H}_{opt}(f)$	matched filter complex envelope impulse response spectrum	
IF	intermediate frequency	
$I(z)$	antenna current distribution	A
$I_0(x)$	modified Bessel function of the first kind	
k	Boltzmann's constant	JK ⁻¹
k_c	attenuation coefficient due to clouds	dB/km
k_g	attenuation coefficient due to atmospheric gas	dB/km
k_n^e	asymmetric even power terms polynomial coefficients	
k_n^o	asymmetric odd power terms polynomial coefficients	
k_p	attenuation coefficient due to precipitation	dB/km
K	FM signal modulation rate	Hz ²
K_{lfm}	linear FM signal modulation rate	Hz ²
K_p	radiometric resolution	dB
ΔK_p	relative radiometric resolution	dB
K_{pfd}	linear FM signal predistortion function modulation rate	Hz ²
K_w	refractive index of water	
LO	local oscillator	
L_a	compressed pulse average loss	dB
L_{ad}	decorrelated compressed pulse average loss	dB
L_d	decorrelated compressed pulse loss	dB
L_p	compressed pulse peak loss	dB
L_{pd}	decorrelated compressed pulse peak loss	dB
L_r	finite bandwidth loss	dB
L_s	system loss	dB
L_{SNR}	signal-to-noise ratio loss	dB
MACSIM	Millimetre wave Active Cloud Structure Imaging Mission	
m	along track integration length available samples	

M	interference and thermal noise correlation matrix	
M	cloud liquid water constant	gm m^{-3}
NASA	National Aeronautics and Space Administration (U.S.A.)	
NASDA	National Aeronautics and Space Development Agency (Japan)	
n	multiple look average processing available samples	
n_{rb}	number of range bins	
NEXRAD	Next Generation Radar	
$\frac{N}{V}$	density of raindrops per unit volume	m^{-3}
$n_0^2(t)$	average thermal noise output power	W
N_0	thermal noise power spectral density	W/Hz
$N(f)$	noise power spectral density	W/Hz
PRI	pulse repetition interval	s
PRF	pulse repetition frequency	Hz
P_{av}	average power	W
P_n	noise power	W
P_r	received power	W
P_r	rainfall return power	W
P_s	Earth's surface return power	W
P_t	transmitted power	W
P_0	transmitter peak power	W
q	instantaneous frequency nominal bandwidth coefficient	
RA	Radar Altimeter	
RADAR	Radio Detection and Ranging	
RSL	FM signal compressed pulse range sidelobe level	dB
R_x	radar receiver	
r	range	m
Δr	range resolution	m
Δr_{rb}	range bin shift	m
Δr_{bl}	blind layer	m
r_r	rainfall range	m
r_s	surface range	m
r_{max}	maximum detection range	m
R	rainfall rate	mm/h
$R_s(t)$	autocorrelation function of $s(t)$	
$R_{\tilde{s}, \tilde{s}w}(t)$	crosscorrelation between $\tilde{s}(t)$ and $\tilde{s}(t)w(t)$	
$R_1(t)$	mismatched linear FM signal compressed pulse	V
$R_3(t)$	crosscorrelation between mismatched linear FM matched filter and linear FM signal predistortion function	V

SAW	surface acoustic wave	
SEASAT	NASA Remote Sensing Satellite launched in 1978	
SNR	signal-to-noise ratio	dB
$s(t)$	radar signal	V
$\tilde{s}(t)$	radar signal complex envelope	V
$\tilde{s}_a(t)$	asymmetric FM signal complex envelope	V
$s_d(t)$	altimeter full-deramped signal	V
$\tilde{s}_d(t)$	altimeter full-deramped signal complex envelope	V
$\tilde{s}_{dt}(t)$	radar signal with amplitude and phase distortion	V
$s_i(t)$	in-phase radar signal complex envelope component	V
$\tilde{s}_{lfm}(t)$	linear FM signal complex envelope	V
$s_{LO}(t)$	local oscillator reference signal	V
$\tilde{s}_{pf}(t)$	linear FM signal predistortion function complex envelope	V
$s_q(t)$	quadrature radar signal complex envelope component	V
$s_r(t)$	radar received signal	V
$s_0(t)$	radar signal reception filter signal output	V
$\langle s_0(t) ^2 \rangle$	ensemble average of FM signal compressed pulse instantaneous power	W
$s_{0a}(t)$	asymmetric FM signal compressed pulse	V
$s_{0a}(t)$	ARMAR amplitude modulated signal compressed pulse	V
$s_{0lfm}(t)$	linear FM signal compressed pulse	V
S_{min}	minimum detectable signal	W
$S(f)$	radar signal spectrum	
$\tilde{S}(f)$	radar signal complex envelope spectrum	
$S(x)$	Fresnel integral imaginary component	
$\tilde{S}_d(f)$	altimeter full-deramped signal complex envelope spectrum	
$\tilde{S}_w(f)$	altimeter full-deramped signal weighted complex envelope spectrum	
TRMM	Tropical Rainfall Measuring Mission	
TWT	Travelling Wave Tube	
T_x	radar transmitter	
t	time	s
t_d	altimeter received linear FM signal delay	s
t_h	altimeter local oscillator reference signal delay	s
t_{max}	maximum peak signal-to-noise ratio instant	s
T	radar signal width	s
TB	radar signal time-bandwidth product	
T_p	altimeter transmitted linear FM signal width	s
T_{LO}	altimeter local oscillator reference signal width	s
T_{sys}	system noise temperature	K

v_{sat}	satellite speed	m/s
$v(t)$	scattering fluctuation term	
W_{opt}	optimum complex weighting scheme	
$w(t)$	weighting function	
$w_a(t)$	amplitude weighting function	
$w_a(t)$	ARMAR amplitude modulation function	
$W(r)$	range weighting function	
$W_f(f)$	frequency weighting function	
z	pulse volume altitude	m
Z_e	equivalent radar reflectivity	dBZ
Z_{min}	single pulse sensitivity	dBZ
ΔZ_{min}	relative single pulse sensitivity	dB
α	attenuation coefficient	dB/km
α_C	cloud attenuation coefficient	dB/km
α_R	rainfall attenuation coefficient	dB/km
$\chi(\tau, v)$	ambiguity function	
δ	linear FM signal predistortion function width	s
$\delta\Delta f$	linear FM signal predistortion function time-bandwidth product	
ϕ	radar signal phase	radians
ϕ	azimuth angle	radians
ϕ_B	antenna -3 dB beamwidth (azimuth)	radians
η	volumetric reflectivity	m^2/m^3
$\hat{\eta}$	estimated volumetric reflectivity	m^2/m^3
η_{dc}	DC conversion efficiency	
λ	transmitted signal wavelength	m
θ	elevation angle	radians
θ_B	antenna -3 dB beamwidth (elevation)	radians
$\theta(t)$	radar signal phase	radians
$\theta_a(t)$	asymmetric phase term	radians
$\theta_{dt}(t)$	phase distortion term	radians
$\theta_{lfm}(t)$	linear FM signal phase	radians
$\theta_{pf}(t)$	linear FM signal predistortion function phase	radians
ρ	FM signal compression ratio	
ρ_{eff}	FM signal effective compression ratio	
$\rho(t)$	correlation coefficient	
σ	radar cross section	m^2
σ	standard deviation of Gaussian Doppler spectrum	
σ^0	Earth's surface reflectivity	

$\sigma(f)$	correlation coefficient Fourier transform	
τ	time	s
τ	radar signal width	s
τ_d	decorrelation time	s
τ_{\max}	FM signal compressed pulse peak instant	s
τ_w	FM signal correlation width	s
$\tau_{-3\text{dB}}$	FM signal compressed pulse -3 dB width	s
$\Delta\tau_{-3\text{dB}}$	relative FM signal compressed pulse -3 dB width	
ν	Doppler frequency	Hz
Ω	solid angle	steradians

1 INTRODUCTION

Clouds and rainfall have a direct impact on the Earth's global hydrological cycle between the oceans and the atmosphere, the global heat balance, and eventually, they are key parameters which affect climate changes in our planet. A better knowledge and understanding of these processes would improve weather and climatic modelling, which would be to the advantage of several fields of human activity, such as agriculture and ecology. Furthermore, it could contribute to better long-term forecasting of different meteorological related adversities, such as tornadoes, droughts and floods.

Radars have the capability of quantitatively measuring rain and clouds. In particular, a weather radar on board a satellite covering the whole globe could supply invaluable meteorological data on a global scale. Nonetheless, several technical design difficulties must have been overcome over the years and have delayed the construction of such an instrument. The first dedicated rain radar is expected to be launched into space in 1997. It is the purpose of this PhD Thesis to carry out a detailed review of these technical difficulties, especially with regard to spaceborne meteorological radar waveform design issues in order to enhance the instrument measuring capabilities.

f
⊕

1.1 Historical Background

Radars (RADio Detection And Ranging) transmit radio waves and measure their returned scattered energy by distant targets. As soon as radar technology was initially developed during World War II, meteorological phenomena began to appear on radar displays. Some power calculations at the early radar frequencies showed that rain and thunderstorms could backscatter sufficient energy to give detectable echoes, which could in some cases mask targets such as aircraft. This original hazard for military radar designers was turned into a potential and powerful tool by meteorologists. Nowadays, several ground-based weather radar networks (i.e. NEXRAD) with an extensive territorial coverage are in operation and obtain a large amount of real time meteorological data. Therefore, a term like weather forecast has been transformed into weather nowcast, since the networks can provide an accurate description of the current state of the weather. Nevertheless, the fact that the vast majority of the Earth's surface is covered by oceans and inhospitable regions such as jungles, deserts and ice caps, makes it impossible to cover the whole extent of the globe with ground-based meteorological

radars. Consequently, remote sensing of the Earth is the most suitable alternative to collect weather data on a global scale, although with a coarser spatial and temporal sampling resolution.

The first feasibility studies for spaceborne meteorological radars were undertaken in the mid 50s. Technological limitations seemed to be impossible to overcome until new research in the field was carried out in the 70s. In 1980, a conference on Precipitation Measurements from Space settled the requirements for the application of global precipitation data to climate and weather. A few years later, a number of proposals were made and two of them have already been specified in detail by the U.S.A., Japan and France: TRMM (Tropical Rainfall Measurement Mission) developed by NASA and NASDA and BEST (Bilan Energétique du Système Tropical) developed by CNET-CNRS. The TRMM satellite is at the present moment under construction and is expected to be launched in August 1997.

On the other hand, one of the critical difficulties of spaceborne meteorological radars arises from the inherent characteristics of the system. Cloud and precipitation fields are to be measured over the Earth's surface, but the energy backscattered by the ground is much greater than that of the rain. Hence, the system measurement dynamic range needs to be significantly large in order to avoid the surface return obscuring the rainfall. Furthermore, the fact that power resources are limited on board a satellite trades off the attainment of the required cell measurement resolution. Hence, the radar waveform is one of the key system features which needs to be carefully designed and selected in order to guarantee the success of cloud and precipitation measurement over different heights and the required range of detectable types of cloud and rainfall rates.

1.2 Objectives and Thesis Layout

The primary purpose of this research has been to develop novel frequency modulation functions and range sidelobe reduction processing techniques to accomplish the scientific requirements in order to profile cloud and precipitation fields from spaceborne meteorological radars. A description of two recent studies commissioned by the European Space Agency on design issues for spaceborne radar meteorology (Rain Rate Observation by Radar Altimeter, ESTEC Contract No. 10882/94/NL and MACSIM: Cloud Profiling Radar, ESTEC Contract No. 11751/95/NL), carried out by University College London in collaboration with other European Aerospace Companies are also

presented in this Thesis.

A detailed review of classical radar frequency modulation and pulse compression theory has been carried out, with particular attention to range sidelobe reduction techniques developed over the last 50 years. The specifications and requirements for meteorological radars on board a satellite have also been extensively analysed in relation to the selection of the most suitable modulation candidates in order to guarantee the collection of cloud and precipitation measurements on a global scale.

After a brief introduction of the needs of spaceborne rain radars, Chapter 2 addresses the specifications and the requirements reported in the literature. A comparison of the technical capabilities between the currently specified rain radar missions is presented. A review of the surface interference through range and antenna sidelobes, which impose severe restrictions on the system design, is carried out.


Chapter 3 introduces a concise overview of linear FM classical theory (from the matched filter to the waveform ambiguity function), with particular attention to the signal formulation in the time and frequency domain.

A review of different range sidelobe reduction techniques reported in the literature is presented in Chapter 4. The two main reduction techniques, weighting (time and frequency domains) and the design of nonlinear FM waveforms are described in detail and the influence of Doppler frequency offsets assessed.

A novel waveform design technique based on existing predistorted linear FM theory which allows ultra low range sidelobe levels is reported in Chapter 5. A new approach for the study and design of linear FM predistortion functions is developed and an analytical expression for the point target response is obtained. It is shown that different constituent terms of the predistorted signal compressed pulse are of the same shape but opposite sign, which cancel leaving a significantly lower range sidelobe structure than the linear FM point target response. The performance of the new signals subject to Doppler frequency offsets is also studied.

The fact that meteorological phenomena are only present before the Earth's surface return gives the possibility of employing nonlinear frequency modulated signals which produce asymmetric point target responses. Thus, the signal compressed pulse may be compliant with the range sidelobe level requirement before the leading edge of the compressed ground return, and not elsewhere. A novel design procedure for both asymmetric and symmetric nonlinear FM signals is presented in Chapter 6, which

consists of the modification of the linear FM signal phase of a given time-bandwidth product by a phase polynomial of terms of even or odd powers. It is also shown that the resulting asymmetric FM signal is Doppler invariant.

Chapter 7 consists of a research study carried out in order to analyse waveform design options for a rain mode for the RA-2 radar altimeter on board ESA's ENVISAT satellite. However, the rain mode is restricted by the altimeter mode specification and needs to be devised with the least impact to its original design. Some modifications to the normal altimeter full deramp mode of operation are necessary in order to guarantee the feasibility of rain measurement. The most suitable option is to increase the width[?] of the Local Oscillator Reference Signal to allow the deramp of the whole extent of the range window in one pulse scan. Since the rain data is retrieved from the power spectrum, it is possible to combine amplitude and phase weighting schemes which are capable of enhancing and optimising rain detectability. 

Chapter 8 describes waveform design issues and provision alternatives for ESA's Pre Phase A Study on a Millimetre wave Active Cloud Structure Imaging Mission. The required range resolution for cloud measurements can be achieved with a relatively small time-bandwidth product, but does not allow the achievement of the -80 dB range sidelobe level specification. It is shown that an amplitude modulated linear FM signal (implemented in NASA's ARMAR Mission) is capable of attaining such a specification with better radiometric resolutions than the unmodulated pulse option.

Finally, the conclusions in Chapter 9 highlight the achievements of this research and introduce some suggestions for further work on the spaceborne meteorological radar waveform design field.

2 SPACEBORNE METEOROLOGICAL RADAR

The basic spaceborne meteorological radar fundamental concepts are reviewed in this chapter. The instrument constraints and requirements are followed by a technical description and comparison of two existing rain radar Missions. The analysis of the different types of Earth's surface interference is based on the examination of the meteorological radar equation and the returned power levels, taking into consideration the geometry of the system. These sources of interference impose severe restrictions on the design of the radar waveform and the antenna radiation pattern.

2.1 Introduction

The advantages of measuring meteorological phenomena from space are obvious when the primary objective is cloud and precipitation field profiling on a global scale. In addition, an active radar has important advantages over other passive remote sensing techniques, such as visible and infrared sensors or microwave radiometers. The radar requirements and specifications are briefly reviewed in this section, along with a description of the main technical features of two proposed spaceborne radar Missions.

2.1.1 Need for Spaceborne Meteorological Radars

Rainfall rate is defined as the volume of liquid water that falls through a unit area per unit time and normally measured in millimetres per hour (mm/h). Clouds cover 50% of the Earth's surface on average (Figure 2.1). However, it has been assessed that the percentage of the Earth's surface under precipitation at a particular time is much less than 5%. Rainfall over the tropical regions (between 30°N and 30°S) results in more than 60% of the global precipitation. Hence, tropical rain has a major and decisive impact on the Earth's global hydrological cycle and heat balance, and any local alteration may directly influence global climatic changes. The fact that the tropical area is mostly occupied by oceans, jungles and deserts, makes it impossible to monitor its rainfall with ground-based sensors. Therefore, it is no surprise that tropical rainfall has been targeted by remote sensing Missions like TRMM and BEST. Frequent monitoring and rain mapping over the Tropics would supply meteorologists with inestimable data to derive improved climate models.



Figure 2.1. METEOSAT optical image (source: University of Nottingham).

Remote sensing of clouds and precipitation can be divided into passive (visible/infrared sensors and microwave radiometers) and active (radar) techniques. Visible and infrared sensors take advantage of the indirect relation between external radiation reflected by clouds and probability of rainfall (related to the amount of cloudiness) on satellite images. However, these algorithms, which need to be devised for a given region and may not be the same for a different location or season, lack in accuracy. Microwave radiometers measure and quantify cloud and rain thermal absorption from the Earth microwave radiation, giving better results over ocean than land surfaces (due to better radiation properties). A thorough description of these remote sensing passive methods can be found in [Collier et al., 1990].

The radar, being an active sensor, discriminates backscattered energy from the hydrometeors from different ranges in the precipitation field. Thus, it has the capability to profile the cloud and precipitation field, which is not possible with either of the passive techniques. Furthermore, some of the parameters measured by the radar (i.e. radar reflectivity and spectrum spread) are directly related to the cloud liquid water content, rainfall rate and the motion of hydrometeors.

Several rain retrieval techniques have been proposed in the literature. Direct methods estimate the rainfall rate directly through the calibrated radar equation. Surface reference methods employ measurements of the surface target (free of precipitation) as a reference in order to estimate the two-way path attenuation as a function of rainfall rate. Dual frequency measurements have also been proposed in order to reduce uncertainties in the estimation. All the reported methods rely on the reflectivity and attenuation relations as a function of rainfall rate with different degrees of accuracy depending on the radar operative conditions.

Although the meteorological radar can provide more information than any other

technique, a combination of weather data collected by active and passive sensors appears to be the optimum solution in order to supply a quantitative cloud and rain estimation.

2.1.2 Spaceborne Rain Radar Requirements (TRMM and BEST Missions)

Having stated the importance of tropical rainfall and the unique capabilities of spaceborne rain radars in its measurement, the scientific requirements and specifications of two proposed rain radar Missions are described in detail along this section. A description of a cloud profiling radar Pre Phase A Study can be found in Chapter 8.

The Tropical Rainfall Measuring Mission (TRMM), a joint scientific cooperation programme between NASA (National Aeronautics and Space Administration, USA) and NASDA (National Aeronautics and Space Development Agency, Japan), was originally proposed in 1986. The TRMM main objective is to “determine the distribution and variability of precipitation and latent-heat release on a monthly average over areas of about 10^5 km^2 , for use in improving short-term climate models, global circulation models and in understanding the hydrological cycle, particularly as it is affected by tropical oceanic rainfall and its variability” [Simpson et al., 1988].

The first feasibility study of the TRMM satellite and its spaceborne rain radar dates from 1987 [Okamoto et al., 1988] (briefly summarised in [Nakamura et al., 1990]). Design technical features and critical issues ranging from the transmitted frequency choice to power consumption and weights were comprehensively reviewed. The satellite will also carry on board a Visible/Infrared Scanner, a Microwave Imager, a Passive Scanning Radiometer and a Lightning Imaging Sensor. The TRMM satellite is expected to be launched in August 1997 from Tanegashima Space Centre, Kagoshima, Japan. Information about the Mission and its new developments can be found on line through the Internet in the following site: http://trmm.gsfc.nasa.gov/trmm_office/index.html.

The Bilan Energétique du Système Tropical Mission was initiated in 1988 by CNES (Centre National d'Etudes Spatiales, France) and ESA (European Space Agency) in collaboration with other Aerospace Companies. Its main purpose is to gather Tropical rainfall data for a “contribution to monthly mean rainfall estimates within sub-domains of about $500 \times 500 \text{ km}^2$ in the tropical belt” [Marzoug et al., 1988]. A full account of the technical features of the rain radar can be found in [Mavrocordatos and Gaille, 1993]. Although the BEST Mission has not yet reached the construction stage, a breadboard system to assess the radar future performance has already been built.

A comparison between the system configurations of both Missions is shown in Table 2.I. It should be noted that these parameters have been extracted from their feasibility study proposals and may have been altered during the construction stage. The main difference between TRMM and BEST Missions in relation to this work is found in the rain radar waveform implemented. The TRMM radar will transmit an unmodulated RF short pulse to attain the required range resolution. The BEST rain radar has been designed to take advantage of the *pulse compression technique*. As will be reviewed later in this thesis, the frequency modulation of the pulse carrier frequency enables the radar to attain the same range resolution properties with a longer RF pulse and thus a less demanding peak power specification. Therefore the radar transmitter power capabilities are used more efficiently, which allow to reduce the necessary amount of power supply on board the satellite in comparison to the unmodulated pulse system alternative.

Table 2.I: Comparison between TRMM and BEST Mission configurations

	<i>TRMM</i>	<i>BEST</i>
frequency	13.8 - 24.15 GHz	13.75 - 13.76 GHz
satellite altitude	320 km	430 km
scan swath	220 km	200 km
scan angle	$\pm 17^\circ$	$\pm 14^\circ$
range resolution	250 m	250 m
horizontal resolution	~ 4 km (nadir)	~ 2.9 km (nadir)
range of measurable rain	0.5 to 50 mm/h	0.6 to 60 mm/h
independent samples	64	60
antenna gain	47.5 dB	60 dB
antenna sidelobe level	< -30 dB	< -30 dB
antenna beamwidth (-3 dB)	$0.76^\circ \times 0.76^\circ$	$0.18^\circ \times 0.18^\circ$
transmitted RF power	1500 W	300 W
pulse width	1.67 μ s	1.67 μ s (compressed)

2.2 Meteorological Radar Equation

The first power radar equation in meteorology which gave a good agreement with available radar rainfall measurements is due to Probert-Jones [Probert-Jones, 1962]. The development of the equation has been reproduced several times in the literature [Meneghini and Kozu, 1990]. The meteorological radar equation is the corner stone in

the assessment of the requirements of any spaceborne meteorological radar. Therefore, it is the purpose of this section to derive this equation in a straightforward manner to address further research on the specifications and capabilities to be achieved by the instrument.

The reflected power from a differential volume inside a pulse volume filled with hydrometeors is given by:

$$dP = \frac{P_t G(\theta, \phi) \eta}{4\pi} d\Omega dr \quad (1)$$

where P_t is the transmit power, $G(\theta, \phi)$ the antenna gain pattern, η the cloud/rainfall radar reflectivity (area per unit volume), θ the elevation angle, ϕ the azimuth angle, $d\Omega$ a solid angle element and dr a range element. It is assumed that the radar reflectivity factor η remains constant inside the pulse volume under consideration.

The backscattered power from the differential volume received at the radar is given by:

$$dP_r = \frac{P_t G(\theta, \phi) \eta}{4\pi} \cdot \frac{A_{eff}(\theta, \phi)}{4\pi r^2} d\Omega dr \quad (2)$$

where A_{eff} is the antenna effective area and r the range to the target volume (from the radar). The relation between the antenna effective area and its gain at the polar angles θ and ϕ is:

$$A_{eff}(\theta, \phi) = \frac{\lambda^2}{4\pi} G(\theta, \phi) \quad (3)$$

where λ is the transmitted wavelength.

The received power returned from the illuminated pulse volume is then obtained by integration and completed by the addition of an attenuation term due to the two way path ray penetration inside the cloud/precipitation field:

$$P_r = \int_V dP_r = \frac{P_t \lambda^2}{(4\pi)^3} \int_{\Omega} G^2(\theta, \phi) d\Omega \int_r \frac{1}{r^2} dr \eta e^{-0.2 \ln 10 \int_{r'} \alpha dr} \quad (4)$$

where r' represents the penetration depth and α the rainfall attenuation coefficient. It is common to approximate the antenna radiation pattern by a two-dimensional Gaussian power distribution (pencil-beam approximation):

$$G = G_0 e^{-\ln 2 \left(\left(\frac{2\theta}{\theta_B} \right)^2 + \left(\frac{2\phi}{\phi_B} \right)^2 \right)} \quad (5)$$

where G_0 is the antenna maximum gain, and θ_B and ϕ_B the half-power beamwidths along the two principal directions. The solution to the angular integral is given by:

$$\int_{\Omega} G^2(\theta, \phi) d\Omega = \frac{\pi G_0^2 \theta_B \phi_B}{8 \ln 2} \quad (6)$$

The range integral needs to be evaluated over the pulse volume, assuming that the range r is defined as the range to the centre of the pulse volume:

$$\int_{r - \frac{cT}{4}}^{r + \frac{cT}{4}} \frac{1}{r^2} dr \approx \frac{cT}{2r^2} \quad (7)$$

where c is the propagation speed and T the pulse width. Therefore, the meteorological radar equation is finally given by:

$$P_r = \frac{P_t \lambda^2 G_0^2 c T \theta_B \phi_B}{1024 \pi^2 \ln 2 r^2 L} \eta e^{-0.2 \ln 10 \int_{r'} \alpha dr} \quad (8)$$

where L accounts for the system losses.

2.3 Signal-to-Noise Ratio

The design of the radar must ensure the detectability of the Mission required range of measurable cloud reflectivities or rainfall rates. This range normally varies from light rain (tenths of mm/h) to severe storms (rainfall rates between 50 and 60 mm/h) in the case of rain, and from reflectivities between -40 to 30 dBZ in the case of clouds.

Therefore, the radar configuration needs to allow that all the different cloud/rainfall intensities will backscatter sufficient power, and hence provide sufficient signal-to-noise ratio to be detected. This section describes the predicted rainfall signal-to-noise ratios for both TRMM and BEST Missions.

In order to evaluate the signal-to-noise ratio for the required range of rainfall rates, it is necessary to review some approximations for rain backscattering and absorption coefficients in the literature. When the pulse volume is filled with hydrometeors, their radar reflectivity is given by:

$$\eta = \int_0^{\infty} \sigma(D)N(D)dD \quad (9)$$

where $\sigma(D)$ is a D diameter raindrop cross section and $N(D)dD$ the number density of raindrops with diameters in the range between D and $D + dD$ per unit volume. This radar reflectivity is related to the equivalent reflectivity factor Z_e :

$$\eta = \frac{\pi^5}{\lambda^4} |K_w|^2 Z_e \quad (10)$$

where K_w is the refractive index of water. The equivalent reflectivity Z_e is mainly dependent on the wavelength and the rainfall rate R , and the relationship Z_e - R is normally approximated by a power law relation given by:

$$Z_e = \alpha R^\beta \quad (11)$$

The rain attenuation coefficient is also dependent mainly on the wavelength and rainfall rate, and also approximated by a power law relation given by:

$$\alpha_R = aR^b \quad (12)$$

The carrier frequency is determined by the satellite antenna size and the meteorological horizontal resolution requirement (approximately of 4 km). Allocated frequency bands for active Earth remote sensing make a frequency of 14 GHz an optimum choice for the rain radar, due to its relatively small wavelength attenuation [Li et al., 1988]. The η - R and the α_R - R relationships for a frequency of 13.8 GHz (a frequently assumed frequency for spaceborne rain radar proposals) are due to the works

of [Im et al., 1987]¹ and [Olsen et al., 1978], and given by:

$$\eta(R) = 4.757 \cdot 10^{-7} R^{1.54} \tag{13}$$

$$\alpha_R(R) = 0.032 R^{1.124} \tag{14}$$

Cloud reflectivity and attenuation empirical relations are given in Chapter 8. Consequently, the rainfall return signal-to-noise ratio is given by the ratio between the received power level P_r and the system noise power level P_n , and can be expressed as:

$$SNR = \frac{P_r}{P_n} = \frac{P_r}{kT_{sys}B_nF} \tag{15}$$

where k is the Boltzmann constant, T_{sys} the system noise temperature, B_n the receiver noise equivalent bandwidth and F the receiver noise figure. A comparison between the predicted signal-to-noise ratios for TRMM and BEST Missions is shown in Figure 2.2. The design of both instruments make it possible to achieve successful detection of rain in the range between 0.5 and 60 mm/h.

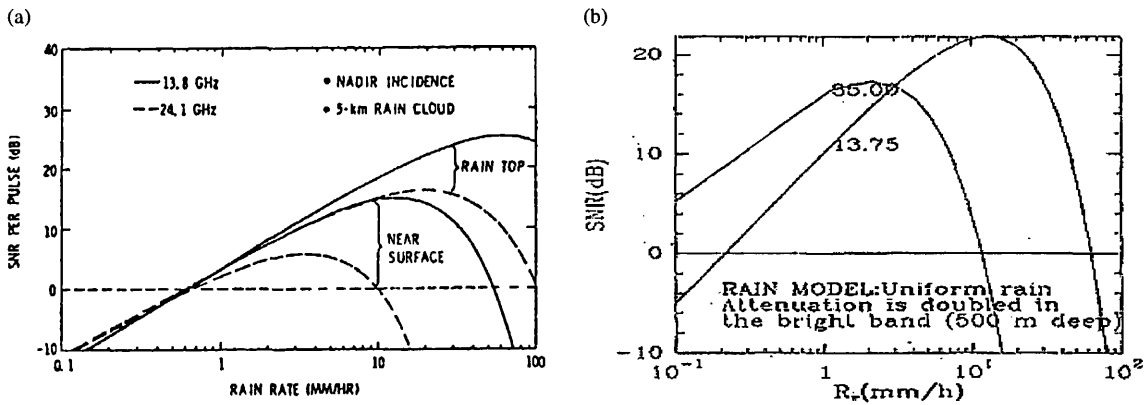


Figure 2.2. Predicted signal-to-noise ratio for: (a) TRMM rain radar (5-km rain cloud height and nadir incidence). Reproduced from [Li et al., 1988]; (b) BEST rain radar (power measurement at the bottom of a 5 km depth rain layer with uniform rainfall rate). Reproduced from [Marzoug et al., 1988].

¹Empirical fits of the Joss experiment supplied by Ulbrich.

2.4 Earth Surface Clutter Interference

Although there is sufficient rainfall returned power to make the signal detectable, it is very low compared to the returned power from the Earth's surface, especially for small cloud and rain reflectivities. The dynamic range of the measurements can easily achieve a figure of 60 dB. The ground clutter can easily be rejected by gating in the unmodulated pulse system alternative. However, for pulse compression systems, the ground point target response is overlapped with those of the rain, and can interfere and obscure the measurement (linear FM signal theory is developed in Chapter 3).

Pulse compression systems are characterised by the modulation of the carrier frequency of the radar pulse, so that it is possible to attain better range resolutions with a less demanding peak power requirement, increasing the number of available independent samples (section 2.5). However, when the returned echoes are processed in the receiver, range sidelobes appear on both sides of the pulse main peak response, being a source of self-clutter interference. On the other hand, the sidelobes of the antenna radiation pattern must also be under a certain level to prevent surface interference.

In order to characterise the specifications imposed on the radar waveform and the antenna radiation pattern by the ground clutter return, the spaceborne surface radar equation is derived and compared to the levels of rainfall return power in this Section.

2.4.1 Earth Surface Radar Equation

In order to calculate the surface radar equation, equal steps are followed as for the calculation of the meteorological radar equation (Section 2.2), but considering now the surface integration over the antenna footprint (the area intercepted by the antenna beamwidth on the ground). The radar cross section of the surface is defined as the backscattering coefficient per unit area, $\sigma^0(\theta)$. A particular case of a sideways looking radar and an antenna radiation pattern which has symmetric Gaussian distribution along the two principal directions are assumed. Thus, the surface return power, according to the system geometry shown in Figure 2.3, is given by:

$$P_s = \frac{P_t \lambda^2 G_0^2 \theta_B^2}{512 \pi^2 \ln 2 h^2 \sec \theta} \sigma^0(\theta) e^{-0.2 \ln 10 \int_{(h-h_{st}) \sec \theta}^{h \sec \theta} \alpha_R dr} \quad (16)$$

where h is the satellite altitude and h_{st} the storm top height.

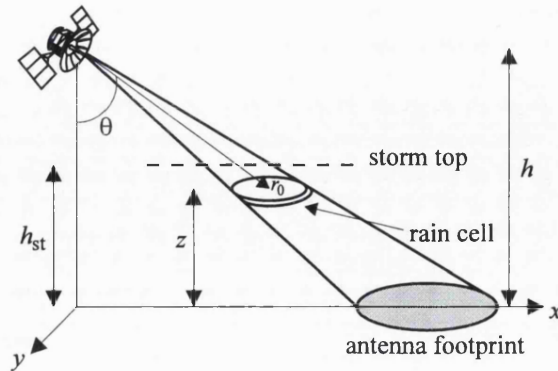


Figure 2.3. Spaceborne meteorological radar target scenario and geometry.

The surface radar cross section σ^0 depends on the type of surface (land or sea), its roughness, the transmitted frequency and the angle of incidence. In the following sections, surface power calculations are assumed to be over the sea surface, with a scattering model described in the TRMM design proposal [Manabe and Ihara, 1988].

2.4.2 Interference through Range Sidelobe

When the pulse compression technique is implemented by frequency modulating the radar waveform, range sidelobes appear on both sides of the filtered pulse in reception. Since there is a very significant difference between the backscattered power from the precipitation and the Earth's surface, the compressed pulse range sidelobes must be kept at a very low level. Otherwise, ground clutter range sidelobes could mask the precipitation return, in particular at low heights and low rainfall rates or cloud reflectivities. The rainfall to surface power ratio gives a good estimate of the range sidelobe level which needs to be achieved in order to prevent Earth's surface clutter interference. The rain to surface power ratio is given by (Eq. 8 and Eq. 16):

$$\frac{P_r}{P_s} = \frac{cTh^2}{2(h-z)^2 \sec(\theta)} \frac{\eta(R)}{\sigma^0(\theta)} e^{0.2 \ln 10 \alpha_R \frac{z}{10^3} \sec(\theta)} \quad (17)$$

where z is the pulse volume altitude.

TRMM Mission rain to surface power ratio contour maps are displayed in Figure 2.4, considering a compressed pulse range sidelobe level factor of 50 dB. Hence, it

should be noted that the 0 dB contour shown in the plots represent a power level 50 dB below the ground power level.

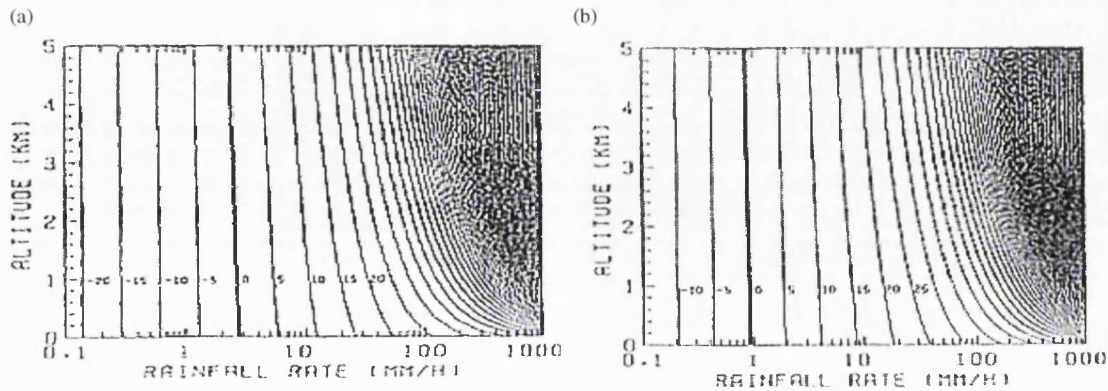


Figure 2.4. P_r/P_s ratio contour maps (in dB) for sea clutter through range sidelobe at 13.8 GHz: (a) Scan angle $\theta = 0^\circ$; (b) Scan angle $\theta = 15^\circ$. Reproduced from [Manabe et al., 1988].

In order to prevent the Earth's surface return interfering the rainfall signal through range sidelobe, the compressed pulse sidelobe level must be at least 60 dB below the main peak. Such a stringent specification has not yet been achieved with the current state of technology. Due to the difficulty of generating a FM waveform giving the required compressed pulse range sidelobe level of -60 dB, TRMM designers ruled out the implementation of the pulse compression technique. Hence, the specified range resolution of 250 m is obtained by transmitting an unmodulated short pulse (1.67 μ s). Pulse compression range sidelobe level considerations in terms of Doppler frequency are developed in section 2.5.

2.4.3 Interference through Antenna Sidelobe

The ground backscattered power received through antenna sidelobes can also interfere with cloud/rain rate measurements. For off-nadir angles, the ground clutter which interferes a particular pulse volume at a range r from the satellite consists of an annular area on the ground at the same range r [Manabe and Ihara, 1988]. The width of this annular area is determined by the extent of the transmit pulse width ($r \pm cT/2$). Therefore, power from the pulse volume (through antenna main lobe) is received simultaneously with power from that particular area of ground clutter (through antenna sidelobes).

Manabe and Ihara calculated the P_r/P_s ratio for an antenna with an isotropic sidelobe pattern of -35 dB. Some contour maps of the P_r/P_s ratio are shown in Figure

2.5. They concluded that there is a critical altitude below which light rainfall rates are interfered with by ground clutter through the antenna sidelobes. However, if the sidelobes of the antenna radiation pattern are kept below -30 dB, the interference has no significant impact on most measurable rainfall rates. A different study [Hanado and Ihara, 1992] considered a more realistic antenna radiation pattern (a phased array fed with a Taylor distribution). They showed that for a sidelobe level of -30 dB, the critical interference height (depending on the scan angle) extends to 1.2 km over the sea surface for an incidence angle of 17° .

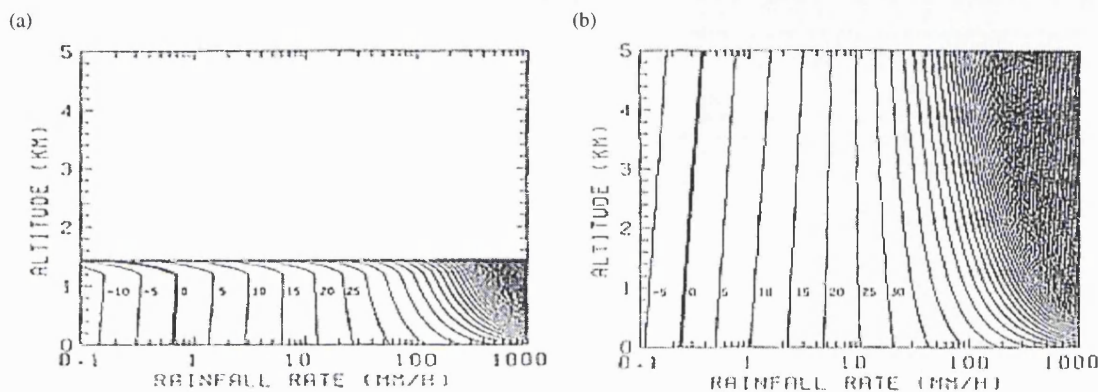


Figure 2.5. P_r/P_s ratio contour maps (in dB) for sea clutter through antenna sidelobe at 13.8 GHz. (a) Scan angle $\theta = 0^\circ$; (b) Scan angle $\theta = 15^\circ$. Reproduced from [Manabe et al., 1988].

2.5 Signal Doppler Spectrum

In the case of meteorological targets, the returned signal from a pulse volume consists of a number of randomly distributed scatterers. As the position of these scatterers varies at every scan, successive echoes from the same pulse volume fluctuate. Therefore, a sufficiently large number of independent samples are required in order to estimate the true average of the precipitation within the pulse volume. The rate of signal fluctuation is directly related to the particle relative movement rate inside the pulse volume and its measurement must contain significant meteorological information. The absolute motion of the particles in the pulse can be measured through the Doppler spectrum of the returned signal.

In order to derive an expression for Doppler frequency offsets, a point target at a distance r from the radar is considered. The phase position of a stationary target relative to the radar is $4\pi r/\lambda$. When the target is in motion with respect to the radar with a radial

velocity of $v = dr/dt$, its phase position changes proportionally. The phase change with time represents angular frequency [Levanon, 1988], given by:

$$2\pi f = -\frac{d\phi}{dt} = -\frac{4\pi v}{\lambda} \quad (18)$$

Hence, the resultant Doppler frequency offset can be expressed as:

$$f_d = -\frac{2v}{\lambda} \quad (19)$$

Horizontal winds may have significant velocity tangential components, especially at off-nadir pointing angles which can broaden the Doppler spectrum width by hundreds of Hz. The hydrometeors vertical motion may reach velocities in the range of ± 10 m/s which translate into Doppler shifts in the order of 1 kHz. Independently from the intrinsic motion of the backscatterers in the pulse volume, an extra Doppler frequency component is introduced by the spaceborne rain radar platform motion. Assuming without loss of generality satellite motion along the x axis, the Doppler offset as a function of elevation and azimuth is given by (a detailed calculation can be found in Appendix A):

$$f_d = -\frac{2v_{sat}}{\lambda} \sin\theta \cos\phi \quad (20)$$

It must be pointed out that the Doppler frequency caused by the satellite motion is independent of slant range and is only dependent on the scanning angles. For nadir pointing, the Doppler spread over the antenna footprint is given by:

$$\Delta f_d = -\frac{4v_{sat}}{\lambda} \sin\frac{\theta_B}{2} \quad (21)$$

Assuming typical parameters of the TRMM system, the Doppler spread at the edges of the footprint reaches a value of 8 kHz. A Doppler frequency map is shown in Figure 2.6, as a function of the surface x and y coordinates. Geometrically, the iso-Doppler contours correspond to hyperbolas on the ground. For the TRMM system geometry, Doppler shifts caused by the platform motion can reach values as large as 300 kHz, which represent the main Doppler frequency component and may amount to a significant fraction of the signal bandwidth.

Doppler offsets degrade the performance of pulse compression ^{receivers} in terms of the

waveform range sidelobe level (Chapter 4). Therefore, an increase of the compressed pulse range sidelobe level is expected for off-nadir pointing angles. It has generally been assumed that the range sidelobe level requirement for spaceborne rain radars (-60 dB, Section 2.4.2) remains constant as a function of Doppler frequency. However, the surface return power is weaker for scanning angles departing off-nadir pointing, since its reflectivity decreases with incidence angle. Assuming typical parameters for the BEST Mission, the pulse illumination remains in the beamwidth limited region and no further power reduction due to pulse limited illumination is considered.

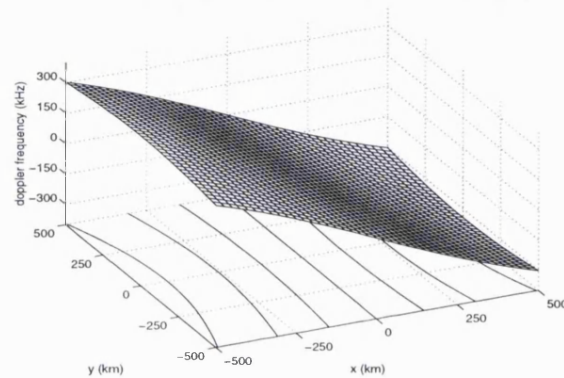


Figure 2.6. Doppler frequency offset map as a function of ground coordinates.

In order to calculate the range sidelobe level specification as a function of Doppler frequency, the surface reflectivity variation as a function of incidence angle model assumed for the TRMM clutter evaluation [Manabe and Ihara, 1985] has been adopted. The reflectivity model for elevation angles below 20° [Valenzuela, 1978] is based on ocean surface radar cross section experimental data at 13.9 GHz [Schroeder et al., 1984]. The ocean surface reflectivity model is given by:

$$\sigma^0(\theta) = \sigma^0(0) \sec(\theta)^4 e^{-\frac{\tan(\theta)^2}{S^2}} \quad (22)$$

where S^2 is the total variance of the surface slopes. The interference through range sidelobe (Eq. 17) has been evaluated at ground level as a function of Doppler frequency and rainfall rate, without considering attenuation in the precipitation field (Figure 2.7(a)).

It can be concluded that a limited range sidelobe level degradation in the compressed pulse due to Doppler frequency offsets is allowed without interfering rainfall detection and estimation. The range sidelobe interference as a function of minimum detectable rate can reduce the range sidelobe specification up to 11 dB for Doppler shifts up to 200 kHz. The range sidelobe level curves shown in Figure 2.7(b) represent an

effective limit for the envelope of the ambiguity function along the v axis for any pulse compression waveform candidate. It should be noted that the range sidelobe level specification results are strongly dependent on the surface reflectivity assumptions made.

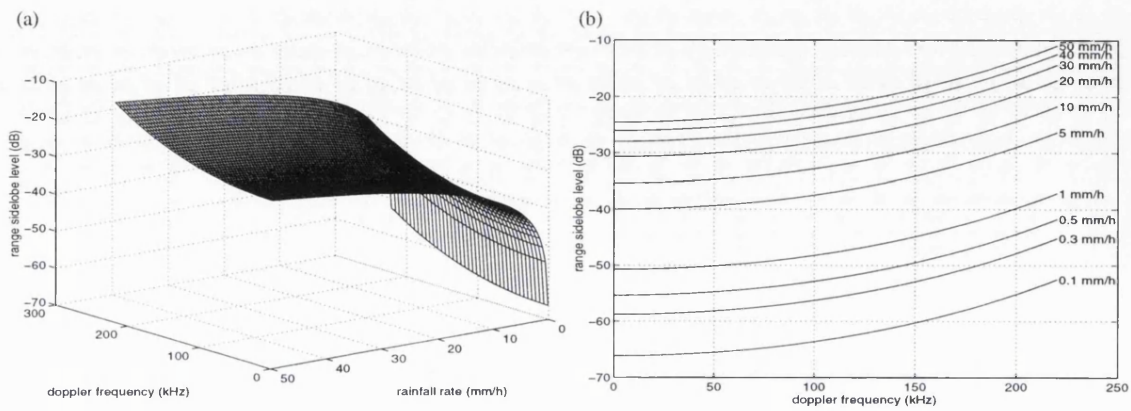


Figure 2.7. Range sidelobe level specification as a function of: (a) Rainfall rate and Doppler frequency; (b) Doppler frequency and minimum detectable rainfall rate.

2.6 References

- Atlas D.: 'Advances in Radar Meteorology', *Adv Geophysics*, Vol. 10, pp. 317-478, 1964.
- Awaka J., Kozu T., and Okamoto K.: 'A Feasibility Study of Rain Radar for the Tropical Rainfall Measuring Mission, 2. Determination of Basic System Parameters', *J. Communications Research Laboratory*, Vol. 35, No. 145, pp. 111-133, 1988.
- Collier C.G., Szejwach G. and Testud J.: 'Rain Radar, Report of a Consultancy Group', *ESA SP-1119*, April 1990.
- Hanado H. and Ihara T.: 'Evaluation of Surface Clutter for the Design of the TRMM Spaceborne Radar', *IEEE Trans. on Geoscience and Remote Sensing*, Vol. 30, No. 3, pp. 444-453, May 1992.
- Ihara T. and Nakamura K.: 'A Feasibility Study of Rain Radar for the Tropical Rainfall Measuring Mission, 3. Radar Type and Antenna', *J. Communications Research Laboratory*, Vol. 35, No. 145, pp. 135-148, 1988.
- Im K.E., Rosing D., Li F. and Wilson W.J.: 'Final Report - Phase A Conceptual Design study for a Rain Radar on the Tropical Rain Mapping Mission', *Technical Report*, Jet Propulsion Laboratory, Pasadena CA, February 1987.
- Levanon N.: 'Radar Principles', John Wiley & Sons, 1988.
- Li F.K., Im K.E., Wilson W.J. and Elachi C.: 'On the Design Issues for a Spaceborne Rain Mapping Radar', *Proceedings of the International Symposium on Tropical Precipitation Measurement*, pp. 387-393, Tokyo 1987.
- Manabe T. and Ihara, T.: 'A Feasibility Study of Rain Radar for the Tropical Rainfall Measuring Mission, 5. Effects of Surface Clutter on Rain Measurements from Satellite', *J. Communications Research Laboratory*, Vol. 35, No. 145, pp. 163-181, 1988.
- Marzoug M., Amayenc P. and Karouche N.: 'Design of a Spaceborne Radar for

Tropical Rain Mapping at the Climatological Scale', *Proc. IGARSS '88*, pp. 247-248, 1988.

- Mavrocordatos G. and Caille G.: 'Instrument Design and Critical Technologies', Alcatel Espace, Presentation on Rain Radar, *ESA Workshop on Rain/Cloud Radar*, ESTEC, September 1993.
- Meneghini R. and Kozi T.: 'Spaceborne Rain Radar', Artech House, Norwood MA, 1990.
- Nakamura K., Okamoto K., Ihara T., Awaka J. and Kozi T.: 'Conceptual Design of Rain Radar for the Tropical Rainfall Measuring Mission', *International Journal of Satellite Communications*, Vol. 8, pp. 257-268, 1990.
- Nakamura K. and Ihara T.: 'A Feasibility Study of Rain Radar for the Tropical Rainfall Measuring Mission, 4. A Discussion of Pulse Compression and Adaptive Scanning', *J. Communications Research Laboratory*, Vol. 35, No. 145, pp. 149-161, 1988.
- Okamoto K.: 'A Feasibility Study of Rain Radar for the Tropical Rainfall Measuring Mission, 1. Introduction', *J. Communications Research Laboratory*, Vol. 35, No. 145, pp. 109-110, 1988.
- Okamoto K., Awaka J. and Kozi T.: 'A Feasibility Study of Rain Radar for the Tropical Rainfall Measuring Mission, 6. A Case Study of Rain Radar System', *J. Communications Research Laboratory*, Vol. 35, No. 145, pp. 183-208, 1988.
- Probert-Jones J.R.: 'The Radar Equation in Meteorology', *Quart. J. Roy. Met. Soc.*, Vol. 88, pp. 485-495, 1962.
- Schroeder L.C., Jones W.L., Schaffner P.R. and Mitchell J.L.: 'Flight Measurement and Analysis of AAFE RADSCAT Wind Speed Signature of the Ocean', *NASA Tech. Memo.*, TM-85646, 1984.
- Simpson J. and Adler R.E. and North, G.R.: 'A Proposed Tropical Rainfall Measuring Mission (TRMM) Satellite', *Bull. Amer. Meteor. Soc.*, Vol. 69, pp. 278-295, 1988.
- Valenzuela G.R.: 'Theories for the Interaction of Electromagnetic and Oceanic Waves - A Review', *Boundary-Layer Meteorol.*, Vol. 13, pp. 61-85, 1978.

3 LINEAR FM PULSE COMPRESSION

Linear frequency modulated waveforms are widely used in radar systems since they achieve higher resolution capabilities than with unmodulated pulses, with lower transmit power requirements. Classical linear FM pulse compression theory is reviewed in this chapter, from matched filter concepts to the linear FM signal spectrum and its compressed pulse formulation. The effect of target motion is also analysed through the signal ambiguity function, which determines the performance of a radar waveform both in time delay and Doppler frequency. The linear FM matched filter in its own does not give a compressed pulse which meets the spaceborne meteorological radar range sidelobe level specification. However, linear FM theory is the starting point in order to develop either mismatched systems or nonlinear frequency modulations to attain such a requirement.

3.1 Historical Background

Pulse compression theory was originally conceived during World War II to overcome power limitations of early radar transmitters. Similar methods were proposed by several scientists serving on both sides. After the War, when the necessary transmitter components were developed, research programmes began and eventually pulse compression was successfully implemented in radar systems. Since the technique was militarily declassified, it has been applied to an extensive number of radar applications.

Pulse compression provides a solution for the conflicting requirements of simultaneous long range and high resolution performance in radar systems. In a simple pulsed radar system, the range resolution Δr is given by:

$$\Delta r = \frac{cT}{2} \tag{1}$$

where c is the propagation speed and T the signal duration. For the same system, the maximum unambiguous detection range r_{\max} is given by:

$$r_{\max} = 4 \sqrt{\frac{P_t G^2 \lambda^2 \sigma}{(4\pi)^3 S_{\min}}} \tag{2}$$

where P_t is the transmitted power, G the gain of the transmitting and receiving antenna, λ the transmitted signal wavelength, σ the target radar cross section and S_{\min} the minimum detectable signal power level. Therefore, there is a trade off between the desired range resolution (limited by the pulse length, Eq. 1) which determines the separability of close targets, and the attainable maximum detection range (limited by the average power radiated, Eq. 2). The need to use the smallest pulse width in order to increase the resolution of the system is restricted by the requirement of maximising the energy of the pulse by using the longest pulse width in order to extend the maximum detection range.

The large frequency contents (or bandwidth) of a short pulse are responsible for its high resolution properties. Directly related to Fourier analysis, a narrow bandwidth is contained in a long pulse of constant carrier, thus giving a poor resolution. However, the spectrum of the signal can be significantly broadened by introducing frequency modulation of the carrier frequency. In order to utilise the transmitter tubes efficiently, the envelope of the transmit pulse must remain constant [Nathanson, 1969]. Therefore, the frequency spread characteristic of a short pulse can be introduced within the envelope of a long duration signal. The extraction of the wideband information contained in the type of signal implied by the frequency modulation technique requires the use of a more complex system than the one needed for a pulsed radar. The receiver system is designed to be a *matched filtered* signal processing system.

3.2 The Matched Filter

Almost the totality of radar receivers are designed to maximise the signal-to-noise ratio at a particular observation time, which is equivalent to maximising the peak instantaneous *SNR*. The filter whose impulse response achieves this maximisation is known as matched filter [North, 1943]. The peak instantaneous signal-to-noise ratio (to be maximised) is defined as:

$$SNR = \frac{|s_0(t_{\max})|^2}{n_0^2(t)} \quad (3)$$

where $s_0(t_{\max})$ is the output at a given time t_{\max} of a linear filter $h(t)$, which processes the input signal $s(t)$ with added thermal noise characterised by its spectral density $N(f)$.

The output $s_0(t_{\max})$ can be expressed by its inverse Fourier transform at the given time t_{\max} :

$$s_0(t_{\max}) = \int_{-\infty}^{\infty} S(f)H(f)e^{j2\pi ft_{\max}} df \quad (4)$$

The average noise output power $\overline{n_0^2(t)}$ is given by:

$$\overline{n_0^2(t)} = E\{n_0^2(t)\} = \int_{-\infty}^{\infty} N(f)|H(f)|^2 df \quad (5)$$

if $N(f)$ is a PSD \oplus

Thus, the peak instantaneous signal-to-noise ratio at the given time t_{\max} is expressed as:

$$SNR = \frac{\left| \int_{-\infty}^{\infty} S(f)H(f)e^{j2\pi ft_{\max}} df \right|^2}{\int_{-\infty}^{\infty} N(f)|H(f)|^2 df} \quad (6)$$

if $N(f) = \text{const} = N$
 $\rightarrow N \int_{-\infty}^{\infty} |H(f)|^2 df$

Taking advantage of the Schwarz inequality for complex signals:

$$\left| \int_{-\infty}^{\infty} a(f)b(f)df \right|^2 \leq \int_{-\infty}^{\infty} |a(f)|^2 df \cdot \int_{-\infty}^{\infty} |b(f)|^2 df \quad (7)$$

where equality only holds if:

$$a(f) = kb^*(f) \quad (8)$$

where k is an arbitrary constant, the transfer function of the filter which maximises the peak instantaneous signal-to-noise ratio is given by:

$$H_{\text{opt}}(f) = k \frac{S^*(f)e^{-j2\pi t_{\max}}}{N(f)} \quad (9)$$

The optimum or matched filter is weighted by the system noise spectral density.

Assuming additive Gaussian noise (white noise) with a spectral density $N_0/2$ (Watt/Hz) and using Parseval's theorem, the maximum attainable SNR is given by:

$$SNR = \frac{2E}{N_0} \quad (10)$$

where E is the signal energy. The matched filter impulse response in the time domain can be formulated as:

$$h_{\text{opt}}(t) = k' s^*(t_{\text{max}} - t) \quad (11)$$

Therefore, for any given radar signal $s(t)$, the impulse response of the filter matched to the signal is given by a delayed conjugated replica of the signal itself, and the output signal-to-noise ratio is then proportional to the transmitted signal energy. It must be pointed out that the matched filter output $s_0(\tau)$ (given by the convolution between the signal and its matched filter) is equivalent to the signal autocorrelation function $R_s(\tau)$ (without loss of generality it is assumed that $t_{\text{max}} = 0$ and $k' = 1$):

$$s_0(\tau) = \int_{-\infty}^{\infty} s(t) h_{\text{opt}}(\tau - t) dt = \int_{-\infty}^{\infty} s(t) s^*(t - \tau) dt = R_s(\tau) \quad (12)$$

3.3 Linear Frequency Modulation

Pulse compression was originated from the idea of transmitting a wide pulse with a linear frequency modulation of its carrier frequency (also widely known as a *chirp* signal). At the receiver, the pulse is processed through a filter which has a time versus frequency characteristic which is inverse to the generating one. Thus, the receiver filter delays some frequencies of the received pulse by a greater amount than others, forcing the pulse to compress in time and increase in amplitude.

Unfortunately, when compressing the rectangular chirp pulse, range *sidelobes* appear on both sides of the main central lobe, extending up to twice the duration of the transmitted signal. These range sidelobes can introduce undesired ambiguities on target detection, and may even mask overlapped weaker signals. Range sidelobe reduction can be achieved by significant attenuation at the edges of the pulse spectrum. However, there

is a trade off between the range sidelobe level reduction and the compressed pulse mainlobe width and degradation of the signal-to-noise ratio.

Pulse compression theory can be found in numerous books and papers ([Klauder et al., 1960], [Bernfeld et al., 1964], [Cook and Bernfeld, 1967] and [Rihaczek, 1969]). In order to provide full understanding of linear FM signals and other modulation schemes described in this thesis, the theory and fundamentals of pulse compression are reviewed without following any of the previously mentioned references in particular.

3.3.1 Linear FM Signal Formulation

A radar bandpass signal $s(t)$ (of bandwidth $2B$ Hz centred at a carrier frequency f_0) can be expressed as:

$$s(t) = e(t) \cos(2\pi f_0 t + \theta(t)) \quad (13)$$

where $e(t)$ is the signal envelope and $\theta(t)$ the signal phase. In order to ease the signal formulation, it is common to use its *complex envelope* $\tilde{s}(t)$ notation, which is defined as:

$$\tilde{s}(t) = s_i(t) + js_q(t) \quad (14)$$

where $s_i(t)$ is the signal *in-phase* component $e(t) \cos \theta(t)$ and $s_q(t)$ is the signal *quadrature* component $-e(t) \sin \theta(t)$, which constitute bandpass signals of bandwidth B Hz centred at a zero frequency. The original radar signal $s(t)$ is therefore the real component of the product of its complex envelope and a phasor of frequency f_0 :

$$s(t) = \text{Re}(\tilde{s}(t) e^{j2\pi f_0 t}) \quad (15)$$

The instantaneous frequency of a linear frequency modulated signal of duration T over a bandwidth of B (shown in Figure 3.1(a)), can be formulated as:

$$f_i(t) = f_0 + \frac{B}{T} t \quad (16)$$

where B/T is the modulation rate (normally referred as K). The total frequency sweep is then equivalent to the signal bandwidth. The linear FM signal instantaneous frequency is

defined as:

$$f_i(t) = \frac{1}{2\pi} \frac{d\theta(t)}{dt} \quad (17)$$

Therefore, the linear FM signal phase is obtained by integration of the pulse instantaneous frequency, given by:

$$\theta(t) = 2\pi \int f_i(t) dt = \pi \frac{B}{T} t^2 \quad (18)$$

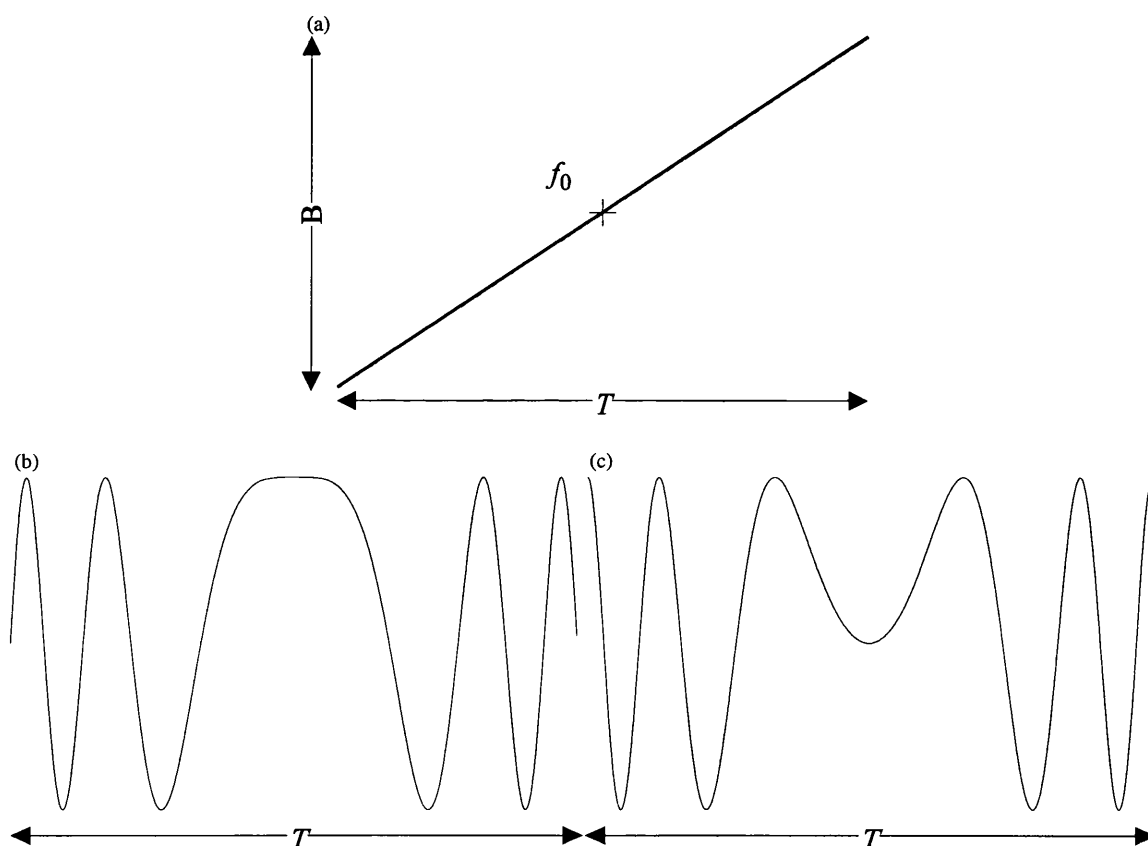


Figure 3.1. Linear FM signal: (a) Instantaneous frequency; (b) Complex envelope, in-phase component; (c) Complex envelope, quadrature component.

Thus, the complex envelope of a linear FM radar pulse of duration T and bandwidth of B (normalised to its energy) is defined as [Klauder et al., 1960]:

$$\tilde{s}(t) = \frac{1}{\sqrt{T}} \text{rect} \left(\frac{t}{T} \right) e^{j\pi \frac{B}{T} t^2} \quad (19)$$

where $\text{rect}(t)$ is a rectangular envelope of unity amplitude given by:

$$\text{rect}\left(\frac{t}{T}\right) = \begin{cases} 1 & -\frac{T}{2} \leq t \leq \frac{T}{2} \\ 0 & \text{elsewhere} \end{cases} \quad (20)$$

The in-phase and quadrature components of a linear FM signal are shown in Figure 3.1(b) and 3.1(c). The matched filter impulse response of a linear FM signal is therefore given by the conjugated replica of the signal itself, with an opposite time vs. frequency characteristic, and can be formulated as:

$$\tilde{h}_{\text{opt}}(t) = \frac{1}{\sqrt{T}} \text{rect}\left(\frac{t}{T}\right) e^{-j\pi\frac{B}{T}t^2} \quad (21)$$

3.3.2 Linear FM Signal Spectrum

The spectrum of a linear FM radar signal cannot be expressed by a closed analytical expression due to the presence of Fresnel ripples in the signal frequency domain. Hence, the compressed pulse can only be obtained through the inverse Fourier transform of the modulus of the signal spectrum based on the approximation of a large time-bandwidth product in order to minimise the Fresnel distortion. The Fourier transform of a linear FM radar signal is given by:

$$\tilde{S}(f) = \frac{1}{\sqrt{T}} \int_{-\infty}^{\infty} \text{rect}\left(\frac{t}{T}\right) e^{j\pi Kt^2} e^{-j2\pi ft} dt \quad (22)$$

where K is the modulation rate. The integral in Eq. 22 is equivalent to:

$$\tilde{S}(f) = \frac{e^{-j\pi\frac{f^2}{K}}}{\sqrt{T}} \int_{-\frac{T}{2}}^{\frac{T}{2}} e^{j2\pi K\left(t-\frac{f}{K}\right)^2} dt \quad (23)$$

Changing the variable t into:

$$x = \sqrt{2K}\left(t - \frac{f}{K}\right) \quad (24)$$

Eq. 23 can be expressed as:

$$\tilde{S}(f) = \frac{1}{\sqrt{2B}} e^{-j\pi \frac{f^2}{K} x_1} \int_{x_0}^{x_1} e^{j\frac{\pi x^2}{2}} dx \quad (25)$$

where:

$$\begin{aligned} x_0 &= -\sqrt{\frac{K}{2}} \left(T + \frac{f}{K} \right) \\ x_1 &= \sqrt{\frac{K}{2}} \left(T - \frac{f}{K} \right) \end{aligned} \quad (26)$$

The Fresnel integral is defined as:

$$F(x) = \int_0^x e^{j\frac{\pi y^2}{2}} dy = \int_0^x \cos \frac{\pi y^2}{2} dy + j \int_0^x \sin \frac{\pi y^2}{2} dy = C(x) + jS(x) \quad (27)$$

where $C(x)$ and $S(x)$ are the real and imaginary components (shown in Figure 3.2). The final expression for the linear FM signal spectrum is given by:

$$\tilde{S}(f) = \frac{1}{\sqrt{2B}} e^{j\pi \frac{f^2}{K}} [C(x_1) + jS(x_1) - C(x_0) - jS(x_0)] \quad (28)$$

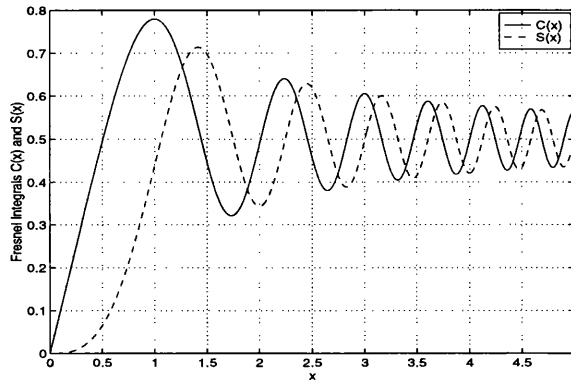


Figure 3.2. Fresnel integral, $C(x)$ and $S(x)$ components.

The spectra of linear FM signals of time-bandwidth products of 25, 100, 500 and 1000 are shown in Figure 3.3. It should be noted that the reduction of Fresnel ripples is directly related to the increase of the signal time-bandwidth product. Some spectrum approximations yield a derivation of an expression for the linear FM signal compressed pulse in the time domain. However, an exact analytical expression can also be achieved

through the autocorrelation of the linear FM signal in the time domain.

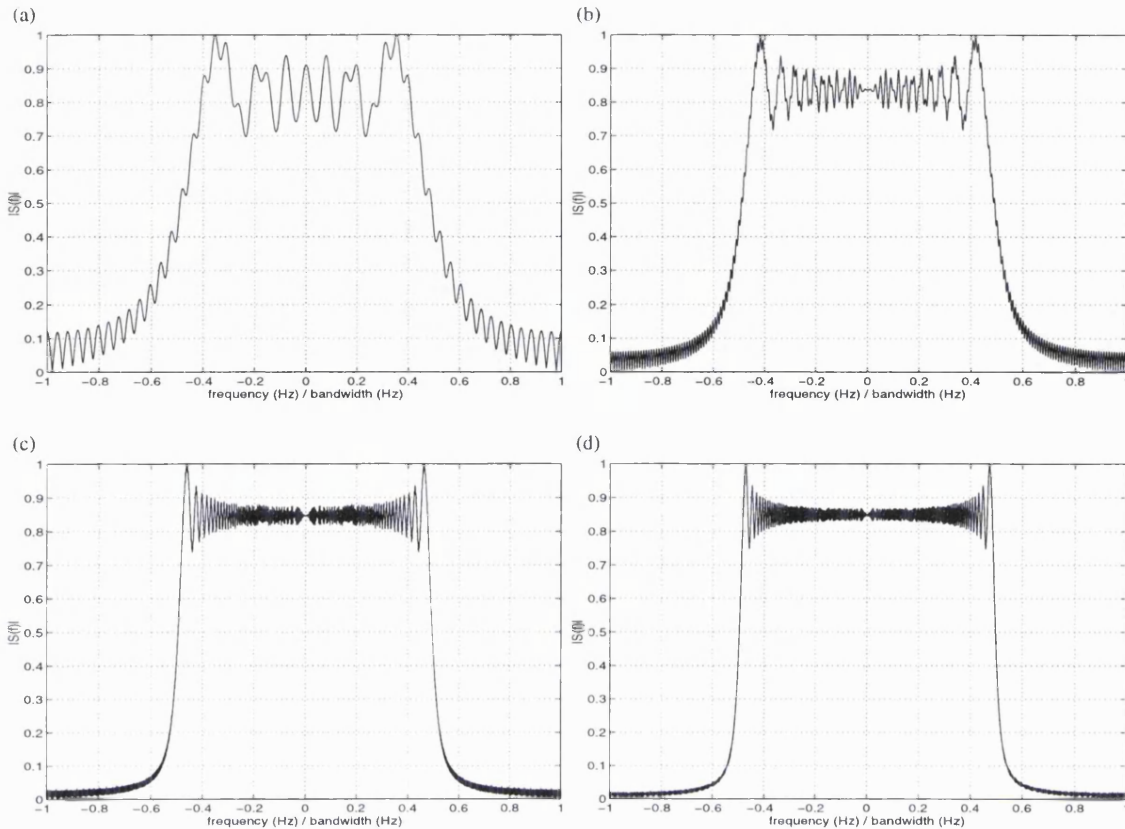


Figure 3.3. Linear FM signal spectrum: (a) $TB = 25$; (b) $TB = 100$; (c) $TB = 500$; (d) $TB = 1000$.

3.3.3 Linear FM Compressed Pulse

The linear FM signal compressed pulse analytical expression in the time domain is obtained through the convolution between the radar signal and its matched filter (or the autocorrelation function of the linear FM signal itself). Replacing Eq. 19 and Eq. 21 in Eq. 12, the compressed pulse is given by:

$$s_0(\tau) = \frac{1}{T} \int_{-\infty}^{\infty} \text{rect}\left(\frac{t}{T}\right) \text{rect}\left(\frac{t-\tau}{T}\right) e^{j\pi K t^2} e^{-j\pi K (t-\tau)^2} dt \quad (29)$$

Eq. 29 needs to be integrated separately for positive and negative times, as shown in Figure 3.4 (a detailed calculation can be found in Appendix B.1). For $\tau > 0$, Eq. 28 can be expressed as:

$$s_0(\tau) = \frac{e^{-j\pi K\tau^2}}{T} \int_{\tau - \frac{T}{2}}^{\tau + \frac{T}{2}} e^{j2\pi Kt\tau} dt \tag{30}$$

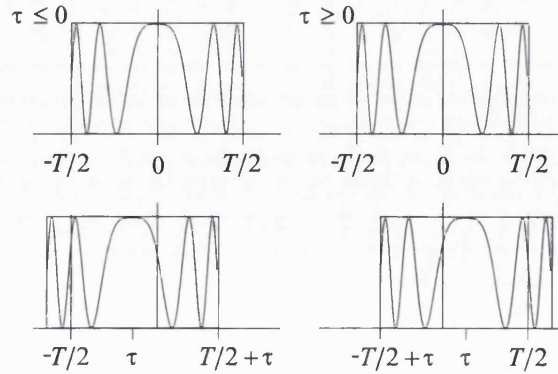


Figure 3.4. Diagram of Linear FM signal autocorrelation integration limits.

The combined solution to Eq. 29 for both positive and negative times gives the final linear FM signal compressed pulse expression:

$$s_0(\tau) = \left(1 - \frac{|\tau|}{T}\right) \text{sinc}\left(B\tau\left(1 - \frac{|\tau|}{T}\right)\right) \tag{31}$$

Figure 3.5(a) shows a diagram of the shape of the linear FM signal compressed pulse whereas Figure 3.5(b) shows the same compressed pulse for a time-bandwidth product of 250.

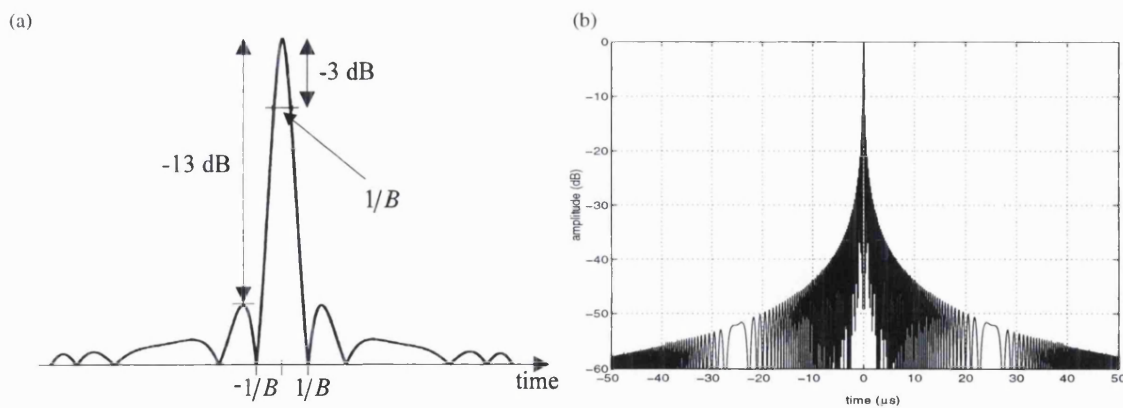


Figure 3.5. Linear FM signal: (a) Compressed pulse diagram; (b) Compressed pulse $TB = 250$.

The compressed pulse width $\Delta\tau_{-3\text{dB}}$ is approximately given by the inverse of the signal bandwidth. Thus, the compression ratio defined as the ratio between the expanded and compressed linear FM signal widths, is given by:

$$\rho = \frac{T}{\Delta\tau_{-3\text{dB}}} = TB \quad (32)$$

which is equivalent to the signal time-bandwidth product. The range resolution can be calculated replacing the linear FM signal width T by its compressed pulse width $\Delta\tau_{-3\text{dB}}$ in Eq. 1, and given by:

$$\Delta r = \frac{c}{2B} \quad (33)$$

The range resolution of a linear FM signal is then no longer proportional to its time duration, but inversely proportional to its signal bandwidth. Therefore, it is possible to increase the width (and energy) of the pulse, and consequently increase the system maximum detectable range without compromising the system range resolution.

3.4 Linear FM Signal Ambiguity Function

As was described in section 2.5, the radar platform motion and the hydrometeors motion introduce Doppler frequency offsets on the nominal carrier frequency of the returned signal. Doppler frequency shifts may degrade the performance of the matched filter. The *ambiguity function* [Woodward, 1953] shows graphically the influence of a Doppler shifted signal filtered through its matched filter.

The ambiguity function is usually defined as the absolute value of the output of a matched filter when the input to the filter is a Doppler-shifted replica of the original transmitted signal, to which the filter was matched. Thus, the ambiguity function $\chi(\tau, \nu)$ is given by:

$$\chi(\tau, \nu) = \int_{-\infty}^{\infty} \tilde{s}(t) \tilde{s}^*(t - \tau) e^{j2\pi\nu t} dt = \int_{-\infty}^{\infty} \tilde{S}(f - \nu) \tilde{S}^*(f) e^{j2\pi f \tau} df \quad (34)$$

where the two parameters of the function are the time delay τ and the additional Doppler frequency shift ν , different from the nominal delay and centre frequency to which the filter was matched. Substituting Eq. 19 in Eq. 34, the linear FM signal ambiguity function can be expressed as:

$$\chi(\tau, \nu) = \frac{1}{T} \int_{-\infty}^{\infty} \text{rect}\left(\frac{t}{T}\right) \text{rect}\left(\frac{t-\tau}{T}\right) e^{j\pi K t^2} e^{-j\pi K (t-\tau)^2} e^{j2\pi \nu t} dt \quad (35)$$

which can be solved in a similar way to the linear FM autocorrelation function described in section 3.3.3 (a detailed calculation can be found in Appendix B.2). The final expression of the linear FM ambiguity function is given by:

$$\chi(\tau, \nu) = \left(1 - \frac{|\tau|}{T}\right) \text{sinc}\left((B\tau + T\nu)\left(1 - \frac{|\tau|}{T}\right)\right) e^{j\pi \nu \tau} \quad (36)$$

A cut along the delay axis ($\nu = 0$) in the ambiguity function, yields the autocorrelation function of the signal $R_s(t)$. Successive cuts at different Doppler frequencies give the distortion introduced into the compressed pulse by target motion. The ambiguity functions of an unmodulated pulse and a linear FM signal are shown in Figure 3.6. It should be noted that the volume under the ambiguity function (which always remains constant) is reshaped, forming the typical diagonal ridge whose orientation is proportional to the modulation rate. Ambiguity function contour plots are displayed in Figure 3.7, which show the linear FM signal characteristic ambiguity function shearing. Range-Doppler coupling is introduced in the linear FM signal compressed pulse, which makes it impossible to achieve simultaneous accurate resolutions both in target range and velocity.

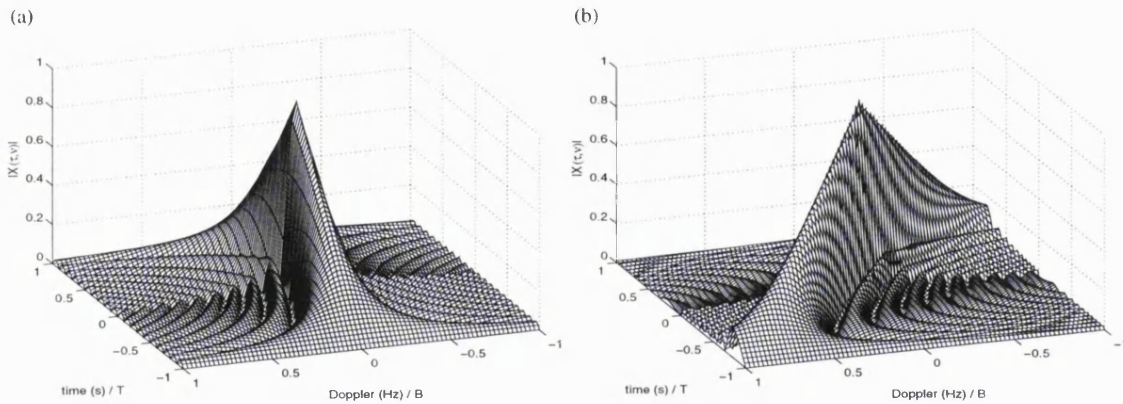


Figure 3.6. Ambiguity functions of: (a) Unmodulated pulse; (b) Linear FM signal.

Making the argument of the sinc function equal to zero, the position of the compressed pulse mainlobe is given by:

$$\tau_{\max} = -\frac{T\nu}{B} \quad (37)$$

Hypothetically, the error in the range estimation due to linear FM range-Doppler coupling could be compensated if the magnitude of the Doppler frequency offset was known. However, both the range and velocity of the detected target are unknown in practice.

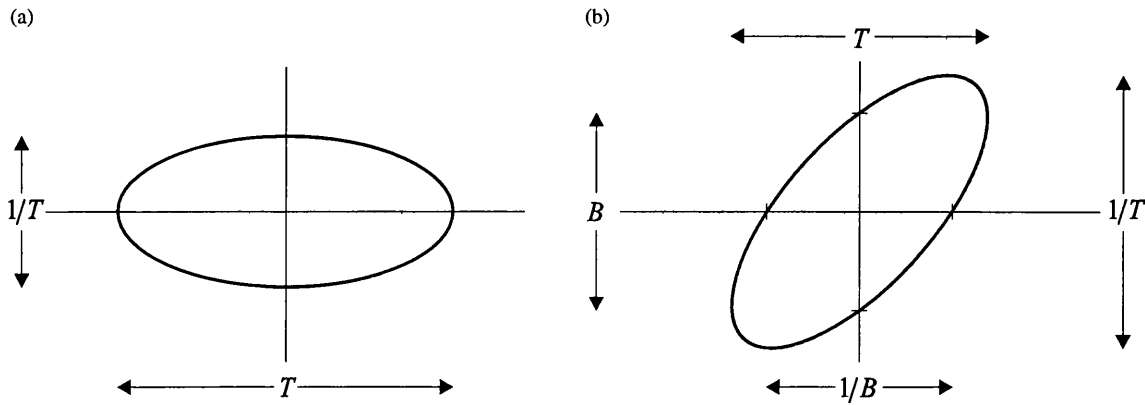


Figure 3.7. Ambiguity function constant amplitude level contour plots relative to $|\chi(0,0)|$ for: (a) Unmodulated pulse; (b) Linear FM signal. Reproduced from [Cook and Bernfeld, 1967].

The ambiguity function volume invariance property is defined as:

$$\iint |\chi(\tau, \nu)|^2 d\tau d\nu = |\chi(0,0)|^2 \quad (38)$$

independently of the waveform. Such a property, normally referred as the ‘radar uncertainty principle’, states that it is not possible to achieve a narrow ideal ambiguity function mainlobe without avoiding a volume redistribution somewhere else in the $\tau - \nu$ plane, which may constitute a source of self-clutter. Related to the range sidelobe reduction problem, it also states that it is not possible to reduce the compressed pulse range sidelobe level without degrading the range resolution of the waveform.

3.5 References

- Bernfeld M., Cook C.E., Paolillo J. and Palmieri C.A.: 'Matched Filtering, Pulse Compression and Waveform Design', *Microwave Journal*, October 1964 to January 1965.
- Cook C.E. and Bernfeld M.: 'Radar Signals: An Introduction to Theory and Applications', Academic Press, 1967.
- Klauder J.R., Price A.C., Darlington S. and Albersheim W.J.: 'The Theory and Design of Chirp Radars', *Bell System Tech. J.*, Vol.XXXIX, 1960, No.4, pp.745-809; reprinted in *Radars-Vol.3, Pulse Compression*, D.K.Barton ed., Artech House, 1975.
- Nathanson F.E.: 'Radar Design Principles', McGraw Hill, 1969.
- North D.O.: 'An Analysis of the Factors which Determine Signal-Noise Discrimination in Pulse Carrier Systems', *RCA Lab. Report PTR-6C*, June 1943.
- Rihaczek A.W.: 'Principles of High-Resolution Radar', McGraw Hill, 1969.
- Woodward P.M.: 'Probability and Information Theory with Applications to Radar', McGraw Hill, New York, 1953.

4 PULSE COMPRESSION RANGE SIDELOBE REDUCTION THEORY

The output of a perfectly matched linear FM filter gives a compressed pulse of a $\text{sinc}(x)$ shape, with a -13 dB range sidelobe level. For most applications, such range sidelobe level does not guarantee a sufficient dynamic range to avoid weak signals being obscured by stronger targets through the compressed pulse self-clutter. The output of a linear FM matched filter is given by the autocorrelation function of the transmit signal or equivalently, the inverse Fourier transform of the modulus of the signal spectrum:

$$s_0(t) = \int_{-\infty}^{\infty} |\tilde{S}(f)|^2 e^{j2\pi ft} dt \quad (1)$$

The totality of FM radar range sidelobe reduction techniques are based on the modification of the signal spectrum modulus, in order to attain its most suitable shape to produce a low range sidelobe pattern. Two principal methods have been proposed for this purpose: (i) weighting the signal in the time or frequency domain, and (ii) controlling the frequency modulation function. Both techniques achieve a signal spectrum Fresnel ripple reduction and a decrease of the energy at the edges of the signal frequency response (reducing time domain discontinuities). The influence of Doppler-offsets on range sidelobe reduction processing is also assessed in the end of this Chapter.

4.1 Frequency and Amplitude Weighting

Linear FM range sidelobe reduction was originally related to the extensively researched classical theory of antenna radiation pattern design. The electric field intensity (in the far field region) of an antenna of length d (where $d \gg \lambda$) is given by the Fourier transform of the current distribution $I(z)$:

$$E(\phi) = \int_{-\infty}^{\infty} I(z) e^{j2\pi \frac{z}{\lambda} \sin(\phi)} dz \quad (2)$$

where ϕ is the azimuth angle. It can be seen that Eq. 1 and Eq. 2 are equivalent relating the product of the linear FM signal spectrum and its matched filter frequency response

(which may be mismatched), to the Fourier transform of the antenna current distribution:

$$|\tilde{S}(f)| \cdot |\tilde{H}(f)| = I(f) \quad (3)$$

Therefore, based on a rectangular linear FM signal spectrum model combined with a square law phase term (only valid for large time-bandwidth products), several antenna theory sidelobe reduction functions (such as the Taylor approximation of the Dolph-Chebyshev distribution) have been applied to pulse compression [Klauder et al., 1960], [Bernfeld et al., 1964] and [Cook and Bernfeld, 1967]. The frequency (or externally) weighted compressed pulse can be formulated as:

$$s_0(t) = \int_{-\infty}^{\infty} |\tilde{S}(f)|^2 \cdot W_f(f) e^{j2\pi ft} df \quad (4)$$

where $W_f(f)$ is the frequency weighting function. Thus, the compressed pulse shape is directly related to the Fourier transform of the weighting function.

It can also be shown that amplitude (or internal) weighting of the signal envelope in the time domain leads to a compressed pulse with a lower sidelobe pattern. The amplitude weighted compressed pulse is given by:

$$s_0(\tau) = \int_{-\infty}^{\infty} \text{rect}\left(\frac{t}{T}\right) \text{rect}\left(\frac{t-\tau}{T}\right) e^{j\pi K t^2} e^{-j\pi K (t-\tau)^2} \cdot w_a(t-\tau) dt \quad (5)$$

where $w_a(t)$ is the amplitude weighting function. Rearranging Eq.5, the modulus of the compressed pulse can be formulated as:

$$|s_0(\tau)| = \left| \int_{\frac{-T}{2}}^{\frac{T}{2}} w_a(t-\tau) e^{j2\pi K \tau t} dt \right| \quad (6)$$

which again is directly related to the Fourier transform of the weighting function. Unfortunately, amplitude modulation cannot be applied to the reception filter without reducing the efficiency of the radar high power amplifier operating in the saturation region [Nathanson, 1969]. Recently, in spite of the inefficiency of amplitude weighting of the transmitting pulse, a linear FM amplitude modulated waveform has been reported

to give a range sidelobe level of -60 dB during most of the duration of the compressed pulse, which has been generated for the Airborne Rain Mapping Radar Mission (ARMAR, [Im, 1990] and [Tanner et al., 1994]). Any amplitude modulation applied to a linear FM signal forces the transmitter amplifier to operate in the linear region, which is associated with a subsequent signal-to-noise ratio loss. A comprehensive study on the ARMAR waveform performance can be found in Chapter 8.

For any particular weighting function in either domain, it is possible to find an equivalent function in the opposite domain which gives an identical output when weighting is applied in that domain (although it cannot always be synthesised in practice). The compressed pulse spectrum of a linear FM signal weighted in the frequency domain is given by:

$$S_0(f) = \tilde{S}(f)\tilde{S}^*(f)W_f(f) \quad (7)$$

whereas for a linear FM signal weighted in the time domain, it can be formulated as:

$$S_0(f) = \tilde{S}(f) \left(\int_{-\infty}^{\infty} \tilde{s}(t)w_a(t)e^{-j2\pi ft} dt \right)^* \quad (8)$$

Hence, the relation between equivalent amplitude and frequency weighting functions is then given by the following expression:

$$W_f(f) = \frac{(\tilde{S}(f)*W_a(f))^*}{\tilde{S}(f)} \quad (9)$$

Unfortunately, weighting is associated with some undesired effects on the compressed pulse. Since the applied weighting function mismatches the reception filter, a degradation of the signal-to-noise ratio is inevitable. Furthermore, the compressed pulse main lobe broadens, worsening the range resolution. Four weighting functions from classical families [Harris, 1978] and [Nuttal, 1981] have been chosen in order to study their related performance on weighted linear FM compressed pulses.

1) The Hamming window (or modified Hanning window) achieves a perfect cancellation of the first range sidelobe (of the Fourier transform of a rectangular function of the same width), and is defined as:

$$w(t) = \text{rect}\left(\frac{t}{T}\right) \left(0.54 + 0.46 \cos\left(\frac{2\pi t}{T}\right) \right) \quad (10)$$

2) The Dolph-Chebyshev window minimises the main lobe width for a given sidelobe level, and is defined in its discrete form as:

$$w(k) = (-1)^k \frac{\cos\left[N \cos^{-1}\left[\cosh\left[\frac{1}{N} \cosh^{-1}(10^a) \right] \cos\left(n \frac{k}{N} \right) \right] \right]}{\cosh\left[N \cosh^{-1}\left(\cosh\left[\frac{1}{N} \cosh^{-1}(10^a) \right] \right) \right]} \quad 0 \leq |k| \leq N-1 \quad (11)$$

where a is the logarithm of the desired sidelobe level.

3) The Kaiser-Bessel window maximises the energy in a determined band of frequencies, and is defined as:

$$w(t) = \text{rect}\left(\frac{t}{T}\right) \frac{I_0\left[\pi a \sqrt{1 - \left(\frac{2t}{T}\right)^2} \right]}{I_0[\pi a]} \quad (12)$$

where I_0 is the modified Bessel function of the first kind and πa is equivalent to the desired time-bandwidth product.

4) The minimum 3-term Blackman-Harris window is designed to position zeros on the 3rd and 4th range sidelobe (of the Fourier transform of a rectangular function of the same width) while minimising the sidelobe level, and is defined as:

$$w(t) = \text{rect}\left(\frac{t}{T}\right) \left(0.42323 + 0.49755 \cos\left(\frac{2\pi t}{T}\right) + 0.07922 \cos\left(\frac{4\pi t}{T}\right) \right) \quad (13)$$

The time domain windows are shown in Figure 4.1. The range sidelobe level (*RSL*), peak loss L_p (defined as the mainlobe peak level ratio between the Fourier transforms of a given weighting function and a rectangular envelope of the same width) and the relative main lobe width $\Delta\tau_{-3\text{dB}}$ (defined as the -3 dB width with respect to the mainlobe peak level) for the four weighting functions are given in Table 4.I (from [Harris, 1978] and [Nuttal, 1981]). The Fourier transforms of the four mismatching functions are shown in Figure 4.2.

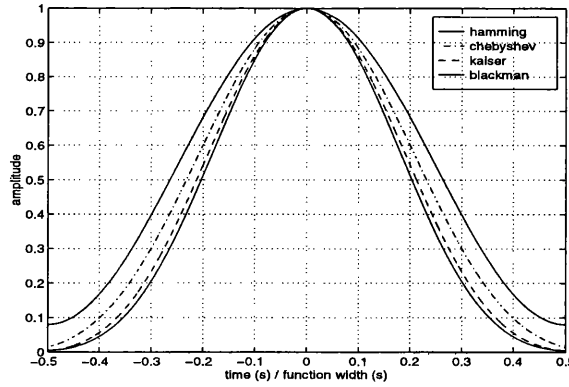


Figure 4.1. Hamming, Dolph-Chebyshev, Kaiser-Bessel and minimum 3-term Blackman-Harris weighting functions.

Table 4.I: Weighting Function Fourier Transform characteristics

	RSL	L_p	$\Delta\tau_{-3dB}$
Rectangular	-13 dB	0 dB	1
Hamming	-43 dB	2.6 dB	1.4
Dolph-Chebyshev ($a=3$)	-60 dB	3.1 dB	1.6
Kaiser-Bessel ($a=2.5$)	-57 dB	3.5 dB	1.8
Blackman-Harris	-71 dB	3.7 dB	1.8

The previous 4 weighting functions have been internally applied to a linear FM signal (for a TB of 300, a figure likely to be employed in spaceborne meteorological radars). The range sidelobe levels obtained are between 1 and 20 dB higher than the nominal weighting function levels, due to Fresnel ripple distortion in the linear FM spectrum.

The compressed pulse peak and average (or energy) losses for a given matched filter mismatching window are defined as:

$$L_p = \frac{|s_{0lfm}(0)|^2}{|s_0(0)|^2} \tag{14}$$

$$L_a = \frac{\int_{-2T}^{2T} |s_{0lfm}(t)|^2 dt}{\int_{-2T}^{2T} |s_0(t)|^2 dt} \tag{15}$$

where $s_{0lfm}(t)$ is the compressed pulse of a linear FM signal processed with its true matched filter and $s_0(t)$ the compressed pulse of a linear FM signal processed with an internally mismatched filter for a given weighting function.

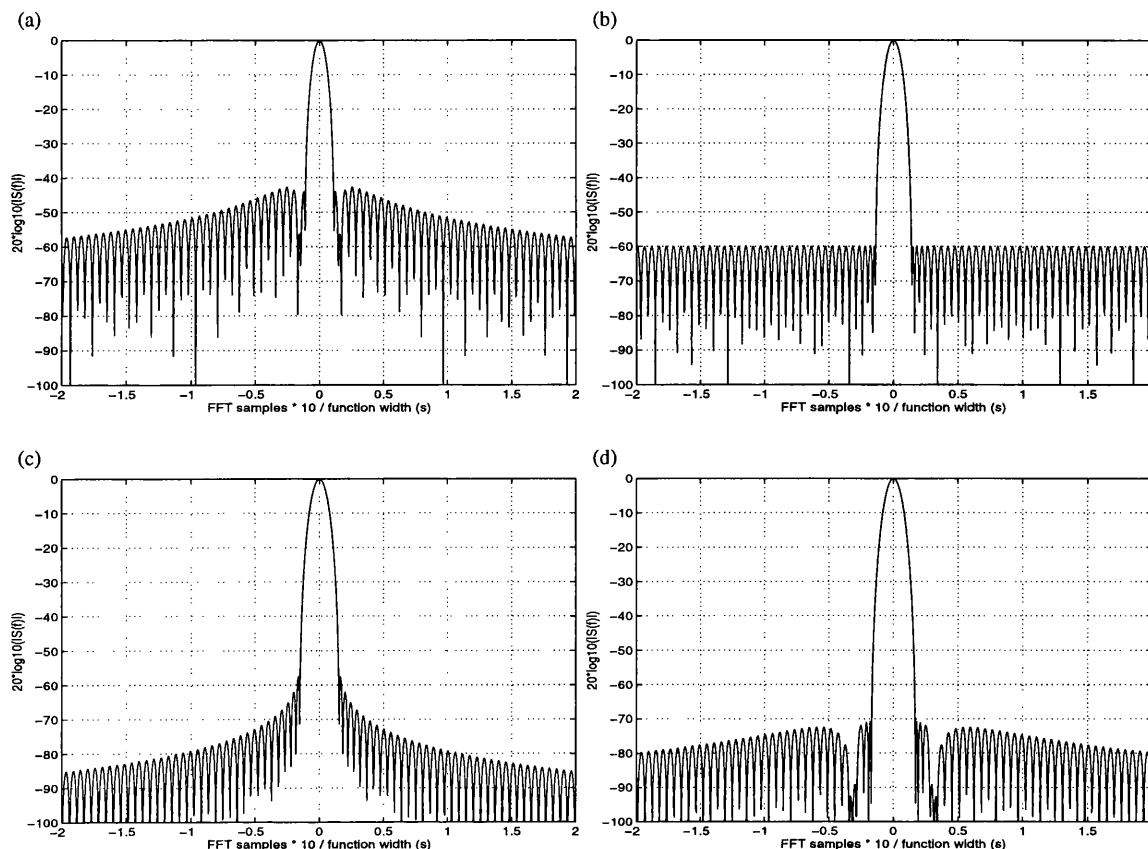


Figure 4.2. Fourier transforms of: (a) Hamming function; (b) Dolph-Chebyshev function; (c) Kaiser-Bessel function; (d) Minimum 3-term Blackman-Harris function.

Table 4.II: Mismatched linear FM (amplitude weighted) compressed pulse characteristics

	RSL	L_p	L_a	$\Delta\tau_{-3dB}$
linear FM	-13 dB	0 dB	0 dB	1
Hamming	-42 dB	5.3 dB	4.0 dB	1.4
Dolph-Chebyshev ($a=3$)	-50 dB	6.4 dB	4.5 dB	1.6
Kaiser-Bessel ($a=2.5$)	-51 dB	7.1 dB	4.9 dB	1.8
Blackman-Harris	-51 dB	7.5 dB	5.0 dB	1.8

The maximum mainlobe degradation (-7.5 dB) and the worse main lobe broadening (1.8) relative to an unweighted compressed pulse, correspond to the minimum 3-term Blackman-Harris window, which is the most severe taper. Table 4.II displays the range sidelobe level, peak and average losses and the relative main lobe width for a compressed pulse processed with a matched filter mismatched with a given mismatching function (shown in Figure 4.3).

For a sufficiently large time-bandwidth product (where the Fresnel ripple distortion has minimal impact), the compressed pulse range sidelobe level equals the

theoretical sidelobe level of the weighting function frequency response. Figure 4.4 shows the range sidelobe level as a function of time-bandwidth product for the four mismatching functions. A minimum time-bandwidth product of 800 would be required to attain a range sidelobe level below -60 dB using a minimum 3-term Blackman-Harris amplitude weighting function.

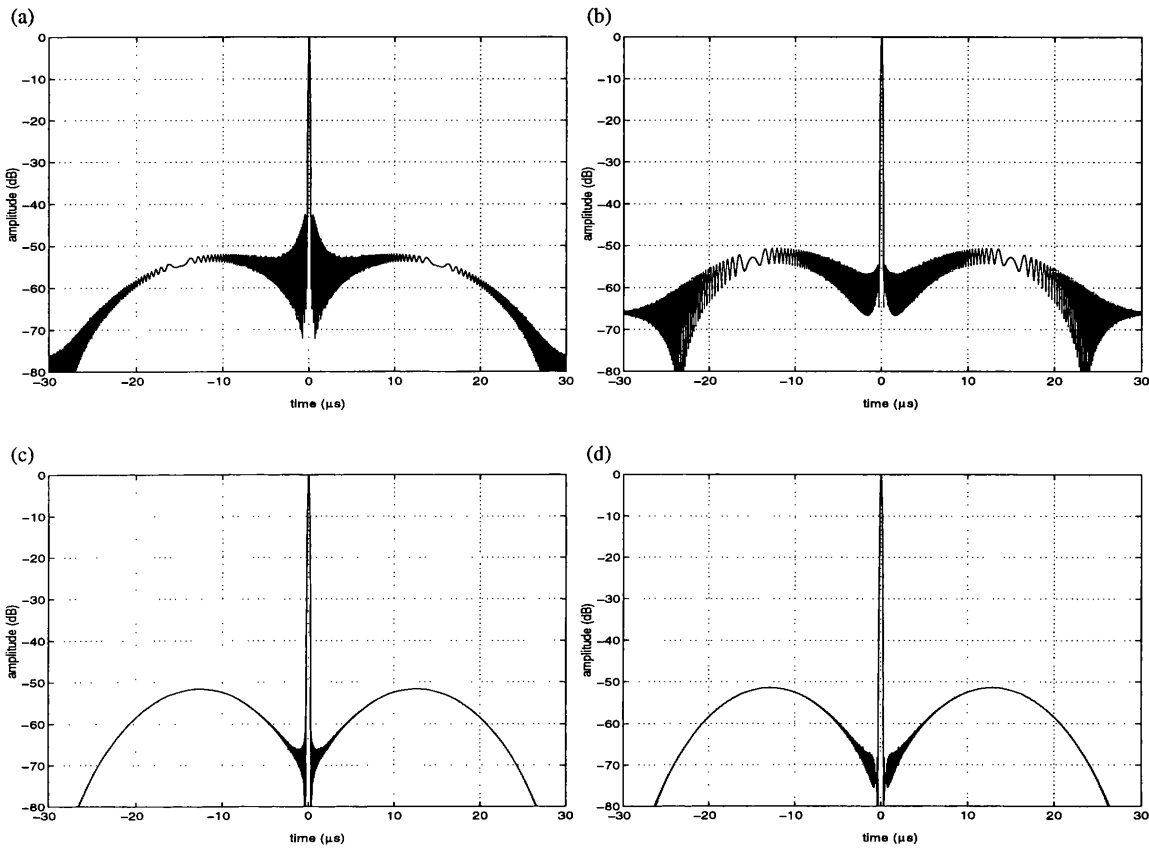


Figure 4.3. Compressed pulses for different linear FM matched filter amplitude mismatching functions: (a) Hamming window; (b) Dolph-Chebyshev window; (c) Kaiser-Bessel window; (d) Minimum 3-term Blackman-Harris window.

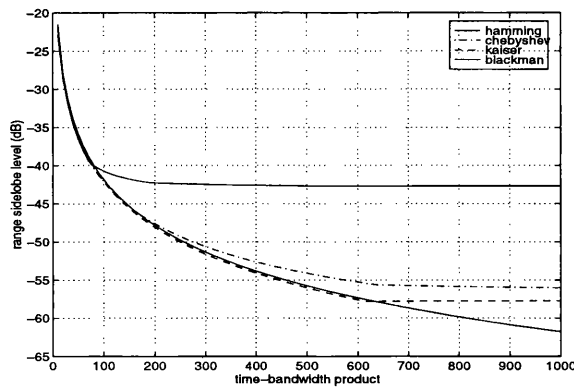


Figure 4.4. Linear FM range sidelobe level as a function of time-bandwidth product for different matched filter amplitude mismatching functions.

Frequency weighted systems present the problem of truncation over the nominal bandwidth of the linear FM, giving compressed pulses of infinite duration in the time domain (extending over the $2T$ width corresponding to the linear FM autocorrelation width). These pulses are bound to be affected by Fresnel ripples due to the imposed truncation discontinuity. Several sidelobe levels for different frequency weighting functions are reported in [Cook and Bernfeld, 1967], which vary from -23 to -42.8 dB assuming a rectangular shaped linear FM spectrum. El-Shennawy et al. [El-Shennawy et al., 1987] report compressed pulse range sidelobe levels of -42 and -38 dB for time-bandwidth products of 50 and 720 respectively, using an external Hamming weighting function.

Finally, Judd [Judd, 1973] devised a hybrid FM system in which the compression filter is designed to allow a suitable shape for the compressed pulse spectrum in order to achieve low range sidelobes. The hybrid compression filter response is given by:

$$\tilde{H}(f) = \frac{S_0(f)}{\tilde{S}(f)} \quad (16)$$

and is equivalently obtained through external weighting by designing the frequency weighting function to be expressed as:

$$W_f(f) = \frac{S_0(f)}{|\tilde{S}(f)|^2} \quad (17)$$

Judd applied the hybrid FM theory for small compression ratios and obtained a range sidelobe level of -34 dB with a reciprocal ripple line for a TB of 8. This type of compression filter could only be implemented digitally since its impulse response would be of infinite duration, and its efficiency would be limited by Doppler frequency offsets. Newton [Newton, 1976] used the same technique to design a compression filter to give a spectrum of a Taylor distribution extended by half cycles of a cosine function on each end, reducing the close sidelobes caused by Doppler offsets by 15 dB.

4.2 Nonlinear FM Range Sidelobe Reduction

An adequate control of the signal frequency modulation can also give low range sidelobe levels. If the modulation rate of change of phase is higher at the edges of the

signal than the modulation rate of the centre band, the energy of the signal decreases at the edges of its spectrum, producing a similar effect as of that of weighting. Thus, the compressed pulse can be obtained through a true matched filter with no mismatch loss. A numerical method by Johnston is described in this section, which allows to calculate the modulation function to match the compressed pulse spectrum to a selected weighting function.

4.2.1 Nonlinear FM Theory

Key et al [Key, Fowle and Haggarty, 1959] showed that a nonlinear FM signal would allow low range sidelobes to be obtained from its true matched filter with no mismatch loss. The compressed pulse is given by the inverse Fourier transform of the modulus of the spectrum of the frequency modulated signal (Eq.1). A suitable compressed pulse spectrum could be specified (from classical weighting theory) to give the required range sidelobe level. The frequency modulated signal frequency response is equal to the square root of the compressed pulse spectrum, and is then given by the inverse Fourier transform of the square root of the specified weighting function with an added (and unknown) phase term. In order to specify this signal spectrum phase $\theta(f)$, the signal envelope is assumed to be rectangular over the pulse width ($-T/2 \leq t \leq T/2$):

$$\left| \int_{-\infty}^{\infty} |\tilde{S}(f)| e^{j2\pi\theta(f)} e^{j2\pi ft} df \right| = 1 \tag{18}$$

The signal instantaneous frequency $f(t)$ can then be obtained through the Fourier transform of the FM signal, given by:

$$\int_{-\infty}^{\infty} \text{rect}\left(\frac{t}{T}\right) e^{j2\pi \int_T f(\tau) d\tau} e^{-j2\pi ft} dt = |\tilde{S}(f)| e^{j2\pi\theta(f)} \tag{19}$$

The previous equation can only be solved approximately using Kelvin's principle of stationary phase [Cook and Bernfeld, 1967], which theorises that the major contribution to a Fourier integral occurs when the rate of change of oscillation is minimal. Hence, the stationary phase point is defined as:

$$\frac{d}{df} (2\pi ft - \theta(f)) = 0 \tag{20}$$

Following a 3-term Taylor series expansion of the stationary point ($f = \lambda$), the nonlinear FM signal in the time domain can be approximated by [Key et al., 1959]:

$$\tilde{s}(t) \cong \sqrt{2\pi} \frac{|\tilde{S}(\lambda)|}{\sqrt{\left. \frac{d^2\theta(f)}{df^2} \right|_{f=\lambda}}} e^{j2\pi\lambda t + j\theta(\lambda) \pm j\frac{\pi}{4}} \quad (21)$$

Thus, the second derivative of the signal spectrum phase is approximately given by:

$$\frac{d^2\theta(f)}{df^2} \cong \frac{1}{2\pi} |\tilde{S}(f)|^2 \quad (22)$$

and can be obtained by double integration. Therefore, the signal in the time domain can be calculated through its spectrum inverse Fourier transform. Unfortunately and due to the approximation made, the signal envelope is not of rectangular shape due to Fresnel ripple distortion which decreases as a function of time-bandwidth product.

4.2.2 Design of Nonlinear FM Signals

The dual of the stationary phase principle states that the major contribution to the spectrum at any frequency f is made by the part of the signal with the same instantaneous frequency value of f . The instantaneous frequency stationary point is defined as:

$$\frac{d}{dt}(2\pi ft - \varphi(t)) = 0 \quad (23)$$

where $\varphi(t)$ is the signal instantaneous frequency. Based on this principle, Fowle [Fowle, 1964] obtained an expression for the modulation function in terms of frequency, given by:

$$t = \int_B |\tilde{S}(f)|^2 df \quad (24)$$

The signal modulation can then be found by direct integration of the compressed pulse spectrum, and is given in terms of frequency instead of time, which is not always possible to be rearranged in terms of time. An analytical solution was obtained for a

compressed pulse spectrum of the form of a truncated Gaussian function by Brandon [Brandon, 1973].

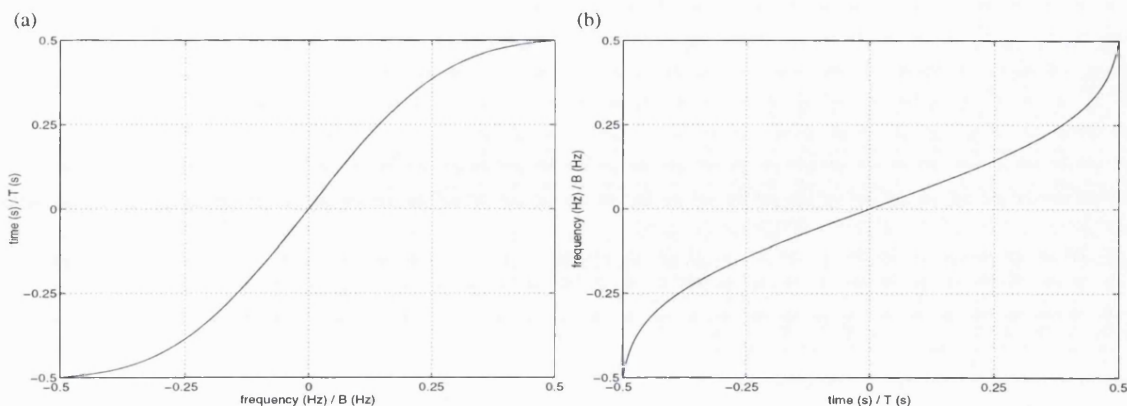


Figure 4.5. Frequency modulation for a Hamming function compressed pulse spectrum as a function of: (a) Frequency; (b) Time (after iteration and fitting into a Chebyshev polynomial). Reproduced from [Johnston, 1983].

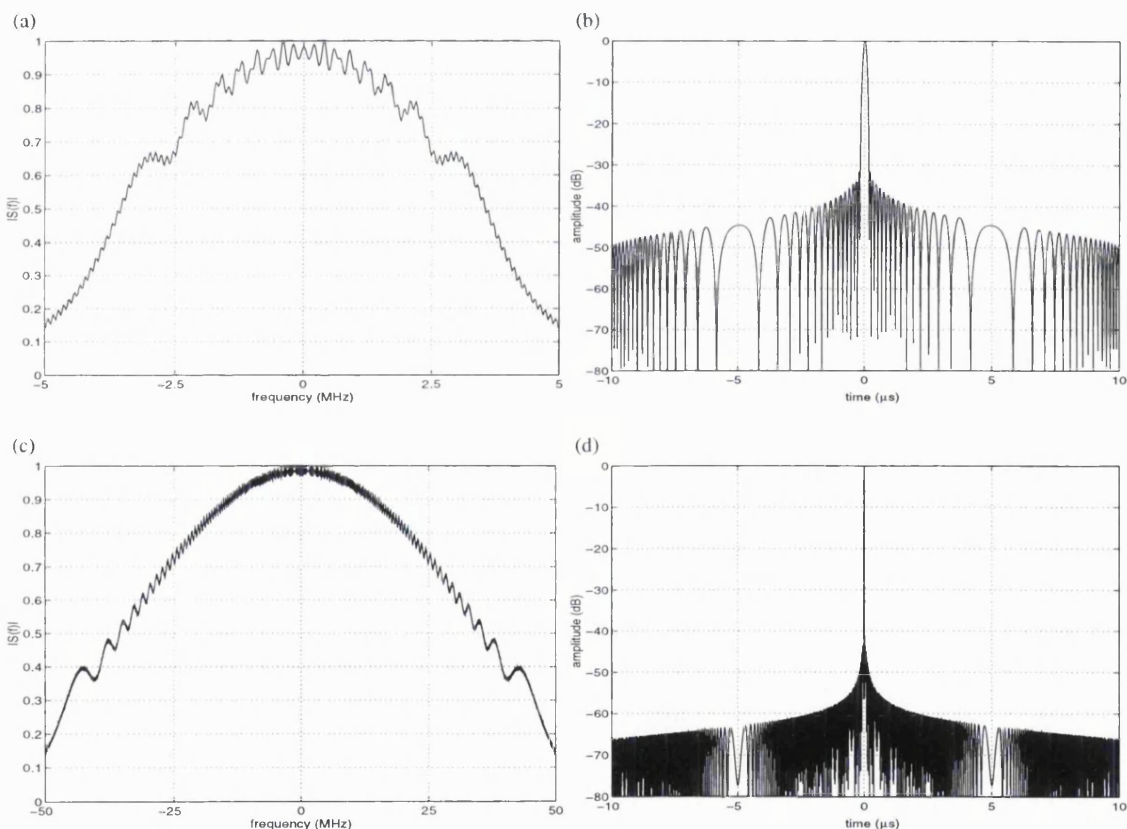


Figure 4.6. Design of nonlinear FM signals with a Hamming function compressed pulse spectrum: (a) Nonlinear FM signal spectrum ($TB = 100$); (b) Nonlinear FM compressed pulse ($TB = 100$), range sidelobe level -32 dB; (c) Nonlinear FM signal spectrum ($TB = 1000$); (d) Nonlinear FM compressed pulse ($TB = 1000$), range sidelobe level -41 dB. Reproduced from [Johnston, 1983].

Johnston [Johnston, 1983] devised a numerical method in which the value of

frequency for a particular instant of time is found by iteration and then fitted to a Chebyshev polynomial with time as the independent variable. This process is reproduced for a compressed pulse spectrum of the form of a Hamming function in Figure 4.5.

It is straightforward to obtain the signal phase by integration of the Chebyshev polynomial. Figure 4.6 shows the calculated spectrum and compressed pulse following the method of Johnson, for time-bandwidth products of 100 and 1000, achieving range sidelobe levels of -32 and -41 dB. The nonlinear FM compressed pulse characteristics are listed in Table 4.III.

Table 4.III: Nonlinear FM (after [Johnston, 1983]) compressed pulse characteristics

	<i>RSL</i>	<i>L_p</i>	<i>L_a</i>	$\Delta\tau_{-3dB}$
nonlinear FM	-32 dB	0 dB	-1.3 dB	1.6

The designed nonlinear FM modulations based on selected spectra is distorted by Fresnel ripple distortion since the integration of the modulus of the spectrum is carried out over a finite bandwidth. The Fresnel ripples decrease as a function of time-bandwidth product. Therefore, the theoretical weighting function frequency response sidelobe level cannot be achieved. As will be described in the next Section, nonlinear FM signals are not Doppler invariant, and their range sidelobe level is significantly degraded when the return signal is subject to relatively small Doppler frequency offsets.



4.3 Influence of Doppler Frequency Shifts on Range Sidelobe Reduction

The nature of the received signal Doppler spectrum was briefly discussed in section 2.5. It was shown that Doppler offsets up to 300 kHz could be expected due to the inherent spaceborne geometry of the radar system. Rihaczek [Rihaczek, 1969] showed that linear FM signals are not properly compressed if the range rate of change is bigger than a fraction of the ratio of the propagation speed over the time-bandwidth product, given by:

$$\frac{dR}{dt} \geq 0.1 \frac{c}{TB} \tag{25}$$

For a time-bandwidth product of 300, the previous ratio is equivalent to 100 kHz. If the frequency modulation employed is not Doppler-tolerant over such a frequency

offset range, there is an obvious need for Doppler compensation processing in order to adjust such value to the expected maximum Doppler shift introduced by the system geometry. Rihaczek also calculated the ambiguity function for an amplitude weighted linear FM (Hamming function). Such calculation has been extended to any amplitude weighting function consisting of a sum of sinusoidal terms of the form:

$$w(t) = \text{rect}\left(\frac{t}{T}\right) \sum_0^n a_n \cos\left(\frac{2\pi n t}{T}\right) \tag{26}$$

The amplitude weighted linear FM ambiguity function is then given by (a detailed calculation can be found in Appendix B.3):

$$\chi(\tau, \nu) = (T - |\tau|) \sum_{-n}^n \frac{a'_n}{2} \text{sinc}\left((B\tau + T\nu + n)\left(1 - \frac{|\tau|}{T}\right)\right) e^{j\pi\nu\tau} e^{-j\pi\frac{n}{T}\tau} \tag{27}$$

where $a'_n = a'_{-n} = a_n$ and $a'_0 = 2a_0$.

Figure 4.7(a) shows the ambiguity function of a linear FM signal when its matched filter is mismatched in amplitude with a minimum 3-term Blackman-Harris function ($TB = 10$), whereas Figure 4.7(b) shows the same ambiguity function for a time-bandwidth product of 300. Figure 4.8 shows that a Doppler offset of 100 kHz degrades the range sidelobe level by only 0.4 dB. The range-Doppler coupling is of 1.2 μs for a Doppler shift of the same magnitude.

Johnston studied the effect of Doppler offsets on nonlinear FM pulse compression, [Johnston and Fairhead, 1986]. Table 4.IV summarises the range sidelobe level for a Doppler-shifted nonlinear FM signal designed by his own method [Johnston, 1983], for a time-bandwidth product of 300.

Amplitude mismatched linear FM systems give excellent Doppler tolerant properties whereas the performance of nonlinear FM systems in terms of range sidelobe level is significantly degraded for relatively small Doppler frequency offsets. Part of the frequency response of a FM signal subject to a Doppler frequency shift lays outside the frequency response band of its matched filter, thus producing an asymmetric compressed pulse spectrum. Such asymmetry is accentuated for nonlinear FM signals, since the energy at the edges of its frequency response is attenuated by the instantaneous frequency nonlinearity. For a linear FM signal of the same time-bandwidth product, the frequency response contents are much higher at the edges of its 'rectangular' frequency response

(distorted by Fresnel ripple distortion due to the signal quadratic phase), being the same asymmetries not so critical in terms of the compressed pulse range sidelobe level.

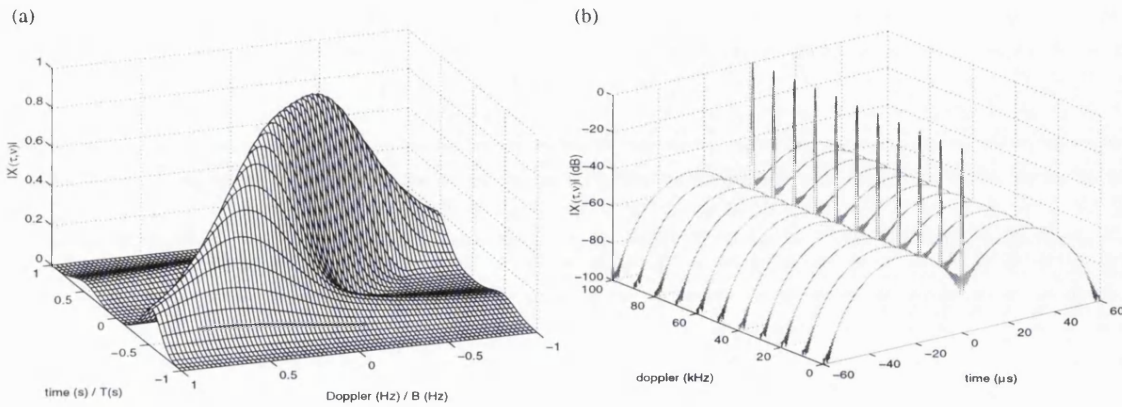


Figure 4.7. Ambiguity function (Blackman-Harris amplitude mismatch): (a) Linear FM; (b) Linear FM, $TB = 300$, .

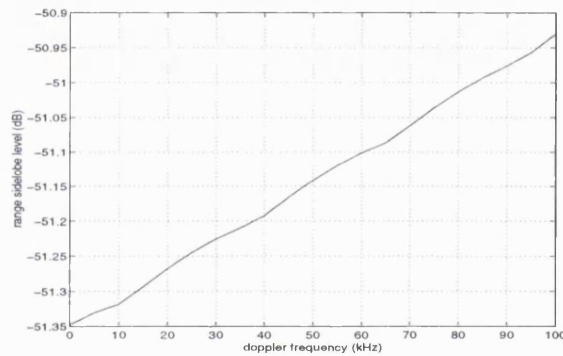


Figure 4.8. Range sidelobe level as a function of Doppler frequency for a linear FM matched filter mismatched in amplitude with a minimum 3-term Blackman-Harris function ($TB = 300$).

Table 4.IV: Range sidelobe level of Doppler shifted nonlinear FM signals ($B = 5$ MHz), reproduced from [Johnston et al., 1986]

	0 kHz	10 kHz	20 kHz
Hamming	-39.6 dB	-16.0 dB	10.9 dB
Truncated \cos^4	-38.3 dB	-16.0 dB	-10.8 dB
Truncated Gaussian	-41.6 dB	-16.6 dB	-10.4 dB
Prolate Spheroidal Wave Functions	-39.6 dB	-16.1 dB	-10.7 dB

Johnston observed that the influence of Doppler shifts on the range sidelobe level of nonlinear FM signals was mostly independent of the weighting function employed to design the signal modulation, and that it was directly related to the signal duration. It was shown that the Doppler-shifted compressed pulse consisted of a summation of scaled and shifted replicas of the linear FM compressed pulse, and reached the conclusion that the

range sidelobe level increases as a function of signal width for a given Doppler offset.

Finally, it should be noted that the performance of phase-coded radar pulses have been studied for their application to spaceborne rain radar systems ([Griffiths and Azami, 1992], [Larvor, 1992] and [De Fazio and Studer, 1994]). It is assumed that the range sidelobe level for a polyphase code is inversely proportional to the number of phase sections. Therefore, a very large number of sections would be required to achieve range sidelobe patterns below -60 dB and thus having an unsuitably large time-bandwidth product.

On the other hand, phase-coded waveforms possess poor Doppler tolerance properties. Rihaczek [Rihaczek, 1969] studied the ambiguity functions of different phase and frequency shift coding techniques. The ambiguity functions of phase reversal coded waveforms (such as the Barker code or pseudo-Barker codes of greater length than 13) give a considerable volume (and consequently high range sidelobe levels) for relatively small Doppler frequency offsets compared to the signal bandwidth. The ambiguity function of a Barker coded signal of length 13 is shown in Figure 4.9(a). Other polyphase codes (the ambiguity function of a Frank coded signal of length 16 is shown in Figure 4.9(b)) present the same problem. The inferior Doppler performance of phase coded signals have rule them out for spaceborne radar meteorology purposes in favour of continuous frequency modulations.

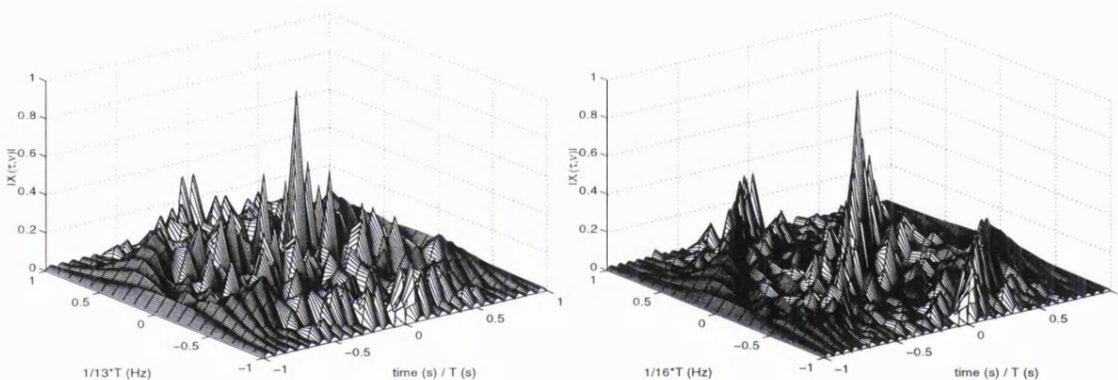


Figure 4.9. Ambiguity functions of: (a) Barker code of length 13; (b) Frank code of length 16.

4.4 References

- Bernfeld M., Cook C.E., Paolillo J. and Palmieri C.A.: 'Matched Filtering, Pulse Compression and Waveform Design', *Microwave Journal*, Oct. 1964 - Jan. 1965.
- Brandon P.S.: 'The Design of a Nonlinear Pulse Compression System to Give a Low Loss High Resolution Performance', *Marconi Rev.*, Volume XXXVI, No.188, pp.1-45, 1973.
- Brandon P.S.: 'The Spectra of Linear and Nonlinear FM used in Pulse Compression, and the Effects on the Resultant Compressed Pulse', *Marconi Rev.*, Volume XXXVI, No.189, pp.69-92, 1973.
- Cook C.E. and Bernfeld M.: 'Radar Signals: An Introduction to Theory and Applications', Academic Press, 1967.
- De Fazio M. and Studer F.A.: 'Application of Pulse-Compression Radar to Weather Observation', *International Conference on Radar*, Paris, May 1994.
- El-Shennawy K.M., Abdel Alim O. and Ezz-el-Arab M.: 'Sidelobe Supression in Low and High Time-Bandwidth Products of Linear FM Pulse Compression Filters', *IEEE Transactions on Microwave Theory and Techniques*, Vol.35, No.9, pp.807-811, September 1987.
- Fowle E.N.: 'The Design of FM Pulse Compression Signals', *IEEE Trans.*, IT-10, pp.61-67, January 1964.
- Griffiths H.D. and Azami H.: 'Development of a Spaceborne Rain Radar: Critical Subsystem Breadboard', WP1010 Technical Note, University College London, November 1992.
- Harris F.: 'On the Use of Windows for Harmonic Analysis with the Discrete Fourier Transform', *Proc. IEEE*, Vol.66, No.1, pp.51-83, January 1978.
- Im E.: 'Pulse Compression with very Low Sidelobes in an Airborne Rain Mapping Radar: Preliminary Results', Technical Report, Jet Propulsion Lab, June 1990.

- Johnston J.A.: 'Digital Techniques in Pulse Compression Signals', Ph.D. Thesis, University of Cambridge, 1983.
- Johnston J.A. and Fairhead A.C.: 'Waveform Design and Doppler Sensitivity Analysis for Nonlinear FM Chirp Pulses', *IEE Proceedings*, Vol.133, Pt. F, No.2, pp.163-175, April 1986.
- Judd G.W.: 'Technique for Realising Low Time Sidelobe Levels in Small Compression Ratio Chirp Waveforms', *Proceedings of IEEE Ultrasonics Symposium*, pp.478-481, 1973.
- Key E.L., Fowle E.N. and Haggarty R.D.: 'A Method of Pulse Compression Employing Nonlinear Frequency Modulation', *MIT Lincoln Laboratory Report 207*, 1959.
- Klauder J.R., Price A.C., Darlington S. and Albersheim W.J.: 'The Theory and Design of Chirp Radars', *Bell System Tech. J.*, Vol.XXXIX, 1960, No.4, pp.745-809; reprinted in *Radars-Vol.3, Pulse Compression*, D.K.Barton ed., Artech House, 1975.
- Larvor J.P.: 'Digital Pulse Compression with Low Range Sidelobes', *Proc. IEE International Conference RADAR-92*, IEE Conference Publication No. 365, pp.391-394, Brighton 1992.
- Nathanson F.E.: 'Radar Design Principles', McGraw Hill, 1969.
- Newton C.O.: 'Nonlinear Chirp Radar Signal Waveforms for Surface Acoustic Wave Pulse Compression Filters', *Wave Electron.* Vol.1, pp.387-401, 1976.
- Nuttall A.H.: 'Some Windows with Very Good Sidelobe Behaviour', *IEEE Trans.* , Vol. ASSP-29, No,1, pp 84-91, February 1981.
- Rihaczek A.W.: 'Principles of High Resolution Radars', McGraw-Hill, 1969.
- Tanner A., Durden S.L., Denning R., Im E., Li F.K., Ricketts W. and Wilson W.: 'Pulse Compression with Very Low Sidelobes in an Airborne Rain Mapping Radar', *IEEE Trans. on Geoscience and Remote Sensing*, Vol. 32, No. 1, pp. 211-213, January 1994.

5 PREDISTORTED LINEAR FM SIGNAL DESIGN

Cook and Paolillo devised a range sidelobe reduction technique based on predistorting linear FM signals. Predistortion functions are to be applied to the BEST radar waveform, and its performance has already been tested on a breadboard system using SAW technology, attaining a range sidelobe level of -60 dB. A novel linear FM predistortion function design method has been developed which significantly improves the compressed pulse range sidelobe level with respect to the original design procedure. The signal Doppler tolerance is studied through the analysis of the signal ambiguity function.

5.1 Linear FM Predistortion

Linear FM spectrum Fresnel ripple distortion can be reduced by increasing the rise and fall times of the pulse. Since it is preferred not to modulate the signal amplitude, the same effect can be attained by predistorting the transmitted waveform phase. The predistorted and undistorted linear FM compressed pulses give a similar range sidelobe level. However, when the predistorted matched filter is mismatched in amplitude, it is possible to achieve a significant improvement in range sidelobe level.

5.1.1 Theory and Design

Cook and Paolillo devised a sidelobe reduction technique by means of a predistortion function applied to linear FM waveforms [Cook and Paolillo, 1964]. They showed that the linear FM rectangular spectrum model based on phase approximations was only valid for very large time-bandwidth products. The linear FM signal spectrum contains amplitude ripples which are a source of errors in the idealised flat spectrum analysis. They observed that by controlling the rise and fall times of the linear FM envelope, the spectrum Fresnel ripple was less than that of the theoretical signal spectrum, and that the range sidelobes in the $\pm T/2$ region of the compressed pulse were cancelled. Since the modification of the transmitted pulse envelope is not suitable for high-power radars, they achieved the same results by predistorting the phase or frequency modulation of the signal. From basic distortion theory, they showed that amplitude and phase distortion have functional similarities, and can produce similar effects on the waveform when the distortion

factors are small. A diagram of the resulting predistorted linear frequency modulation is shown in Figure 5.1. The predistorted linear FM signal is defined as:

$$\tilde{s}(t) = \frac{1}{\sqrt{T}} \text{rect}\left(\frac{t}{T}\right) e^{j(\pi Kt^2 + \theta_{pf}(t))} \quad (1)$$

where $\theta_{pf}(t)$ is the phase predistortion function.

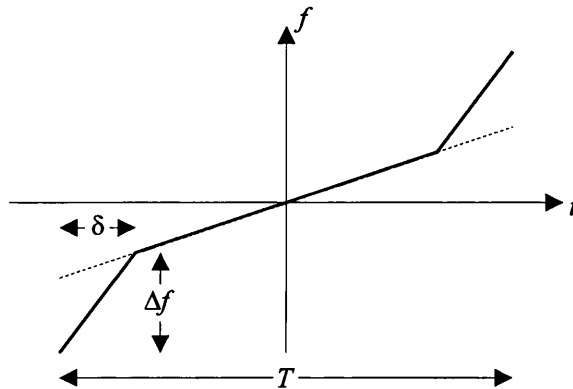


Figure 5.1. Predistorted linear FM instantaneous frequency characteristic versus time. Reproduced from [Cook and Paolillo, 1964].

Cook and Paolillo devised a quantitative estimation for the parameters δ and Δf (that is the predistortion function time bandwidth product), based on paired-echo theory [Klauder et al, 1960]. Paired-echo concepts show that small sinusoidal amplitude and phase distortion terms in a linear FM signal produce a pair of point target response delayed replicas of low magnitude before and after the main response. It can be shown that the position of these echoes is $\pm m/B$, where m is the number of cycles of sinusoidal distortion. They assumed that the main predistortion function frequency component that reduced the range sidelobes at $\pm T/2$ was $1/2\delta$ (based on the Fourier expansion of the predistortion function). In order to force the predistortion function response to cancel the range sidelobe pattern at the positive and negative halves of the compressed pulse, the width of the predistortion function must be designed to be:

$$\delta = \frac{1}{B} \quad (2)$$

They also showed that in order to obtain complete range sidelobe cancellation at $\pm T/2$ with the paired-echoes (whose amplitude is given by Bessel functions, [Cook, 1963]), the bandwidth of the predistortion function must be equivalent to:

$$\Delta f = 0.75B \quad (3)$$

They predicted that the expected value for the $\delta\Delta f$ product should be approximately of 0.75. In their paper, Cook and Paolillo also state that: “An alternate approach is to treat the increased-slope segments of the signal as individual mismatched linear FM signals. However, this does not as readily lead to intuitive conclusions as to the effects of desired parameters of the predistortion function.” It is shown in sections 5.2 and 5.3 that the study of the predistorted linear FM crosscorrelation function leads to a novel predistortion function design procedure which significantly improves the results attained by the paired-echo theory approach.

5.1.2 Practical Application: BEST Radar Waveform

A linear FM predistortion function of this kind has been employed by Alcatel Espace on a breadboard system for the BEST radar using SAW technology, ([Mavrocordatos et al, 1993] and [Griffiths, 1993]). Range sidelobe levels below -60 dB were achieved except within a range of $\pm 1.5 \mu\text{s}$ (225 m.) from the peak of the response. Figure 5.2 shows a diagram of the BEST modulation scheme. The bandwidth of the linear FM central band is 4.5 MHz over a pulse width of 59.6 μs , with a resulting $\delta\Delta f$ product of 0.54. The parameters of the BEST radar waveform are listed in Table 5.I.

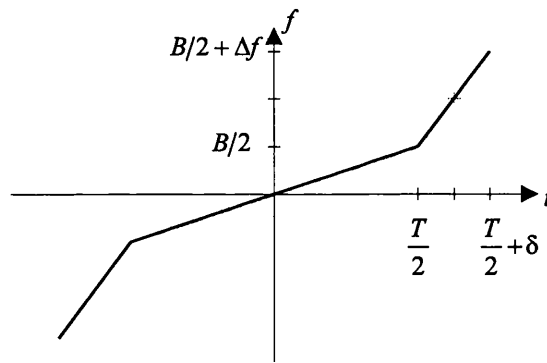


Figure 5.2. Modulation scheme employed for the BEST radar.

The predistorted linear FM waveform can be formulated as:

$$\tilde{s}(t) = \frac{1}{\sqrt{T+2\delta}} \text{rect}\left(\frac{t}{T+2\delta}\right) e^{j2\pi \int_{T+2\delta} f_i(\tau) d\tau} \quad (4)$$

where $f_i(t)$ is the instantaneous frequency of the combined linear FM signal and its predistortion function, and $T+2\delta$ is the total pulse width. The instantaneous frequency of the waveform can therefore be mathematically expressed as:

$$f_i(t) = \begin{cases} \frac{\Delta f}{\delta} \left(t - \frac{T + \delta}{2} \right) + \frac{B + \Delta f}{2} & \frac{T}{2} \geq t \geq \frac{T}{2} + \delta \\ \frac{B}{T} t & |t| \leq \frac{T}{2} \\ \frac{\Delta f}{\delta} \left(t + \frac{T + \delta}{2} \right) - \frac{B + \Delta f}{2} & -\left(\frac{T}{2} + \delta \right) \leq t \leq -\frac{T}{2} \end{cases} \quad (5)$$

Table 5.I: BEST radar waveform parameters

B	4.5 MHz
$B + 2\Delta f$	9.9 MHz
T	59.6 μ s
$T + 2\delta$	60.0 μ s
$\delta\Delta f$	0.54

The signal constituent phase terms are obtained through direct integration of the instantaneous frequency function. Therefore, Eq. 4 can be rewritten as:

$$\tilde{s}(t) = \frac{1}{\sqrt{T + 2\delta}} \text{rect} \left(\frac{t}{T + 2\delta} \right) e^{j(\theta_{lfm}(t) + \theta_{pf}(t))} \quad (6)$$

The central linear FM signal phase (for $|t| \leq \frac{T}{2}$) is given by:

$$\theta_{lfm}(t) \Big|_{|t| \leq \frac{T}{2}} = 2\pi \int K_{lfm} \tau d\tau = \pi K_{lfm} t^2 \quad (7)$$

where $K_{lfm} = \frac{B}{T}$ is the central linear FM signal modulation rate. The signal predistortion function phase is given by a second order polynomial:

$$\theta_{pf}(t) = \begin{cases} \pi K_{pf} t^2 + 2\pi \left(\frac{B + \Delta f}{2} - K_{pf} \frac{T + \delta}{2} \right) t + c_0 & \frac{T}{2} \geq t \geq \frac{T}{2} + \delta \\ 0 & |t| \leq \frac{T}{2} \\ \pi K_{pf} t^2 - 2\pi \left(\frac{B + \Delta f}{2} - K_{pf} \frac{T + \delta}{2} \right) t + c_0 & -\left(\frac{T}{2} + \delta \right) \leq t \leq -\frac{T}{2} \end{cases} \quad (8)$$

where $K_{pf} = \frac{\Delta f}{\delta}$ is the predistortion function modulation rate and c_0 an integration

constant which is determined by phase continuity between both phase terms

$$\theta_{lfm}\left(\pm \frac{T}{2}\right) = \theta_{pf}\left(\pm \frac{T}{2}\right), \text{ and given by:}$$

$$c_0 = \pi \frac{T^2}{4} (K_{lfm} - K_{pf}) - \pi \left(\frac{B + \Delta f}{2} - K_{pf} \frac{T + \delta}{2} \right) T \quad (9)$$

Figure 5.3 shows a comparison between the linear and predistorted linear FM signal spectra. Note that the predistorted linear FM spectrum gives lower Fresnel ripple distortion, especially at the centre of the band.

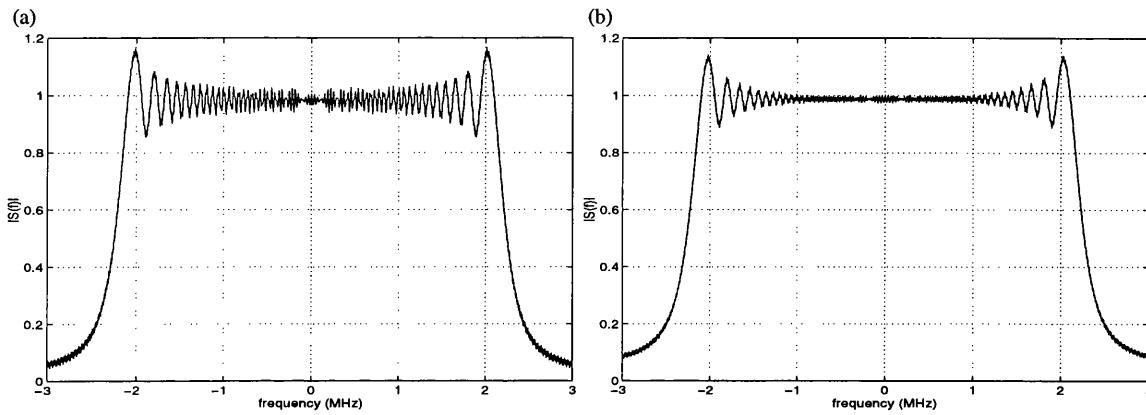


Figure 5.3. Signal spectra ($B = 4.5$ MHz): (a) Linear FM; (b) Predistorted linear FM.

The matched filter amplitude mismatching function employed in the BEST breadboard was a minimum 3-term Blackman-Harris function (Eq. 4.13):

$$w(t) = \text{rect}\left(\frac{t}{T + 2\delta}\right) \sum_{n=0}^2 a_n \cos(2\pi n f_T t) \quad (10)$$

where $f_T = 1/(T + 2\delta)$.

5.2 Predistorted Linear FM Compressed Pulse Analysis

The mathematical analysis of the predistorted linear FM compressed pulse when its matched filter is mismatched in amplitude leads to the understanding of its compression cancellation. It is shown that the two main terms of its crosscorrelation function are of the same shape but of opposite sign, which cancel giving a lower range sidelobe pattern than

that of the undistorted linear FM signal.

5.2.1 Crosscorrelation Function

The predistorted linear FM signal compressed pulse (when no mismatch is considered) is given by its autocorrelation function:

$$s_0(\tau) = \int_{-\infty}^{\infty} \tilde{s}(t) \tilde{s}^*(t - \tau) dt \quad (11)$$

Although linear and predistorted linear FM compressed pulses produce an identical range sidelobe level, they have completely different range sidelobe patterns (the linear FM compressed pulse of $TB = 250$ was shown in Figure 3.5(b)). The predistorted linear FM compressed pulse (shown in Figure 5.4) gives a range sidelobe pattern cancellation on the $\pm T/2$ region.

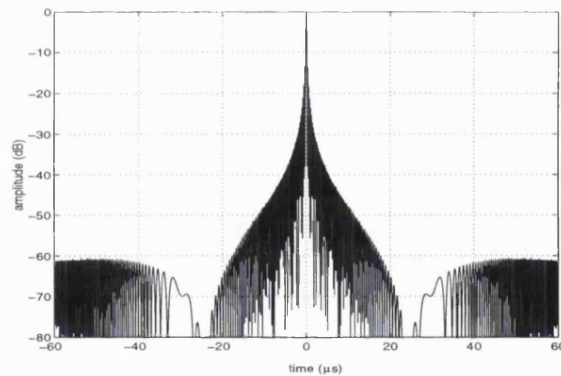


Figure 5.4. Predistorted linear FM compressed pulse ($BT = 270$, $\delta\Delta f = 0.54$)

The compressed pulse when the matched filter is mismatched in amplitude is given by:

$$s_0(\tau) = \int_{-\infty}^{\infty} \tilde{s}(t) \tilde{s}^*(t - \tau) w(t - \tau) dt \quad (12)$$

A comparison between the linear and predistorted linear FM compressed pulse spectra (minimum 3-term Blackman Harris amplitude mismatching function) is shown in Figure 5.5 and their compressed pulses are shown in Figure 5.6.

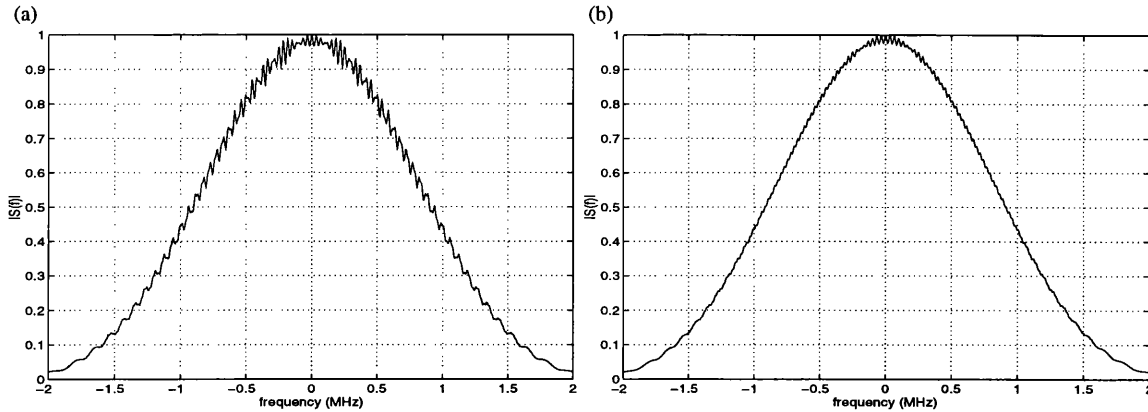


Figure 5.5. Compressed pulse spectra ($B = 4.5$ MHz), minimum 3-term Blackman-Harris amplitude mismatching function: (a) Linear FM; (b) Predistorted linear FM.

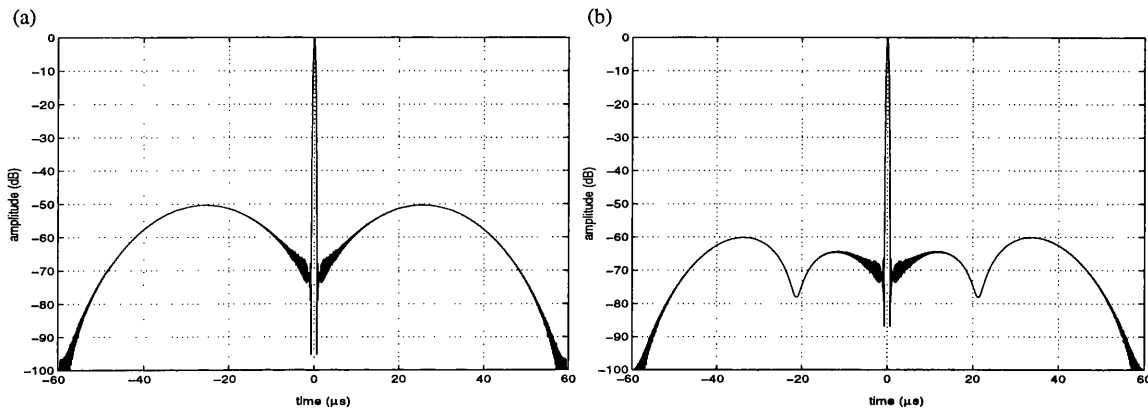


Figure 5.6. Compressed pulses ($B = 4.5$ MHz), minimum 3-term Blackman-Harris amplitude mismatching function: (a) Linear FM; (b) Predistorted linear FM.

Table 5.II: Linear and predistorted linear FM compressed pulse characteristics

	RSL	L_p	L_a	$\Delta\tau_{-3dB}$
linear FM	-13.3 dB	0 dB	0 dB	1
Linear FM (Blackman-Harris)	-50.4 dB	7.5 dB	5.5 dB	1.85
Predistorted linear FM (Blackman-Harris)	-60.0 dB	7.5 dB	5.5 dB	1.67

An improvement of nearly 10 dB in range sidelobe level (Table 5.II) is attained by predistorting linear FM signals. The addition of a different modulation rate predistortion function introduces two minima (approximately at $\pm T/2$) in the linear FM compressed pulse, lowering its range sidelobe level from nearly -50 to -60 dB. The predistortion function does not introduce additional losses compared to the mismatched undistorted linear FM compressed pulse.

5.2.2 Compressed Pulse Analytical Expression

A rather different approach to the original paired-echo theory one is developed in this section, in order to devise an alternative design method to improve the predistorted linear FM compressed pulse range sidelobe level. The new approach consists of the calculation of the predistorted linear FM signal crosscorrelation function in the time domain. The compressed pulse is given by the crosscorrelation between the predistorted signal and its matched filter impulse response (mismatched in amplitude):

$$R_{\tilde{s}, \tilde{s}_w}(\tau) = \frac{1}{T+2\delta} \int_{-\infty}^{\infty} \text{rect}\left(\frac{t}{T+2\delta}\right) \text{rect}\left(\frac{t-\tau}{T+2\delta}\right) w(t-\tau) \cdot e^{j(\theta_{lfm}(t)+\theta_{pf}(t))} e^{-j(\theta_{lfm}(t-\tau)+\theta_{pf}(t-\tau))} dt \quad (13)$$

The crosscorrelation function $R_{\tilde{s}, \tilde{s}_w}$ may be separated into its four constituent terms. Eq. 13 is then reformulated as:

$$R_{\tilde{s}, \tilde{s}_w}(\tau) = R_1(\tau) + R_2(\tau) + R_3(\tau) + R_4(\tau) \quad (14)$$

In order to define each correlation term (shown in Figure 5.7), the predistorted linear FM signal is redefined as:

$$\tilde{s}(t) = e^{j2\pi \int_{T+2\delta} f_i(\tau) d\tau} = \tilde{s}_{lfm}(t) + \tilde{s}_{pf}(t) \quad (15)$$

where $\tilde{s}_{lfm}(t)$ corresponds to the linear FM signal and $\tilde{s}_{pf}(t)$ to the predistortion function. The correlation function terms can now be expressed as:

$$R_1(\tau) = \frac{1}{T+2\delta} \int_{-\infty}^{\infty} \text{rect}\left(\frac{t}{T}\right) \text{rect}\left(\frac{t-\tau}{T}\right) w(t-\tau) e^{j\theta_{lfm}(t)} e^{-j\theta_{lfm}(t-\tau)} dt \quad (16)$$

$$R_2(\tau) = \frac{1}{T+2\delta} \int_{-\infty}^{\infty} \text{rect}\left(\frac{t}{T}\right) \text{rect}\left(\frac{t-\tau}{T+2\delta}\right) w(t-\tau) e^{j\theta_{lfm}(t)} e^{-j\theta_{pf}(t-\tau)} dt \quad (17)$$

$$R_3(\tau) = \frac{1}{T+2\delta} \int_{-\infty}^{\infty} \text{rect}\left(\frac{t}{T+2\delta}\right) \text{rect}\left(\frac{t-\tau}{T}\right) w(t-\tau) e^{j\theta_{pf}(t)} e^{-j\theta_{lfm}(t-\tau)} dt \quad (18)$$

$$R_4(\tau) = \frac{1}{T+2\delta} \int_{-\infty}^{\infty} \text{rect}\left(\frac{t}{T+2\delta}\right) \text{rect}\left(\frac{t-\tau}{T+2\delta}\right) w(t-\tau) e^{j\theta_{pf}(t)} e^{-j\theta_{pf}(t-\tau)} dt \quad (19)$$

The time widths of each crosscorrelation function term are given in Table 5.III, and their different intervals must be taken into account in order to formulate the point target response.

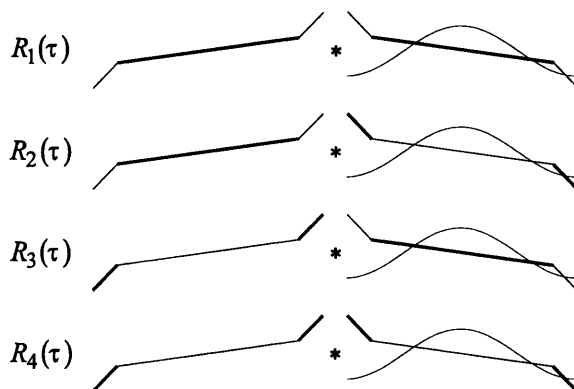


Figure 5.7. Predistorted linear FM crosscorrelation function constituent terms diagram.

Table 5.III: Predistorted linear FM signal crosscorrelation function term widths

	<i>width</i>
$R_{\tilde{s}, \tilde{s}_w}(\tau)$	$ \tau \leq 2T + 4\delta$
$R_1(\tau)$	$ \tau \leq 2T$
$R_2(\tau)$	$ \tau \leq 2T + 2\delta$
$R_3(\tau)$	$ \tau \leq 2T + 2\delta$
$R_4(\tau)$	$\begin{cases} -(2T + 4\delta) \leq \tau \leq -(2T + 2\delta) \\ \tau \leq 2\delta \\ 2T + 2\delta \leq \tau \leq 2T + 4\delta \end{cases}$

The amplitude mismatching function attenuates the predistortion function of the matched filter by approximately -23 dB (Eq. 17 and Eq. 19). $R_4(\tau)$ has no influence on the range sidelobe level cancellation and the level of $R_2(\tau)$ at $\pm T/2$ is approximately -20 dB below the other two terms, and may therefore be disregarded. Hence, the compressed pulse can be approximated by the addition of only two of its four components, given by:

$$R_{\tilde{s}, \tilde{s}_w}(\tau) \approx R_1(\tau) + R_3(\tau) \quad (20)$$

It should be noted that Eq. 20 shows that it is not necessary to apply predistortion to the linear FM matched filter. $R_1(\tau)$ is equivalent to the central linear FM compressed

pulse given by:

$$R_1(\tau) = \frac{1}{T+2\delta} e^{-j\pi K_{lfm}\tau^2} \int_{-\infty}^{\infty} \text{rect}\left(\frac{t}{T}\right) \text{rect}\left(\frac{t-\tau}{T}\right) w(t-\tau) e^{j2\pi K_{lfm}t} dt \quad (21)$$

The solution to Eq. 21 is given by:

$$R_1(\tau) = \frac{1}{2} \left(\frac{T}{T+2\delta} - \frac{|\tau|}{T+2\delta} \right) \sum_{n=-2}^2 a'_n \text{sinc} \left(\left(1 - \frac{|\tau|}{T} \right) \left(B\tau + n \frac{T}{T+2\delta} \right) \right) e^{j\pi f_T \tau} \quad (22)$$

where $a'_0 = 2a_0$ and $a'_n = a'_{-n} = a_n$. A detailed calculation can be found in Appendix B.3 (notice that $R_1(\tau) = \chi(\tau, 0)$ with the appropriate corrections due to the fact that the length of the linear FM pulse is no longer equivalent to the length of the weighting function).

The range sidelobe patterns of $R_1(\tau)$ and $R_3(\tau)$ are of the same basic shape but of opposite sign. When both terms are added in compression, their peaks cancel leaving a double sidelobe structure with a lower peak sidelobe level than for the undistorted linear FM response. The real and imaginary components of $R_1(\tau)$ and $R_3(\tau)$ are shown in Figure 5.8.

The calculation of $R_3(\tau)$ can be eased by exploiting the symmetry of the function. The calculation of $R_3(\tau)$ in the interval $0 \leq \tau \leq T_2$ automatically determines the negative interval of the function. $R_3(\tau)$ (for $\tau \geq 0$) is formulated as:

$$R_3(\tau)|_{\tau \geq 0} = \frac{1}{T+2\delta} \int_{-\infty}^{\infty} \text{rect}\left(\frac{t}{T+2\delta}\right) \text{rect}\left(\frac{t-\tau}{T}\right) w(t-\tau) e^{j\theta_{pf}(t)} e^{-j\theta_{lfm}(t-\tau)} dt \quad (23)$$

A detailed calculation of Eq. 23 is developed in Appendix C, whose solution is expressed as:

$$R_3(\tau)|_{\tau \geq \delta} = \sqrt{\frac{\pi}{2}} \frac{1}{2b(T+2\delta)} e^{-j(\pi K_{lfm}\tau^2 + \lambda^2(\tau) - c_0)} \cdot \sum_{n=-2}^2 a'_n e^{-j\frac{(\pi f_T)^2}{b^2} e^{-j2\pi f_T \left(\frac{\lambda(\tau)}{b} + \tau \right)}} \left(F(z_2 + nz_0) - F(z_1 + nz_0) \right) \quad (24)$$

where:

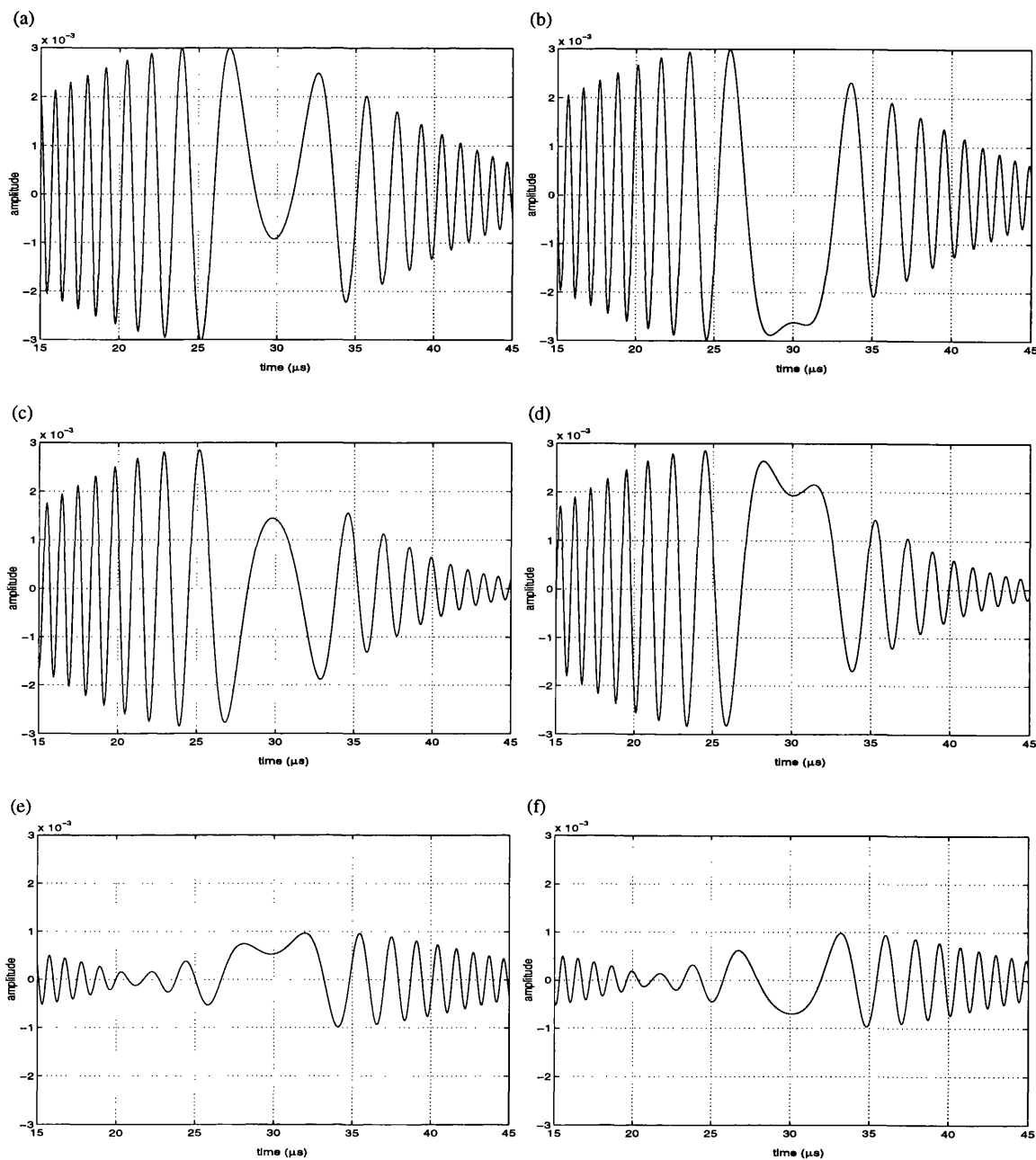


Figure 5.8. Predistorted linear FM signal crosscorrelation function (real and imaginary components): (a) $\text{Re}(R_1(\tau))$; (b) $\text{Im}(R_1(\tau))$; (c) $\text{Re}(R_3(\tau))$; (d) $\text{Im}(R_3(\tau))$; (e) $\text{Re}(R_{\delta, \delta_w}(\tau))$; (f) $\text{Im}(R_{\delta, \delta_w}(\tau))$.

$$b = \sqrt{\pi(K_{pf} - K_{lfm})} \quad (25)$$

$$\lambda(\tau) = \frac{\pi \left(K_{lfm} \tau + \frac{B + \Delta f}{2} - K_{pf} \frac{T + \delta}{2} \right)}{\sqrt{\pi(K_{pf} - K_{lfm})}} \quad (26)$$

$$F(z) = \int e^{j\frac{\pi z^2}{2}} dz = C(z) + jS(z) \quad (27)$$

$$z_0 = \sqrt{\frac{2}{\pi}} \frac{\pi f T}{b} \quad (28)$$

$$z_1 = \sqrt{\frac{2}{\pi}} \left(b \frac{T}{2} + \lambda(\tau) \right) \quad (29)$$

$$z_2 = \sqrt{\frac{2}{\pi}} \left(b \left(\frac{T}{2} + \delta \right) + \lambda(\tau) \right) \quad (30)$$

The comparison between predistorted linear FM compressed pulses obtained through FFT processing and through its analytical calculation is shown in Figure 5.9. The small ripples observed in the theoretical calculation are due to the approximation made, and correspond to the disregarded crosscorrelation term. A very large sampling rate was used (1 GHz) and the sidelobe level of both pulses is -62.1 dB, which does not match the sidelobe level figure of -60.0 dB obtained at a sampling rate of 40 MHz. Although both sampling frequencies are greater than the Nyquist Criterion ($f_s \geq 2B_2$), the resolution of the samples of the predistortion function is better at high sampling frequencies (where more samples for the relatively short predistortion function are available), which causes the range sidelobe level to fluctuate a few dB as a function of sampling rate.

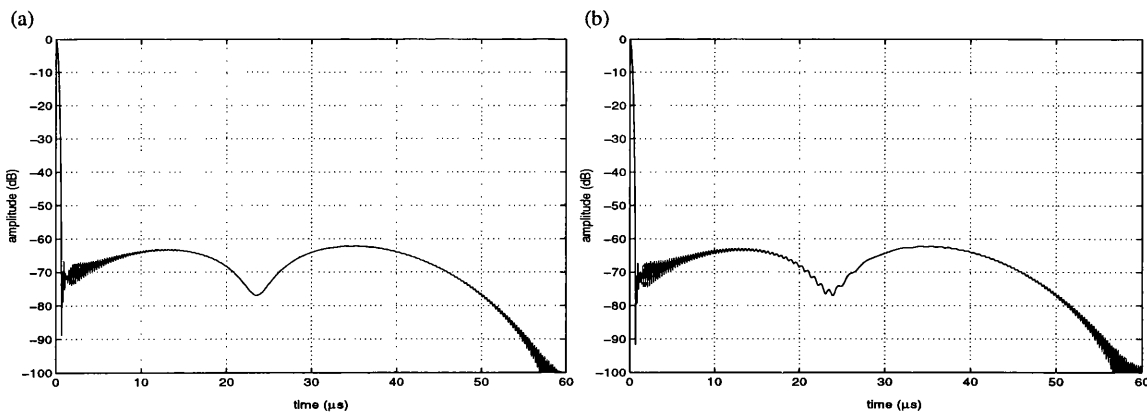


Figure 5.9. Predistorted linear FM compressed pulse: (a) FFT signal processing; (b) Analytical calculation.

5.3 Predistortion Function Range Sidelobe Matching Design Method

The range sidelobe level of a predistorted linear FM compressed pulse can be improved by enhancing the sidelobe pattern matching between the linear FM compressed pulse and the crosscorrelation between the predistortion function and the linear FM signal. A novel design procedure has been devised in order to determine the parameters of the predistortion function δ and Δf that achieve optimum cancellation of the range sidelobe pattern of $R_{\tilde{s}, \tilde{s}^*}(\tau)$.

The position of the range sidelobe maxima of $R_1(\tau)$ can be found by solving the following equation:

$$\frac{\partial R_1(\tau_{\max})}{\partial \tau} = 0 \quad (31)$$

Analytical differentiation of $R_1(\tau)$ with respect to time has been carried out, leading to an unwieldy expression. The differentiation can instead be obtained numerically. Once the value of τ_{\max} is obtained, optimum sidelobe cancellation occurs if its value corresponds to the same position for the range sidelobe maxima of $R_3(\tau)$; thus cancelling in both amplitude and phase:

$$\left| R_1(\tau_{\max}) \right| = \left| R_3(\tau_{\max}) \right| \text{ and } \frac{\partial \text{Im} R_1(\tau_{\max})}{\partial \tau} = - \frac{\partial \text{Im} R_3(\tau_{\max})}{\partial \tau} \quad (32)$$

The parameters of the predistortion function δ and Δf are chosen through a recursive numerical method in order to force the same peak position in both $R_1(\tau)$ and $R_3(\tau)$, by solving the following equation:

$$\frac{\partial R_3(\tau_{\max}, \delta, \Delta f)}{\partial \tau} = 0 \quad (33)$$

The previous design procedure has been applied to the BEST radar modulation scheme and the range sidelobe level has been reduced to -62.8 dB ($\delta \Delta f = 0.51$). The new predistorted linear FM compressed pulse and its constituent terms are shown in Figure 5.10.

Figure 5.11(a) shows the range sidelobe matching method results as a function of pulse width for a constant linear FM time-bandwidth product of 270. The point target responses are shown in Figure 5.11(b). The new design procedure provides an average range sidelobe level of -62.6 dB (which represents an improvement of 5.7 dB compared to

the original design method). It has been found that the predistortion function time-bandwidth product is not constant (Figure 5.11(c)) and oscillates around an average value of 0.53.

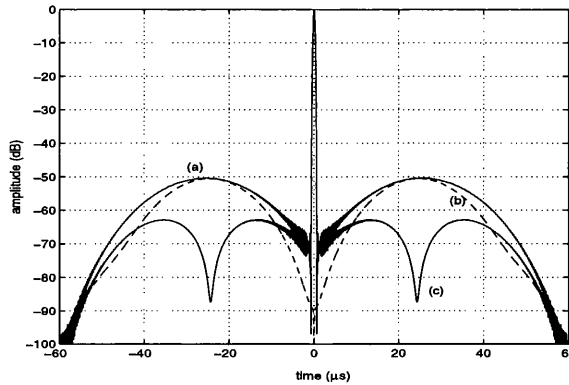


Figure 5.10. (1) Linear FM (amplitude weighted) compressed pulse $R_1(t)$, time-bandwidth product = 270, sidelobe level -50.4 dB; (2) Crosscorrelation between the predistortion function and the linear FM signal (amplitude weighted); (3) Predistorted linear FM (amplitude weighted) compressed pulse, sidelobe level -62.8 dB.

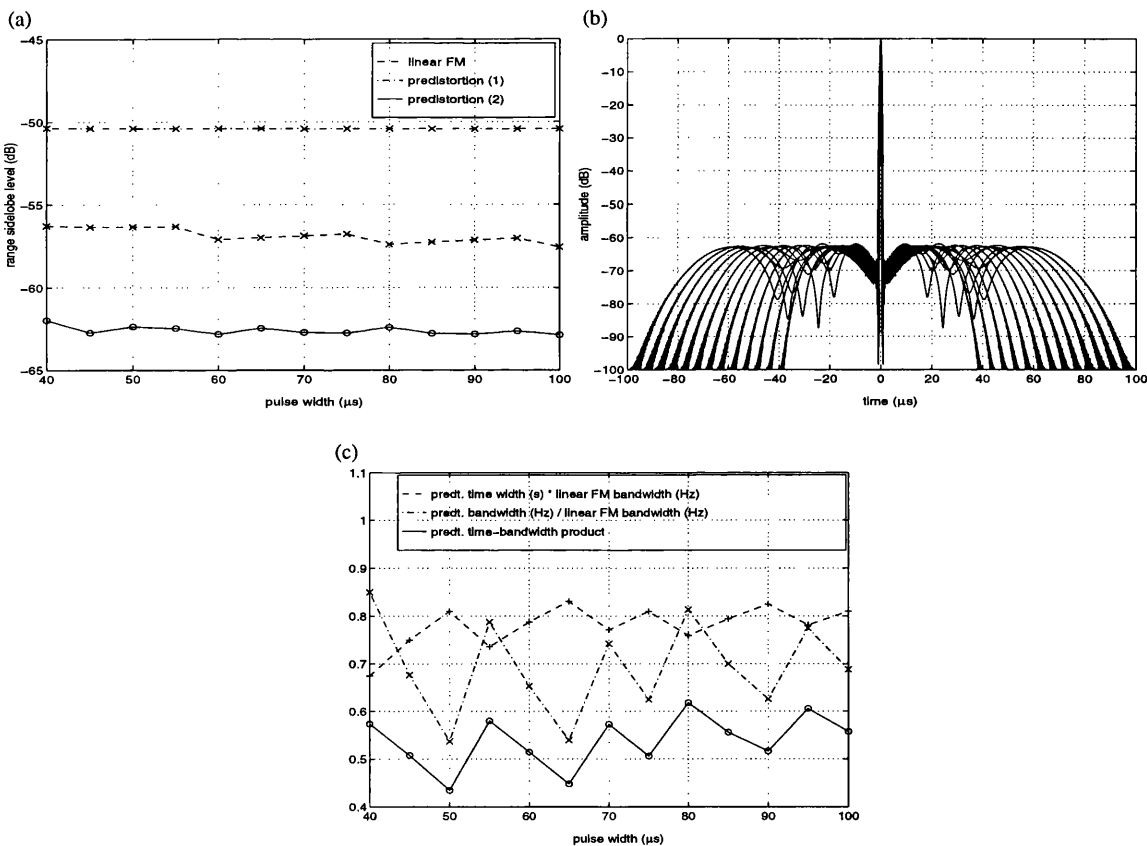


Figure 5.11. Comparison between predistortion function design procedures as function of pulse width for a constant time-bandwidth product of 270, (1) indicates the Cook and Paolillo method ($\delta\Delta f = 0.75$) and (2) the range sidelobe matching method (mismatching: minimum 3-term Blackman-Harris function). (a) Range sidelobe levels; (b) Compressed pulses for the range sidelobe matching method; (c) Predistorted function parameters for the range sidelobe matching method.

In order to determine the required linear FM time-bandwidth product to attain a range sidelobe level below -70 dB when applying predistortion, the design procedure has been applied for a constant bandwidth of 4.5 MHz as a function of pulse width. Notice that in the previous case, the bandwidths were adjusted to maintain a constant product of 270 . A predistortion function applied to a linear FM function with a time-bandwidth product of 630 gives a range sidelobe level of -70 dB (Figure 5.12 (a-b)). It should be noted that amplitude mismatching of an undistorted linear FM signal matched filter could only achieve range sidelobe levels below -60 dB for higher time-bandwidth products than 800 (Figure 4.4). The average range sidelobe improvement is of 6 dB and the predistortion function time-bandwidth product is again consistent with the two previous cases, oscillating around an average value of 0.52 (Figure 5.12(c)). The same results were obtained applying the design procedure as a function of signal bandwidth.

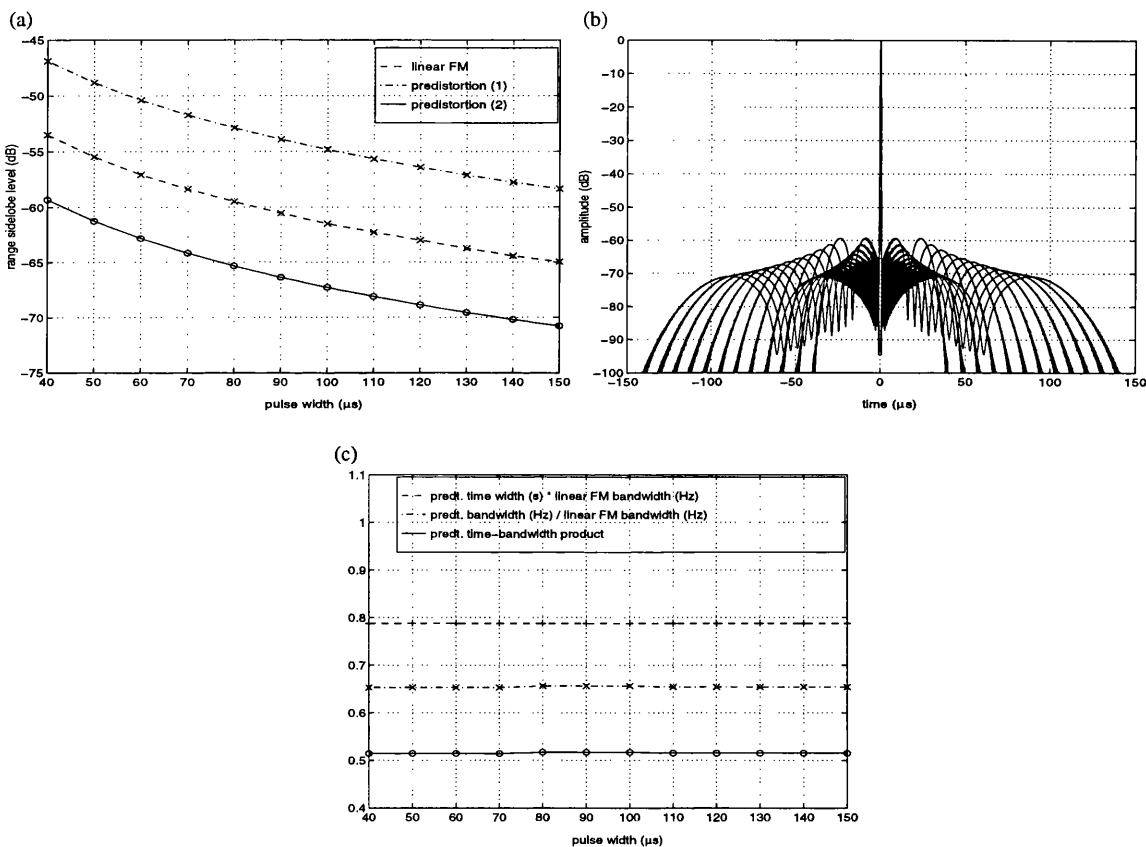


Figure 5.12. Comparison between predistortion function design procedures as function of pulse width for a constant time-bandwidth product of 270 ($B = 4.5$ MHz), (1) indicates the Cook and Paolillo method ($\delta\Delta f = 0.75$) and (2) the range sidelobe matching method (mismatching: minimum 3-term Blackman-Harris function). (a) Range sidelobe levels; (b) Compressed pulses for the range sidelobe matching method; (c) Predistorted function parameters for the range sidelobe matching method.

The range sidelobe matching method has also been applied to other matched filter mismatching functions obtaining very similar results. However, the family of Blackman-

Harris functions give the best results in terms of range sidelobe level reduction. These weighting functions are designed to cancel the sidelobes adjacent to the main lobe and their maximum range sidelobes are located around $\pm T/2$, being the cancellation due to predistortion optimum. For other weighting functions, such as the Hamming or Dolph-Chebyshev windows, the maximum sidelobes are located in the vicinity of the mainlobe. Although the predistortion function also produces sidelobe cancellation around $\pm T/2$, relatively little is gained in terms of peak range sidelobe level.

In particular, the new predistortion function design procedure was applied for a minimum 4-term Blackman-Harris amplitude mismatching function, defined as:

$$w(t) = \text{rect}\left(\frac{t}{T}\right) \sum_{n=0}^3 a_n \cos\left(\frac{2\pi n t}{T}\right) \quad (34)$$

where $a_0 = 0.35875$, $a_1 = 0.48829$, $a_2 = 0.14128$ and $a_3 = 0.01168$ [Harris, 1978]. The window spectrum (shown in Figure 5.13) gives a sidelobe level of -92 dB.

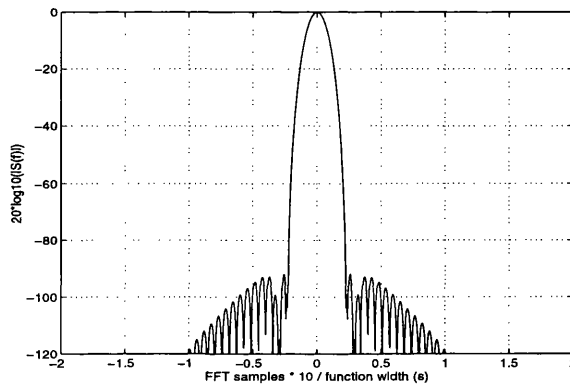


Figure 5.13. Minimum 4-term Blackman-Harris function Fourier transform.

Range sidelobe levels as a function of pulse width for a constant time-bandwidth product of 270 are shown in Figure 5.14(a) and the compressed pulses in Figure 5.14(b). The obtained average range sidelobe level is of -63.6 dB (1 dB better than with the minimum 3-term Blackman Harris function) with an average improvement of 8.3 dB compared to the original design method. The predistortion function time-bandwidth product oscillates around an average value of 0.5. The predistortion function values obtained through the range sidelobe matching design procedure are summarised in Table 5.IV.

The range sidelobe matching design procedure has been successfully applied to different time-bandwidth products and various amplitude mismatching functions. It has

been found that the optimum value of the product $\delta\Delta f$ is not constant, showing very little dependence on the mismatching function. The new product $\delta\Delta f$ is smaller than the originally proposed value of 0.75 and oscillates as a function of time-bandwidth product around an average value of 0.5.

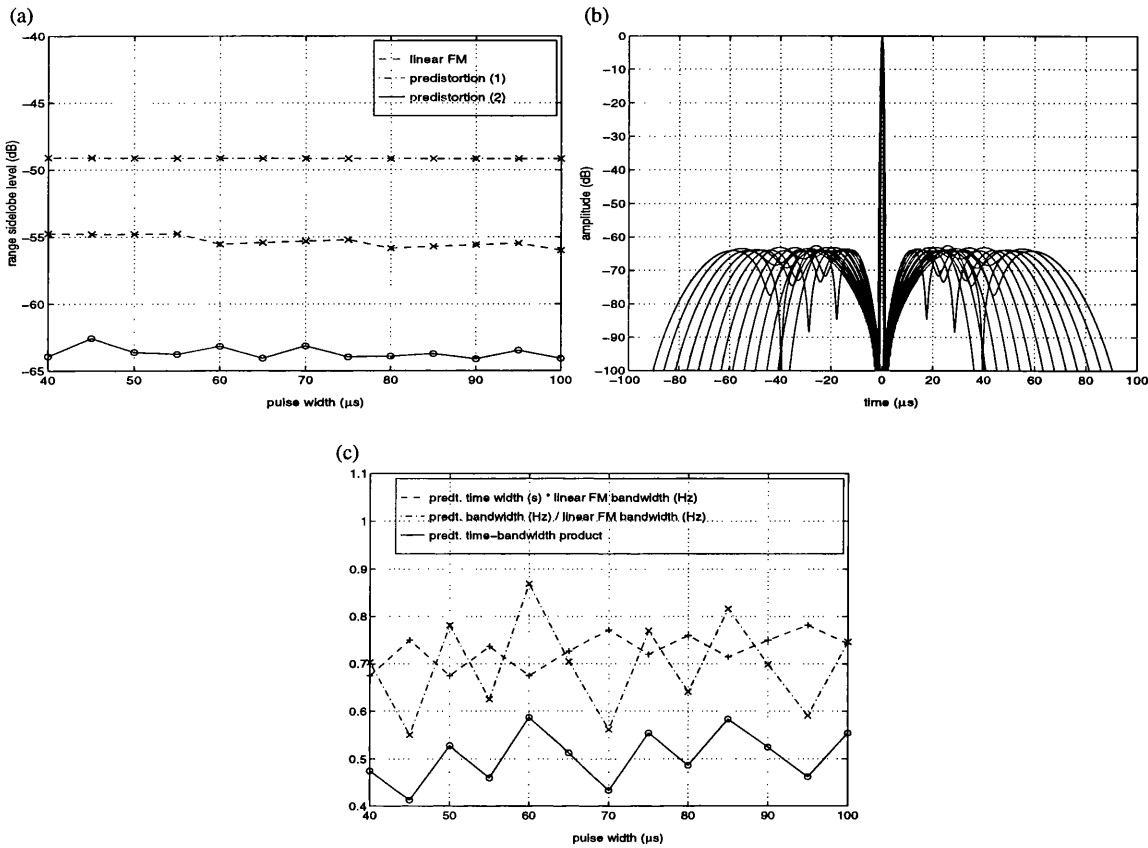


Figure 5.14. Comparison between predistortion function design procedures as function of pulse width for a constant time-bandwidth product of 270, (1) indicates the Cook and Paolillo method ($\delta\Delta f = 0.75$) and (2) the range sidelobe matching method (mismatching: minimum 4-term Blackman-Harris function). (a) Range sidelobe levels; (b) Compressed pulses for the range sidelobe matching method; (c) Predistorted function parameters for the range sidelobe matching method.

Table 5.IV: Range sidelobe matching method, predistorted linear FM average parameter values

	TB	$\delta\Delta f$	δ	Δf	\overline{RSL}	ΔRSL^1	ΔRSL^2
3-term B-H	270	0.53	$0.78/B$	$0.69 B$	-62.6 dB	5.7 dB	12.0 dB
3-term B-H	180-675	0.52	$0.74/B$	$0.71 B$		6.0 dB	12.0 dB
4-term B-H	270	0.50	$0.72/B$	$0.69 B$	-63.6 dB	8.3 dB	14.5 dB

According to the previous results, it seems a reasonable assumption to introduce a

¹ Predistorted Linear FM range sidelobe level improvement with respect to $\delta\Delta f = 0.75$.

² Predistorted Linear FM range sidelobe level improvement with respect to undistorted linear FM signals.

correction factor to the original predistortion parameters. The new values for the predistortion function duration and bandwidth are given by:

$$\delta = 0.75 \frac{1}{B} \quad (35)$$

$$\Delta f = 0.66B \quad (36)$$

On the other hand, Kowatsch et al. [Kowatsch and Stocker, 1982] describe a linear FM predistortion function based on cubic predistortion instead of a second order law phase at the edges of the linear FM pulse. A novel method has been developed (described in Chapter 6) in which a continuous linear FM predistortion function is achieved, avoiding modulation discontinuities and attaining a range sidelobe level of -64.5 dB for a time-bandwidth product of 300.

5.4 Predistorted Linear FM Ambiguity Function

The Doppler performance of the predistorted linear FM waveform has been studied through the analysis of its ambiguity function (shown in Figure 5.15). Small Doppler frequency offsets up to 100 kHz (2% of the signal bandwidth) have very little impact on the compressed pulse range sidelobe level.

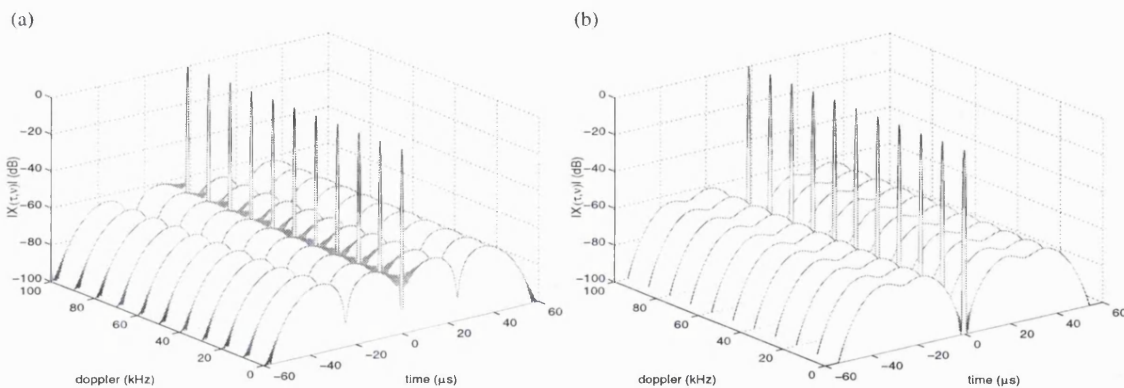


Figure 5.15. Predistorted linear FM ambiguity functions ($BT = 270$): (a) Minimum 3-term Blackman-Harris mismatching function; (b) Minimum 4-term Blackman-Harris mismatching function.

The range sidelobe patterns continue to cancel in spite of Doppler shifts, since frequency offsets affects both components of the compressed pulse in the same way. Predistorted linear FM signals exhibit equal Doppler invariability properties as linear FM

waveforms, although giving a significantly lower range sidelobe level. It has been observed that for Doppler offsets of larger fractions of the signal bandwidth, a cessation of sidelobe cancellation takes place and the range sidelobe level is then equal to that of the Doppler shifted linear FM point target response.

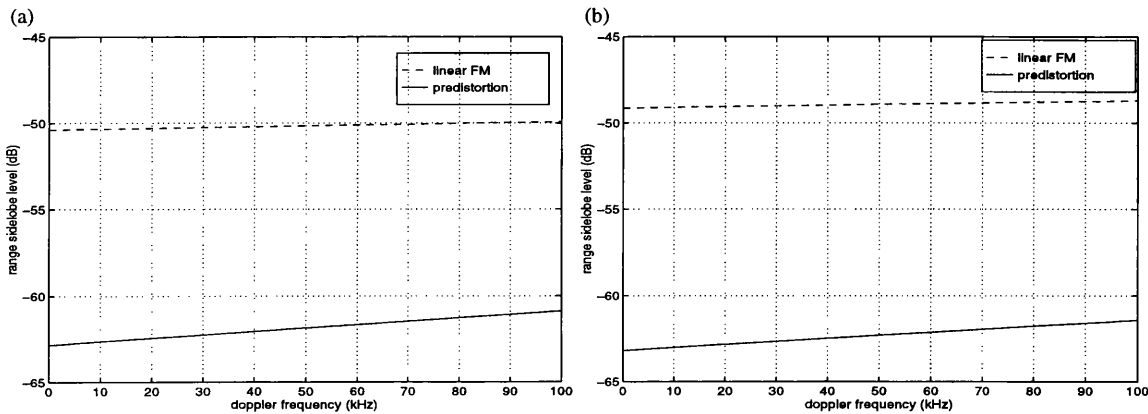


Figure 5.16. Range sidelobe level degradation as a function of Doppler frequency for linear and predistorted linear FM signals ($BT = 270$): (a) minimum 3-term Blackman-Harris amplitude mismatching function; (b) minimum 4-term Blackman-Harris amplitude mismatching function.

Range sidelobe levels as a function of Doppler are shown in Figure 5.16 for minimum 3 and 4 term Blackman-Harris mismatching functions. The range sidelobe level degradation for a shift of 100 kHz is of approximately 2 dB (minimum 3-term) and of 1.7 dB (minimum 4-term). The range-doppler coupling for a Doppler offset of 100 kHz is equivalent for both linear and predistorted FM signals and equal to $1.3 \mu\text{s}$ for both mismatching functions.

5.5 References

- Cook C.E. and Paolillo J.: 'A Pulse Compression Predistortion Function for Efficient Sidelobe Reduction in a High-Power Radar', *Proc. IEEE*, pp. 377-389, April 1964.
- Cook C.E.: 'Transmitter Phase Modulation Errors and Pulse Compression Waveform distortion', *Microwave Journal*, pp. 63-69, May 1963.
- Griffiths H.D.: 'Ultra-Low Range Sidelobe Pulse Compression for Satellite-Borne Rain Radar', *Proc. IEEE National Radar Conference*, IEEE Publication No. 93CH3253-2, Boston, MA, pp. 140-145, April 1993.
- Griffiths H.D. and Vinagre L.: 'Design of Low-Sidelobe Pulse Compression Waveforms', *Electronics Letters*, Vol.30, No.12, pp. 1004-1005, June 1994.
- Harris F.: 'On the Use of Windows for Harmonic Analysis with the Discrete Fourier Transform', *Proc. IEEE*, Vol.66, No.1, January 1978, pp. 51-83.
- Klauder J.R., Price A.C., Darlington S. and Albersheim W.J.: 'The Theory and Design of Chirp Radars', *Bell System Tech. J.*, Vol.XXXIX, 1960, No.4, pp.745-809; reprinted in *Radars-Vol.3, Pulse Compression*, D.K.Barton ed., Artech House, 1975.
- Kowatsch M. and Stocker H.R.: 'Effect of Fresnel Ripples on Sidelobe Suppression in Low Time-Bandwidth Product Linear FM Pulse Compression', *IEEE Proceedings*, No.1, Vol. 129, pp. 41-44, February 1982,.
- Mavrocordatos C. and Caille G.: 'Rain Radar. Instrument Design and Critical Technologies', Alcatel Espace Presentation, ESA Workshop on Rain/Cloud Radar, ESTEC, September 1993.

6 ASYMMETRIC FM SIGNAL DESIGN

Range sidelobe reduction techniques reported in the literature do not take into account the particular spaceborne meteorological radar target scenario. Meteorological information is only present before the leading edge of the surface return compressed pulse mainlobe. Therefore, an asymmetric point target response whose range sidelobe pattern is below the required level on only one side of the compressed pulse could be employed to carry out the meteorological measurements. A novel asymmetric nonlinear FM design method has been devised which achieves asymmetric compression giving range sidelobe levels below -60 dB with an excellent performance in terms of Doppler frequency offsets. The design method can also be applied in order to obtain ‘continuous’ predistorted linear FM signals which improve the range sidelobe level results reported in Chapter 5.

6.1 Introduction

An asymmetric pulse compression frequency modulation was described by Kroszczynski [Kroszczynski, 1969] in order to minimise the impact of large Doppler frequency offsets (of significant fractions of the signal bandwidth) on linear FM compression losses. A Doppler-invariant waveform by means of linear period modulation was defined as:

$$s(t) = \frac{1}{\sqrt{T}} \operatorname{rect}\left(\frac{t}{T}\right) e^{j2\pi f_0^2 T \ln\left(1 - \frac{Bt}{f_0 T}\right)} \quad (1)$$

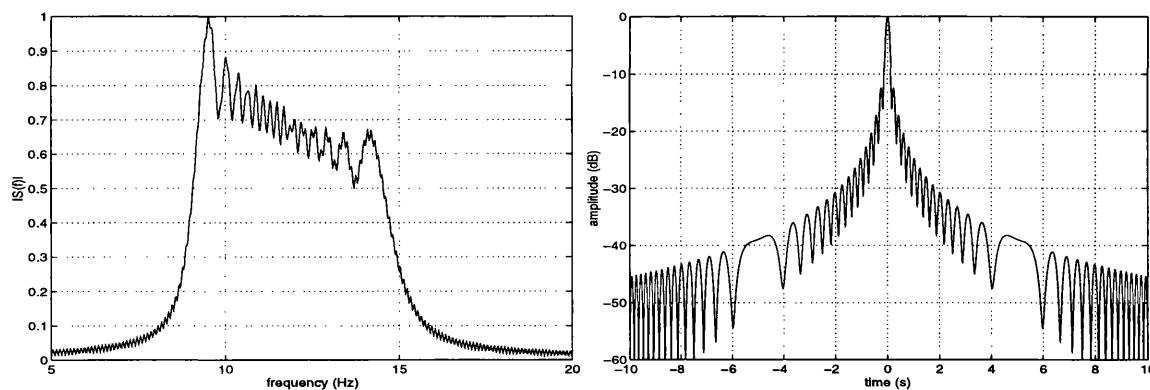


Figure 6.1. Linear period-modulated ($TB = 100$): (a) spectrum; (b) compressed pulse. Reproduced from [Kroszczynski, 1969].

Figure 6.1 shows the spectrum and compressed pulse of a linear period modulated waveform of a similar time-bandwidth product and characteristics to the sonic pulses transmitted by bats. Since the returned signal is processed through a true matched filter, the compressed pulse is symmetric, and does not improve the performance of linear FM signals in terms of range sidelobe level.

Asymmetric pulse compression has also been proposed by Wilson [Wilson, 1990], based on waveform generation from a finite set of samples, but the method did not produce asymmetric frequency modulation laws.

6.2 Asymmetric Nonlinear FM Pulse Compression

Asymmetric pulse compression can be achieved by means of nonlinear frequency modulation. An asymmetric instantaneous frequency characteristic allowing a non uniform group delay over the pulse frequency spectrum has been developed in order to force asymmetric compression at the output of a linear FM matched filter. The asymmetric modulation is obtained through the addition of a nonlinear phase term to the phase of a linear FM signal. The resulting signal complex envelope is defined as:

$$\tilde{s}_a(t) = \frac{1}{\sqrt{T}} \text{rect}\left(\frac{t}{T}\right) e^{j2\pi\left(\frac{B}{2T}t^2 + \theta_a(t)\right)} \quad (2)$$

where $\theta_a(t)$ is a time dependent phase term which controls the degree of nonlinearity across the waveform frequency modulation. A novel design procedure is described in this section which consists of modifying the linear FM signal instantaneous frequency by adjusting the values of the signal nominal bandwidth through a controlling phase polynomial. The asymmetric FM design procedure is based on the addition of an even frequency function to a linear FM signal instantaneous frequency of a given time-bandwidth product, so that the modulation rate is no longer constant and of the same sign throughout the pulse. The nonlinear phase term can be defined as an odd function expressed as a polynomial of terms of odd powers, given by:

$$\theta_a(t) = \sum_{n=3}^N k_n \left(\frac{2t}{T}\right)^n \quad (3)$$

where $n = 3, 5, \dots, N$. Therefore, the instantaneous frequency of the combined nonlinear FM signal can be expressed as:

$$f_i(t) = \frac{B}{T}t + \frac{2}{T} \sum_{n=3}^N k'_n \left(\frac{2t}{T}\right)^{n-1} \quad (4)$$

where $k'_n = nk_n$. The nonlinear term in the waveform instantaneous frequency constitutes now an even function expressed as a polynomial of terms of even powers. The polynomial coefficients k'_n are then calculated in order to attain selected values at the edges of the signal instantaneous frequency:

$$f_i\left(\pm \frac{T}{2}\right) = \pm \frac{B}{2} + \frac{2}{T} \sum_{n=3}^N k'_n (\pm 1)^{n-1} = (\pm 1 + q) \frac{B}{2} \quad (5)$$

where q is a coefficient which determines the desired increment (or decrement) of the signal instantaneous frequency. In order to ease the design procedure, the polynomial coefficients are simplified as follows:

$$k'_n = nk \quad (6)$$

where a straightforward relation can be found between k , q and the polynomial order N , given by:

$$k = \frac{qBT}{4 \sum_{n=3}^N n} = \frac{qBT}{N^2 + 2N - 3} \quad (7)$$

It should be noted that an asymmetric point target response could not be achieved through a true matched filter, since the autocorrelation of the transmitted signal would always produce a symmetric response. Therefore, the nonlinear FM signal $s_a(t)$ is processed in reception with a linear FM matched filter (which may be mismatched by a weighting function). The point target response $s_{a0}(t)$ is given by:

$$s_{a0}(\tau) = \frac{1}{T} \int_{-\infty}^{\infty} \text{rect}\left(\frac{t}{T}\right) \text{rect}\left(\frac{t-\tau}{T}\right) e^{j2\pi\left(\frac{B}{2T}t^2 + \sum_{n=3}^N k_n \left(\frac{2t}{T}\right)^n\right)} e^{-j\pi\frac{B}{T}(t-\tau)^2} dt \quad (8)$$

The resulting asymmetric compressed pulse range sidelobe level is dependent on

the asymmetric phase polynomial order (Figure 6.2) and gives optimum values depending on the nominal instantaneous frequency increase. Although for large order polynomial the point target range sidelobe pattern continues to be asymmetric, the level of the 1st range sidelobe adjacent to the mainlobe increases, causing a degradation in terms of range sidelobe level. The asymmetric point target response characteristics for a time-bandwidth product of 300 for a 33rd order phase polynomial giving bandwidth increases of $0.25 B$, $0.5 B$ and B with respect to the signal nominal instantaneous frequency of $B/2$ at $f_i(\pm T/2)$ (corresponding to maximum instantaneous frequency values of $0.75 B$, $1.0 B$ and $1.5 B$ at $f_i(+T/2)$), are listed in Table 6.I. The asymmetric compressed pulse range sidelobe pattern before the mainlobe leading edge gives a considerable improvement (14 to 30 dB) compared to the symmetric linear FM compressed pulse, at the expense of some mainlobe peak losses L_p and negligible average losses L_a (the losses L_p and L_a are defined in Section 4.1). The asymmetric instantaneous frequency, point target response and frequency response of an asymmetric FM signal for a 33rd order phase polynomial giving a maximum instantaneous frequency of $1.5 B$ at $f_i(+T/2)$ (with respect to a linear FM signal TB of 300), are shown in Figure 6.3(a-c).

Table 6.I: Asymmetric FM compressed pulse characteristics ($TB = 300$)

	<i>RSL (left)</i>	<i>RSL (right)</i>	L_p	L_a	$\Delta\tau_{-3dB}$
0.75 B	-27.8 dB	-7.4 dB	2.0 dB	0.2 dB	1.20
1.00 B	-39.6 dB	-6.4 dB	3.0 dB	0.2 dB	1.26
1.50 B	-43.3 dB	-5.4 dB	4.0 dB	0.3 dB	1.46

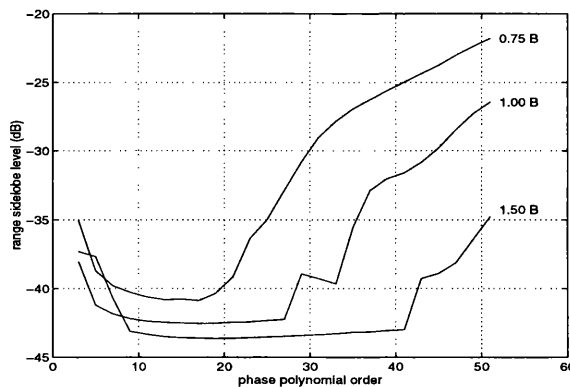


Figure 6.2. Asymmetric FM compressed pulse range sidelobe level as a function of phase polynomial order for instantaneous frequencies of $0.75 B$, $1.0 B$ and $1.5 B$ at $f_i(+T/2)$ with respect to a linear FM nominal TB of 300.

The asymmetric nonlinear FM waveform has been designed in order to reduce the impact of self-clutter through range sidelobe. The increase in the signal instantaneous frequency represents an inevitable increase in the width of the signal frequency response.

The signal generation must ensure the provision of the required bandwidth, since any truncation of the tails of the waveform spectrum may degrade the point target response range sidelobe level. On the other hand, thermal noise is not critical in reception since the returned echoes are processed with a linear FM matched filter with a nominal time-bandwidth product, with no required increase in the filter frequency response width. The spectrum contents can be attenuated increasing the phase polynomial order. Figure 6.3(d) shows the frequency response of an asymmetric nonlinear FM signal for a phase polynomial of order 501 giving a maximum instantaneous frequency of $1.5 B$ at $f_i(+T/2)$.

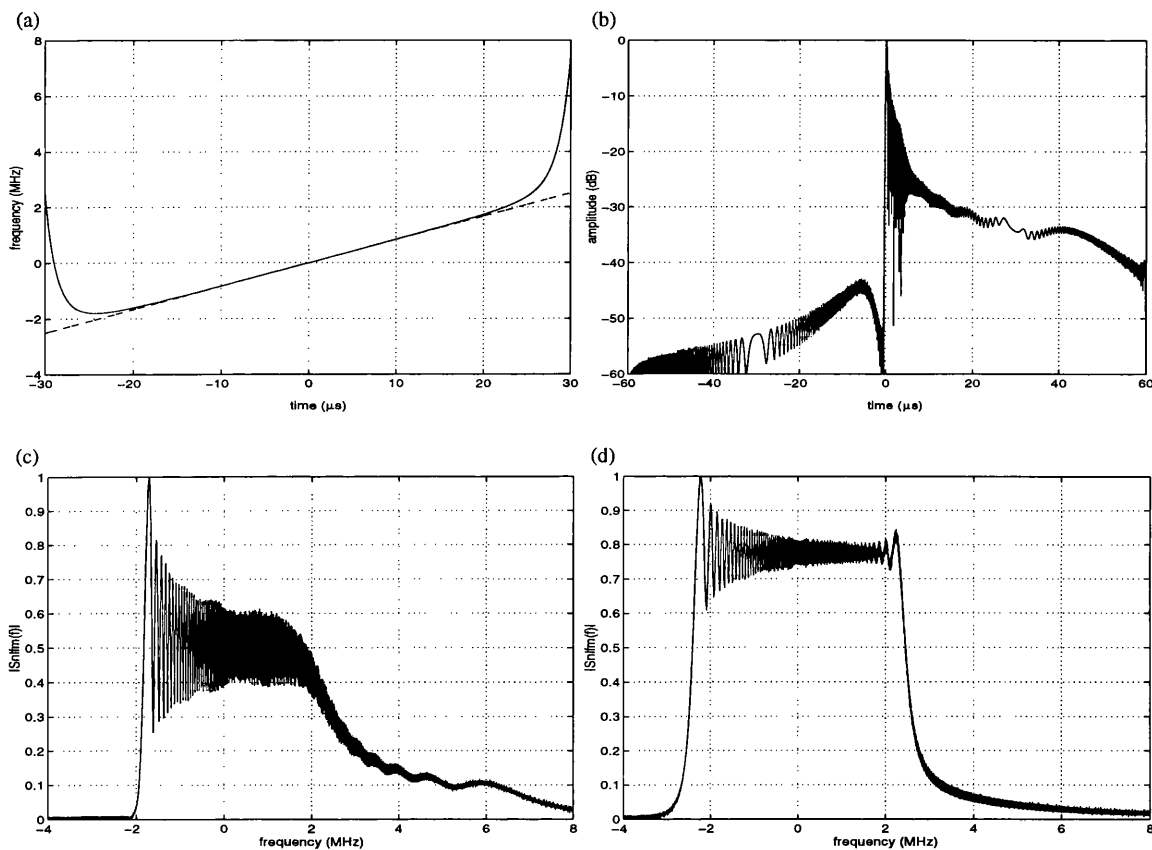


Figure 6.3. Asymmetric FM signal (33rd order phase polynomial giving an instantaneous frequency of $1.5 B$ at $f_i(+T/2)$ with respect to a linear FM TB of 300): (a) Instantaneous frequency; (b) Compressed pulse, $RSL = -43.3$ dB; (c) Spectrum; (d) Spectrum (phase polynomial of 501 order).

The asymmetric nonlinear FM point target response can be improved in terms of range sidelobe level when the reception linear FM matched filter is mismatched in amplitude. Figure 6.4 shows the asymmetric compressed pulse range sidelobe level as a function of phase polynomial order for instantaneous frequency increases of $0.25 B$, $0.5 B$ and B at $f_i(+T/2)$ with respect to a linear FM TB of 300, employing a minimum 3-term Blackman-Harris mismatching function. The point target response characteristics for a 33rd order phase polynomial are listed in Table 6.II. The asymmetric FM compressed pulse

gives a range sidelobe level improvement between 5 and 10 dB with respect to a linear FM compressed pulse tapered with the same weighting function and produces very similar peak and average losses.

Table 6.II: Asymmetric FM (mismatched) compressed pulse characteristics

	$RSL (left)$	$RSL (right)$	L_p	L_a	$\Delta\tau_{-3dB}$
0.75 B	-55.0 dB	-31.6 dB	7.5 dB	5.1 dB	1.73
1.00 B	-57.4 dB	-23.0 dB	7.7 dB	5.0 dB	1.86
1.50 B	-60.4 dB	-16.7 dB	8.0 dB	4.9 dB	2.00

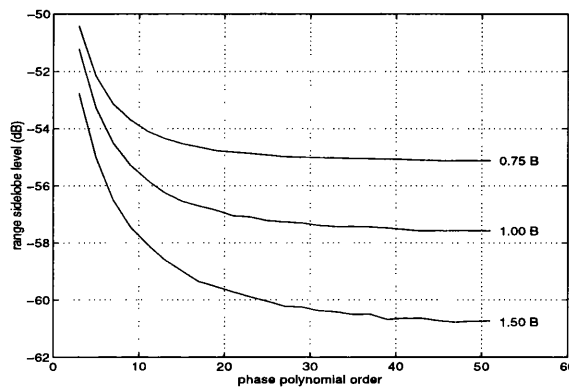


Figure 6.4. Asymmetric FM compressed pulse range sidelobe level (minimum 3-term Blackman-Harris weighting) as a function of phase polynomial order for instantaneous frequencies of 0.75 B, 1.0 B and 1.5 B at $f_i(+T/2)$ with respect to a linear FM nominal TB of 300.

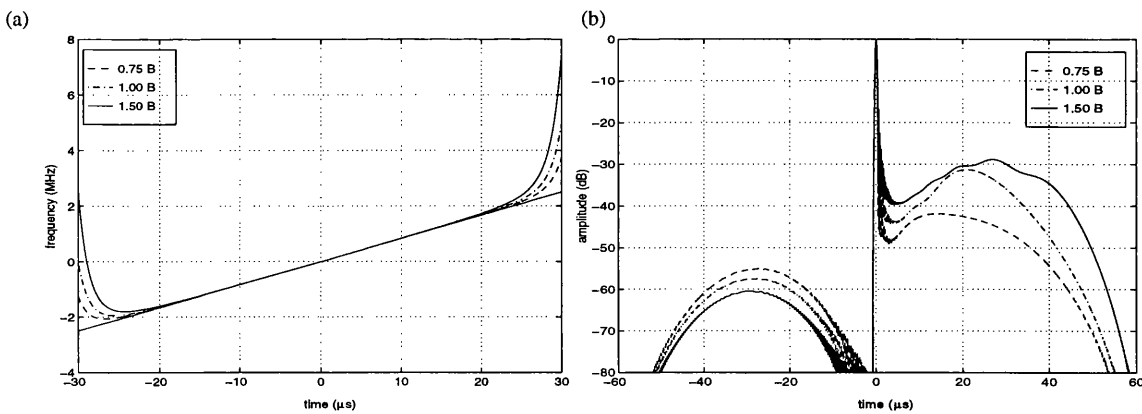


Figure 6.5. Asymmetric FM for a 33rd order phase polynomial giving different instantaneous frequency increases with respect to a linear FM nominal TB of 300: (a) Instantaneous frequency (b) Compressed pulse (minimum 3-term Blackman-Harris mismatching function).

The asymmetric nonlinear FM waveform can attain a range sidelobe pattern below -60 dB (Figure 6.5) with a time-bandwidth product of 300 and nominal instantaneous frequency increases between 0.5 B and B at $f_i(\pm T/2)$. The asymmetric FM compressed pulse range sidelobe level as a function of time-bandwidth product for different

instantaneous frequency increases is shown in Figure 6.6.

Finally, the ambiguity function of the asymmetric FM signal is shown in Figure 6.7. The signal Doppler tolerance is excellent over frequency offsets in the range imposed by spaceborne radar meteorology. The range sidelobe level is increased by only 0.2 dB for a Doppler frequency shift of 150 kHz.

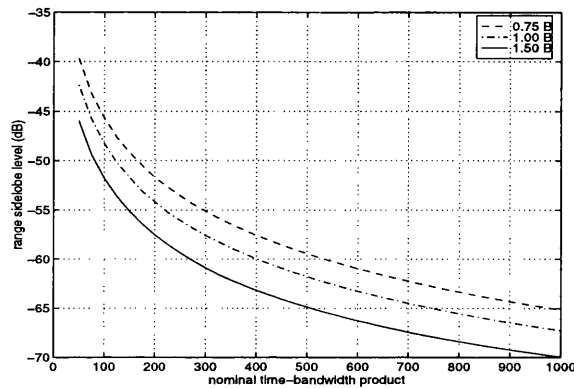


Figure 6.6. Asymmetric FM compressed pulse range sidelobe level as a function of time-bandwidth product, for a 33rd order phase polynomial giving different maximum instantaneous frequencies with respect to a linear FM nominal TB of 300 (minimum 3-term Blackman-Harris mismatching function).

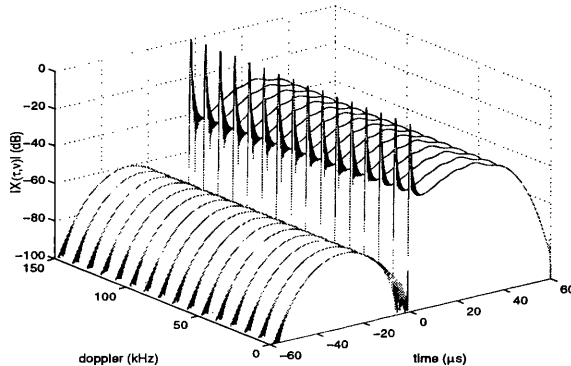


Figure 6.7. Asymmetric FM signal ambiguity function for a 33rd order phase polynomial giving an instantaneous frequency of $1.5 B$ at $f_i(+T/2)$ with respect to a linear FM nominal TB of 300 (minimum 3-term Blackman-Harris mismatching function).

6.3 Symmetric Nonlinear FM Pulse Compression

The previous asymmetric FM design procedure modifies the waveform nominal instantaneous frequency by the same amount at $f_i(\pm T/2)$. The superposition of an even and an odd phase functions expressed as polynomials of terms of even and odd powers

allow a different control of the modulation function for positive and negative values of time. The nonlinear phase polynomial is defined as:

$$\theta_a(t) = \sum_{n=3}^N k_n^o \left(\frac{2t}{T}\right)^n + \sum_{n=4}^{N+1} k_n^e \left(\frac{2t}{T}\right)^n \quad (9)$$

where k_n^o are the coefficients of the polynomial of odd powers, k_n^e the coefficients of the polynomial of even powers and N the odd powers polynomial order. The signal combined instantaneous frequency is given by:

$$f_i(t) = \frac{B}{T}t + \frac{2}{T} \sum_{n=3}^N k_n^{o'} \left(\frac{2t}{T}\right)^{n-1} + \frac{2}{T} \sum_{n=4}^{N+1} k_n^{e'} \left(\frac{2t}{T}\right)^{n-1} \quad (10)$$

where $k_n^{o'} = nk_n^o$ and $k_n^{e'} = nk_n^e$. The polynomial coefficients are again calculated in order to attain determined and independent values at the edges of the signal instantaneous frequency:

$$f_i\left(-\frac{T}{2}\right) = -\frac{B}{2} + \frac{2}{T} \sum_{n=3}^N k_n^{o'} - \frac{2}{T} \sum_{n=4}^{N+1} k_n^{e'} = -(1+q_1)\frac{B}{2} \quad (11)$$

$$f_i\left(\frac{T}{2}\right) = \frac{B}{2} + \frac{2}{T} \sum_{n=3}^N k_n^{o'} + \frac{2}{T} \sum_{n=4}^{N+1} k_n^{e'} = (1+q_2)\frac{B}{2} \quad (12)$$

where q_1 and q_2 are coefficients which determine the desired different increments (or decrements) of the nominal signal instantaneous frequency. In order to simplify the design procedure, the polynomial coefficients are considered to be as follows:

$$k_n^{o'} = nk_o \quad (13)$$

$$k_n^{e'} = nk_e \quad (14)$$

The relations between k_o , k_e , q_1 , q_2 and the maximum polynomial order N (of odd powers) are now given by:

$$k_o = \frac{BT}{2(N^2 + 2N - 3)}(q_2 - q_1) \quad (15)$$

$$k_e = \frac{BT}{2((N+1)^2 + 2(N+1) - 8)}(q_2 + q_1) \quad (16)$$

A symmetric compressed pulse is achieved by passing the signal through its true matched filter, regardless any asymmetries which may be introduced by the phase polynomial. The compressed pulse can be formulated as:

$$s_0(\tau) = \frac{1}{T} \int_{-\infty}^{\infty} \text{rect}\left(\frac{t}{T}\right) \text{rect}\left(\frac{t-\tau}{T}\right) e^{j2\pi \left(\frac{B}{2T} t^2 + \sum_{n=3}^N k_n^o \left(\frac{2t}{T}\right)^n + \sum_{n=4}^{N+1} k_n^e \left(\frac{2t}{T}\right)^n \right)} \cdot e^{j2\pi \left(\frac{B}{2T} (t-\tau)^2 + \sum_{n=3}^N k_n^o \left(\frac{2(t-\tau)}{T}\right)^n + \sum_{n=4}^{N+1} k_n^e \left(\frac{2(t-\tau)}{T}\right)^n \right)} dt \quad (17)$$

However, and in order to produce a symmetric frequency modulation, the condition $q_1 = q_2$ must be imposed on the instantaneous frequency design, obtaining a phase polynomial formed by terms of even powers. Figure 6.8 shows the nonlinear FM compressed pulse range sidelobe level as a function of phase polynomial order for different symmetric instantaneous frequency increases. A combined 10th order phase polynomial appears to be the optimum choice before the range sidelobe level is degraded by a raising sidelobe adjacent to the mainlobe. The instantaneous frequency and symmetric compressed pulse of a nonlinear FM signal designed with the described method are shown in Figure 6.9(a) and Figure 6.9(b), and its characteristics listed in Table 6.III (nominal linear FM TB of 300). Although the peak range sidelobe level of -35.5 dB is far above the spaceborne meteorological requirement, the range sidelobe pattern is compressed below -60 dB for most of the duration of the compressed pulse (with no required filter mismatch). A further increase in the order of the phase polynomial yields a non optimum peak range sidelobe level, but reduces the range in which the range sidelobe pattern is above -60 dB.

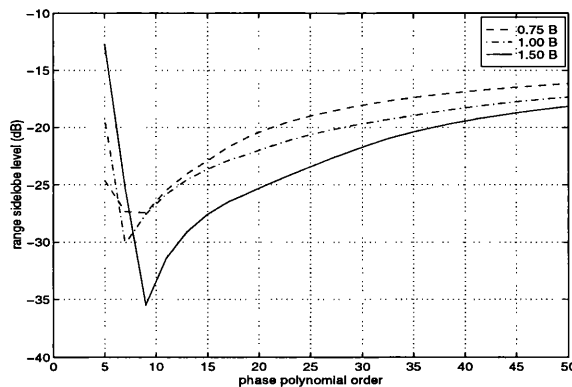


Figure 6.8. Nonlinear FM compressed pulse range sidelobe level as a function of phase polynomial order giving instantaneous frequencies of $\pm 0.75 B$, $\pm 1.0 B$ and $\pm 1.5 B$ at $f_i(\pm T/2)$ with respect to a linear FM nominal TB of 300.

Unfortunately, the described compressed pulse shows the typical degradation of

nonlinear frequency modulations as a function of Doppler frequency offsets. The ambiguity function (displayed in Figure 6.9(c)) shows the rapid degradation of the range sidelobe pattern for very relatively small Doppler shifts, reaching a peak range sidelobe level value of approximately -5 dB for a Doppler offset of 150 kHz.

Table 6.III: Symmetric nonlinear FM compressed pulse characteristics

	RSL	L_p	L_a	$\Delta\tau_{-3dB}$
1.50 B	-35.5 dB	0.0 dB	2.0 dB	0.71

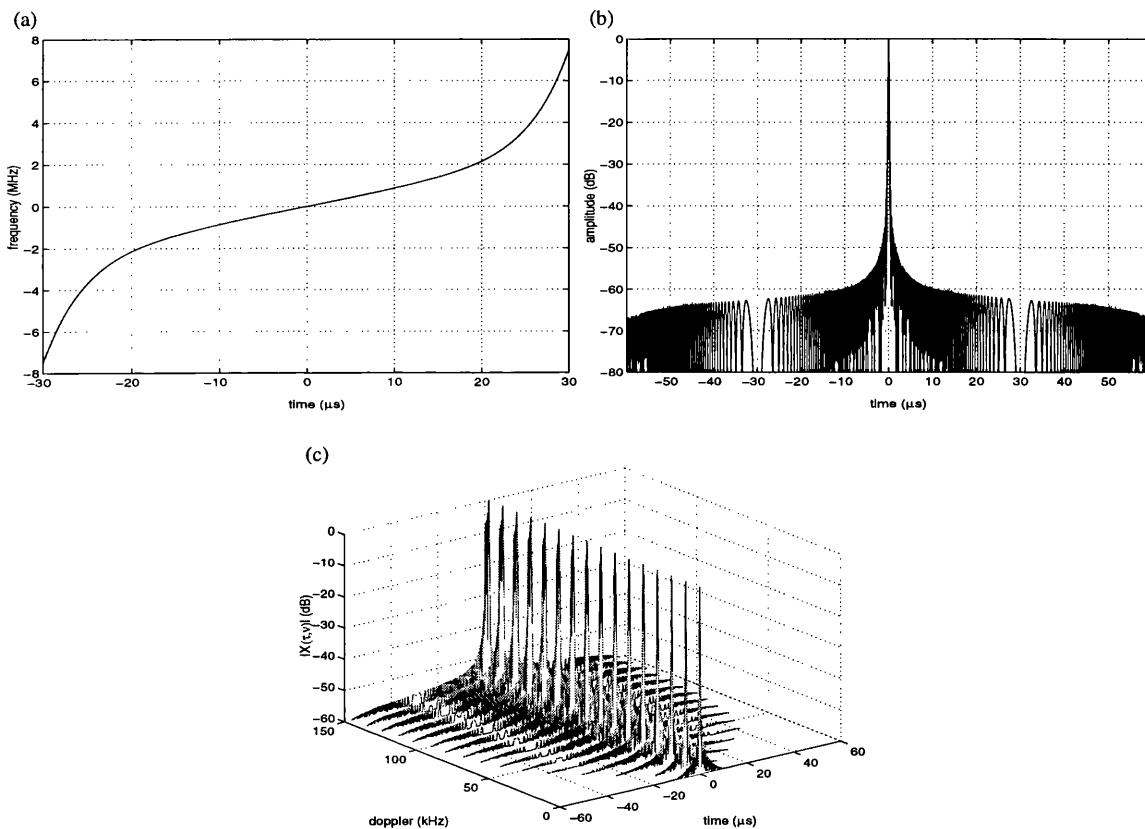


Figure 6.9. Nonlinear FM signal (10^{th} order phase polynomial giving an instantaneous frequency of $\pm 1.5 B$ at $f_i(\pm T/2)$ with respect to a linear FM TB of 300): (a) Instantaneous frequency; (b) Compressed pulse, $RSL = -35.5$ dB; (c) Ambiguity function.

Finally, it should be pointed out that ‘continuous’ linear FM predistortion functions may be generated by the previous design method. For a very large phase polynomial order, the overlapped phase function resembles the linear FM predistortion function described in Chapter 5, and gives better results than in the case of predistortion functions consisting of short portions of different linear modulation rates. The nonlinear FM signal can be compressed in reception by a linear FM mismatched filter, and its compressed pulse is given by:

$$s_0(\tau) = \frac{1}{T} \int_{-\infty}^{\infty} \text{rect}\left(\frac{t}{T}\right) \text{rect}\left(\frac{t-\tau}{T}\right) w(t-\tau) \cdot e^{j2\pi\left(\frac{B}{2T}t^2 + \sum_{n=3}^N k_n^o \left(\frac{2t}{T}\right)^n + \sum_{n=4}^{N+1} k_n^e \left(\frac{2t}{T}\right)^n\right)} e^{j\pi\frac{B}{T}(t-\tau)^2} dt \quad (18)$$

where $w(t)$ is the mismatching function. The instantaneous frequency and compressed pulse for a nonlinear FM (phase polynomial of order 1042, for a nominal linear FM TB of 300) are shown in Figure 6.10(a-b) and its characteristics listed in Table 6.IV.

Table 6.IV: ‘Continuous’ predistorted linear FM compressed pulse characteristics

	RSL	L_p	L_a	$\Delta\tau_{-3dB}$
1.50 B	-64.4 dB	7.5 dB	5.1 dB	1.85

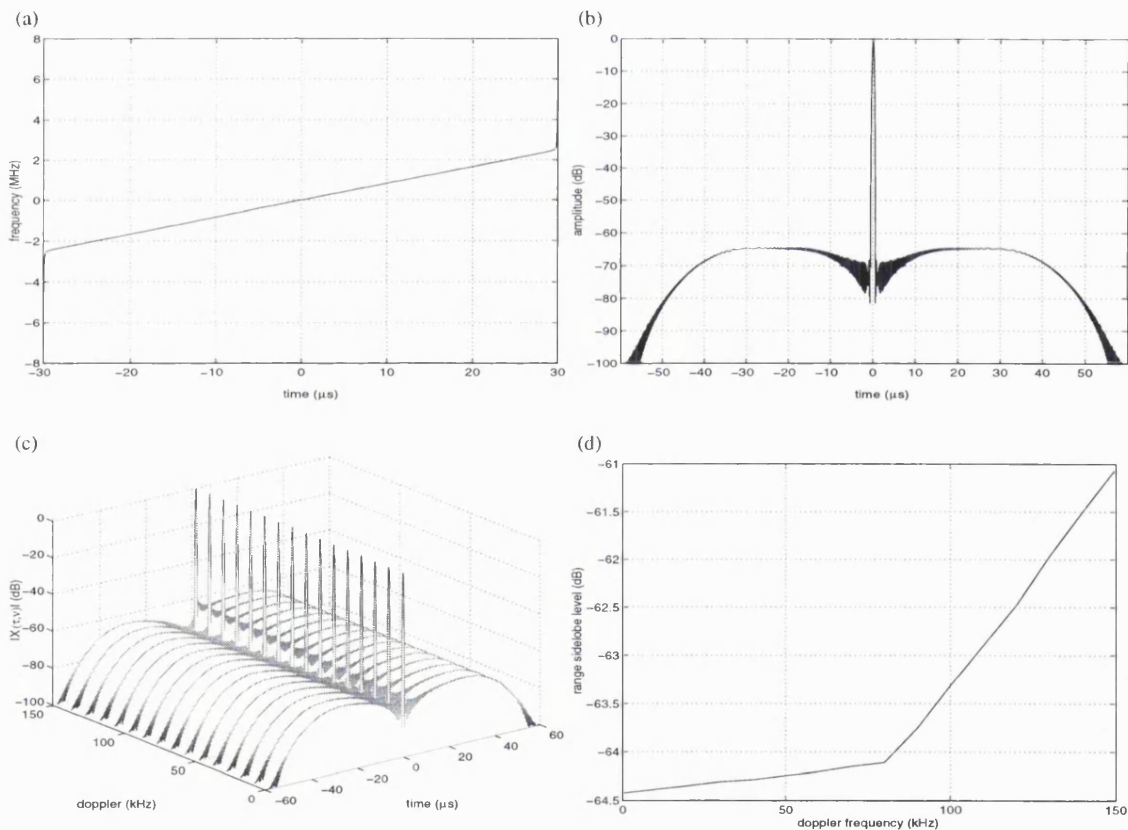


Figure 6.10. Nonlinear FM signal (phase polynomial of order 1042 giving an instantaneous frequency of $\pm 1.5 B$ at $f_i(\pm T/2)$ with respect to a linear FM TB of 300, minimum 3-term Blackman-Harris mismatching function): (a) instantaneous frequency; (b) compressed pulse, $RSL = -64.5$ dB; (c) Ambiguity function; (d) Range sidelobe level as a function of Doppler frequency.

The ‘continuous’ predistorted linear FM compressed pulse gives a range sidelobe

level improvement of approximately 2 dB (-64.4 dB) with identical loss factors with respect to the predistortion functions described in Chapter 5. The 'continuous' predistortion function improves the cancellation of the compressed pulse constituent terms in a significantly longer time range of the compressed pulse.

The ambiguity function of the 'continuous' predistorted linear FM is shown in Figure 6.10(c). The Doppler tolerance of the waveform is excellent up to Doppler frequency offsets of 80 kHz (1.6% of the signal bandwidth). However, larger shifts rapidly distort the range sidelobe pattern adjacent to the mainlobe. The range sidelobe level is degraded 3.4 dB for a Doppler frequency offset of 150 kHz (Figure 6.10(c)).

6.4 Waveform Generation Considerations

Griffiths et al. ([Griffiths and Bradford, 1992] and [Griffiths, 1993]) studied signal digital generation and compression for spaceborne rain radars. Digital waveform generation has some advantages over conventional techniques using dispersive delay lines. Parameter changes in the digital generation circuit allows to vary the modulated signal time-bandwidth product as opposed to the provision of different SAW devices (required to generate different bandwidths). ① ②

Two different linear FM digital waveform generation approaches have been proposed in the literature. The single-bit generation technique [Johnston, 1984] specifies the signal with a frequency modulated square wave, or equivalently with the linear FM signal zero crossing times. The square wave signal spectrum produces a series of harmonics of the fundamental signal spectrum which can be rejected by filtering. However, a sufficiently large sampling rate must guarantee accurate quantisation of the zero crossing times in order to minimise generation errors, especially for large signal bandwidths. In multiple-bit generation techniques [Eber and Soule, 1975], the waveform is specified as a collection of quantised amplitude samples as a function of time and upconverted to IF with a single side band modulator. For linear FM signals (where the modulation rate is constant), the signal phase is obtained with two accumulators and the corresponding signal samples calculated through look-up tables. In the generation of nonlinear FM waveforms, the signal pre-calculated complex sample values could be retrieved from a fast access memory.

Multiple-bit generation is preferred to single-bit generation since a lower clock rate

is required for equivalent range sidelobe levels at the expense of some circuitry complexity. In reception, the compression process can be implemented in the frequency domain which reduces the computational load with respect to time domain convolution. A diagram of the system digital generation and compression is shown in Figure 6.11.

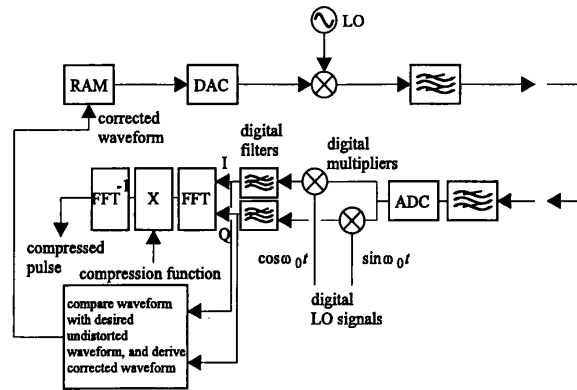


Figure 6.11. Block diagram of pulse generation and compression system, showing adaptive scheme for compensation of phase and amplitude errors. Reproduced from [Griffiths, 1993].

On the other hand, quantisation errors (number of bits), filter and mixers nonlinear amplitude and phase responses and imbalances in the in-phase and quadrature branches may introduce generation and compression distortion errors, which can degrade the compressed pulse range sidelobe level by a considerable amount. The evaluation of compression range sidelobe level degradation as a function of permissible distortion errors (calculated in terms of the pair-echo theory [Klauder et al., 1960]) for amplitude and phase errors of periodic variation is shown in Figure 6.12. In order to guarantee the range sidelobe level of -60 dB amplitude and phase distortions must be kept at a very low level during the waveform generation (amplitude deviation below 0.02 dB and phase deviation below 0.1°).

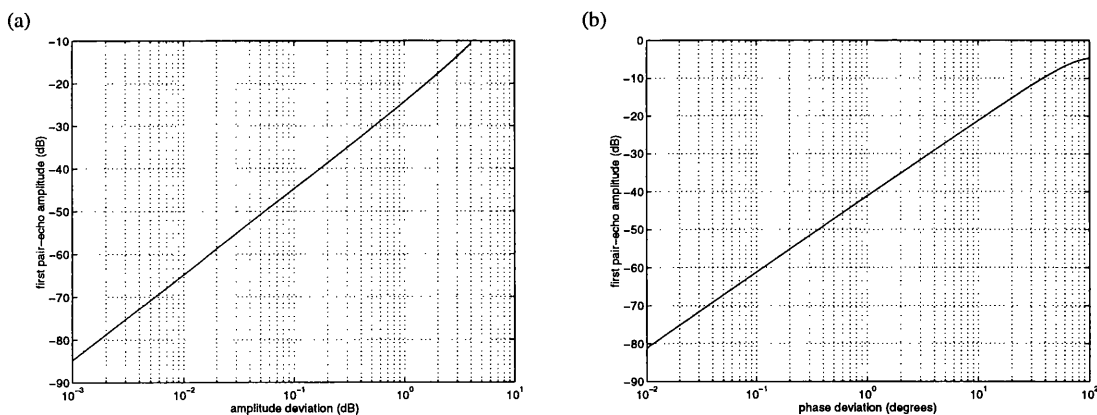


Figure 6.12. Pair-echo amplitude [Klauder et al., 1960] for: (a) amplitude distortion; (b) phase distortion

As suggested in [Griffiths, 1993], generation and compression distortion may be

characterised and its variation as a function of time determined for a given system. An adaptive compensation branch linking the receiver and the transmitter could compare the received distorted waveform to the desired undistorted signal, introducing a correction term in order to minimise the impact of distortion in the compressed pulse range sidelobe pattern. Linear FM distortion compensation can also be carried out through predistortion of the digitally generated waveform [Mavrocordatos and Caille, 1993]. The distorted signal $s_{dt}(t)$ is formulated as:

$$s_{dt}(t) = (w_a(t) + e_{dt}(t)) e^{j\left(\pi \frac{B}{T} t^2 + \theta_{dt}(t)\right)} \quad (19)$$

where $e_{dt}(t)$ is an additive amplitude distortion term and $\theta_{dt}(t)$ an additive phase distortion term. A predistortion compensation function can be applied to the signal before transmission. The correction ratio between the undistorted transmitted signal $s(t)$ and the generated signal affected by amplitude and phase distortion is given by:

$$\frac{s(t)}{s_{dt}(t)} = \frac{w_a(t)}{w_a(t) + e_r(t)} e^{-j\theta_r(t)} \quad (20)$$

Further research must address the derivation of appropriate models for adaptive distortion compensation of combined distortion terms in both digital generation and compression.

6.5 References

- Eber L.O. and Soule H.H. Jr.: 'Digital generation of Wideband LFM Waveforms', Proc. IEEE International Radar Conference, IEEE Publication 75 CHO 938-1 AES, pp. 170-175, 1975.
- Griffiths H.D. and Bradford W.J.: 'Digital Generation of High Time-Bandwidth Product Linear FM Waveforms for Radar Altimeters', *IEE Proc. F.*, Vol.139, No.2, pp.160-169, April 1992.
- Griffiths H.D.: 'Ultra-Low Range Sidelobe Pulse Compression for Satellite-Borne Rain Radar', *Proc. IEEE National Radar Conference*, IEEE Publication No. 93CH3253-2, pp. 140-145, Boston, MA, April 1993.
- Johnston J.A.: 'Generating Analogue FM Pulses using a 1-Bit Digital Technique', IEEE Proceedings Pt. F, No.4, pp. 349-356, July 1984.
- Klauder, J.R., Price, A.C., Darlington, S. and Albersheim, W.J.: 'The Theory and Design of Chirp Radars', *Bell System Tech. J.*, Vol.XXXIX, 1960, No.4, pp.745-809; reprinted in *Radars-Vol.3, Pulse Compression*, D.K.Barton ed., Artech House, 1975.
- Kroszczynski J.J.: 'Pulse Compression by Means of Linear-Period Modulation', *Proceedings of the IEEE*, Vol. 57, No. 7, pp. 1260-1266, July 1969.
- Mavrocordatos C. and Caille G.: 'Rain Radar. Instrument Design and Critical Technologies', Alcatel Espace Presentation, ESA Workshop on Rain/Cloud Radar, ESTEC, September 1993.
- Wilson J.J.: 'A Design Procedure for the Design of Advanced Coded Pulse Radar Waveforms Generated from a Finite Set of Samples', *IEE Electronics Division Colloquium*, London, April 1990.

7 RAIN OBSERVATION BY RADAR ALTIMETER

Several waveform design options for a rainfall measurement mode for the RA-2 Radar Altimeter due to fly on ESA's ENVISAT mission (ESTEC Contract No. 10882/94/NL) have been investigated. The basic task was to develop a feasible operational rain mode with the least impact to the existing original altimeter design. The range sidelobe level requirement for a full deramp mode of operation is of approximately -50 dB, but only for the surface return whose time position is accurately known through the altimeter tracking. A full deramp technique simulation is described, which predicts the rain and Earth's surface power levels taking into account the waveform and range sidelobe reduction processing technique employed. The results of these simulations show that a combination of amplitude and phase weighting schemes can meet the sidelobe level specification at the expense of a signal-to-noise ratio loss and signal distortion.

7.1 Introduction

The consideration of different waveform design options for the provision of a rain mode for the RA-2 radar altimeter must take into account the severe restrictions imposed by the Earth's surface clutter. The overall and primary objective is to provide an effective mode of altimeter operation to measure rainfall, ideally with as little modification as possible to the basic altimeter design. The required range extent of the measurements (i.e. range window) will extend up to 9 km above the Earth's surface.

7.1.1 RA-2 Instrument and Rain Mode Objectives

The RA-2 is a nadir looking pulse-limited radar altimeter based on the heritage of ERS-1, and operating at a main nominal frequency of 13.575 GHz (Ku-band). A secondary channel at a nominal frequency of 3.2 GHz (S-band) is also used to give the ionospheric correction. The main objectives of the instrument are to provide continuous sampling of the ocean circulation and mesoscale structure, to monitor changes in the ice cap volume and sea ice extent, and to provide the best attainable land mapping. The RA-2 system parameters are summarised in Table 7.I.

The RA-2 chirp generator uses SAW devices to produce linear frequency

modulated 20 μ s pulses of three different bandwidths (20, 80 and 320 MHz) for the primary channel and of 160 MHz for the secondary channel. In reception, the received signal is full deramped (mixed with a replica of the transmitted signal) and converted from the I and Q signal components to digital samples. The signal power spectrum is obtained through a 128-point FFT calculation.

Table 7.I: RA-2 system parameters

	<i>Main</i>	<i>Common</i>	<i>Secondary</i>
Operational orbit range	764 - 825 km		
Operational frequency	13.575 GHz		3.2 GHz
Pulse length		20 μ s	
Chirp bandwidth	320 / 80 / 20 MHz		160 MHz
Tx peak power	60 W (TWTA)		60 W (solid state)
PRI	557 μ s		2228 μ s
FFT samples		128	
Echoes averaged on-board	100		25
Antenna diameter		1.2 m	
Power consumption		168 W	
Mass		106 kg	
Nominal data rate		64 kbits/s	

The main spaceborne rain radar requirements ([Nakamura et al, 1990] and [Meneghini and Kozu, 1990]) are: (i) to measure a wide range of rainfall rates (typically from 0.5 mm/h to 50 mm/h) at all appropriate altitudes; and (ii) to achieve a vertical resolution of 250 m. This requirements can be relatively accomplished providing the altimeter rain mode with the appropriate frequency modulated waveforms and signal processing techniques which would have little impact in the instrument original design. (P)

However, the fact that the RA-2 instrument was designed for other purposes than radar meteorology (some of the system characteristics must remain unaltered), means that some technical difficulties must be overcome in order to achieve an optimum rain mode performance. Signal-to-noise ratio limitations impose severe constraints in precipitation detectability, especially at high rainfall rates and low altitudes. On the other hand, the Earth's surface return represents the main source of interference, obscuring rain information especially at low altitudes.

The main purpose of this work consists of the choice of waveform and the minimisation of the ground clutter interference in order to maximise rain detectability

with the help of the necessary signal processing techniques. The formulation of the radar altimetry full deramp technique is reviewed and updated for meteorological purposes.

7.1.2 Rain Mode for SEASAT Altimeter

Goldhirsh and Walsh described the feasibility of a rain mode for the SEASAT altimeter [Goldhirsh and Walsh, 1982]. They presented a set of calculations showing the relationship between the rain echo power and rain rate estimation, and proposing a modification to the basic altimeter design to carry out rain measurements. Their proposed rain mode uses an unmodulated transmitted pulse of 3.2 μ s, which gives a range resolution of $c\tau/2 = 480$ m. It is fortunate that for the SEASAT case, the basic pulse width of the instrument is reasonably compatible with the desired range resolution of the rain mode.

To give an idea of the relative levels of the signals for the modified SEASAT altimeter, the rain echo power as a function of rain rate and penetration depth is shown in Figure 1. The noise level ($SNR = 1$) is given by $P_n = kTBF$, where $k = 1.38 \cdot 10^{-23}$, $T = 290$ K, $B = 1/3.2 \mu\text{s} = 312$ kHz and $F = 5$ dB, giving a noise power level of -114 dBm.

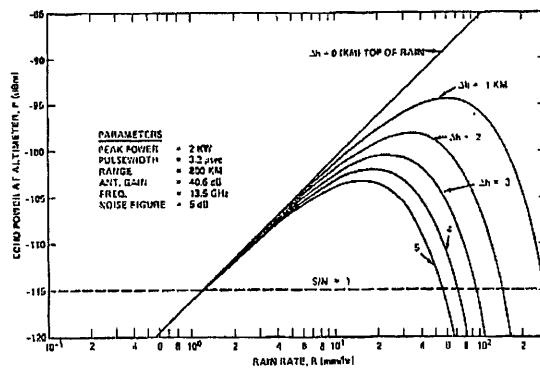


Figure 7.1. Echo power returned to altimeter from various distances below the top of rain versus rain rate. Reproduced from [Goldhirsh and Walsh, 1982].

The radar equation for the surface return power P_r is given by:

$$P_r = \frac{P_t G^2 \lambda^2 \sigma^0 c \tau L_s}{64\pi^2 h^3} \quad (1)$$

where P_t is the transmit power, G the antenna gain, λ the wavelength, σ^0 the surface reflectivity, c the propagation speed, τ the pulse length, L_s the combined system losses

and h the satellite altitude. Taking parameter values appropriate to the SEASAT altimeter ($\sigma^0 = 10$ dB and $L_s = -2.2$ dB), the surface return level is of -86.5 dBm, giving a signal-to-noise ratio of 27.5 dB.

7.1.3 RA-2 Rain Mode Design Options

Two basic approaches have been considered for the provision of a rain mode for the RA-2 instrument. The first of these is to use an unmodulated pulse of an appropriate duration, in a similar way to that proposed by Goldhirsh and Walsh. An immediate problem is that the RA-2 pulse width (20 μ s) does not give the required range resolution ($c\tau/2 = 3$ km). However, the use of an unmodulated pulse allows the rejection of ground clutter by time gating.

The second approach is to retain the full deramp principle of operation, but reducing the signal bandwidth to give the appropriate range resolution. The implementation of pulse compression in the rain mode has the advantage that all the receiver circuitry and processing remains essentially unchanged. However, it is necessary to ensure that the range sidelobes of the surface echo are sufficiently low in order to avoid the waveform self-clutter interference in the frequency domain.

The rain return level is given by the modified Probert-Jones radar equation [Probert-Jones, 1962]:

$$P_r = \frac{P_t G^2 \lambda^2 \theta_B^2 c \tau L_s \eta}{1024 \pi^2 h^2 \ln 2} \cdot f(B_0) 10^{-0.2 \int_0^r (k_g + k_p + k_c) dr} \quad (2)$$

where θ_B is the antenna beamwidth, η the rain reflectivity, and k_g , k_p and k_c are attenuation coefficients due to atmospheric gas, precipitation and clouds respectively. The factor L_s includes the losses on both transmit and receive paths. The SEASAT calculations may simply be scaled to give those for the RA-2 instrument, taking into account the different values of P_t , G , θ_B and τ . The pulse duration is chosen to be of 1.67 μ s to give a range resolution of 250 m. The previous differences (summarised in Table 7.II) give a signal-to-noise ratio deficit of -18.0 dB for the RA-2 altimeter unmodulated pulse configuration.

The noise level is decreased by the noise figure ratio (i.e. 3 dB rather than 5 dB)

and increased by the receiver bandwidth ratio (i.e. $1/1.67 \mu\text{s}$ instead of $1/3.2 \mu\text{s}$), giving a value of -113 dBm. The net RA-2 signal-to-noise ratio balance is approximately -19.0 dB worse than the proposed SEASAT rain mode.

Table 7.II: SEASAT and RA-2 configuration comparison

	<i>SEASAT</i>	<i>RA-2</i>	<i>difference</i>
P_t	2 kW	60 W	-15.2 dB
G^2	2 x 40.6 dB	2 x 41.5 dB	+ 1.8 dB
θ_B^2	$7.8 \cdot 10^{-4} \text{ rad}^2$	$5.1 \cdot 10^{-4} \text{ rad}^2$	-1.8 dB
τ	3.2 μs	1.67 μs	-2.8 dB

The hardware implications are: (i) in the transmitter, the provision of a shorter, unmodulated pulse, and (ii) in the receiver, an appropriate fixed-frequency first LO, and a separate lower-bandwidth channel at IF followed by a separate detector, sampler, pulse accumulator etc.

On the other hand, and maintaining the altimeter full deramp mode of operation, the chirp bandwidth needs to be reduced to give the required range resolution (for $\Delta r = 250 \text{ m}$, $B = c/2\Delta r = 600 \text{ kHz}$). The pulse duration remains unchanged.

In order to determine the rain return level, the same considerations previously described apply, giving the same values as in Figure 7.1, but offset by -19.0 dB. The receiver noise level is given by $kTBF$, where B is now the reciprocal of the uncompressed pulse length ($1/20 \mu\text{s} = 50 \text{ kHz}$), giving a system noise level of -123 dBm. The RA-2 rain mode pulse compression performance is therefore 7.8 dB worse than the proposed SEASAT rain mode.

To determine the level of the surface echo we must realise that with this value of compressed pulse length the altimeter is beam-limited, since $2\sqrt{hc\tau} \geq h\theta_B$. The appropriate radar equation is therefore (note the similarity to Eq. 2):

$$\begin{aligned}
 P_s &= \frac{P_t G}{4\pi h^2} \cdot \frac{\pi h^2 \theta_B^2 \sigma^0}{4} \cdot \frac{1}{4\pi h^2} \cdot \frac{G \lambda^2}{4\pi} \cdot L_s \\
 &= \frac{P_t G^2 \lambda^2 \theta_B^2 \sigma^0 L_s}{256\pi^2 h^2}
 \end{aligned} \tag{3}$$

Inserting appropriate values ($P_t = 60 \text{ W}$, $G = 41.5 \text{ dB}$, $\lambda = 0.022 \text{ m}$, $\theta_B = 1.3^\circ$, $\sigma^0 = 10 \text{ dB}$, $L_s = -2.2 \text{ dB}$, $h = 800 \text{ km}$), the surface return level is of -78.8 dBm. It is

required that the range sidelobes of the surface return do not interfere the rain signal. Specifying the range sidelobes to be no higher than the system noise level, the range sidelobe level must be below -50 dB. Whilst such specification is more stringent than achieved with current radar altimeters, it is less demanding than the specification for dedicated spaceborne rain radars (typically of -60 dB).

The hardware implications seem relatively minor. The main one is the provision of a much lower bandwidth chirp, which should be straightforward if digital chirp generation is to be employed, or alternatively a second dedicated chirp generator could be provided.

7.2 RA-2 Rain Mode: Full Deramp Alternative

Some full deramp modifications need to be devised in the RA-2 rain mode since the extent of the measurements is larger than in the normal altimetry mode. Two options to deramp the range window are presented, together with a comprehensive signal-to-noise ratio analysis deriving the required sidelobe level specification. This section ends up with some considerations related to the effect of Doppler offsets on the rain mode of operation.

7.2.1 Range Window Configuration

The full deramp mode of operation constitutes a particular form of FM radar pulse compression implemented in altimetry systems. A linear FM waveform is transmitted, and the returned signal (Eq. 4) is mixed with a replica of the transmitted signal (Local Oscillator Reference signal, Eq. 5) in reception. Such process is illustrated in Figure 7.2. The instantaneous frequency difference between the echo and the LO signal is proportional to the target range, and can be recovered by spectral analysis of the beat frequency (Eq. 6). The LO signal needs to be triggered at the appropriate instant so that it coincides in time with the echo from the surface (altimeter tracking). The deramped echo power spectrum is given by Eq.7. The altimeter frequency domain point target response can be considered equivalent to the compressed pulse of a pulse compression radar. A detailed calculation of the full-deramp process can be found in Appendix D.1.

$$s_r(t) = \frac{1}{\sqrt{T_p}} \text{rect}\left(\frac{t-t_d}{T_p}\right) \cos\left(2\pi f_0(t-t_d) + \frac{1}{2} \frac{B}{T_p}(t-t_d)^2\right) \quad (4)$$

$$s_{\text{LO}}(t) = \frac{1}{\sqrt{T_p}} \text{rect}\left(\frac{t}{T_p}\right) \cos\left(2\pi f_0 t + \frac{1}{2} \frac{B}{T_p} t^2\right) \quad (5)$$

$$\tilde{s}_d(t) = \frac{1}{2T_p} \text{rect}\left(\frac{t-t_d}{T_p-t_d}\right) \cos\left(2\pi \frac{B}{T_p} t_d t + \phi\right) \quad (6)$$

$$|\tilde{S}_d(f)|^2 = \frac{1}{4} \left(1 - \frac{t_d}{T_p}\right)^2 \left| \text{sinc}\left(\left(\frac{B}{T_p} t_d - fT\right) \cdot \left(1 - \frac{t_d}{T_p}\right)\right) \right|^2 \quad (7)$$

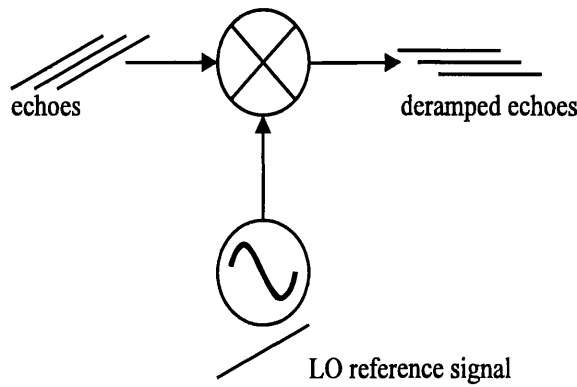


Figure 7.2. Full deramp mode of operation diagram.

The design of the rain mode range window is restricted by the original altimetry system design. In order to avoid any alteration of the transmitter TWT amplifier, the transmit pulse length ($20 \mu\text{s}$) is maintained. The expected precipitation measurement is likely to extend between 4 and 5 km [Amayenc et al., 1994], although it can amount in some cases to three or four times such height. In order to keep an appropriate range resolution (300 m), the linear FM signal bandwidth is selected to be of 500 kHz.

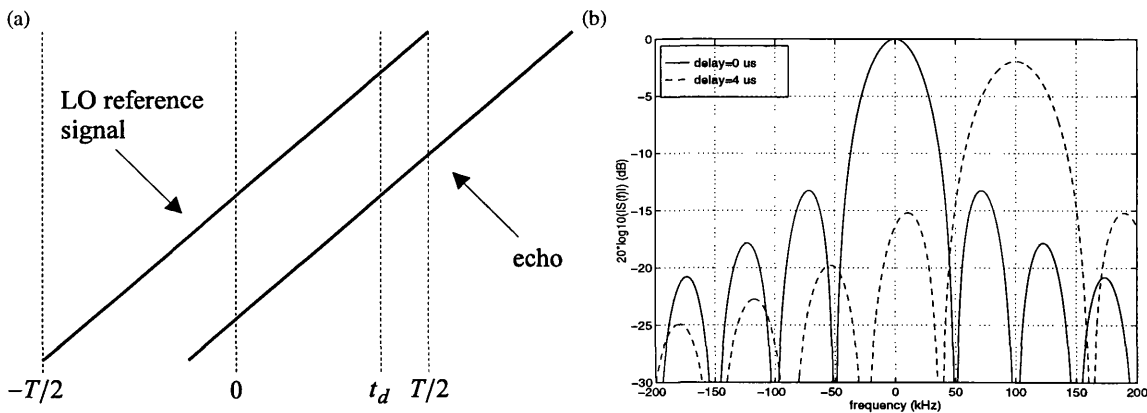


Figure 7.3. Full deramp: (a) Delay between received chirp and LO reference signal; (b) Power spectrum, ($T_p = 20 \mu\text{s}$, $B = 500 \text{ kHz}$, $t_d = 4 \mu\text{s}$).

Under the previous design considerations, the range window extent is no longer small compared with the pulse length. The time delay between the received echo and the LO reference signal can easily exceed several times the length of the transmit pulse, and severe mainlobe broadening and power losses (associated effects due to the decrease of the deramped pulse width) need to be minimised (Figures 7.3 and 7.4).

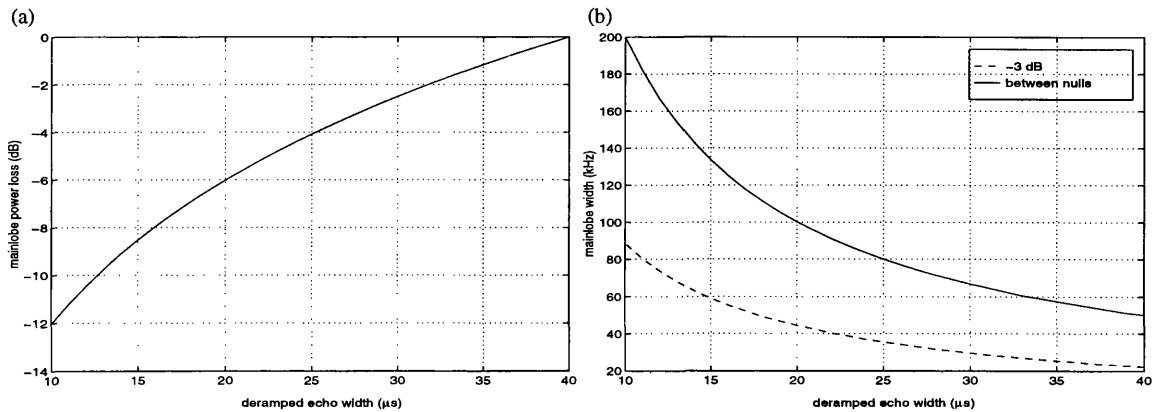


Figure 7.4. Full deramp power spectrum: (a) Power loss as a function of deramped pulse width; (b) Mainlobe broadening (-3 dB and between nulls) as a function of deramped pulse width.

Two options are considered in order to configure the range window. The first approach is to employ several LO pulses to build the range window (Figure 7.5 (a)). Different LO pulses triggered at different instants are necessary to deramp and assemble the range window for successive pulse scans. This option would require the transmission of a larger number of pulses to acquire a sufficient number of independent samples to average the rain return. The second alternative is the generation of a longer LO reference signal (Figure 7.5 (b)). The single LO pulse option is preferred, since the whole range window is assembled with only one LO pulse allowing the acquisition of the maximum number of independent samples per scan.

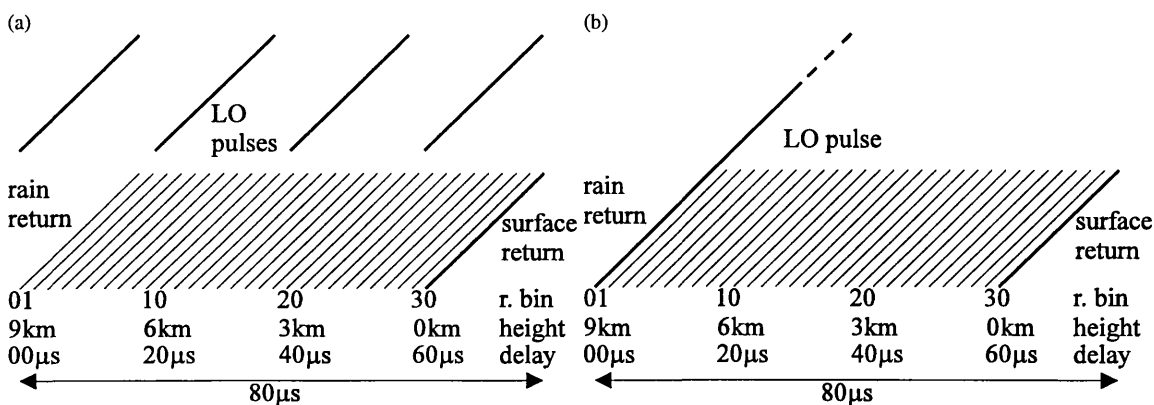


Figure 7.5. RA-2 range window configuration options: (a) Multiple LO pulse; (b) Single LO pulse.

The range window is designed to extend 9 km above the Earth's surface, which amounts to the provision of a 80 μs range window. The LO reference signal bandwidth needs to be four times the bandwidth of the transmitted signal in order to keep the modulation rate constant. The final baseline solution scheme is displayed in Figure 7.6. Pulse widths and bandwidths for the RA-2 rain mode transmitted linear FM waveform and LO reference signal are listed in Table 7.III. On the other hand, the number of range bins in the range window is given by:

$$n_{\text{rb}} = \frac{c(T_{\text{LO}} - T_p)}{2\Delta r} = 30 \quad (8)$$

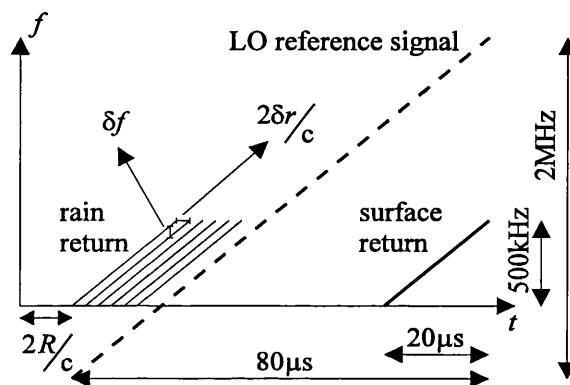


Figure 7.6. RA-2 rain mode range window baseline solution.

Table 7.III: RA-2 rain mode signal characteristics

	<i>transmitted waveform</i>	<i>LO reference signal</i>
pulse width	20 μs	80 μs
bandwidth	500 kHz	2 MHz

It remains to be decided how the rain mode would fit in with the conventional operating mode of the altimeter. *The extended bandwidth of the LO reference signal implies some impact on the IF filter bandwidths in the original altimeter design.*

7.2.2 Rain and Surface Return Power Levels

In the altimeter mode, the target to be detected is the Earth's surface whereas for the rain mode, the surface return represents the main source of interference. The fact that the ground clutter is overlapped with weaker rain echoes means that once these signals have been deramped and transformed into the frequency domain, the range sidelobes of the surface return may interfere the rain power spectrum unless they are kept at a

sufficient low level.

Range sidelobe reduction processing techniques need to be implemented in reception to reject, or at least minimise the ground clutter interference. In order to assess the exact magnitude of the range sidelobe level requirement, the rain and surface return power levels have been quantified. According to the Probert-Jones meteorological radar equation (Eq. 2) the rain power level is given by:

$$P_r = \frac{P_t G^2 \lambda^2 \theta_B^2 c \tau L_s \eta}{1024 \pi^2 r^2 \ln 2} \cdot 10^{-0.2 k_p \Delta h} \quad (9)$$

Rain return power levels as a function of depth below the storm top are shown in Figure 7.7(a). The rain return falls below the instrument noise floor level for high precipitation rates, making the detection of near-the-surface rain cells virtually impossible without modifying the original altimeter transmitted power values.

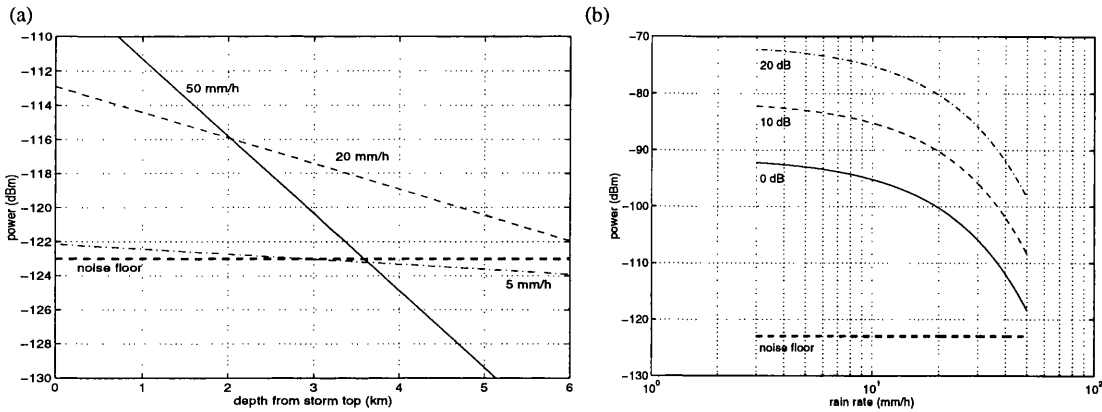


Figure 7.7. RA-2 predicted power levels: (a) Rain power level for different precipitation rates as a function of depth below the storm top; (b) Ground clutter power level for different backscattering coefficients as a function of precipitation rate (storm top 4 km above the ground).

Ground clutter power levels have been estimated as a function of precipitation rate according to Eq. 3, for different backscattering coefficient values (Figure 7.7(b)). The surface return may also fall below the instrument noise floor level if the precipitation spans over the whole range window, due to rain attenuation introduced along the two way path. According to the previous calculations, the rain to ground clutter power ratio is defined as:

$$\frac{P_r}{P_s} = \frac{c \tau_c \eta r_s^2}{4 \ln 2 \sigma_0^2 r_r^2} \cdot 10^{0.2 k_p (\Delta h_s - \Delta h_r)} \quad (10)$$

where Δh_s is the storm top height over the Earth's surface.

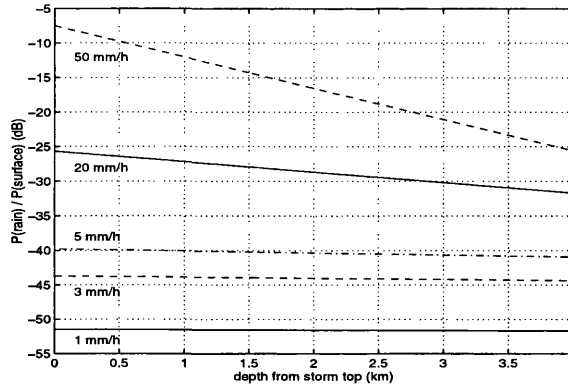


Figure 7.8. Rain to ground clutter power ratio for different precipitation rates as a function of depth below the storm top ($\sigma^0 = 10$ dB).

The ground clutter sidelobe level requirement varies as a function of precipitation rate, depending on the strength of the returned rain signal. In order to avoid range sidelobe interference at low rainfall rates, the power spectrum range sidelobe level must be below -50 dB in order to attain a minimum detectable rain of 1 mm/h (Figure 7.8). For larger rainfall rates, sidelobe masking is only significant in range bins adjacent to the surface.

7.2.3 Signal-to-Noise Ratio Analysis

The signal-to-noise ratio is given by:

$$SNR = \frac{P_r}{kT_{sys}B_nF} \quad (11)$$

The altimeter secondary channel (S-band) gives an insufficient signal-to-noise ratio for rain detection and its rain mode implementation is ruled out. The main channel (Ku-band) gives appropriate signal-to-noise ratios (shown in Figure 7.9(a)) to measure precipitation between 3 and 50 mm/h at a depth of 4 km below the storm top.

However, it should be noted that for higher penetration depths than 4 km, the maximum detectable rain is only of 10 mm/h (8 km depth). The signal-to-noise ratio is shown as a function of rain rate and depth from storm top in Figure 7.9(b). The right hand side ridge shows very clearly that rain attenuation severely reduces rain detectability at low depths (rain cells adjacent to the surface).

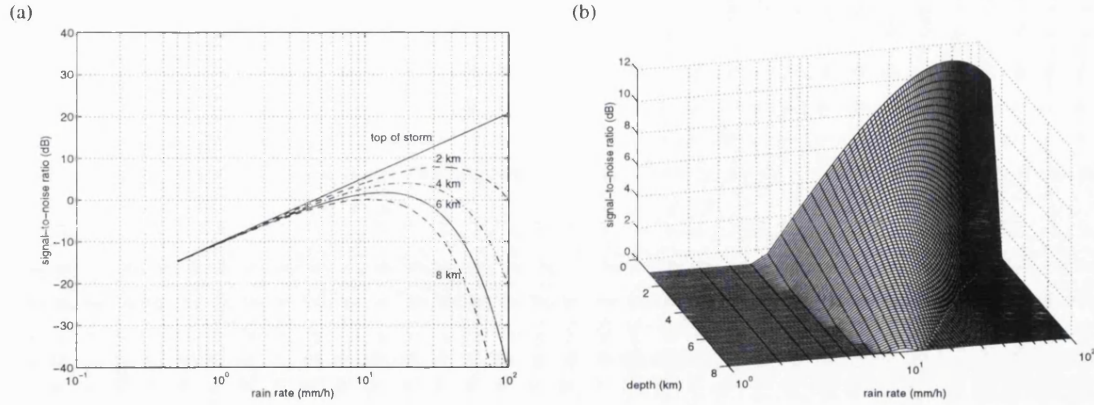


Figure 7.9. RA-2 signal-to-noise ratio: (a) SNR from various distances below the storm top as a function of rain rate (Ku Band, $f_0=13.575$ GHz, $\sigma^0 = 10$ dB); (b) SNR as a function of rain rate and depth from storm top (Ku Band, $f_0=13.575$ GHz, $\sigma^0 = 10$ dB).

7.2.4 Rain Mode Doppler Frequency Offset Analysis

Independently from the intrinsic velocity of the backscatterers in the pulse volume, an extra Doppler offset component is caused due to the radar platform motion. The power spectrum Doppler width corresponds to the antenna footprint Doppler spread (Figure 7.10(a)), given by:

$$f_d = \pm \frac{2v_s}{\lambda} \cdot \sin\left(\frac{\theta_B}{2}\right) \quad (12)$$

Inserting appropriate values in Eq. 12 ($v_s = 7000$ m/s, $\lambda = 0.022$ m and $\theta_B = 15^\circ$), a Doppler spectrum spread of 8.3 kHz is expected (Figure 7.10(b)).

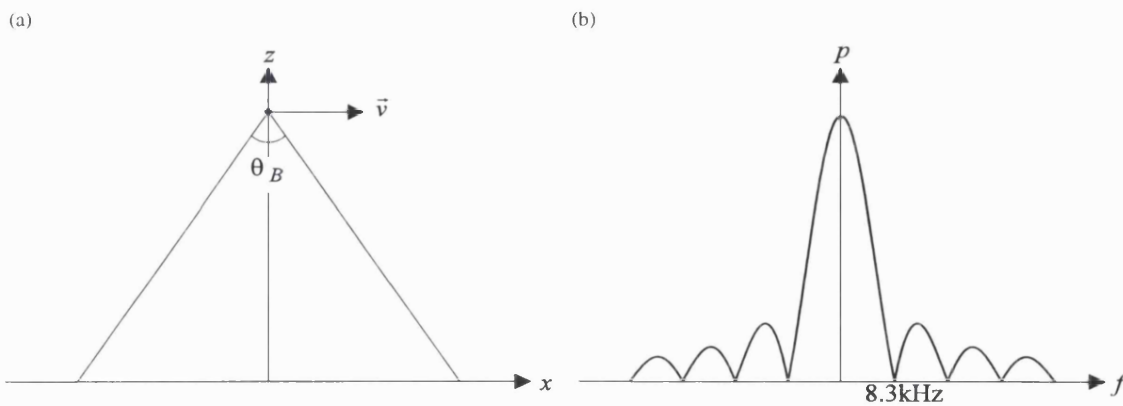


Figure 7.10. Doppler frequency: (a) Offset at the edges of the antenna footprint; (b) Spectrum spread.

The value of the Doppler spread directly translates into a range shift of 1/3 of a range bin (100 m), given by:

$$\Delta r_{\text{tb}} = \frac{c}{2} \cdot \Delta f \cdot \frac{T}{B} \quad (13)$$

where T is the pulse width and B the pulse bandwidth. Therefore, Doppler frequency offsets imposed by the system geometry result in a slight ‘blurring’ of the power spectrum. On the other hand, the Doppler frequency effect of raindrop motion also needs to be quantified. Raindrop vertical velocity reaches maximum values of ± 10 m/s. A velocity of such magnitude is converted into a ± 900 Hz shift in the frequency domain (± 10.8 m in range). Therefore, the hydrometeor motion has a negligible impact in the RA-2 rain mode.

7.3 Full Deramp of Nonlinear FM Waveforms

The use of a nonlinear frequency modulated waveform allows a compressed pulse with a low range sidelobe level to be obtained from the signal true matched filter. The possible advantages of nonlinear FM full deramp has been analysed. Nonlinear FM signals give point target responses similar to those of linear FM signals when the returned signal and the LO reference pulse are perfectly synchronised in time. However, their performance is degraded when both signals are delayed in time.

7.3.1 Predistorted Linear FM signals

Cook and Paolillo devised a pulse compression range sidelobe reduction technique [Cook and Paolillo, 1964] based on predistortion of linear FM signals (Chapter 5). They observed that by controlling the rise and fall times of the linear FM signal envelope, the spectrum amplitude ripple was less than that of the theoretical Fresnel distortion. Since the modification of the transmitted pulse envelope is not suitable for high-power radars, the same effect was achieved by predistorting the signal phase. From basic concepts of distortion theory, they showed that amplitude and phase distortion have functional similarities and produce similar effects on the time waveform when the distortion factors are small. The resultant predistorted linear FM instantaneous frequency was shown in Figure 5.1. Effectively, the modulation can be described as a linear FM signal combined

with short portions of higher modulation rate at the beginning and end of the pulse.

A linear FM predistortion function has been designed for the RA-2 altimeter selected time-bandwidth product of 10. The resulting predistorted linear FM instantaneous frequency is shown in Figure 7.11(a). When the matched filter is mismatched in amplitude with a Blackman-Harris function, the pulse compression range sidelobe level is of -34.5 dB (shown in Figure 7.11(b)). However, full deramp of the predistorted linear FM gives a power spectrum point target response with a range sidelobe level of -11 dB (approximately 2 dB worse than for full-deramped linear FM signals). The full deramped point target response is shown in Figure 7.11(c).

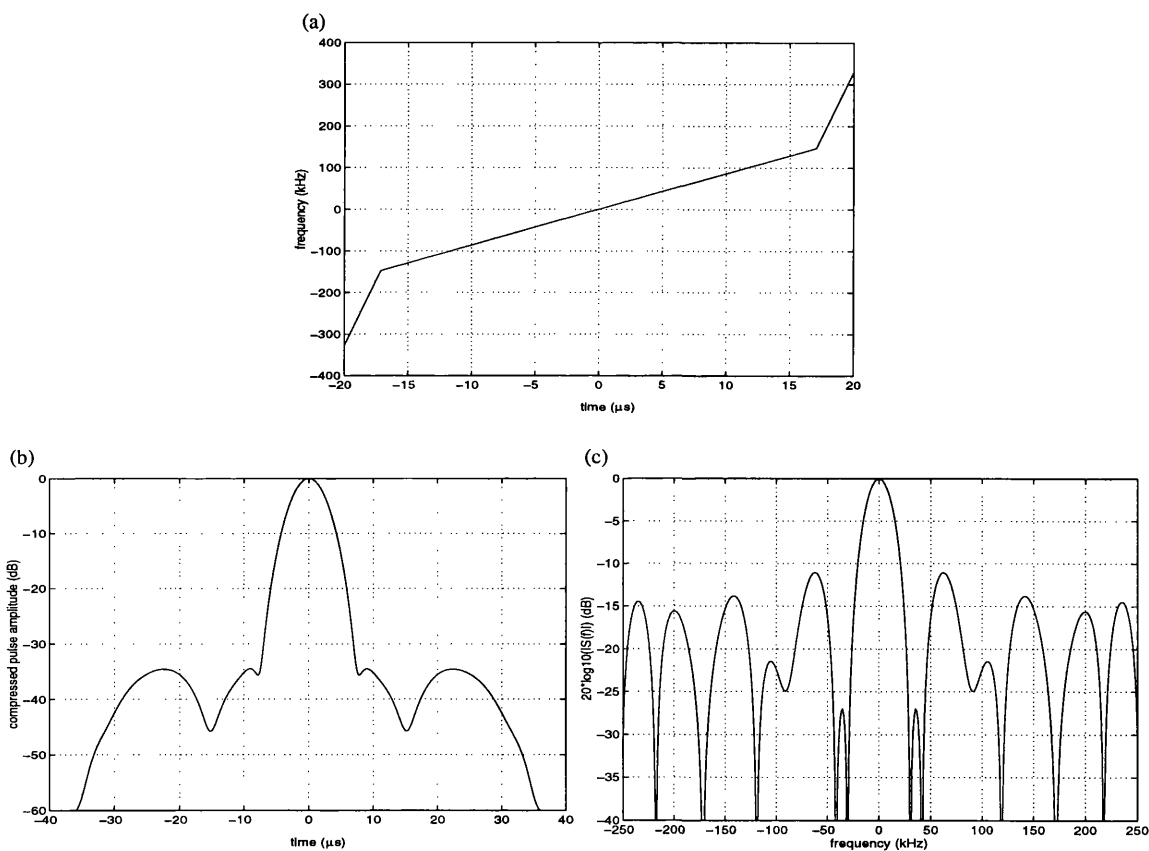


Figure 7.11. Predistorted linear FM ($TB = 10$): (a) Instantaneous frequency; (b) Compressed pulse, $RSL = -34.5$ dB; (c) Full deramp power spectrum, $RSL = -11$ dB.

7.3.2 Nonlinear FM Signals

The full deramp technique has been applied to nonlinear frequency modulations. Nonlinear FM signals produce a low range sidelobe level compressed pulse at the output of a true filter with no mismatch loss [Key et al, 1959]. A nonlinear FM signal design

technique was described in Section 4.2.2, where the compressed pulse output with a sufficient low range sidelobe level was specified and its spectrum directly obtained through the Fourier transform of a selected weighting function. In order to specify the signal spectrum phase $\theta(f)$, the inverse Fourier transform of the spectrum was assumed to be rectangular, given by:

$$\left| \int_{-\infty}^{\infty} |S(f)| \cdot e^{j2\pi\theta(f)} e^{j2\pi ft} df \right| = 1 \quad -\frac{T}{2} \leq t \leq \frac{T}{2} \quad (14)$$

The previous equation can only be solved approximately using Kelvin's principle of stationary phase. The numerical method of Johnston [Johnston, 1983] has been employed to obtain a nonlinear modulation scheme of the RA-2 required time-bandwidth product (Figure 7.12(a)). The compressed pulse spectrum is designed to approximate the square root of a Hamming window. A pulse compression range sidelobe level of -20.7 dB (Figure 7.12(b)) is obtained for a time-bandwidth product of 10. The full deramp of the continuous nonlinear FM signal gives a range sidelobe level of -10.5 dB, which is 2.5 dB worse than for linear FM signals. The frequency point target response is shown in Figure 7.12(c).

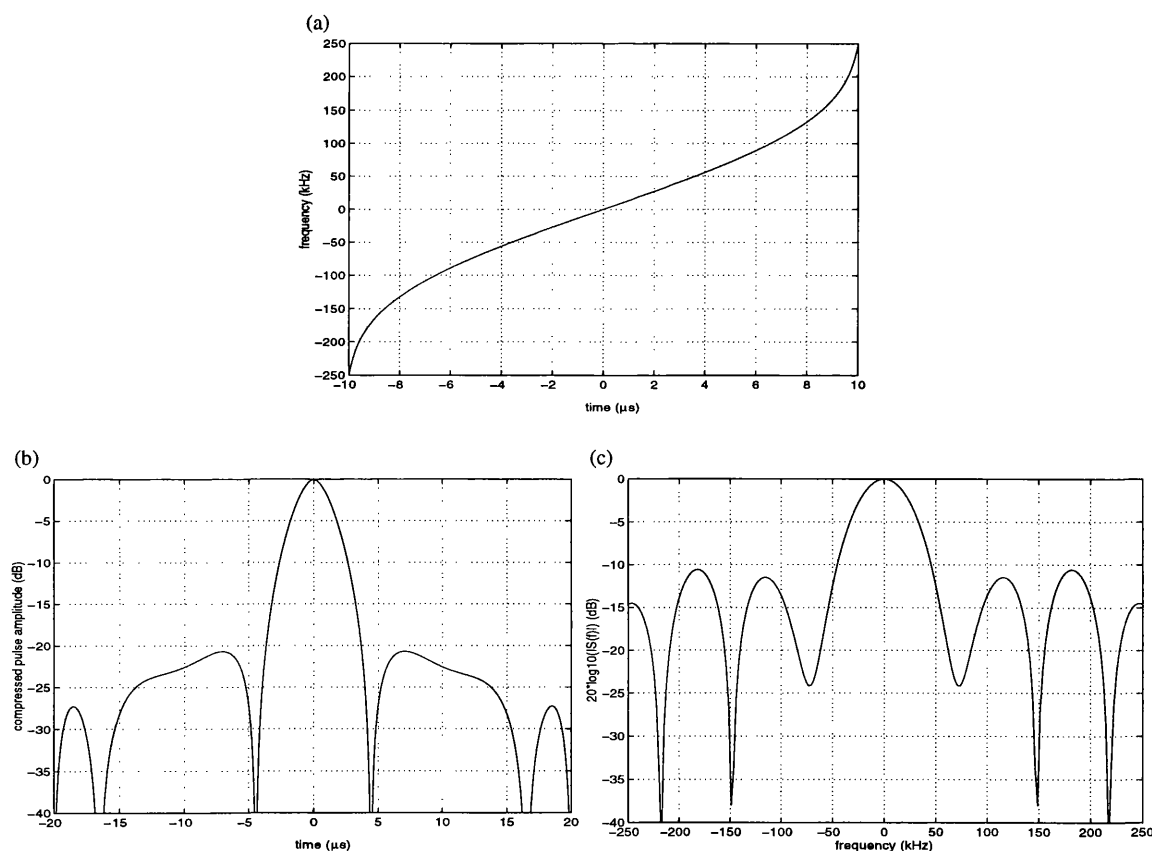


Figure 7.12. Nonlinear FM ($TB = 10$): (a) Instantaneous frequency (after [Johnston, 1983]); (b) Compressed pulse, $RSL = -20.7$ dB; (c) Full deramp power spectrum, $RSL = -10.5$ dB.

It has been established that full deramp of nonlinear frequency modulations does not match the performance of linear FM signals. A diagram of nonlinear FM waveform full deramp is shown in Figure 7.13. When the returned nonlinear FM signal and the LO pulse are perfectly aligned in time, the performance in terms of range sidelobe level is similar to the one obtained with linear FM waveforms. However, if there is a time shift in between both signals, the output beat frequency is not uniform since some different modulation rate signal sections are mixed. Therefore, the sinusoidal deramped echo frequency is no longer constant, and some of its frequency response may even be outside the intermediate frequency filter. Such a problem is worsened when a longer nonlinear LO reference signal is employed.

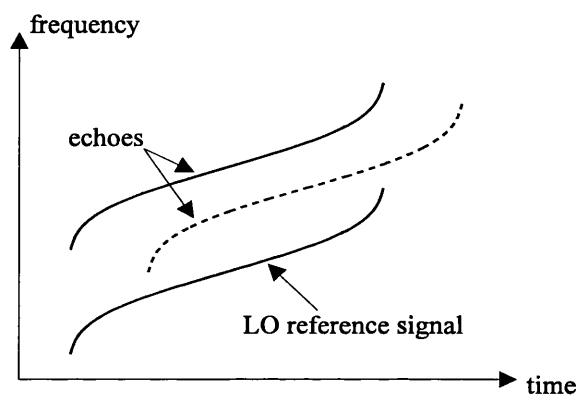


Figure 7.13. Diagram of nonlinear FM waveform full deramp.

It is concluded that nonlinear frequency modulated signals are not compatible with the full deramp technique, and therefore, their use in the RA-2 rain mode can be ruled out.

7.4 RA-2 Rain Mode: Full Deramp Formulation

The RA-2 rain mode has been designed to have transmitted and LO reference pulses of different lengths in order to configure the range window, allowing the acquisition of the maximum number of independent samples per scan. Conventional altimetry full deramp formulation has been modified along in order to incorporate the previous condition. A preliminary study of surface return interference shows that severe range sidelobe reduction schemes need to be applied to the deramped signal in order to minimise the ground clutter interference.

7.4.1 Full Deramp Formulation of Signals of Different Lengths

The use of a longer reference signal implies that successive rain echoes are deramped by different sections of the LO signal (Figure 7.14). Therefore, it is necessary to introduce some modifications to the RA-2 altimeter mode formulation.

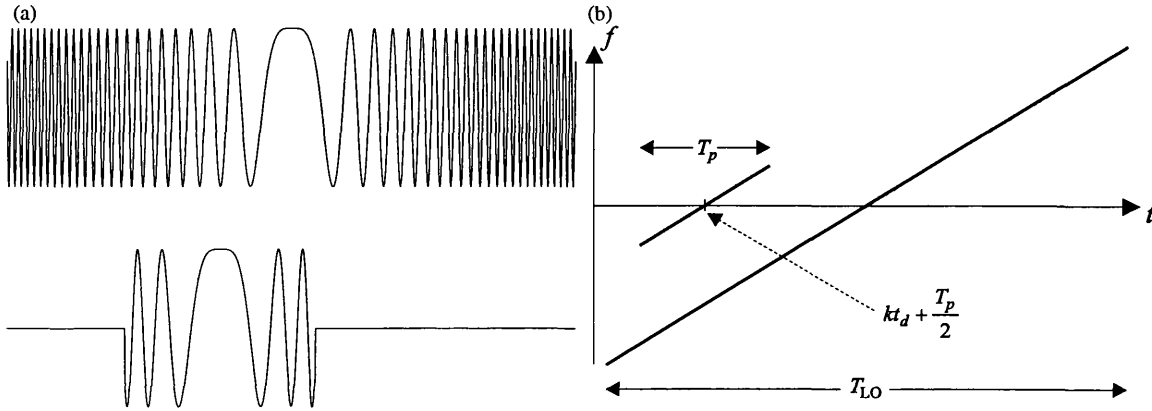


Figure 7.14. Diagram of RA-2 rain mode full deramp of signals of different length.

The linear FM received echo is formulated as:

$$s_r(t) = \frac{1}{\sqrt{T_p}} \text{rect} \left(\frac{t - \left(kt_d + \frac{T_p}{2} \right)}{T_p} \right) \cos \left(2\pi f_0 \left(t - \left(kt_d + \frac{T_p}{2} \right) \right) + \pi \frac{B}{T_p} \left(t - \left(kt_d + \frac{T_p}{2} \right) \right)^2 \right) \quad (15)$$

where $0 \leq k \leq n_{rb}$ (k represents the position of the echo in the range window). The LO reference signal is defined as:

$$s_{LO}(t) = \frac{1}{\sqrt{T_{LO}}} \text{rect} \left(\frac{t - \frac{T_{LO}}{2}}{T_{LO}} \right) \cos \left(2\pi f_0 (t - T_{LO}) + \pi \frac{B}{T_p} (t - T_{LO})^2 \right) \quad (16)$$

A detailed calculation of the full-deramp formulation of linear FM signals of different lengths can be found in Appendix D.2. The in-phase component of the complex envelope of the deramped echo (after filtering the spectrum component centred at $2f_0$) is given by:

$$\tilde{s}_d(t) = \frac{1}{\sqrt{T_{LO}T_p}} \text{rect}\left(\frac{t - \left(kt_d + \frac{T_p}{2}\right)}{T_p}\right) \cos\left(2\pi \frac{B}{T_p} \left(k - \frac{n_{rb}}{2}\right) t_d t + \phi\right) \quad (17)$$

Notice that the new full deramp formulation only differs from the conventional one by a factor of $k - n_{rb}/2$, which equals zero when the echo and the LO reference signal are of the same length. The previous term repositions the deramped echoes in the range window. The RA-2 rain mode power spectrum point target response is given by:

$$|\tilde{S}_d(f)|^2 = \frac{T_p}{T_{LO}} \left| \text{sinc}\left(B\left(k - \frac{n_{rb}}{2}\right)t_d - fT_p\right) \right|^2 \quad (18)$$

7.4.2 Ground Clutter Range Sidelobe Interference

In order to validate the performance of any sidelobe reduction processing to minimise surface interference, it is indispensable to assess the impact of the technique on both the precipitation signal and surface return spectrums.

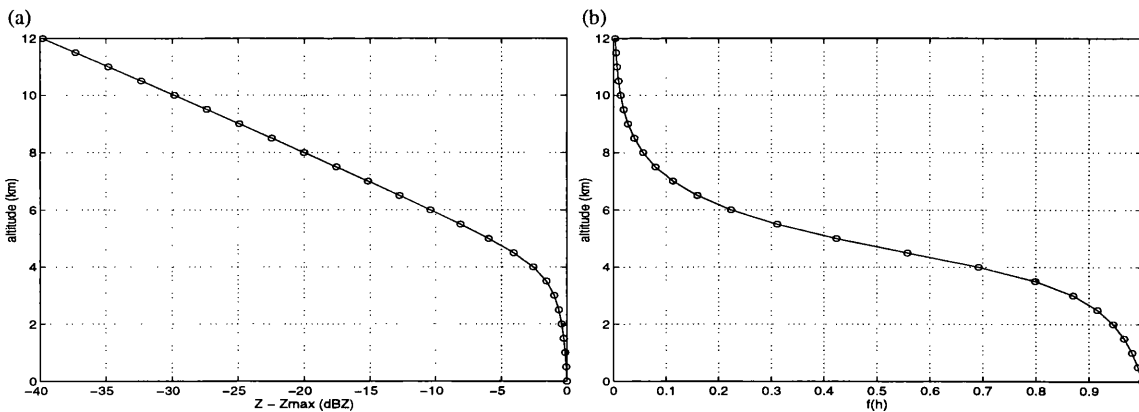


Figure 7.15. Precipitation model: (a) Radar reflectivity as a function of altitude; (b) Altitude variation of rainfall rate. Reproduced from [Amayenc et al., 1994].

Amayenc et al. [Amayenc et al., 1994] derived a rainfall reflectivity model as a function of height, established from radar precipitation measurements. The radar reflectivity obtained at S-Band for a given rain rate is about constant on average up to 4 km above the ground, decreasing with altitude above at a rate of 5 dBZ/km (Figure 7.15). The same model can be extended to the Ku-Band with the appropriate attenuation

coefficients. Such ^a model can be employed as a correction factor for the rain power levels calculated in section 7.2.2. ⊕

In order to ease the calculation, a uniform precipitation field over a height of 4 km above the ground is considered. The rain return spectrum is simulated according to its power level as a function of rain rate (Eq. 9) with the appropriate attenuation coefficients, and disregarding at the moment any waveform or statistical considerations. The simulation does not consider attenuation of the bright band which could be rather significant (3 to 4 dB) for large rainfall rates [Awaka, 1992]. Bright band attenuation could be incorporated to the model by simply scaling the rain and ground power curves. The surface return is simulated as the power spectrum of the superposition of a deramped echo in each range bin, weighted with appropriate power and attenuation coefficients.

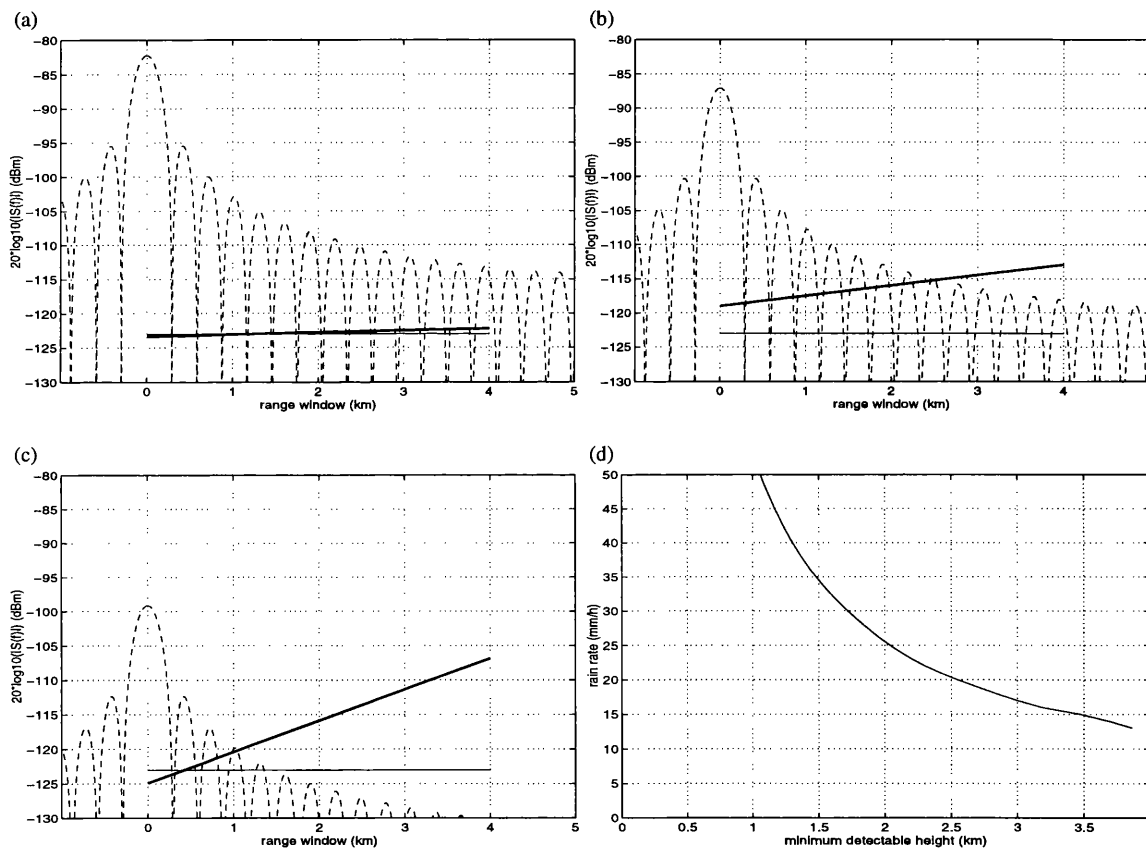


Figure 7.16. Ground clutter range sidelobe interference (4 km precipitation field) for low, medium and high rainfall rates: (a) 5 mm/h; (b) 20 mm/h; (c) 50 mm/h; (d) Minimum detectable height as a function of rain rate.

Three different rain rates are considered, (i) 5 mm/h (low detectable rate), (ii) 20 mm/h (medium detectable rate) and (iii) 50 mm/h (high detectable rate). The results of the simulation are shown in Figure 7.16(a-c) and are considered to be representative for each rainfall rate range (low, medium and high). Figure 7.16(d) shows the minimum

detectable height (below a storm top of 4 km) as a function of rain rate. The rain detectability region corresponds to the area between the storm top and the minimum detectable height curve for each rain rate.

Two factors restrict the performance of the RA-2 rain mode full deramp alternative. Severe ground clutter interference does not allow ^{ion of} to detect the minimum required rainfall rate (only rates above 13 mm/h are free of surface interference). Medium rainfall rates produce ^{ca} sufficient signal-to-noise ratio but are interfered ^{with} in the lower part of the range window. High rainfall rates attenuate the ground clutter return, reducing the interference, but the rain signal falls below the system noise floor at low altitudes. Detectability benefits of any range sidelobe reduction technique will be assessed with respect to the previous considerations.

①

②③

7.5 Range Sidelobe Reduction Techniques

From the simulation derived in the previous section, it is obvious that the RA-2 rain mode needs of some form of range sidelobe reduction in order to, at least, minimise the surface return interference. The full deramp range sidelobe level of -13.3 dB is sufficient to guarantee rainfall signal detection free of interference in itself. Therefore, range sidelobe reduction scheme may only target the ground return power spectrum as opposed to reducing range sidelobes over the whole range window. Since the surface height is accurately known due to the altimeter tracking mode, it is possible to apply severe weighting only to the section of the range window containing the ground clutter return. However, the surface echo overlaps in time with ^{the} rainfall signal for the totality of its 20 μ s duration, and any applied weighting scheme which uniformly attenuates both ground and rain signal, would subsequently damage the detectability of precipitation close to the surface.

a

④

⑤

7.5.1 Amplitude Weighting

Amplitude weighting is one of the main range sidelobe reduction techniques for pulse compression radars. The literature provides comprehensive sets of different families of weighting functions [Harris, 1978]. Amplitude weighting can be applied to the whole extent of the range window in order to reduce the deramped pulse power spectrum range

sidelobe level. Mainlobe broadening due to weighting produces power leakage over adjacent range bins and degrades the system range resolution. Signal-to-noise ratio losses may represent an additional advantage in order to attenuate ground clutter.

The Hamming window gives significant range sidelobe level reduction (-42 dB) at the expense of modest losses, and it is defined as:

$$w(t) = \text{rect}\left(\frac{t}{T_{\text{LO}}}\right) \left(0.54 + 0.46 \cos\left(\frac{2\pi t}{T_{\text{LO}}}\right) \right) \quad (19)$$

A comparison between an unweighted and a Hamming weighted deramped echo is shown in Figure 7.17(a). The mainlobe half width between nulls is doubled from 50 kHz to approximately 100 kHz, and the relative power loss is of 5.5 dB. The Hamming-tapered power spectrum is given by:

$$\tilde{S}_w(f) = 0.54\tilde{S}_d(f) + 0.23 \left(\tilde{S}_d\left(f + \frac{1}{T_p}\right) + \tilde{S}_d\left(f - \frac{1}{T_p}\right) \right) \quad (20)$$

where $\tilde{S}_d(f)$ is the unweighted deramped echo spectrum. A detailed calculation can be found in Appendix D.3. When the Hamming function is applied to the whole range window, the taper in every range bin is no longer uniform. Therefore, the rain power spectrum depends on range, and a loss factor is introduced as a function of deramped echo position in the range window (Figure 7.17(b)). The attenuation at the edges of the range window is of 12 dB.

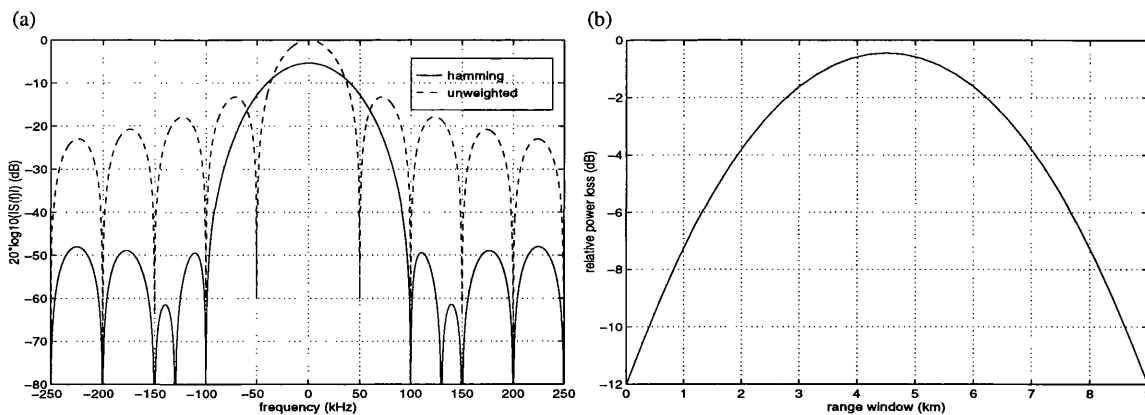


Figure 7.17. Hamming weighting: (a) Comparison between RA-2 rain mode unweighted and weighted power spectra; (b) Power spectrum relative power loss as a function of position in the range window.

The influence of a Hamming taper over the 80 μs range window is shown in Figure 7.18(a-c) for different rainfall rates and a storm top 4 km above the Earth's surface. The rain and ground return power levels have been modified accordingly to the weighting power loss. Although the ground return is highly attenuated and its range sidelobes reduced, the rain return power level adjacent to the ground is still obscured and falls below the system noise floor level. The minimum detectable height as a function of rain rate does no longer decrease monotonically since the attenuation introduced by the Hamming weighting function forces the rain level to be out of the dynamic range of the AGC (Figure 7.18(d)).

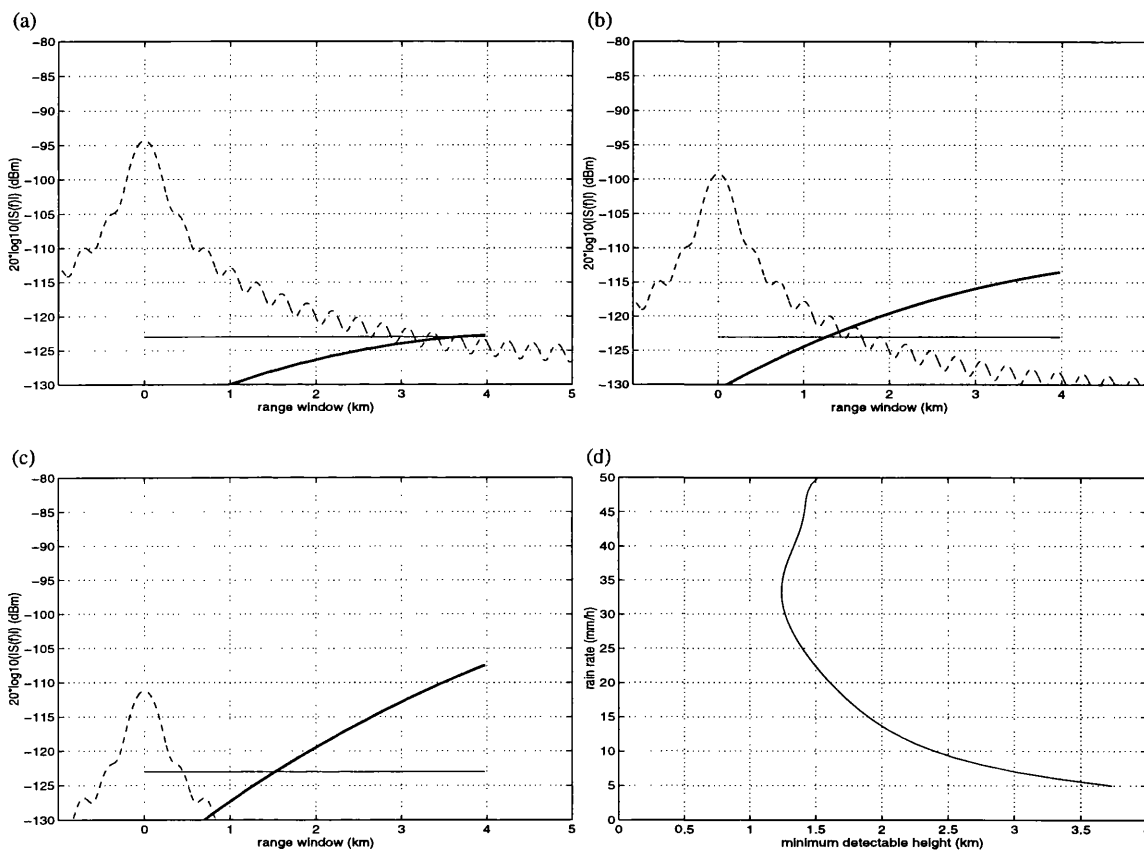


Figure 7.18. Ground clutter range sidelobe interference after Hamming weighting over the range window (4 km precipitation field) for low, medium and high rainfall rates: (a) 5 mm/h; (b) 20 mm/h; (c) 50 mm/h; (d) Minimum detectable height as a function of rain rate.

The length RA-2 rain mode range window excludes the possibility of weighting its whole extent to achieve a unique point target response (as achieved in the normal altimetry mode operation). The different nature of full deramp and FM pulse compression, based on completely different mathematical principles (Figure 7.19), does not allow ^{the application of} (to employ) classical FM pulse compression sidelobe reduction methods in the altimeter rain mode. The mismatched FM pulse compression filter (convolution), allows a point target response independent of range, whereas the full deramp technique (product

and Fourier transform), gives a point target pattern as a function of range. Hence, it is necessary to rule out the option of tapering the whole extent of the range window to attain a constant sidelobe level below -50 dB.

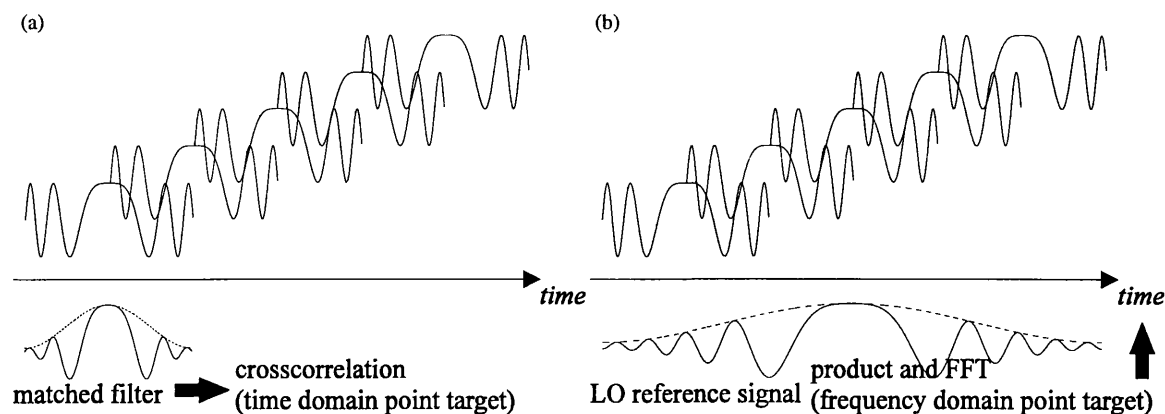


Figure 7.19. Weighting schemes: (a) FM pulse compression; (b) Full deramp technique.

7.5.2 ~~AGC~~ Gain-Varying Functions *at the AGC stage.*

The idea of distorting the signal at the IF stage comes from the fact that in most cases, range sidelobe reduction is not necessary over the whole extent of the range window. Severe ground clutter interference is only present for low rain rates due to the weakness of the returned rain signal. In fact, the ground clutter return only overlaps with the deramped rain echoes for the last 3 km of the range window (Figure 7.20). Therefore, attenuation of the ground clutter echo improves rain detection and range sidelobe reduction only needs to be applied to the overlapped ground and rain return signal after the 21st range bin (60 to 80 μ s). However, it is not possible to attenuate only the surface return without also trading off the adjacent rain cells to the Earth's surface.

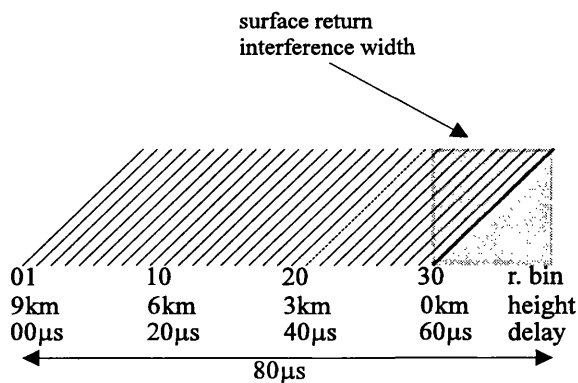


Figure 7.20. Ground clutter sidelobe interference width.

Due to the limitation of the number of bits at the ADC stage (8 bits for the altimeter ADC converter), the maximum dynamic range is of 42 dB. Thus, the AGC stage must ensure that the surface return level does not saturate the receiver and that the rain return level is suitable for digital sampling. The performance of three gain-varying functions have been studied (Hamming, linear and exponential) in order to be incorporated into the AGC stage. The additional losses introduced by the gain-varying functions are known a priori and could be easily corrected after detection without any impact in rain rate estimation.

The Hamming gain-varying function is shown in Figure 7.21(a), consisting of half cycle of a Hamming function attenuating the last quarter of the range window where the ground clutter return is expected. It achieves a power spectrum attenuation of 5.1 dB, which is yet insufficient to reduce the ground clutter level to a suitable extent in which no interference is caused. The RA-2 rain mode point target response attenuated with the described Hamming gain-varying function is shown in Figure 7.21(b).

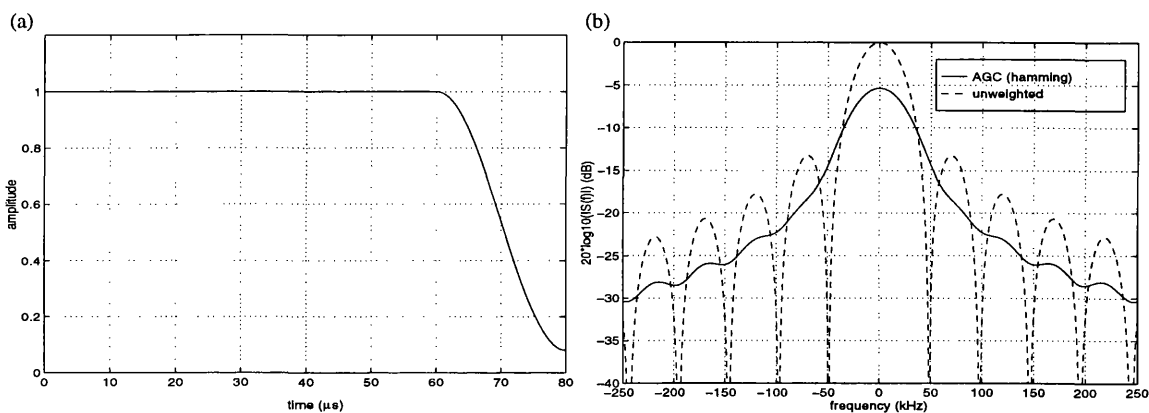


Figure 7.21. Hamming gain-varying function: (a) Diagram; (b) Power spectrum of the test signal of the range window.

Figure 7.22 shows the effect of the attenuation of the surface return for different rainfall rates and a storm top height of 4 km. The gain-varying function effectively improves rain detection of low rain rates.

The attenuated rain return displayed in Figure 7.22 only diverges from its original non attenuated spectrum over a 3 km range adjacent to the Earth's surface. Considering that for higher precipitation rates, the rain return signal is below the instrument noise floor level, the impact of ground clutter echo attenuation is not significant for their detection. Other weighting functions listed in the literature which present a faster sidelobe decay rate (such as $\cos^n(x)$) have been applied to the ground return with no further improvement.

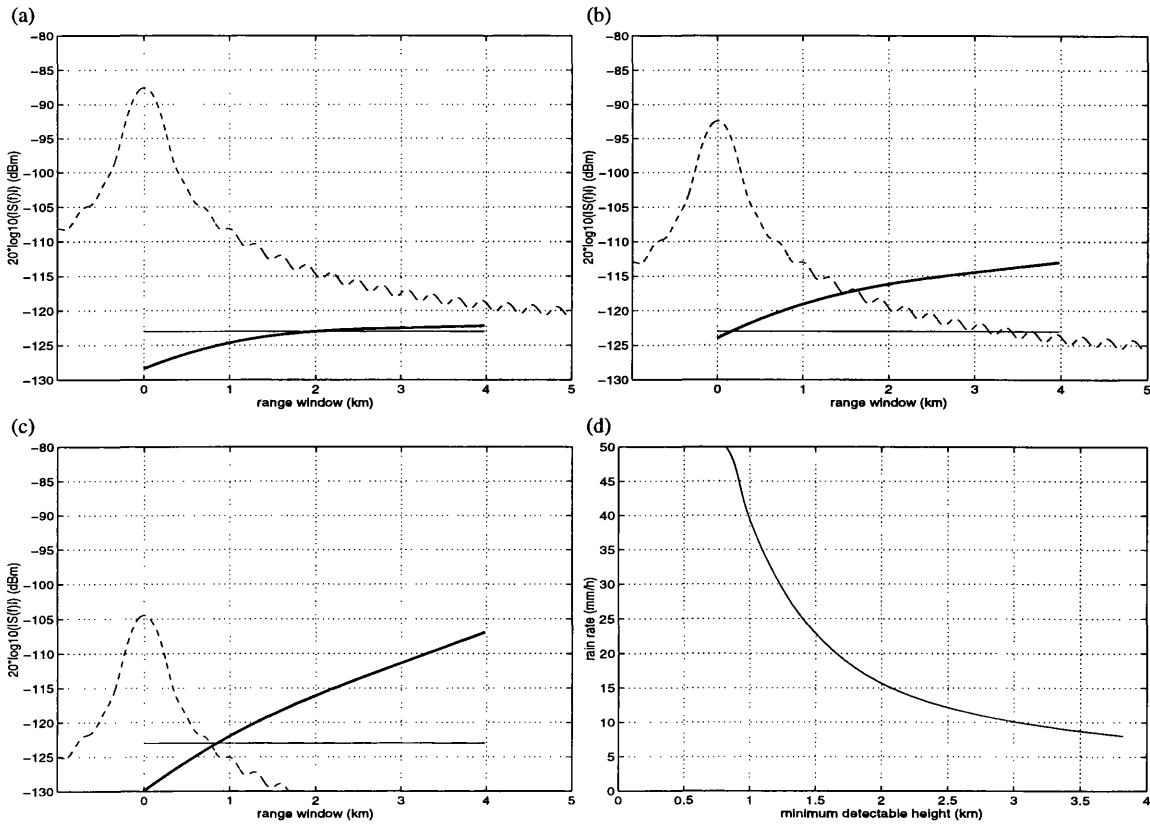


Figure 7.22. Ground clutter range sidelobe interference after an AGC Hamming gain-varying function (4 km precipitation field) for low, medium and high rainfall rates: (a) 5 mm/h; (b) 20 mm/h; (c) 50 mm/h; (d) Minimum detectable height as a function of rain rate.

A similar attenuated frequency point target response can be obtained employing a linear gain-varying function (Figure 7.23(a)). The linear function is designed to attenuate the ground echo 40 dB at the edge of the range window. The surface return point target response attenuation (5.7 dB) is very similar to the one introduced by the half cycle of a Hamming function, giving no additional benefit.

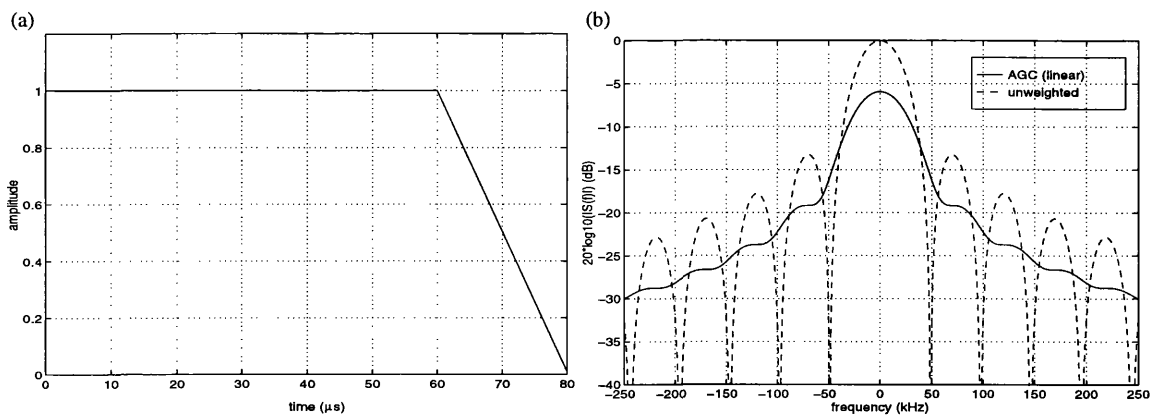


Figure 7.23. Linear gain-varying function: (a) Diagram; (b) Power spectrum.

In order to increase the attenuation of the ground clutter echo, an exponential

gain-varying function has also been studied. Such a function can achieve an arbitrary low attenuation value at the edge of the range window, at the expense of severe mainlobe broadening and forcing the rain signal to fall considerably below the noise floor level. ⊕

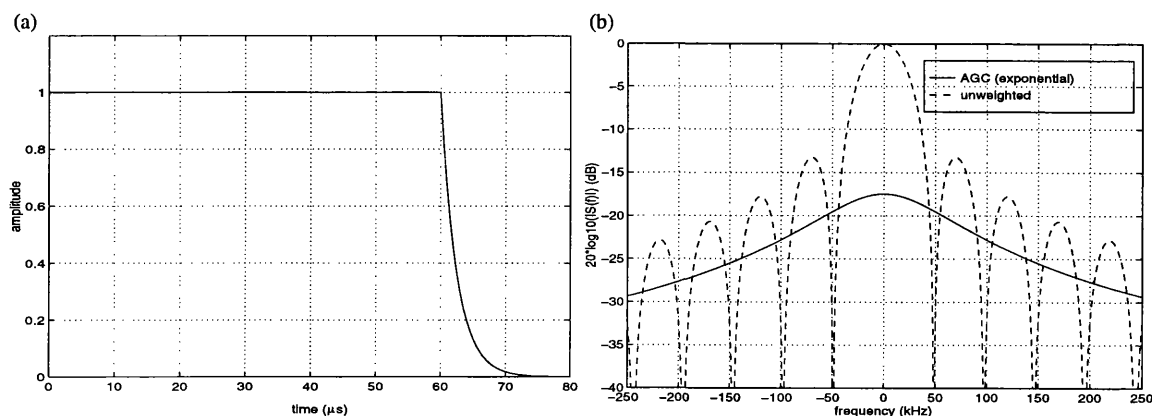


Figure 7.24. Exponential gain-varying function: (a) Diagram; (b) Power Spectrum.

The adjacent range bins to the surface return continue to be masked and very little benefit is obtained for lower penetration depths. The exponential gain-varying function and its frequency point target response (17 dB attenuation) are shown in Figure 7.24. No significant improvement is found in the minimum detectable height as a function of rain rate (Figure 7.25).

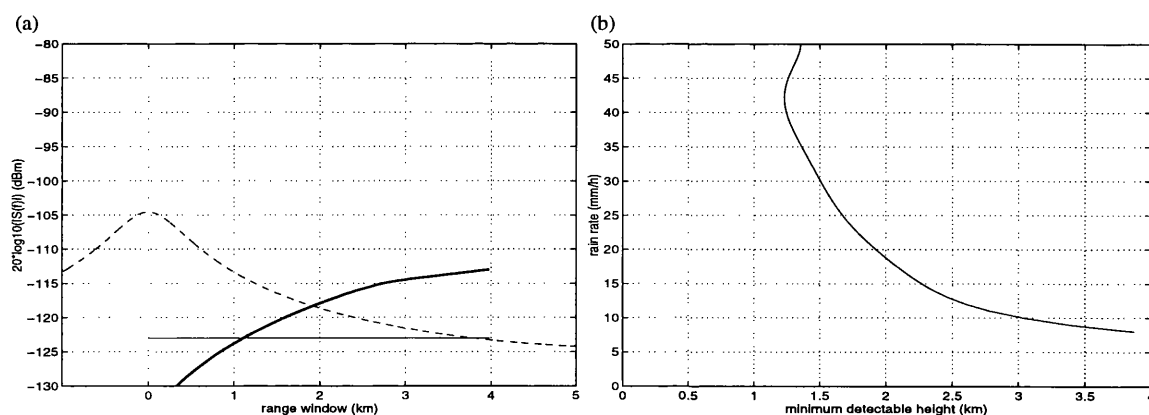


Figure 7.25. Ground clutter range sidelobe interference after an AGC exponential gain-varying function (4 km precipitation field): (a) 20 mm/h; (b) Minimum detectable height as a function of rain rate.

Finally, the possible benefits of ground clutter echo pulse width reduction have also been investigated. In practice, the reduction of the deramped echo width reduces the point target mainlobe level (see Figure 7.3), and the broadening effect of a shorter pulse forces the energy to leak over the whole range window. However, for any ground return pulse width reduction percentage, the range sidelobe decay rate is kept constant and although the energy of the ground power spectrum spreads over the range window, no

interference reduction benefit is obtained. The frequency point target response for a ground clutter echo width reduction of 50 % is shown in Figure 7.26. As expected, the attenuation of the ground clutter power spectrum is of 6 dB.

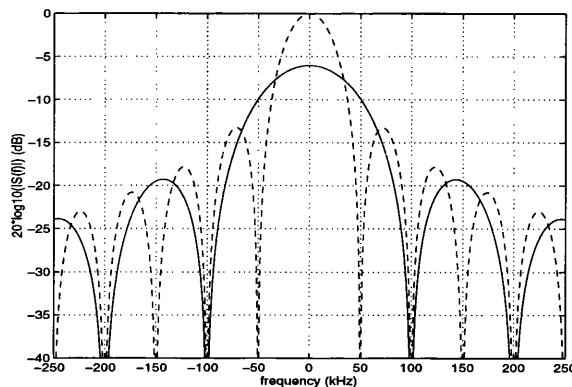


Figure 7.26. RA-2 rain mode: 20 μ s (100%) point target response (dashed line); 10 μ s (50%) point target response (plain line)

7.5.3 Combined Amplitude and Phase Weighting Schemes

Since rain information is retrieved from the modulus of the deramped echoes power spectrum, it is possible to alter the phase of the returned signal with no impact in the data extraction process. A combination of time domain amplitude and phase weighting schemes is capable of meeting the required range sidelobe level requirement. However, the complex weighting law needs to be designed in order to allow low range sidelobes while minimising signal distortion and *SNR* loss.

An example of combination of amplitude and phase weighting is described in [Griffiths et al., 1995] and shown in Fig. 7.27(a). The amplitude weighting is based on the superposition of half a cycle of a Hamming function (75% of the range window) and a Kaiser function (25% of the range window, where the surface return is expected). The phase weighting scheme is only applied to the Kaiser function, and it was obtained following the method of [Brennan and Reed, 1973]. The complex function is given by:

$$W_{\text{opt}} = M^{-1} \cdot S^* \quad (21)$$

where M is the correlation matrix of the ground echo interference and thermal noise and S represents the signal vector. The described weighting scheme achieves a power spectrum range sidelobe level of approximately -50 dB.

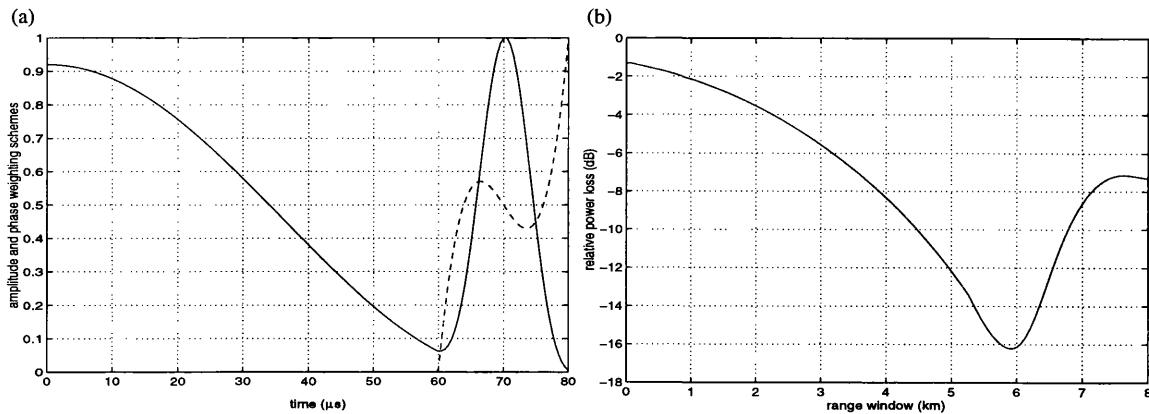


Figure 7.27. Combined amplitude and phase weighting scheme: (a) Diagram (plain line: Hamming and Kaiser amplitude functions, dashed line: phase function); (b) Power spectrum relative power loss as a function of position in the range window.

However, and since the weighting is not uniform, there is a degradation of signal-to-noise ratio as a function of position in the range window. Figure 7.27(b) shows the power spectrum relative power loss with respect to an unweighted deramped echo. As expected, the worst loss (-16.2 dB) occurs at the connection point between both amplitude functions. *The severe losses produced by the previous weighting scheme rule out its application to the RA-2 rain mode.*

On the other hand, the distortion introduced by the weighting scheme on the power spectrum as a function of range needs to be assessed. Such distortion alters significantly the deramped echo point target response over some sections of the range window. Figure 7.28(a) displays the influence of the weighting scheme on the deramped echoes power spectrum as a function of position in the range window, whereas Figure 7.28(b) shows the surface return point target response. Again, the worst distortion is introduced at the connection between the amplitude weighting functions.

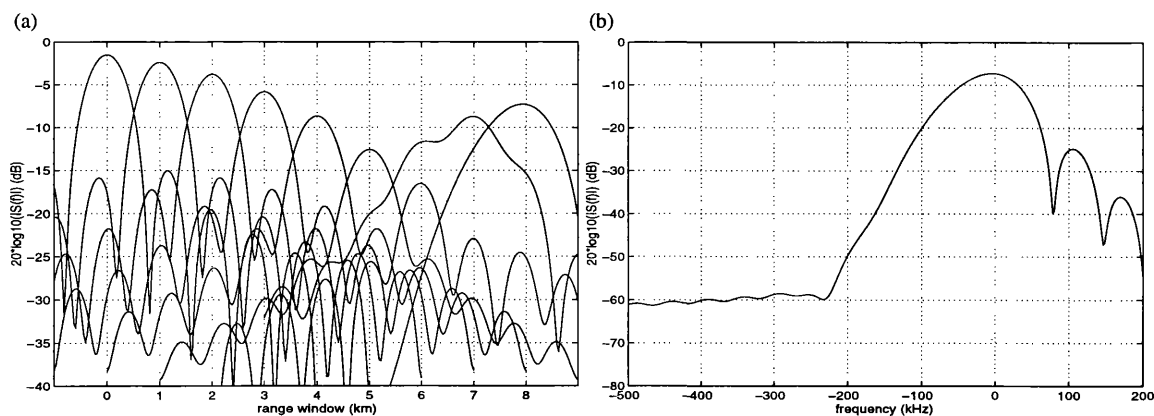


Figure 7.28. Combined amplitude (Hamming and Kaiser) and phase weighting scheme: (a) Point target distortion as a function of position in the range window; (b) Surface return power spectrum.

In order to reduce distortion and signal-to-noise ratio losses on the deramped echo point target response, the amplitude scheme described in section 7.5.2 (Hamming gain-varying function) was combined with the same phase function. The taper remains constant over 75% of the range window with half a cycle of a Hamming function (combined with the additional phase scheme) attenuating the surface return.

Figure 7.29(a) shows a diagram of the proposed weighting scheme whereas Figure 7.29(b) displays the relative power loss with respect to an unweighted deramped echo as a function of position in the range window. The worst loss (-7 dB) occurs at the edge of the range window where the surface return is expected. The range sidelobe level attained with the weighting scheme is of approximately -25 dB. Figure 7.30 shows the power spectrum distortion introduced by the amplitude and phase weighting scheme as a function of range. The resulting distortion is less significant than with the previous weighting scheme (Hamming and Kaiser).

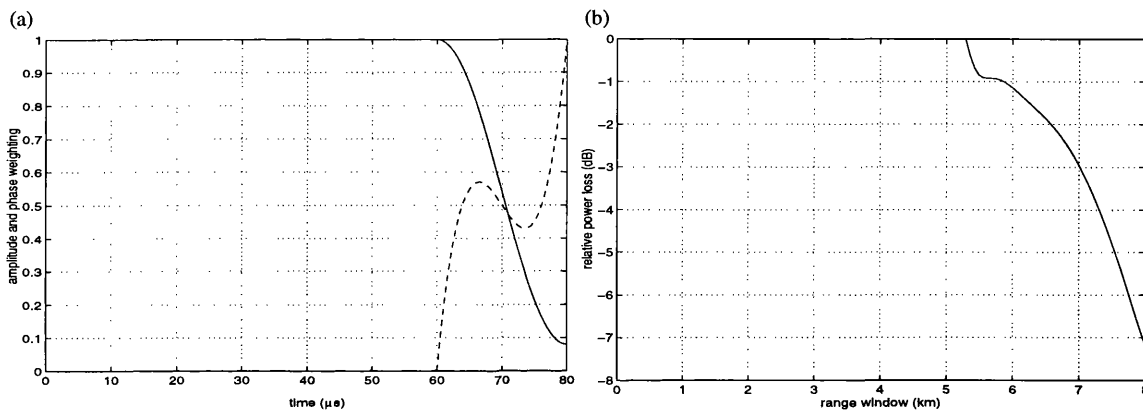


Figure 7.29. Combined amplitude and phase weighting scheme: (a) Diagram (plain line: Hamming amplitude function, dashed line: phase function); (b) Power spectrum relative power loss as a function of position in the range window.

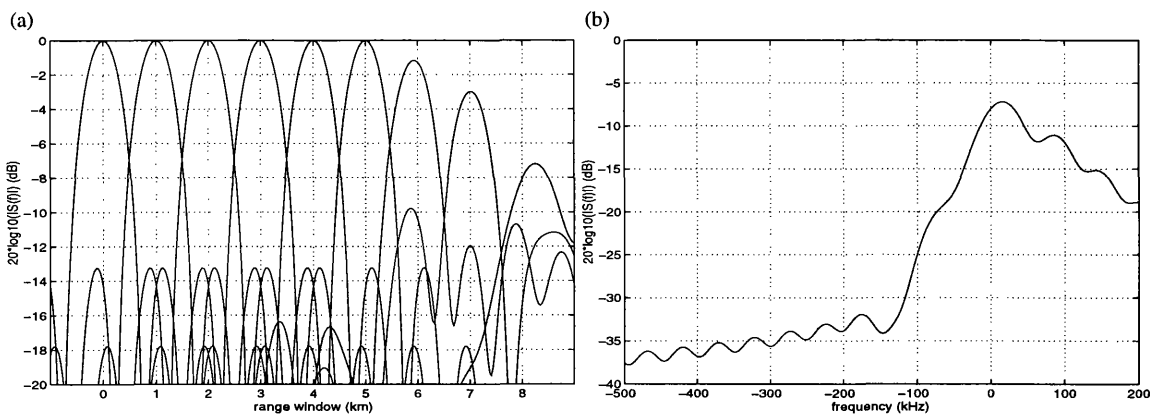


Figure 7.30. Combined amplitude (Hamming) and phase weighting scheme: (a) Point target distortion as a function of position in the range window; (b) Surface return power spectrum.

Although the weighting scheme does not give a sufficient range sidelobe level, the rain signal is only obscured up to 800 m over the Earth's surface at the minimum of the minimum detectable height as a function of rain rate curve. The detectable rain region (Figure 7.31(d)) is the largest of all the range window range sidelobe cancellation techniques.

The rain mode demanding range sidelobe requirement cannot be achieved with any of the range sidelobe suppression techniques studied. A combination of amplitude and phase weighting allows to minimise the surface return interference and maximise rain detectability, at the expense of introducing some losses and distortion over some sections of the range window. While the unmodulated pulse alternative may achieve a suitable rain mode performance (at the expense of major system circuitry changes), the full deramp mode of operation alternative trades better power capabilities with ground clutter interference and signal-to-noise ratio losses and distortion.

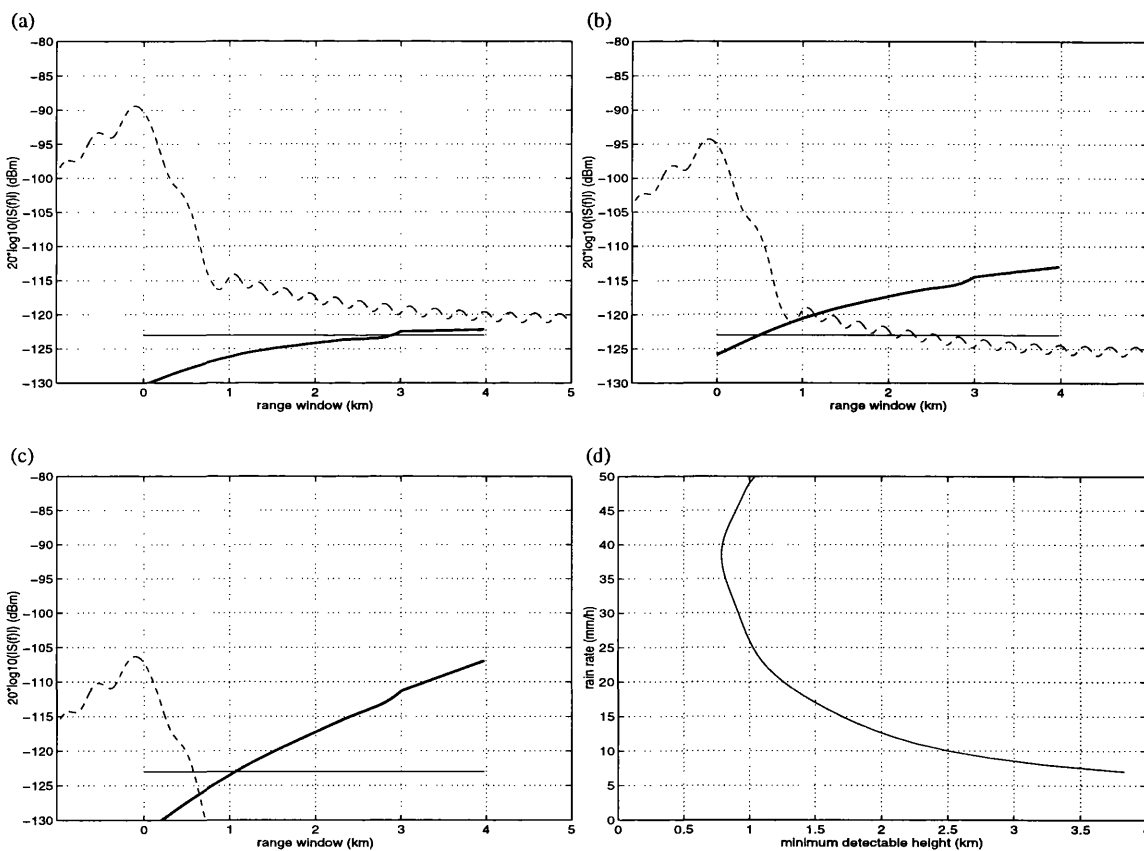


Figure 7.31. Ground clutter range sidelobe interference after amplitude (Hamming) and phase weighting schemes (4 km precipitation field) for low, medium and high rainfall rates: (a) 5 mm/h; (b) 20 mm/h; (c) 50 mm/h; (d) Minimum detectable height as a function of rain rate.

7.5.4 Ground Clutter Echo Cancellation

The cancellation of the surface return is an attractive technique to ^{be} investigated. Even if the cancellation is only successful up to a certain extent, the range sidelobe level specification could be reduced by a few dB. A ground clutter echo cancellation scheme has been proposed for the RA-2 rain mode [Zelli and Provvedi, 1995]. The scheme is based on the altimeter mode capabilities to locate accurately the position of the surface return in the range window. Assuming that the surface deramped echo consists of a sinusoidal tone of constant frequency, it could be possible to determine its amplitude and phase and therefore, its subtraction from the range window carried out.

However, the actual surface return cannot be exactly approximated by a sinusoidal tone of constant frequency. The ground echo shows a Doppler spread of 18 kHz corresponding to the values at the edges of the antenna footprint. A simulation has been carried out in order to study the effect of such Doppler spread on the deramped signal in the time domain, assuming a constant amplitude spectrum and a random phase over 18 kHz (Figure 7.32(a)). As a result of the previous hypothesis, a random amplitude modulation term is introduced in the surface deramped signal Figure 7.32(b), preventing accurate coherent subtraction.

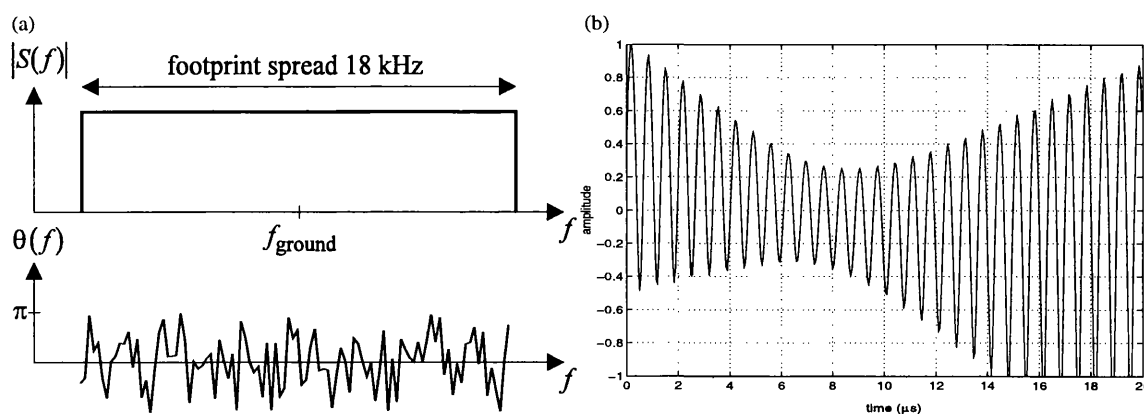


Figure 7.32. Ground echo cancellation: (a) Diagram; (b) Simulated surface full deramped signal.

Further investigation needs to be carried out in order to determine the feasibility of ground clutter echo cancellation. The option of non coherent cancellation seems to be preferable, once the impact of the system (antenna radiation pattern and reception filters) on the compressed pulse is determined.

7.6 References

- Amayenc P., Dou X., Kabeche A., Marzoug M., Tani T. and Testud J.: 'Impact of non Uniform Beam Filling on Rain Radar Algorithms'; Final Report, ESTEC Contract n° 10204/92/NL/NB(SC), June 1994.
- Awaka J.: 'Attenuation and Backscatter Properties of Bright-Band Computed at 13.8 GHz', *Proceedings of the International Symposium on Antennas and Propagation Japan*, pp. 1057-1060, 1992.
- Brennan L.E. and Reed I.S.: 'Theory of Adaptive Radar', *IEEE Trans. Aerospace and Electronic Systems*, Vol.AES-9, No.2, pp237-252, March 1973.
- Cook C.E., and Paolillo J.: 'A Pulse Compression Predistortion Function for Efficient Sidelobe Reduction in a High-Power Radar', *Proc. IEEE*, Vol.52, pp.377-389, 1964.
- Goldhirsh J. and Walsh E.J.: 'Rain Measurement from Space Using a Modified Seasat-Type Radar Altimeter', *IEEE Trans. Antennas & Propagation*, Vol.AP-30, No.4, pp.726-733, July 1982.
- Griffiths H.D. and Bradford W.J.: 'Digital Generation of High Time-Bandwidth Product Linear FM Waveforms for Radar Altimeters', *IEE Proc. F.*, Vol.139, No.2, pp.160-169, April 1992.
- Griffiths H.D. and Vinagre L.: 'Design of Low-Sidelobe Pulse Compression Waveforms', *Electronics Letters*, Vol.30, No.12, pp. 1004-1005, June 1994.
- Griffiths H.D., Zelli C., Vinagre L. and Levrini G.: 'Provision of a Rainfall Measuring Mode in a Satellite-Borne Radar Altimeter', *IEE Colloquium on Radar Meteorology*, February 1995.
- Harris F.: 'On the Use of Windows for Harmonic Analysis with the Discrete Fourier Transform', *Proc. IEEE*, Vol.66, No.1, pp.51-83, January 1978.
- Johnston J.A.: 'Digital Techniques in Pulse Compression Signals', Ph.D. thesis, University of Cambridge, 1983.

- Johnston J.A. and Fairhead A.C.: 'Waveform Design and Doppler Sensitivity Analysis for Nonlinear FM Chirp Pulses', *IEE Proceedings*, Vol.133, Pt. F, No.2, pp.163-175, April 1986.
- Key E.L., Fowle E.N. and Haggarty R.D.: 'A Method of Pulse Compression Employing Nonlinear Frequency Modulation', MIT Lincoln Laboratory Report 207, 1959.
- Meneghini R. and Kozi T.: 'Spaceborne Rain Radar', Norwood, MA: Artech House, Inc, 1990.
- Nakamura K., Okamoto K., Ihara T., Awaka J. and Kozi T.: 'Conceptual Design of Rain Radar for the Tropical Rainfall Measuring Mission', *International Journal of Satellite Communications*, Vol.8, pp.257-268, 1990.
- Probert-Jones J.R.: 'The Radar Equation in Meteorology', *Quart. J. Roy. Met. Soc.*, Vol.88, pp.485-495, 1962.
- Zelli C. and Provvedi F.: 'Ground Echo Cancellation', Alenia Spazio Technical Note WP50, RRO-ALS-TN-18, June 1995.

8 MACSIM: CLOUD PROFILING RADAR

The European Space Agency commissioned a Pre Phase A Study of a Millimetre wave Active Cloud Structure Imaging Mission (MACSIM, ESTEC Contract No. 11751/95/NL), in order to determine the feasibility of cloud measurements from space. It has been found that an amplitude modulated linear FM signal employed in NASA's ARMAR Mission meets the extremely stringent range sidelobe level requirement (-80 dB) at the expense of some signal-to-noise ratio loss and additional system complexity. A multiple look averaging processing over the specified range resolution of 500 m is required due to the fact that a very high time-bandwidth product is needed. A detailed loss balance is described in order to assess as realistically as possible the performance of the pulse compression design alternative. It has been found that signal decorrelation is not critical in the choice of the waveform parameter selection. The amplitude modulated linear FM signal is also capable of attaining the required measurement radiometric resolution accuracy.

8.1 Introduction

Cloud radar measurement from space is a more complex task than measuring rainfall, due mainly to very low reflectivities of some cloud types. The measured equivalent radar reflectivity is directly proportional to the cloud water liquid contents and provide information of the size distribution of cloud particles. An empirical relation between radar reflectivity and cloud water content is given by [Bartnoff and Atlas, 1951]:

$$Z = 2.58 \cdot 10^6 D_0^3 \frac{M}{\rho} \quad (1)$$

where D_0 is the median volume drop diameter, M the cloud liquid water content and ρ the mass density.

In a recent study for a millimetre wave Doppler pulsed radar [Lhermitte, 1989], three different system configurations were considered operating at 15, 35 and 94 GHz, giving similar sensitivities at the cloud top. However, cloud measurements at millimetre wavelengths offer the advantage of achieving the specified range resolution with significant smaller antenna sizes and lower peak power requirements, since radar reflectivities in the Rayleigh region depend on the fourth power of frequency.

However, cloud attenuation is more severe at high frequencies. Meneghini et al. [Meneghini and Koziu, 1990] describe how the attainable penetration depth is severely limited due to attenuation, and the minimum detectable reflectivity decreases below the cloud top (from -25 dBZ at cloud top to -15.4 dBZ at a penetration depth of 1 km for a liquid water content of 1 gm m^{-3} at 94 GHz). Penetration depths as a function of minimum detectable radar reflectivity for different types of clouds are shown in Figure 8.1 [Riegger et al., 1996], which shows that penetration depths improve for lower detectable reflectivities. Detection worst cases are given under clear air conditions, with cells containing clouds close to the minimum reflectivity range. A summary of the MACSIM radar system requirements is shown in Table 8.I.

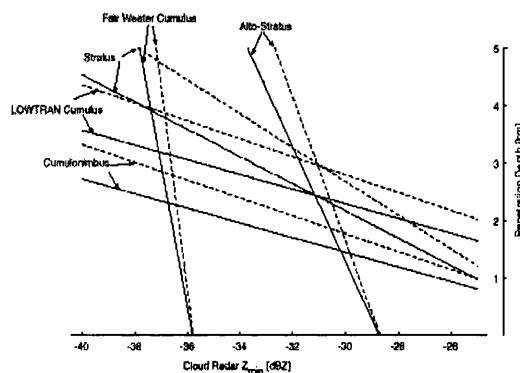


Figure 8.1. Penetration depth as a function of minimum detectable reflectivity and cloud type (solid 95 GHz, dashed 79 GHz). Reproduced from [Riegger et al., 1996].

Table 8.I: MACSIM system requirements

	<i>MACSIM</i>
orbit	near circular, 500 - 600 km
measurement geometry	along ground track (no scanning)
operational frequency	79 or 95 GHz
antenna footprint	1 km
range resolution	500 m
measurement range	0.25 - 20 km
integration range	30 km
maximum average power	300 W
maximum antenna size	2.5 m
maximum mass	250 kg
measurement reflectivity range	10^{-3} to $10^2 \text{ mm}^6/\text{m}^3$ (-30 to 20 dBZ)
measurement radiometric accuracy	1.7 dB
range sidelobe level requirement	-80 dB

8.2 MACSIM Waveform Design Alternatives

Two possible options of choice of waveform (unmodulated pulse and pulse compression frequency modulated signals) are described in this section. The unmodulated pulse alternative is limited in signal-to-noise ratio due to power restrictions on board the satellite. Pulse compression waveforms are capable of achieving better sensitivities than the unmodulated pulse alternative, although no modulation technique can meet the range sidelobe level specification at the time-bandwidth product imposed by the system range resolution.

8.2.1 Unmodulated Pulse Alternative

The unmodulated pulse alternative avoids the range sidelobe pattern corresponding to the ground return masking cloud information in range cells adjacent to the Earth's surface. Ground clutter can then be rejected by time gating. The required pulse length to attain the MACSIM specified range resolution Δr is given by:

$$T = \frac{2\Delta r}{c} \quad (2)$$

A range resolution of 500 m determines an unmodulated pulse length of 3.33 μ s. A signal bandwidth of 300 kHz is given by the inverse of the pulse width. Unfortunately, the fixed pulse width cannot be increased without degrading the range resolution. Hence, an increase in signal-to-noise ratio can only be achieved by increasing the pulse energy through an increase in the transmitter peak power, which is severely limited on board the satellite.

The single pulse sensitivity (calculated at ground level) is employed in order to compare the different system alternatives independently of cloud scenario [Girard et al., 1996]. The single pulse sensitivity is defined as the cloud radar reflectivity whose power return is equivalent to the system noise level ($SNR = 1$):

$$P_r(Z_{\min}) = P_n \quad (3)$$

The cloud return power P_r is given by (Eq. 2.8):

$$P_r = \frac{P_t \lambda^2 G^2 c T \theta_B \phi_B}{1024 \pi^2 \ln 2 r^2 L} \eta e^{-0.2 \ln 10 \int_{r'} \alpha_C dr} \quad (4)$$

where P_t is the transmitted power, λ the wavelength, G the antenna gain, c the propagation speed, T the pulse length, θ_B and ϕ_B the half-power beamwidths, η the cloud volumetric reflectivity, α_C the cloud attenuation coefficient, r the pulse volume range, r' the penetration depth and L the combined system losses.

The system noise power level is given by:

$$P_n = kT_{sys}B_nF \quad (5)$$

where k is Boltzmann's constant, T_{sys} the system noise temperature, B_n the equivalent noise bandwidth and F the receiver noise figure.

The relation between radar reflectivity η and the equivalent radar reflectivity Z_e (Eq. 2.10) is defined as:

$$Z_e = \frac{\lambda^4 \eta}{\pi^5 |K_w|^2} \quad (6)$$

where K_w is the refractive index of water. Disregarding the cloud attenuation term in order to make the single pulse sensitivity independent of the cloud scenario, and for a range equal to the satellite altitude, Eq. 8.4 can be rewritten as:

$$P_r = \frac{P_t G^2 c T \theta_B \phi_B \pi^3 |K_w|^2}{1024 \ln 2 h^2 L \lambda^2} Z_{\min} \quad (7)$$

Combining Eq. 8.5 and Eq. 8.7, the single pulse sensitivity can be expressed as:

$$Z_{\min} = \frac{1024 \ln 2 h^2 \lambda^2 k T_{sys} B_n F L}{P_t G^2 \pi^3 c T \theta_B \phi_B |K_w|^2} \quad (8)$$

MPBT [Girard et al., 1996] have calculated a single pulse sensitivity Z_{\min} of -14.1 dBZ for the MACSIM unmodulated pulse alternative. It is possible to achieve the specified minimum sensitivity of -30 dBZ through the available integration range of 30 km.

8.2.2 Pulse Compression Alternative

The pulse compression option allows ~~to (raise)~~ ^{the designer} the restriction in pulse length and thus to increase the signal energy (and consequently the *SNR*) through an increase in the transmitted signal duration. However, it must be ensured that any feasible frequency modulation or range sidelobe reduction technique gives a range sidelobe level pattern below -80 dB. The signal bandwidth is now determined by the range resolution Δr according to (Eq. 3.33):

$$B = \frac{c}{2\Delta r} \quad (9)$$

A range resolution of 500 m forces a signal bandwidth of 300 kHz. Assuming that the compression ratio is limited by a decorrelation time of 150 μs , the pulse length is fixed to 112 μs [Girard et al., 1996]. The effects of signal decorrelation on pulse compression are analysed later in this chapter (Section 8.4.2). The initial choice of compression ratio is thus of 33.6.

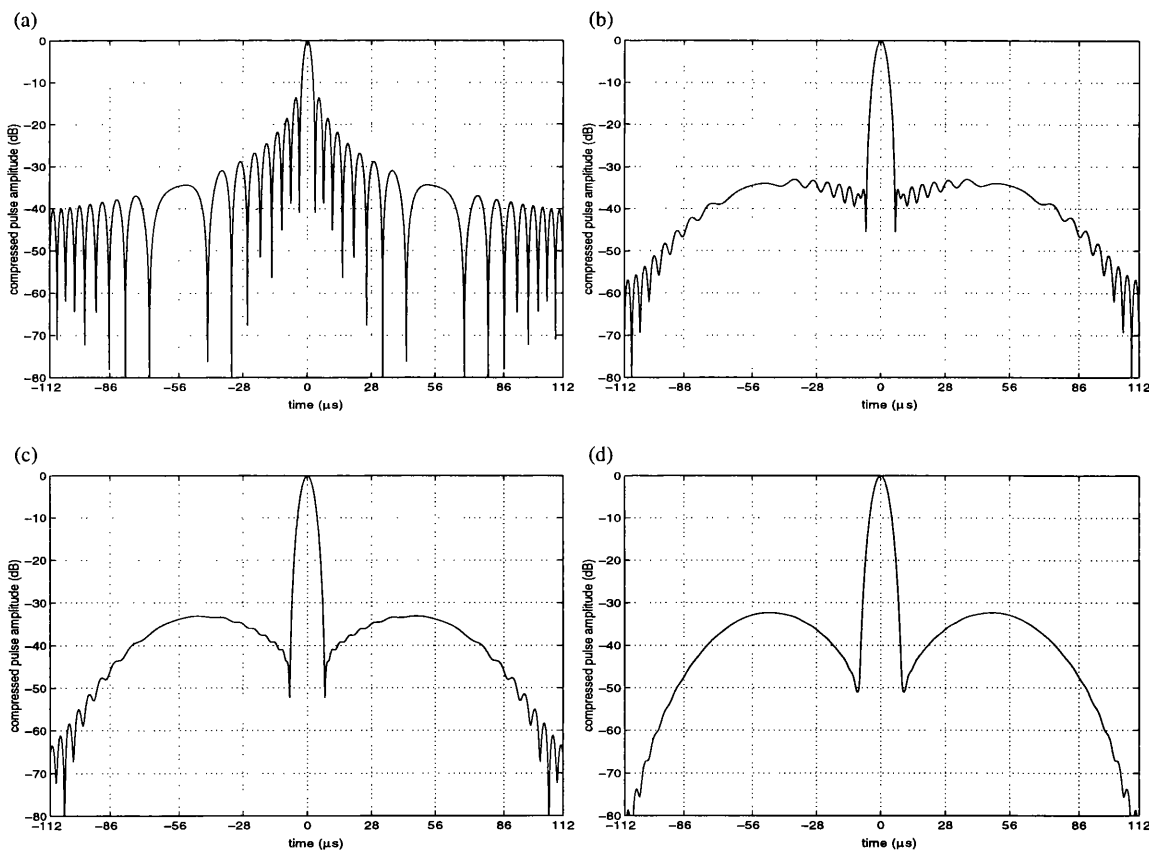


Figure 8.2. Linear FM compressed pulse ($BT = 33.6$) for different mismatching functions: (a) matched filter, $RSL = -13.6$ dB; (b) Hamming, $RSL = -33.0$ dB; (c) Dolph-Chebyshev, $RSL = -33.1$ dB; (d) minimum 3-term Blackman-Harris, $RSL = -32.3$ dB.

MPBT have calculated a single pulse sensitivity for the pulse compression alternative of -26.1 dBZ. Again, the minimum sensitivity of -30 dBZ can be achieved in the available integration range of 30 km, with a considerable decrease of the required number of samples, due to the lower single pulse sensitivity achievable compared to the unmodulated pulse option.

Unfortunately, it is not possible to reduce the range sidelobe level below -80 dB for such a low compression ratio. Figure 8.2 shows the compressed pulses for different amplitude mismatching functions applied to the matched filter (Section 4.1), giving similar range sidelobe levels below -30 dB.

Figure 8.3 shows the compressed pulses for a nonlinear FM signal (designed after [Johnston, 1983], Section 4.2) and a hybrid nonlinear FM system where the matched filter is mismatched with a Hamming function. No significant improvement in range sidelobe level is achieved compared to mismatched linear FM systems.

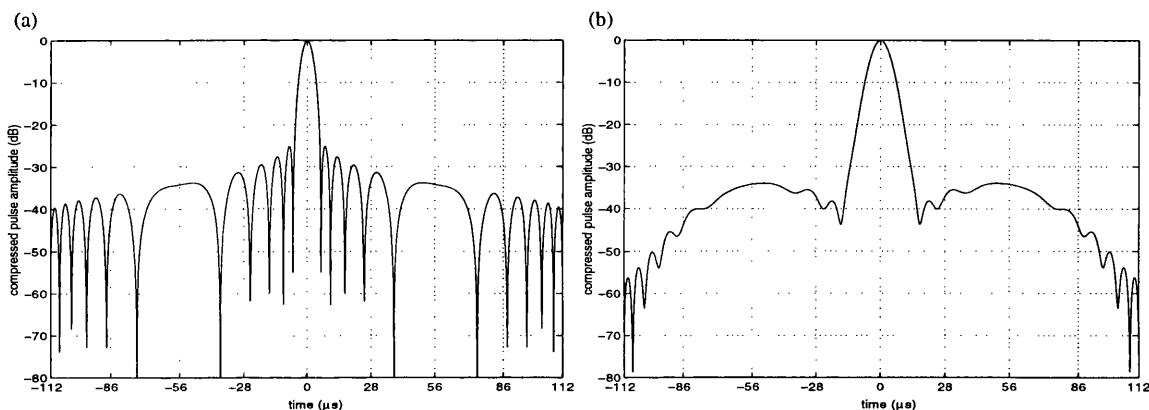


Figure 8.3. Nonlinear FM compressed pulse ($BT = 33.6$) for: (a) matched filter (after [Johnston, 1983]), $RSL = -25.0$ dB; (b) Hybrid (after [Johnston, 1983] and [Judd, 1973]), Hamming mismatching function, $RSL = -33.9$ dB.

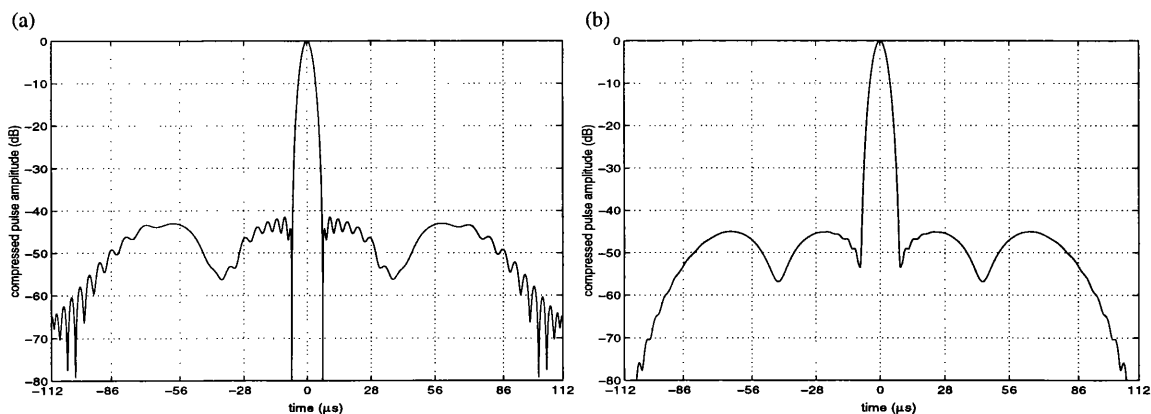


Figure 8.4. Predistorted linear FM compressed pulse ($BT = 33.6$) for: (a) Dolph-Chebyshev mismatching function, $RSL = -41.5$ dB; (b) Minimum 3-term Blackman-Harris mismatching function, $RSL = -45.0$ dB.

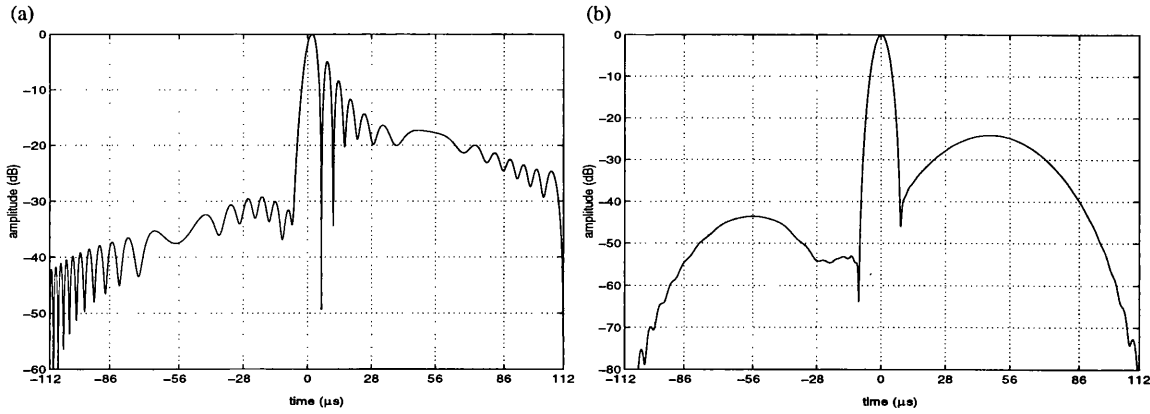


Figure 8.5. Asymmetric FM compressed pulse ($BT = 33.6$) for: (a) linear FM matched filter, $RSL = -29.2$ dB; (b) linear FM matched filter, minimum 3-term Blackman-Harris mismatching function, $RSL = -43.6$ dB.

Predistortion functions have been designed to be applied to mismatched linear FM systems. Figure 8.4 shows the predistorted linear FM compressed pulses for Dolph-Chebyshev and Blackman-Harris mismatching functions, giving range sidelobe patterns below -40 dB. Finally, asymmetric frequency modulations (shown in Figure 8.5) give a range sidelobe level of -43 dB.

In order to compare the performances of the different sidelobe reduction techniques considered (besides the range sidelobe level itself), two loss factors are being considered. The compressed pulse peak loss factor is defined as (Eq. 4.14):

$$L_p = \frac{|s_{0lfm}(0)|^2}{|s_0(0)|^2} \quad (10)$$

where $s_{0lfm}(t)$ is the linear FM compressed pulse and $s_0(t)$ a compressed pulse obtained for a given range sidelobe level reduction technique. A more realistic loss factor for distributed targets is defined as the compressed pulses energy ratio, given by (Eq. 4.15):

$$L_a = \frac{\int_{-2T}^{2T} |s_{0lfm}(t)|^2 dt}{\int_{-2T}^{2T} |s_0(t)|^2 dt} \quad (11)$$

A comparison between the different range sidelobe techniques considered in this section (mismatching, nonlinear FM, linear FM predistortion function and asymmetric FM) is shown in Table 8.II. The lowest sidelobe levels are achieved by a predistorted linear FM signal (-45.0 dB) and by an asymmetric frequency modulation (-43.3 dB). It is clear that a

much larger compression ratio is required to reduce the range sidelobe pattern of any modulation to the required -80 dB level.

Table 8.II: Range sidelobe level reduction techniques characteristics

	RSL	L_p	L_a	$\Delta\tau_{-3dB}$
linear FM	-13.6 dB	0.0 dB	0.0 dB	1.00
linear FM (Hamming)	-33.0 dB	5.3 dB	3.4 dB	1.48
linear FM (Dolph-Chebyshev)	-33.1 dB	6.4 dB	4.5 dB	1.65
linear FM (Blackman-Harris)	-32.3 dB	7.5 dB	5.0 dB	1.85
Nonlinear FM ¹	-25.0 dB	0.0 dB	-1.5 dB	1.50
Hybrid nonlinear FM ¹ (Hamming)	-33.9 dB	5.3 dB	1.6 dB	2.47
Predistorted linear FM (Dolph-Chebyshev)	-41.5 dB	6.4 dB	5.0 dB	1.46
Predistorted linear FM (Blackman-Harris)	-45.0 dB	7.5 dB	5.5 dB	1.67
Asymmetric FM	-29.2 dB	3.9 dB	0.6 dB	1.50
Asymmetric FM (Blackman-Harris)	-43.6 dB	7.4 dB	5.0 dB	1.87

8.3 High Time-Bandwidth Amplitude Modulated Pulse Compression

The existing pulse compression techniques are not capable of meeting the required range resolution and range sidelobe level requirement simultaneously. The required range sidelobe level is achieved through the modulation of the signal envelope. Unfortunately, an important signal bandwidth increase is required with an associated signal-to-noise ratio degradation, which can be compensated to some extent by carrying out a multiple look averaging processing over the user range resolution cell. A detailed comparison between the unmodulated pulse and the amplitude modulated pulse compression alternative performances in terms of single pulse sensitivity is presented at the end of this section.

8.3.1 ARMAR Mission

The ARMAR mission (Airborne Rain Mapping Radar, developed by the Jet Propulsion Laboratory) has been reported in the literature [Durdan et al., 1994]. The Mission was originally conceived to support and simulate the TRMM radar geometry in order to carry out airborne rainfall measurements. Although the TRMM radar employs

¹ [Johnston, 1983]

short unmodulated pulses, it was decided to implement pulse compression on the ARMAR system in provision of future space missions. The main features of the ARMAR radar are shown in Table 8.III.

Table 8.III: ARMAR system parameters

	<i>ARMAR</i>
frequency	18 GHz
horizontal resolution	800 m
range resolution	55 m
pulse width	5-45 μ s
bandwidth	4 MHz
transmitter power	200 W

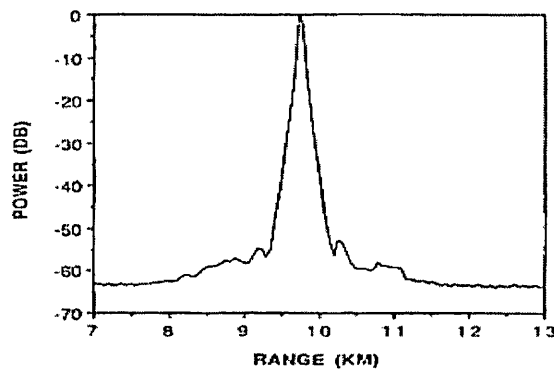


Figure 8.6. ARMAR point target response (average of 6000 compressed pulses from airborne measurements, $T = 20 \mu$ s). reproduced from [Durdin et al., 1994].

The ARMAR radar transmits an amplitude modulated linear FM signal, which prevents the high-power amplifier from working in its saturated region, where an optimum signal-to-noise ratio is achieved using a constant amplitude FM pulse. The reported *SNR* loss is of approximately 2 dB [Tanner et al., 1994], with a range resolution degradation from 35 to 55 m. The ARMAR weighting scheme achieves a range sidelobe level below -55 dB. Figure 8.6 shows the ARMAR point target response after averaging approximately 6000 reflection measurements from the ocean surface.

8.3.2 ARMAR Amplitude Modulation Scheme

The ARMAR amplitude modulation scheme is described to be ‘a raised half-wave sinusoidal function which varies from zero at the start of the chirp to one during the first

third of the chirp: $(1 - \cos\pi t/T)/2$, where T is one-third of the chirp length. The middle third of the chirp has constant amplitude of one, and the final third of the chirp is again multiplied by a raised half-wave sinusoid to vary smoothly from one to zero" [Tanner et al. 1994]. The amplitude modulation can be formulated as:

$$w_a(t) = \frac{1}{2} \text{rect}\left(\frac{t + \frac{2T}{3}}{\frac{T}{3}}\right) \left(1 - \sin\left(\frac{3\pi t}{T}\right)\right) + \text{rect}\left(\frac{t}{\frac{T}{3}}\right) + \frac{1}{2} \text{rect}\left(\frac{t - \frac{2T}{3}}{\frac{T}{3}}\right) \left(1 + \sin\left(\frac{3\pi t}{T}\right)\right) \quad (12)$$

where T is the pulse width. The ARMAR function is displayed in Figure 8.7(a). The ARMAR system point target response is then given by:

$$s_{0a}(\tau) = \frac{1}{T} \int_{-\infty}^{\infty} \text{rect}\left(\frac{t}{T}\right) \text{rect}\left(\frac{t-\tau}{T}\right) w_a(t) w_a(t-\tau) e^{j\pi \frac{B}{T} t^2} e^{-j\pi \frac{B}{T} (t-\tau)^2} dt \quad (13)$$

For convenience, the crosscorrelation between a linear FM signal amplitude modulated with the ARMAR function and a conjugated replica of itself $s_{0a}(\tau)$ will be referred as the ARMAR compressed pulse. A comparison between the linear FM and ARMAR compressed pulses (for a TB compliant with the MACSIM range resolution requirement) is shown in Figure 8.7(b). The ARMAR compressed pulse gives a peak range sidelobe level of approximately -18 dB, associated with a range resolution degradation factor (with respect to an unweighted linear FM) of 1.63, as shown in Table 8.IV.

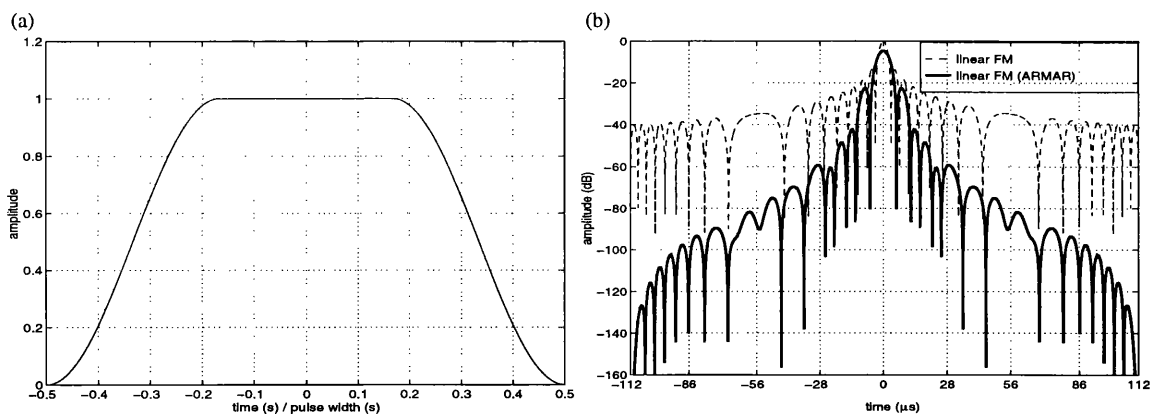


Figure 8.7. ARMAR signal: (a) Amplitude modulation scheme; (b) Comparison between linear FM and ARMAR compressed pulses ($TB = 33$).

Although both compressed pulses give a similar range sidelobe level, the ARMAR compressed pulse exhibits a much faster sidelobe decay rate. The amplitude modulated point target response gives an average energy loss of -2.8 dB. However, such loss is no

longer applicable to the ARMAR waveform since L_a is defined in order to measure the compressed pulse average energy loss when the matched filter is mismatched. For the ARMAR radar, both transmitted signal and reception filter are amplitude modulated with the same function, thus constituting a matched filter system. The optimum peak signal-to-noise ratio at the matched filter output is given by $2E/N_0$, where E is the transmitted waveform energy and N_0 the Gaussian noise spectral density. Thus, the ARMAR waveform SNR loss factor (with respect to a linear FM signal) needs to be redefined as the energy ratio between the transmitted signals.

Table 8.IV: Linear FM and ARMAR compressed pulse characteristics

	RSL	L_p	L_a	$\Delta\tau_{-3dB}$
linear FM	-13.6 dB	0.0 dB	0.0 dB	1.00
linear FM (ARMAR)	-17.9 dB	4.6 dB	2.8 dB	1.63

The signal energy ratio is equivalent to the energy ratio between the linear FM and ARMAR amplitude modulation functions, given by:

$$L_{SNR} = \frac{\int_T \left| \text{rect}\left(\frac{t}{T}\right) \right|^2 dt}{\int_T |w_a(t)|^2 dt} \quad (14)$$

The SNR loss factor for the ARMAR amplitude modulation function has been found to be of 2.3 dB, which is coherent with the loss reported in the literature.

8.3.3 Pulse Volume Multiple Look Averaging

In order to attain the specified range resolution of 500 m with pulse compression systems, a minimum bandwidth of 300 kHz is required. It has been shown that no range sidelobe reduction technique is capable of achieving a range sidelobe level of -80 dB for the specified range resolution. Therefore, a much larger time-bandwidth product is needed to comply with the range sidelobe level requirement. However, such a stringent specification seems to be far beyond current available pulse compression signal processing techniques, even for very high time-bandwidth products. Figure 8.8 shows an optimised predistorted linear FM compressed pulse ($T = 150 \mu\text{s}$, $B = 8 \text{ MHz}$), with an insufficient range sidelobe pattern below -72.5 dB.

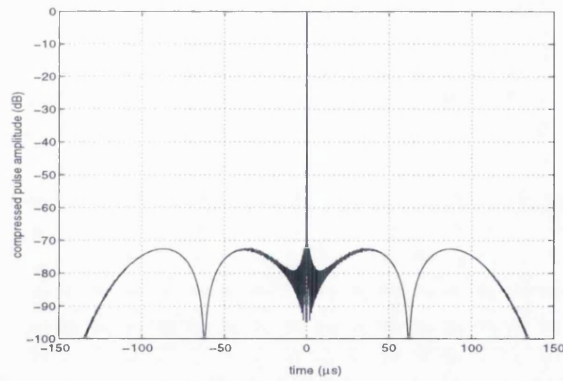


Figure 8.8. Predistorted linear FM compressed pulse ($TB = 1200$).

An additional problem of high time-bandwidth products is the decrease in signal-to-noise ratio due to the reduction of the range resolution for large signal bandwidths. Nevertheless, incoherent multiple look averaging may be carried out with a SNR gain of \sqrt{n} , where n is the number of samples in the original user resolution cell, given by:

$$n = \frac{\Delta r_0}{\Delta r_1} \quad (15)$$

where Δr_0 is the user resolution cell (500 m) and Δr_1 is the decreased range resolution due to an increase of signal bandwidth.

The fact that a blind layer Δr_{bl} of 250 m above the Earth's surface is allowed, combined with the multiple look averaging yields an adjustment of the range sidelobe specification requirement, in particular to the range sidelobe pattern of the compressed pulse (Figure 8.9). Range sidelobes in the interval $2\Delta r_{bl}/c$ do not need to be below -80 dB since they are disregarded before cloud parameter estimation is carried out. Furthermore, the averaging process only requires the mean range sidelobe level below -80 dB for a width of $2\Delta r_0/c$.

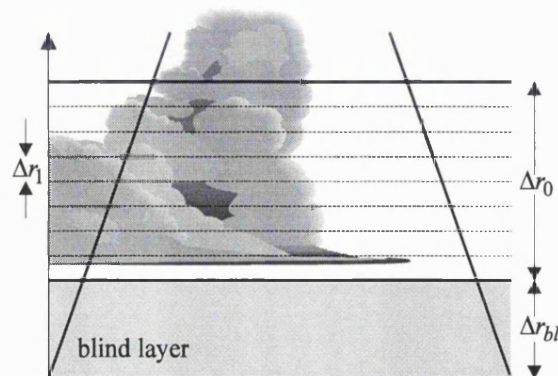


Figure 8.9. Multiple look averaging over the user range resolution cell diagram.

The average range sidelobe level is then redefined as:

$$ARSL = \frac{\int_{2\Delta r_0/c} |s_0(t)|^2 dt}{2\Delta r_0/c} / |s_0(0)|^2 \quad (16)$$

An average range sidelobe level of -80 dB can be attained over the user resolution cell Δr_0 (even though some range sidelobes are above such level in some of the Δr_1 region) without interfering cloud information during the multiple look averaging process. In particular, for compressed pulses with range sidelobe patterns which decrease monotonically (such as the ARMAR point target response), the first user resolution cell adjacent to the blind layer is the most critical one (Figure 8.10).

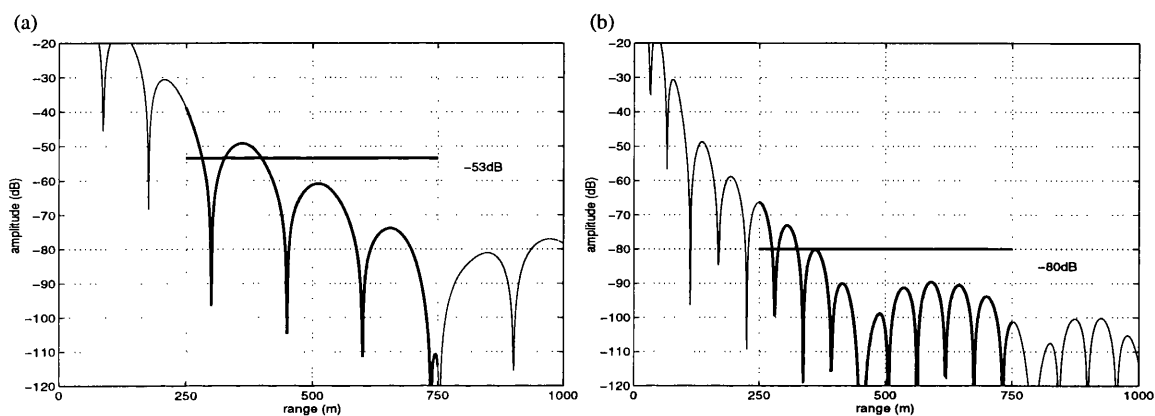


Figure 8.10. ARMAR compressed pulse average range sidelobe level over the first user resolution cell (500 m), for bandwidths of: (a) 3 MHz; (b) 8 MHz.

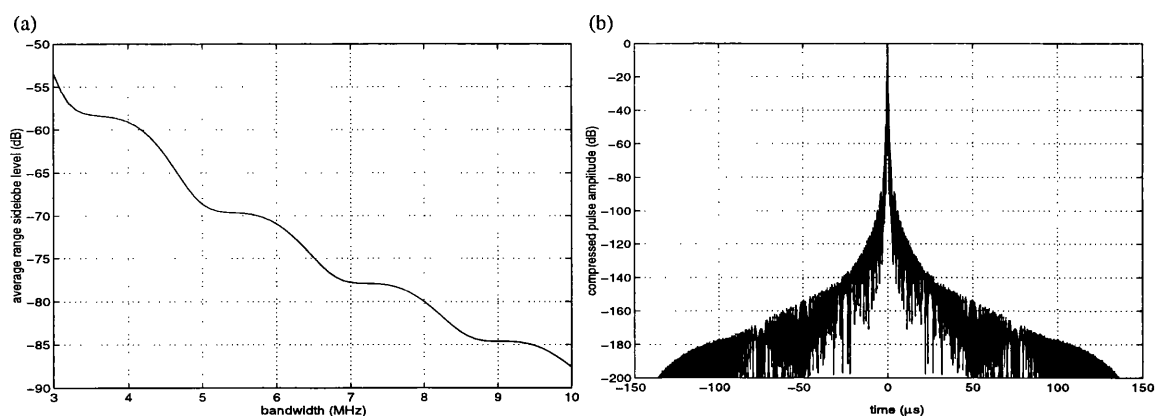


Figure 8.11. ARMAR compressed pulse: (a) Average range sidelobe level over a range of 500 m as a function of signal bandwidth; (b) $TB = 1200$, $ARSL = -80$ dB.

It becomes clear that an amplitude modulated linear FM signal is the most suitable candidate to achieve average range sidelobe levels below -80 dB over the first user range resolution cell, with the lowest possible time-bandwidth product. Unfortunately, for the

ARMAR amplitude modulated signal, it is not possible to reduce the range sidelobe level by increasing the pulse width (a scaled compressed pulse is obtained with the same range sidelobe level). Figure 8.11(a) shows the average range sidelobe level for the ARMAR compressed pulse as a function of signal bandwidth, which shows that a frequency modulation spanning over 8 MHz is required to meet the range sidelobe level specification of -80 dB (Figure 8.11(b)).

8.4 Amplitude Modulated Linear FM Signal Loss Factors

In order to determine a realistic single pulse sensitivity for the ARMAR amplitude modulated linear FM signal, a detailed analysis of the different loss sources is carried out. It is shown that signal decorrelation has no significant impact on linear FM waveforms due to their robustness to Doppler offsets. The multiple look averaging gain alleviates the signal-to-noise ratio loss, caused by the range resolution decrease in order to reduce the compressed range sidelobe pattern^{to} an appropriate level. It is shown that the unmodulated pulse and pulse compression alternatives give a very similar performance in terms of single pulse sensitivity. However, the signal width in the pulse compression option represents a degree of freedom in order to improve cloud detectability. ⊕ ?

8.4.1 Multiple Look Averaging Gain and Effective Compression Ratio

In order to calculate the multiple look averaging gain, the point target response due to amplitude modulation and Doppler decorrelation must be taken into account. The number of looks in the user range resolution cell can be calculated considering the range resolution being determined by the compressed pulse -3dB mainlobe width $\Delta\tau_{-3dB}$ (Figure 8.12(a)).

The -3dB width range resolution Δr_1 for a decorrelated ARMAR compressed pulse ($TB = 1200$) is of 33.3 m (equivalent to 0.2 μ s, Figure 8.12(b)). Hence, there are 16 available independent samples in the user range resolution cell Δr_0 for multiple look averaging processing. Since the averaging is carried out incoherently, the processing gives a gain factor \sqrt{n} of 6 dB.

The compression ratio for a linear FM compressed pulse is defined as:

$$\rho = TB \quad (17)$$

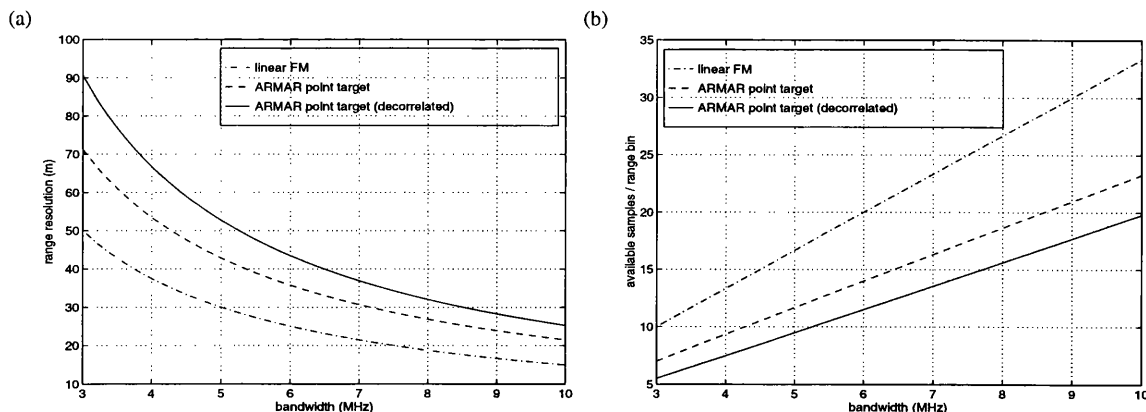


Figure 8.12. Multiple look averaging: (a) Compressed pulse -3dB width range resolution ($T = 150 \mu\text{s}$) for linear FM, ARMAR and decorrelated ARMAR signals as a function of bandwidth; (b) Available number of looks over a range of 500 m for linear FM, ARMAR and decorrelated ARMAR signals as a function of bandwidth.

Since for the decorrelated ARMAR point target response, the inverse of the bandwidth is no longer comparable with the -3 dB mainlobe width, an effective compression ratio is defined as:

$$\rho_{eff} = \frac{T}{\Delta\tau_{-3dB}} \quad (18)$$

An effective compression ratio of 681 will be considered for the ARMAR compressed pulse single pulse sensitivity balance.

8.4.2 Signal Decorrelation Loss

The meteorological return signal is subject to decorrelation due to radar platform motion. Decorrelation introduces conflicting requirements on the transmitted pulse width. On one hand, the duration of the signal width must be adequately long to guarantee sufficient illumination of the pulse volume (and thus enough signal-to-noise ratio). On the other hand, pulse compression decorrelation losses increase as a function of pulse width. It is shown in this section that linear FM decorrelation losses are not critical in the case of distributed targets and are virtually independent of signal width.

It is a general assumption that successive samples are uncorelated when the correlation coefficient $\rho(\tau)$ is smaller than 0.01, which limits the minimum length of the interpulse period (or PRF). The decorrelation time τ_d between samples is given by [Meneghini and Kozu, 1990]:

$$\tau_d = 0.57 \frac{\lambda}{v_{\text{sat}} \theta_B} \quad (19)$$

where λ is the wavelength, v_{sat} the satellite speed and θ_B the antenna beamwidth (Gaussian antenna pattern). A frequency of 95 GHz yields a decorrelation time of 150 μs . Considering a Gaussian Doppler frequency spectrum [Atlas, 1964], the correlation coefficient can be expressed as:

$$\rho(\tau) = e^{-(2\pi\sigma\tau)^2} \quad (20)$$

where the standard deviation is given by:

$$\sigma = 0.34 \frac{1}{\tau_d} \quad (21)$$

Decorrelation effects on pulse compression have been studied [Gary and Farley, 1973] for ionospheric and middle atmospheric measurements using binary Barker codes. The study showed that signal decorrelation effects are less severe for transmitted pulse widths smaller than the signal decorrelation time. In theory, in order to minimise pulse compression decorrelation losses the transmitted pulse width should not exceed a length of 150 μs .

The point target response of a pulse compression system for stationary targets is given by the crosscorrelation between the transmitted signal $\tilde{s}(t)$ (expressed as its complex envelope) and its matched filter (a conjugated replica of the transmitted waveform). The stationary point target response hypothesis can no longer be applied to meteorological targets, since the return signal is composed of the contributions of all the hydrometeors in the pulse volume. Thus, the return signal is considered to be the product of the transmitted signal and a scattering fluctuation term $v(t)$. Therefore, the output of the matched filter $s_0(\tau)$ is then given by:

$$s_0(\tau) = \int_{-\infty}^{\infty} (\tilde{s}(t)v(t))\tilde{s}^*(t-\tau)dt \quad (22)$$

For incoherently distributed targets in the pulse volume the product $\tilde{s}(t)v(t)$ is a random process, and the compressed pulse needs to be treated as the ensemble average of the instantaneous power of $s_0(\tau)$ (according to the formulation by Kozu, [Kozu, 1991]):

$$\langle |\tilde{s}_0(\tau)|^2 \rangle = \int_{-\infty}^{\infty} \int_{-\infty}^{\infty} \tilde{s}(t) \tilde{s}^*(t-\tau) \langle v(t) v^*(t+\xi) \rangle \tilde{s}^*(t+\xi) \tilde{s}(t-\tau+\xi) dt d\xi \quad (23)$$

which can be transformed into:

$$\langle |\tilde{s}_0(\tau)|^2 \rangle = \int_{-\infty}^{\infty} \rho(\xi) |\tilde{s}_0^1(\tau, \xi)|^2 d\xi \quad (24)$$

where:

$$\rho(t) = \langle v(t) v^*(t+\tau) \rangle \quad (25)$$

$$|\tilde{s}_0^1(\tau, \xi)|^2 = \int_{-\infty}^{\infty} \tilde{s}(t) \tilde{s}^*(t-\tau) \tilde{s}(t+\xi) \tilde{s}^*(t-\tau+\xi) dt \quad (26)$$

The first term $\rho(t)$ is the autocorrelation function of the fluctuation and $\tilde{s}_0^1(t, \tau)$ the autocorrelation function of $\tilde{s}(t)$ (corresponding to the non decorrelated linear FM compressed pulse). The ensemble average can also be calculated in the frequency domain:

$$\langle |\tilde{s}_0(\tau)|^2 \rangle = \int_{-\infty}^{\infty} \sigma(f) |\chi(\tau, f)|^2 df \quad (27)$$

where $\sigma(f)$ and $\chi(t, f)$ are the Fourier transform of the autocorrelation function and the signal ambiguity function respectively, and given by:

$$\sigma(f) = \int_{-\infty}^{\infty} \rho(t) e^{-j2\pi ft} dt \quad (28)$$

$$\chi(t, \nu) = \int_{-\infty}^{\infty} \tilde{s}(\tau) \tilde{s}^*(\tau-t) e^{-j2\pi \nu \tau} d\tau \quad (29)$$

The decorrelation losses have been calculated for a linear FM modulated signal. For the Gaussian spectrum approximation of the fluctuation (Eq. 8.20), the Fourier transform of the correlation function is given by:

$$\sigma(w) = \frac{1}{2\sqrt{\pi}\sigma} e^{-\left(\frac{f}{2\sigma}\right)^2} \quad (30)$$

Therefore, inserting Eq. 8.29 and Eq. 8.30 into Eq. 8.27, the ensemble average of the instantaneous power of $s_0(\tau)$ for a linear FM signal is given by:

$$\langle |\tilde{s}_0(\tau)|^2 \rangle = \frac{1}{2\sqrt{\pi}\sigma} \left(1 - \frac{|\tau|}{T}\right)^2 \int_{-\infty}^{\infty} e^{-\left(\frac{f}{2\sigma}\right)^2} \left| \text{sinc} \left((B\tau + Tf) \left(1 - \frac{|\tau|}{T}\right) \right) \right|^2 df \quad (31)$$

closed form analytical expression

Unfortunately, a closed expression for Eq. 8.31 cannot be found, and it needs to be solved numerically. The ensemble average of a linear FM compressed pulses instantaneous power for different pulse widths is shown in Figure 8.13. Associated effects of compressed pulse decorrelation are peak losses, mainlobe broadening (range resolution degradation) and range sidelobe pattern smearing. Two loss factors are then defined, the decorrelation main peak loss L_{pd} and the decorrelation average loss L_{ad} , given by:

$$L_{pd} = \frac{|s_0(0)|^2}{\langle |s_0(0)|^2 \rangle} \quad (32)$$

$$L_{ad} = \frac{\int_{2T} |s_0(t)|^2 dt}{\int_{2T} \langle |s_0(t)|^2 \rangle dt} \quad (33)$$

The main peak loss L_{pd} is not significant for distributed targets, being the average decorrelation loss L_{ad} a more realistic measurement of the actual decorrelation loss. Both loss factors for linear FM signals of different pulse widths are listed in Table 8.V.

The decorrelated compressed pulse mainlobe level decreases as a function of pulse width (especially above the decorrelation time), but there is no average loss due to decorrelation for linear FM signals (Figure 8.14(a)). It should be noted that the original study [Gary and Farley, 1973] employed Barker coded pulses, which give worse Doppler tolerance than linear FM signals. It has been found that the average decorrelation loss is independent of signal bandwidth. As it will be established later in this chapter, when the linear FM matched filter is mismatched in amplitude, the ensemble average of the instantaneous power of the compressed pulse gives a constant average decorrelation loss factor L_{ad} , which in most cases is equivalent to the average weighting loss L_a . In order not to take into account the same loss twice in the total loss budget, the global decorrelation loss for distributed targets is defined as:

$$L_d = \frac{L_a}{L_{ad}} \quad (34)$$

or in the case of amplitude modulated matched filter systems (ARMAR):

$$L_d = \frac{L_{SNR}}{L_{ad}} \quad (35)$$

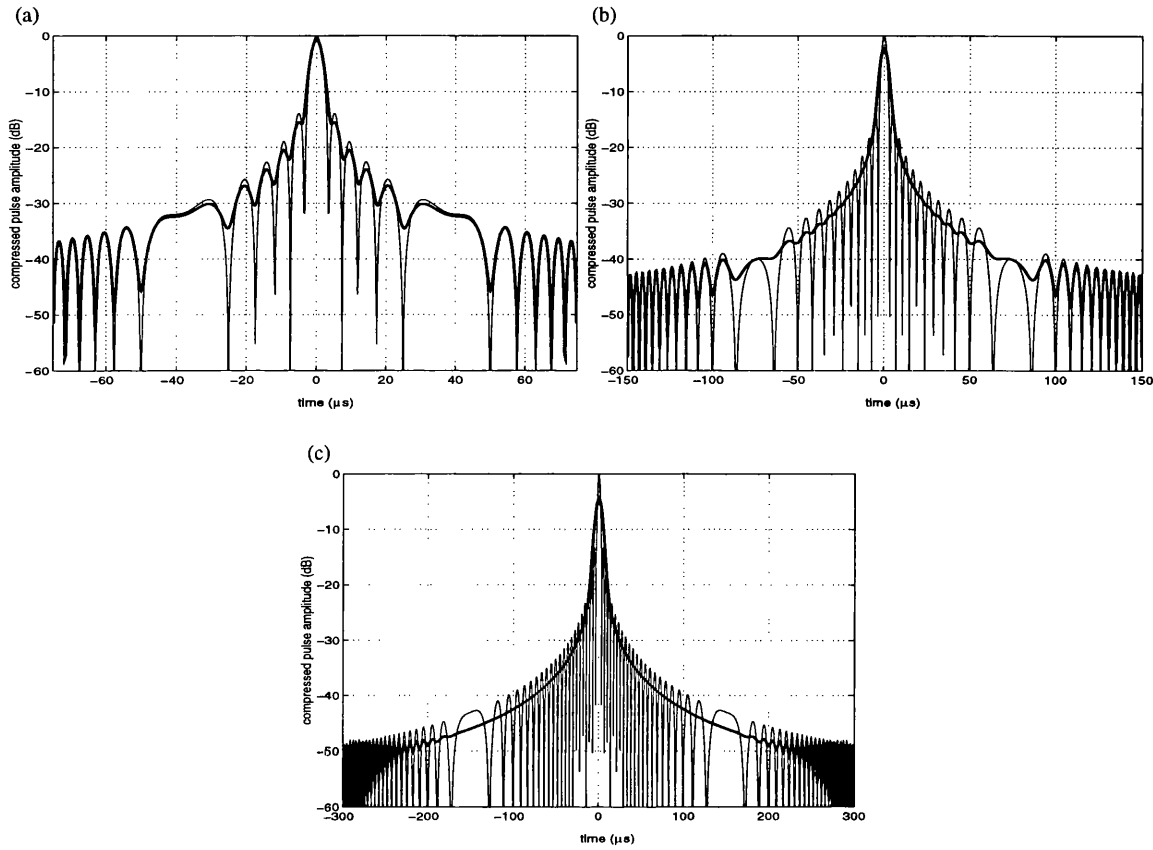


Figure 8.13. Ensemble average of linear FM compressed pulse instantaneous power ($B = 300$ kHz, $\tau_d = 150 \mu\text{s}$) for pulse widths of: (a) $T = 75 \mu\text{s}$; (b) $T = 150 \mu\text{s}$; (c) $T = 300 \mu\text{s}$.

Table 8.V: Linear FM decorrelation losses ($\tau_d = 150 \mu\text{s}$)

<i>pulse width</i>	L_{pd}	L_{ad}
75 μs	-0.7 dB	0 dB
150 μs	-2.1 dB	0 dB
300 μs	-4.4 dB	0 dB

The decorrelation losses for the ARMAR amplitude modulated linear FM signal for a decorrelation time of $150 \mu\text{s}$ as a function of signal width are shown in Figure 8.14(b). As in the case of a rectangular envelope linear FM signal, the average decorrelation loss is has found to be constant and independent of signal width. The decorrelation loss L_d for the ARMAR compressed pulse is considered to be 2.4 dB (Table 8.VI). The decorrelated ARMAR compressed pulse for a time-bandwidth product of 1200 is shown in Figure 8.15.

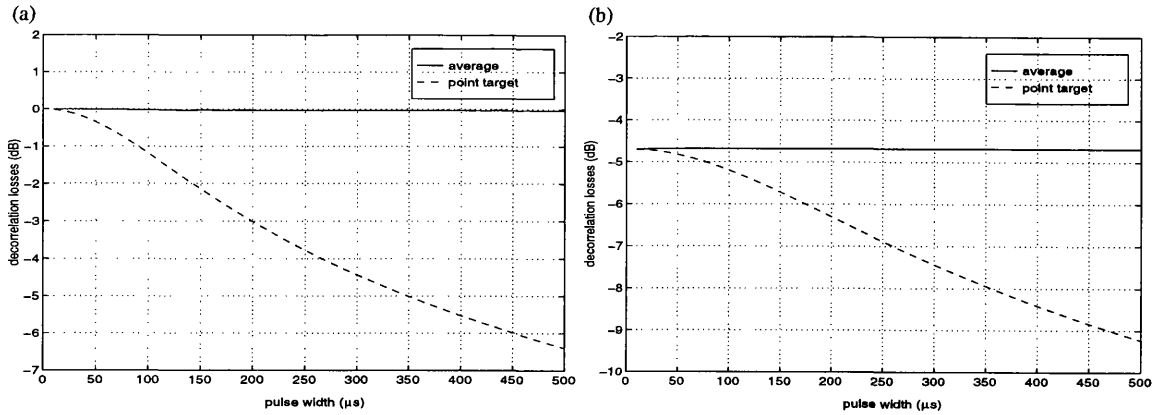


Figure 8.14. Decorrelation losses L_{pd} and L_{ad} as a function of pulse width (decorrelation time τ_d of 150 μ s) for: (a) linear FM signal; (b) ARMAR amplitude modulated linear FM signal².

Table 8.VI: ARMAR amplitude modulated linear FM decorrelation losses ($\tau_d = 150 \mu$ s)

Pulse width	L_{pd}	L_{ad}	L_d
75 μ s	-4.9 dB	-4.7 dB	-2.4 dB
150 μ s	-5.7 dB	-4.7 dB	-2.4 dB
300 μ s	-7.4 dB	-4.7 dB	-2.4 dB

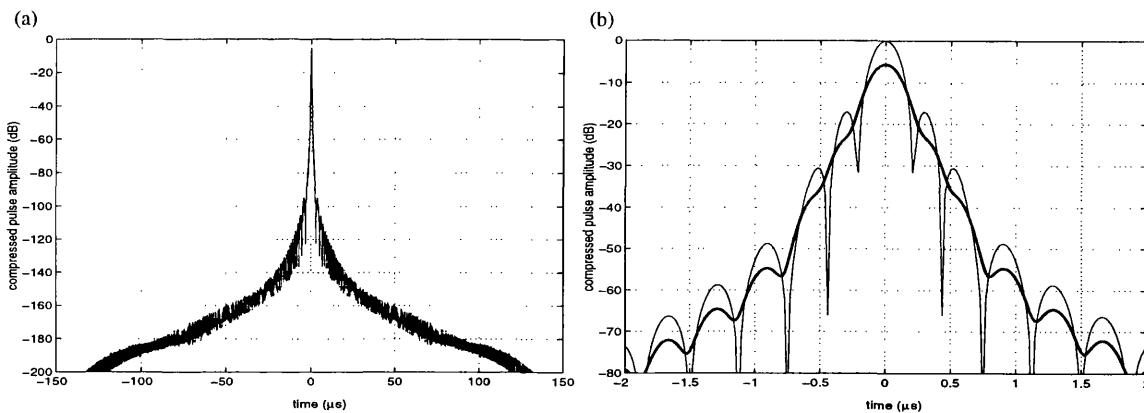


Figure 8.15. Ensemble average of ARMAR amplitude modulated linear FM compressed pulses instantaneous power ($\tau_d = 150 \mu$ s): (a) $TB = 1200$; (b) $TB = 1200$, detail (dashed line shows the non decorrelated compressed pulse).

It can be concluded that continuous frequency modulated signal decorrelation losses for distributed targets are independent of pulse width (even when the transmitted signal length is longer than the fluctuation decorrelation time) and can be only accounted for when the filter in reception is mismatched and the compressed pulse energy loss is not equal to its ensemble average loss.

² It is considered that the signal decorrelation loss L_d for amplitude modulated signals is L_{SNR}/L_{ad}

8.4.3 Finite Bandwidth Loss

Nathanson [Nathanson, 1972] described how the Probert-Jones meteorological radar equation, although sorting out the inconsistencies between predicted and measured rainfall reflectivities, still overestimated the rainfall return by an average of 1.4 dB. It was shown that such power excess could be accounted for due to an overestimation of the range resolution volume. The shape of the receiver video output response was approximated to be equivalent to that of the transmitted waveform (constant amplitude over the duration of the pulse width) while in fact it represents a '*range weighting function*' that applies to the contributions in the pulse volume reducing the extent of the integration width. Nathanson calculated a system loss of 1.8 dB for the case of a matched filter to a rectangular envelope pulse.

Doviak et al [Doviak and Zrnica, 1993] defined the dependency between the range weighting function $W(r)$ and the transmitted signal envelope as:

$$\left| W\left(\frac{ct}{2}\right) \right|^2 = \left| \int_{\Delta r} h\left(r' - \frac{ct}{2}\right) e(r') dr' \right|^2 \quad (36)$$

where $e(r)$ is the waveform envelope and $h(r)$ is the envelope of the receiver filter impulse response, both expressed as a function of range. The effect of the range weighting function was defined as a loss factor L_r in terms of a finite bandwidth loss, given by:

$$L_r = \frac{cT/2}{\int_0^\infty |W(r)|^2 dr} \quad (37)$$

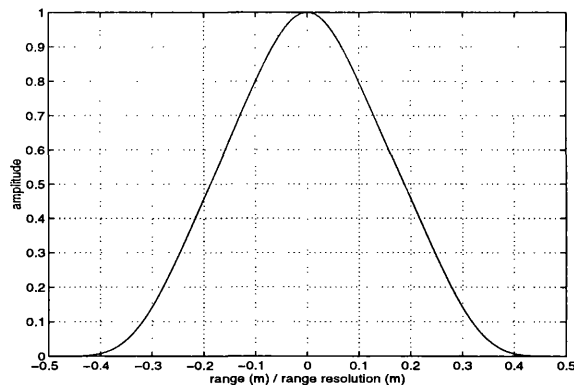


Figure 8.16. ARMAR amplitude modulation range weighting function.

The integral of $|W(r)|^2$ is equivalent to $cT/2$ for a receiver filter with an infinite

bandwidth response. Doviak et al. calculated a finite bandwidth loss of 2.3 dB for an approximation of the receiver impulse response of the form of a $\text{sinc}(x)$ function by a Gaussian function over a bandwidth of $1/T$. Figure 8.16 shows the range weighting function for the ARMAR amplitude modulation. It has been established that the finite bandwidth loss L_r is significantly higher than in the two previous reported cases (since the amplitude modulation function affects twice the range weighting function), and it is equivalent to 7.3 dB.

8.4.4 ARMAR Single Pulse Sensitivity Balance

The single pulse sensitivity gives an adequate comparison between the performances of the unmodulated pulse and pulse compression alternatives. As it has been shown throughout this section, the different alternative signal characteristics introduce significant changes in some of the parameters which may cause additional loss factors. In order to calculate the single pulse sensitivity for the ARMAR amplitude modulated linear FM signal, the following corrections to Eq. 8.22 need to be made.

- The fact that pulse compression is ^{Time duration} capable of achieving the desired range resolution with a significantly larger signal width than in the unmodulated pulse option allows to increase the signal energy without degrading the range resolution. Therefore, the transmitted power is considered to be increased by a factor equivalent to the compression ratio ρ .
- The theoretical linear FM compressed pulse width ($1/B$) is degraded by the amplitude modulation function and signal decorrelation. In principle, the decorrelated ARMAR compressed pulse width is defined to be at its mainlobe -3 dB width, being the correction factor the effective compression ratio ρ_{eff} described in Section 4.4.1.
- The range resolution in pulse compression systems is achieved by the introduction of frequency modulation, making the signal bandwidth independent of its duration. The correction factor is given by the ratio between the modulated signal bandwidth and the inverse of the unmodulated pulse width.
- The ARMAR amplitude modulation function SNR loss L_{SNR} is introduced.
- The signal decorrelation loss L_d for the ARMAR compressed pulse described in

Section 4.4.2 is introduced. It should be noted that the way that such a loss is defined reflects the fact that both signal and matched filter are amplitude modulated.

- The finite bandwidth loss balance between a rectangular envelope matched filter and the ARMAR amplitude weighted linear FM signal is taken into account.
- Due to the stringent range sidelobe requirement, the signal bandwidth needs to be increased significantly, thus reducing the desired range resolution below the system specification. Incoherent multiple look averaging over the user range resolution cell produces a gain given by \sqrt{n} .

A summary of the single pulse sensitivity balance between an unmodulated pulse and the ARMAR amplitude modulated linear FM signal is shown in Table 8.VII. It has been found that the ARMAR compressed pulse ($TB = 1200$) would give an almost equivalent performance in terms of single pulse sensitivity as the unmodulated pulse alternative.

Table 8.VII. ARMAR pulse compression and unmodulated alternative single pulse sensitivities

	<i>ARMAR</i>	<i>unmodulated pulse</i>	<i>balance</i>
transmitted power	ρP_0^3	P_0	30.8 dB
pulse width	T / ρ_{eff}^4	T	-11.8 dB
bandwidth	B	$1 / T$	-14.2 dB
SNR loss (L_{SNR})	2.3 dB		-2.3 dB
decorrelation loss (L_d)	2.4 dB		-2.4 dB
finite bandwidth loss (L_r)	7.3 dB	1.8 dB	-5.5 dB
multiple look averaging gain (\sqrt{n})	6.0 dB		6.0 dB
			<u>0.6 dB</u>

It becomes obvious that the range sidelobe requirement of -80 dB constrains the pulse compression system design, since it is necessary to incorporate additional significant complexity (amplitude modulation and multiple look averaging processing) with little benefit in terms of single pulse sensitivity. However, and since it has been determined that the signal decorrelation loss is constant above the decorrelation time, it could be possible to improve the pulse compression alternative single pulse sensitivity by increasing the signal width. It will be shown in the following section that the pulse compression

³Effective transmitted power is $\rho P_0 / L_{SNR}$.

⁴ ρ_{eff} considers range resolution degradation due to amplitude modulation and decorrelation.

alternative can achieve a better performance than the unmodulated pulse option in terms of radiometric resolution taking advantage of the allowed 30 km integration range.

8.5 Radiometric Resolution

The receiver of the MACSIM system (pulse compression alternative, [Riegger et al., 1996]) estimates the volumetric reflectivity through a short term average of the output of a square law detector after the matched filter. One of the system requirements is that the cloud reflectivity must be estimated within an accuracy of 33% (1.7 dB).

The system radiometric resolution is defined as the ratio between the standard deviation of the estimated cloud volumetric reflectivity $\hat{\eta}$ and its true value η [Fischer, 1972]:

$$K_p = \frac{\sqrt{\text{var}(\hat{\eta})}}{\eta} \quad (38)$$

The radiometric resolution for the MACSIM receiver can be approximated [Riegger et al., 1996] by:

$$K_p = \sqrt{\frac{1}{m} \frac{1}{n} \left(1 + \frac{1}{\text{SNR}}\right)^2} \quad (39)$$

where m is the number of samples available during the integration length and n represents the number of samples for the multiple look averaging processing, which is now redefined as:

$$n = \frac{\tau_w}{2\Delta r/c} \quad (40)$$

where τ_w is the compressed pulse correlation width, which is defined as:

$$\tau_w = 2 \int_0^{2\Delta r/c} \left(1 - \frac{\tau}{2\Delta r/c}\right) \frac{\left(P_r(R_s(t) * R_h(t)) + N_0 R_h(t)\right)^2}{\left(P_r(R_s(t) * R_h(t)) + N_0 R_h(t)\right)^2} \Big|_{t=0} dt \quad (41)$$

where $R_s(t)$ and $R_h(t)$ are the autocorrelation functions of the transmitted signal and the reception filter respectively. It was described in Section 4.4.1 that the number of multiple samples available for the multiple look averaging was determined by the -3 dB compressed pulse width independently of SNR . It is considered that the correlation width, although of similar magnitude of τ_{-3dB} , is a more appropriate measurement to determine the number of samples available in the user range resolution cell.

It has been established that the correlation width for the ARMAR amplitude modulated linear FM signal is independent of the transmitted signal pulse width and shows very little variation as a function of signal-to-noise ratio. Figure 8.17 shows the correlation width as a function of bandwidth and signal-to-noise ratio. For a time-bandwidth product of 1200 and a SNR of 1, the correlation width is equivalent to $0.25 \mu s$, which yields an effective compression ratio ρ_{eff} of approximately 600 and 13 available samples in the user range resolution cell for the multiple look averaging processing (5.5 dB gain).

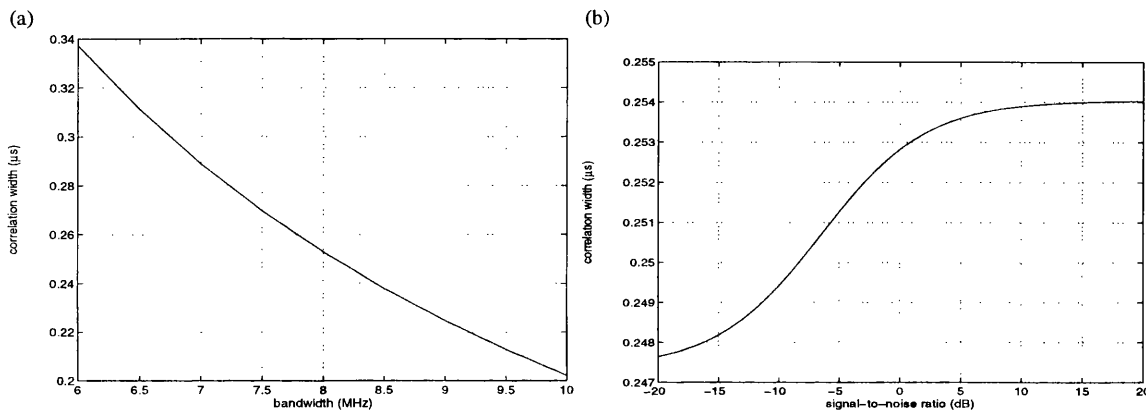


Figure 8.17. Correlation width τ_w for the ARMAR amplitude modulated linear FM signal as a function of: (a) bandwidth; (b) signal-to-noise ratio.

As it was pointed out in the previous section, it is expected to obtain a better single pulse sensitivity for longer transmitted waveforms. Figure 8.18 shows the improvement in performance in terms of relative single pulse sensitivity ΔZ_{min} for the pulse alternative, taking the previous correlation width calculations into account. The single pulse sensitivity for a transmitted signal width of $500 \mu s$ ($TB = 4000$) is -25.3 dB.

Although high cloud reflectivities give a better radiometric resolution accuracy, the waveform parameter selection must ensure that the radiometric resolution is optimum for the minimum sensitivity of -30 dBZ. The performance of both system design alternatives is now compared in terms of the radiometric resolution (which is required to give an accuracy lower than 33%). The ratio between radiometric resolutions for both alternatives ΔK_p is given by:

$$\Delta K_p = \frac{\sqrt{\frac{1}{m_u} \frac{\tau_{w_u}}{2\Delta r/c} \left(1 + \frac{1}{SNR_u}\right)^2}}{\sqrt{\frac{1}{m_c} \frac{\tau_{w_c}}{2\Delta r/c} \left(1 + \frac{1}{SNR_c}\right)^2}} = \sqrt{\frac{PRF_c}{PRF_u} \frac{1}{\tau_{w_c}} \frac{\left(1 + \frac{1}{SNR_u}\right)^2}{\left(1 + \frac{1}{SNR_c}\right)^2}} \quad (42)$$

where the suffixes u and c represent the unmodulated pulse and pulse compression options respectively. The unmodulated pulse alternative pulse repetition frequency has been designed to have a value of 3848 Hz [Girard et al., 1996].

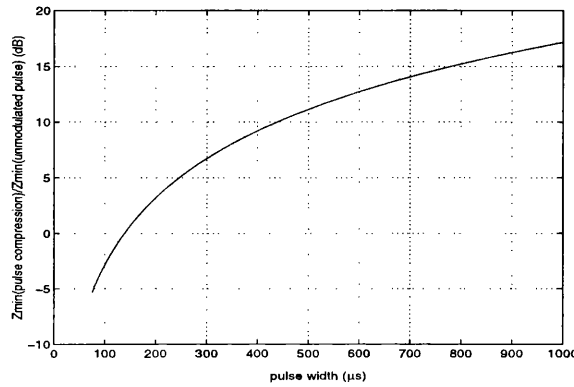


Figure 8.18. ΔZ_{\min} for pulse compression and unmodulated pulse alternatives as a function of signal width ($SNR = 1$)

For the pulse compression alternative, the pulse repetition frequency is calculated in order to maintain a constant average power of 200 W:

$$PRF_c = \frac{P_{av} \eta_{dc}}{P_0 T_c} \quad (43)$$

where P_{av} is the available average power, P_0 the available transmitter peak power, η_{dc} the DC conversion efficiency (20 %) and T_c the transmitted pulse length.

Figure 8.19 shows the radiometric resolution ratio for both design alternatives as a function of signal width ($B = 8$ MHz). The unmodulated pulse gives better radiometric resolutions ($\Delta K_p < 1$) for short frequency modulated signal widths. The performance of the pulse compression option increases significantly as the pulse length is increased due to a significantly better signal-to-noise ratio for weak cloud reflectivities. The optimum signal widths in terms of radiometric resolutions for different radiometric resolutions are summarised in Table 8.VIII. Lower reflectivities than -20 dBZ impose severe demands on the signal width, although it seems feasible that the -30 dBZ reflectivity requirement can be achieved with a pulse width in the range between $200 \mu s < T < 500 \mu s$. Absolute

radiometric resolutions for an ARMAR amplitude modulated linear FM signal as a function of signal width for different cloud reflectivities are shown in Figure 8.20.

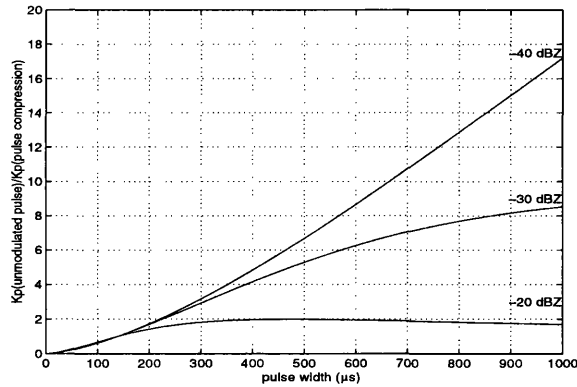


Figure 8.19. ΔK_p for pulse compression and unmodulated pulse alternatives as a function of signal width for different cloud volume reflectivities.

Table 8.VIII. Optimum ΔK_p pulse compression signal width selection

Z	T	ΔK_p	PRF
-10 dBZ	150 μ s	1.0	266 Hz
-20 dBZ	470 μ s	2.0	85 Hz
-30 dBZ	1495 μ s	9.1	26 Hz
-40 dBZ	4725 μ s	50.1	8 Hz

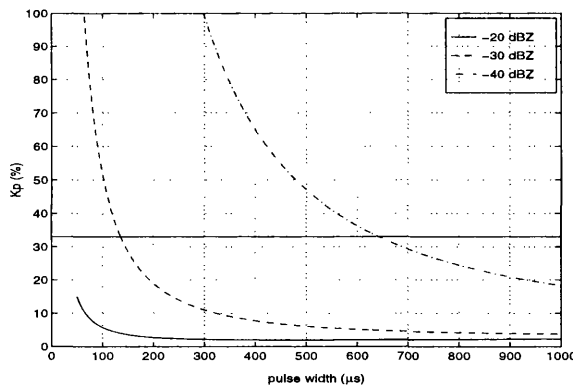


Figure 8.20. Radiometric resolution K_p for the ARMAR amplitude modulated linear FM signal as a function of signal width for different cloud volumetric reflectivities.

It can be concluded that an amplitude modulated linear FM signal is capable of meeting the range sidelobe level requirement at the expense of significant design complexity. The performance of the design option would allow to measure cloud reflectivities with radiometric resolution accuracies below the required 33% specification for compression ratios larger than 1600 (20% for the worst case of a minimum reflectivity of -30 dBZ).

8.6 References

- Atlas D.: 'Advances in Radar Meteorology', *Adv Geophysics*, Vol. 10, pp. 317-478, 1964.
- Bartnoff S. and Atlas D.: 'Microwave Determination of Particle-Size Distribution', *J. Meteorology*, Vol. 8, pp.130-131, 1951.
- Doviak R.J. and Zrnic D.S.: 'Doppler Radar and Weather Observations', Academic Press, 2nd Ed, 1993.
- Durden S.L., Im E., Li F.K., Ricketts W., Tanner A., Denning R., and Wilson W.: 'ARMAR: an Airborne Rain-Mapping Radar', *Journal of Atmospheric and Oceanic Technology*, Vol. 11, pp. 727-737, June 1994.
- Fischer R.E.: 'Standard Deviation of Scatterometer Measurements from Space', *IEEE Transactions on Geoscience Electronics*, Vol. 10, No. 2, April 1972, pp. 106-113.
- Girard R., Jiang W. and Park P.: 'MACSIM: Cloud Profiling Radar', Pre-Phase A Studies, Volume 2, Technical Note on Parametric Study, MPBT Document 495SR-003, July 1996.
- Gray R.W. and Farley D.T.: 'Theory of Incoherent-Scatter Measurements Using Compressed Pulses', *Radio Sci.*, Vol. 8, No. 2, pp.123-131, 1973.
- Johnston, J.A.: 'Digital Techniques in Pulse Compression Signals', Ph.D. thesis, University of Cambridge, 1983.
- Judd G.W.: 'Technique for Realising Low Time Sidelobe Levels in Small Compression Ratio Chirp Waveforms', *Proceedings of IEEE Ultrasonics Symposium*, pp.478-481, 1973.
- Koza T.: 'Effects of Signal Decorrelation on Pulse-Compressed Waveforms for Nadir-Looking Spaceborne Radar', *IEEE Trans. on Geoscience and Remote Sensing*, Vol. 29, No. 5, pp. 786-790, 1991.
- Lhermitte R.: 'Satellite-Borne Millimeter Wave Doppler Radar', URSI Commission F,

Open Symposium, La Londe-Les-Maures, France, September 1989.

- Meneghini R., and Kozi T.: 'Spaceborne Rain Radar', Norwood, MA: Artech House, Inc, 1990.
- Nathanson F.E. and Smith P.L.: 'A Modified Coefficient for the Weather Radar Equation', *Radar Meteorol. Conf.*, 15th, 1972, pp. 228-230, 1972
- Probert-Jones, J.R.: 'The Radar Equation in Meteorology', *Quart. J. Roy. Met. Soc.*, Vol.88, 1962, pp.485-495.
- Riegger S., Schulte H.R., Faulks H., Gollor M. And Schroth J.: 'MACSIM Cloud Profiling Radar Pre-Phase A Study', Technical Note on Trade Off Studies, Daimler-Benz Aerospace, Dornier, 1996.
- Tanner A., Durden S.L., Denning R., Im E., Li F.K., Ricketts W. and Wilson W.: 'Pulse Compression with Very Low Sidelobes in an Airborne Rain Mapping Radar', *IEEE Trans. on Geoscience and Remote Sensing*, Vol. 32, No. 1, pp. 211-213, January 1994.

9 CONCLUSIONS

9.1 Summary

Pulse compression theory provides a solution to the conflicting radar system requirements of simultaneous range resolution and maximum unambiguous detection range, with a less demanding peak power level than with traditional unmodulated pulse alternatives. Frequency modulated signals are processed in reception with a matched filter designed to maximise the output signal peak signal-to-noise ratio. The nature of a matched filter system compressed pulse may introduce range sidelobe self-clutter interference, which is capable of obscuring weak signals in the presence of strong targets. The control of the Fresnel ripple level in the compressed pulse spectrum at the output of the reception filter is the key to pulse compression range sidelobe reduction.

Fresnel ripple reduction can be achieved by either mismatching the matched filter (in the frequency or time domain) or employing nonlinear frequency modulations. Both techniques lead to considerably lower range sidelobe patterns than the one produced with linear FM signals, at the expense of undesired signal-to-noise ratio losses and range resolution degradation. Unfortunately, it is not possible to derive an analytical expression which relates Fresnel ripple reduction levels to frequency modulation design parameters. Therefore, the choice of range sidelobe reduction technique needs to be carefully evaluated for the specific radar application, taking into account factors such as the system geometry and target scenario, the nature and characteristics of the targets, maximum allowable losses to guarantee successful detection and signal generation methods.

In meteorological observation and measurement from low orbit satellites, the on board compressed signal comprises cloud and rain information overlapped with the inevitable Earth's surface return. The signal power level at low rainfall rates and low cloud water contents can be 60 to 80 dB (respectively) below the ground return power level, and thus the range sidelobe pattern of the surface may obscure meteorological information, especially at low altitudes. Therefore, the radar waveform, the antenna radiation pattern and any implemented signal processing technique in reception must ensure that a sufficient dynamic range free of ground interference is attained in order to collect cloud and rain measurements successfully.

On the other hand, restrictions in antenna size in order to achieve the

meteorological scientific horizontal resolution, forces the system to operate in the attenuating frequency band allocated for remote sensing (14 and 95 GHz for rain and cloud respectively). The transmitter peak power level must also guarantee the detection of high rainfall rates and clouds with high water liquid contents, which significantly attenuate their returned power at low altitudes.

Pulse compression range sidelobe reduction techniques have been extensively researched since the early origins of linear FM theory in the 40's. Antenna radiation pattern sidelobe reduction techniques have been applied to pulse compression, achieving range sidelobe levels between -30 and -50 dB. Growing interest in spaceborne radar meteorology during the last 20 years have intensified the search for new frequency modulations and signal processing techniques capable of attaining the stringent range sidelobe level required in order to measure meteorological phenomena from space.

The radar spaceborne system geometry configuration imposes considerable Doppler frequency offsets on the return signal, besides the inherent motion of the hydrometeors (wind and up/downward velocities). For a typical frequency orbit altitude of 500 km and a satellite speed of 7000 m/s, the main Doppler component due to the radar platform motion can amount to 300 kHz, which may represent a significant fraction of the transmitted signal bandwidth. The performance of pulse compression systems in terms of range sidelobe level is degraded when the returned signal is subject to Doppler frequency shifts (especially for nonlinear frequency modulations). A frequency offset in the received signal implies that the downconversion to intermediate frequencies and baseband has no longer the specific value for which the matched filter was designed, and thus resulting to a mismatch depending on the magnitude of the Doppler shift. However, since the Earth radar cross section decreases when the scanning angle departs from nadir, the impact of Doppler frequency offsets may have been overestimated. Figure 2.6 shows the range sidelobe specification as a function of rainfall rate and Doppler frequency (due to platform motion), and a range sidelobe level degradation of approximately 13 dB may be allowed without affecting cloud and rain detectability.

The first spaceborne rain radar satellite (NASA's Tropical Rainfall Measurement Mission) is expected to be launched in August 1997. TRMM designers ruled out the implementation of pulse compression in the radar system since at the beginning of the construction stage, no frequency modulated waveforms could be generated which achieved the range sidelobe level specification. Design studies for the ESA's Bilan Energétique du Système Tropical Mission (BEST) and NASA's Airborne Rain Mapping Radar (ARMAR, in support for a future TRMM-2 Mission) already take full advantage of pulse compression signals in order to reduce the power requirements of the satellite,

thus extending the active life of the mission.

An extensive review of existing range sidelobe reduction techniques has been carried out. Mismatching the linear FM matched filter in either the frequency or time domain can achieve range sidelobe levels below -60 dB with excellent Doppler tolerance for excessively large time-bandwidth products with associated *SNR* losses and range resolution degradation. Combined amplitude and frequency modulation for time-bandwidth products above 1000 currently provide the only satisfactory solution in order to comply with the spaceborne cloud radar range sidelobe specification of -80 dB. The signal bandwidth magnitude required may introduce prohibitive complexity in terms of sampling rate and digital converters. Nonlinear frequency modulations can reduce the range sidelobe pattern at the output of a true matched filter. However, range sidelobe levels attained through such modulations are rarely below -40 dB, and are very sensitive to Doppler frequency offsets.

Two novel waveform design techniques, based on predistorted linear FM theory and asymmetric pulse compression, have been developed and are capable of attaining range sidelobe levels below -60 dB for time-bandwidth products of 300. In spite of the fact that such frequency modulations have been developed for spaceborne radar meteorology, their implementation in other radar and sonar systems would be to the benefit of other applications where the target scenario imposes equivalent range sidelobe level and Doppler tolerance requirements.

9.2 Novel Predistorted Linear FM Waveform Design Technique

Predistortion functions applied to linear FM signals reproduce the effect of rise and fall times different than zero, reducing the Fresnel ripples in the linear FM signal spectrum. The predistortion function consists of two short portions of linear FM of higher modulation rate at the beginning and end of the pulse (Figure 9.1(a)). Research on early predistortion function parameter design (time width and bandwidth) based on paired-echo theory showed that the compressed pulse did not produce optimum results in terms of range sidelobe level.

An analytical expression for the predistorted linear FM compressed pulse has been obtained. The point target response is calculated through the crosscorrelation between a predistorted linear FM signal and its matched filter mismatched in amplitude

with a function of the Blackman-Harris family. The study of the crosscorrelation function constituent terms shows that they are of the same shape but of opposite sign, which cancel and give a considerably reduced range sidelobe pattern. Figure 9.1(b) shows the compressed pulse for a predistorted linear FM signal of $TB = 270$, which gives a range sidelobe level of -62.8 dB.

It has been found that the predistorted linear FM compressed pulse cancellation and range sidelobe level optimisation can be related to the predistorted function parameters. Approximate expressions for the time-bandwidth product of the predistortion function have been given, although the exact values may vary for different linear FM signal time bandwidth products. The design method has also been applied to other weighting functions. The Doppler tolerance of the signal is excellent, and its ambiguity function shows a range sidelobe degradation of only 2 dB for Doppler offsets up to 100 kHz.

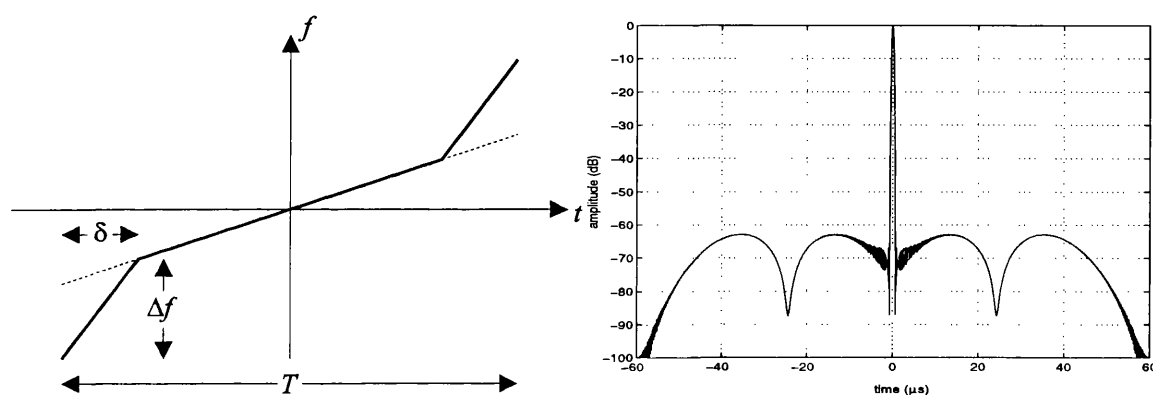


Figure 9.1. Predistorted linear FM ($TB = 270$): (a) instantaneous frequency; (b) compressed pulse.

9.3 Novel Asymmetric FM Waveform Design Technique

Pulse compression range sidelobe reduction techniques reported in the literature do not take into account the peculiar remote sensing system geometry in which meteorological phenomena is only present before the leading edge of the matched filtered surface return. An asymmetric frequency modulation which produced a compressed pulse whose range sidelobe level is compliant with the system requirement on only one side of the compressed pulse, would have no impact on meteorological quantitative estimation.

Asymmetric compression cannot be obtained at the output of a matched filter due to the symmetric properties of the autocorrelation function. However, it has been shown

that an asymmetric frequency modulation processed with a linear FM matched filter is capable of causing asymmetric compression.

A novel nonlinear FM design technique has been developed which consists of the addition of a nonlinear phase term to the phase of a linear FM signal. The nonlinear FM phase term is defined by a polynomial of terms of odd powers. Asymmetric range sidelobe patterns below -40 dB have been obtained with the previous design technique, which can be improved by mismatching the reception linear FM matched filter. The resulting asymmetric FM instantaneous frequency is shown in Figure 9.2(a) for a TB of 300, which gives a compressed pulse range sidelobe level of -60.4 dB, shown in Figure 9.2(b) (minimum 3-term Blackman-Harris mismatching function). The ambiguity function of the asymmetric FM signal shows that its compressed pulse range sidelobe level degradation (where the meteorological information is present) is only of 0.2 dB for Doppler frequency offsets up to 150 kHz.

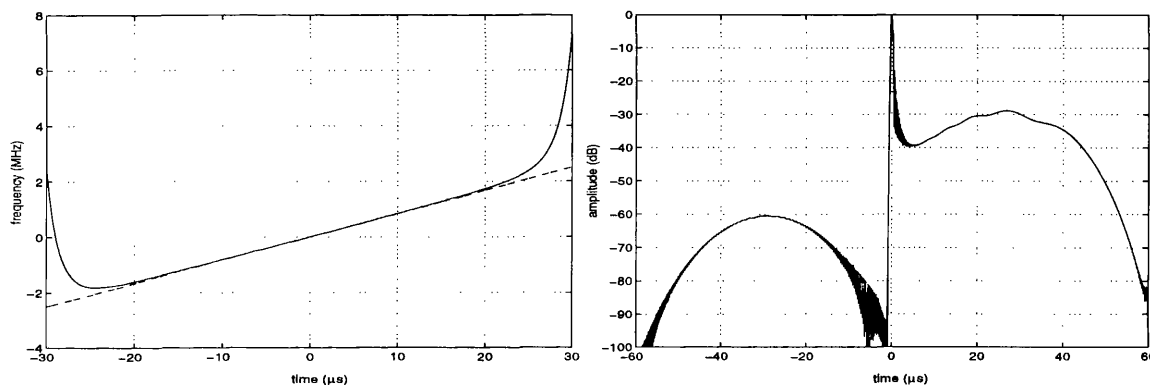


Figure 9.2. Asymmetric FM ($TB = 300$): (a) instantaneous frequency; (b) compressed pulse.

The asymmetric FM design technique has been extended to the design of nonlinear FM signals to produce conventional symmetric point target responses. Although their compressed pulse peak range sidelobe level is of only -35 dB, they present a fast sidelobe decay rate adjacent to the mainlobe producing a range sidelobe pattern below -60 dB for the majority of the duration of the compressed pulse. As expected, the waveforms are not Doppler tolerant and their range sidelobe level is significantly degraded by small Doppler frequency offsets.

The previously described FM signals could easily be digitally generated and compressed in the frequency domain through FFT algorithms, in order to reduce the processing load. However, generation and compression distortion errors must be strictly limited (amplitude deviation below 0.02 dB and phase deviation below 0.1°) to guarantee a range sidelobe level below -60 dB. Such distortion could be corrected through an

adaptive compensation branch. Further research should address appropriate algorithms of adaptive distortion compensation through the digitally generated FM waveform.

9.4 RA-2 Rain Mode Design Discussion

Multiple waveform design options for the provision of a rain mode for a radar altimeter (RA-2) due to fly on ESA's ENVISAT satellite have been considered. A comprehensive analysis has been carried out which has shown that there are two factors which severely constrain the performance of the RA-2 radar altimeter rain mode:

(i) The new rain mode needs to be designed with the least impact on the altimeter instrument. Since the available power on-board is limited (60 W), there are severe signal-to-noise ratio limitations which prevent the detection of high rainfall rates at low altitudes due to the compulsory use of attenuating frequencies (Ku band). Rainfall measurements at the S-band frequency (also available in the RA-2), are ruled out due to insufficient signal-to-noise ratio.

(ii) The inefficiency of a simple pulsed radar (low power availability and major circuitry modification) forces the design of a frequency modulated waveform in order to adjust the range resolution to meteorological requirements. Therefore, ground sidelobe interference may obscure a significant region of the 9 km range window. Data retrieval from precipitation over the surface proves to be one of the most complicated technical difficulties.

The standard altimetry full deramp technique needs to be modified in order to adapt the receiver to the measurement of precipitation. Two options are given for the construction of the RA-2 rain mode range window:

- The use of several LO pulses in order to cover the rainfall return along the whole extent of the range window.

[facilitates] [permits] the analysis of

- The generation of a longer LO reference signal (80 μ s) ~~allows to build up~~ the whole extent of the range window with only one triggered pulse per scan. Due to the existence of a linear FM generator of such characteristics, it is the optimum option. (E)

The effects of Doppler frequency shifts due to the platform motion have been

calculated to be negligible ($1/3$ of a range bin) for the effective operation of the rain mode.

The performance of nonlinear FM waveforms full deramp response has been analysed. Two representative modulations of this kind with the appropriate time-bandwidth product to achieve the required range resolution have been designed and tested. The waveforms considered are: (i) predistorted linear FM signals and (ii) continuous nonlinear FM signals based on a Hamming compressed pulse spectrum. The results show that the full deramp of nonlinear FM waveforms must be ruled out due to its incompatibility with the chosen range window construction option.

A new formulation for the full-deramp of FM signals of different length has been developed which is consistent with existing altimetry full deramp theory. The resultant set of equations have led to the design of a valuable rain mode range window precipitation model. The range window spectrum approximation consists of the combination of the expressions of the RA-2 rain mode frequency point target responses and the appropriate rainfall power level calculations. The Earth's surface interference has been qualitatively and quantitatively assessed with the help of the proposed model.

It must be pointed out that sidelobe reduction is not necessary over the whole extent of the range window, but only for the ground clutter return. The -13.3 dB sidelobe level of full deramped FM signals is enough to guarantee rain detectability in almost two thirds of the range window. Furthermore, the altimeter tracking needs to be employed in order to determine the position of the surface return in the range window. Hence, it is possible to provide the instrument rain mode with a time-accurate sidelobe reduction technique.

Several signal processing techniques have been studied in order to reduce the main source of interference, the surface return sidelobes:

- Time weighting.
- AGC gain-varying functions.
- Ground clutter echo pulse width reduction.
- Combined amplitude and phase weighting schemes.
- Ground Clutter Echo Cancellation.

These techniques cannot reduce the ground clutter return range sidelobe level to

an extent in which no interference or masking is produced. The best results are given by a Hamming or linear gain-varying function combined with phase weighting. The attenuation of the Earth's surface return enhances rain detectability and reduces sidelobe masking.

The minimum detectable rainfall rate varies between 5 mm/h and 15 mm/h depending on the surface backscattering coefficient (sea or land). Further investigation on sidelobe reduction methods needs to be carried out in order to lower such figures. Rainfall rates of 50 mm/h and higher can be detected only at medium heights over the surface due to signal-to-noise ratio limitations.

The combination of amplitude and phase weighting schemes is the option which achieves the best results in terms of ground clutter interference minimisation. Combined severe tapers over the surface return can meet the range sidelobe level specification at the expense of some loss and distortion of the rain echo power spectrum. A less severe taper attains lower loss and distortion at the expense of a section of the range window (800 m) being obscured by the surface return. It is clear that low distortion meeting the sidelobe level requirement cannot be achieved by severe weighting and a compromise is required.

The extent of the range window masking area (over the Earth's surface) and its source (surface return interference or signal-to-noise ratio limitation) for different rainfall rates is summarised in Table 9.I.

Table 9.I: Detection constraints for different range sidelobe reduction techniques

	<i>5 mm/h (low)</i>	<i>20 mm/h (medium)</i>	<i>50 mm/h (high)</i>
Full Deramp	no detection (surf. interference)	2.5 km (surf. interference)	1.0 km (surf. interference)
Hamming	3.7 km (SNR limitation)	1.5 km (surf. interference)	1.5 km (SNR limitation)
AGC (Hamming)	no detection (surf. interference)	1.6 km (surf. interference)	0.8 km (surf. interference)
AGC (Exponential)	no detection (surf. interference)	1.9 km (surf. Interference)	1.3 km (SNR limitation)
Amplitude & Phase	no detection (surf. interference)	1.2 km (surf. interference)	1.0 km (SNR limitation)

Table 9.II shows the minimum detectable rainfall rate and the minimum detectable height for the different signal processing techniques applied to the altimeter

rain mode range window. A relative overall performance figure for each technique has been derived accounting for the interference free detectable rainfall region (Figure 7.33).

Finally, typical horizontal resolutions (2 km) and attenuating frequencies employed in spaceborne rain radars lead to the beam filling problem, in which the measurement of ground reflectivity especially when the attenuation is large (high rainfall rates) introduce errors in the derived rainfall rate estimates. Further work should address the study of the impact of non uniform beam filling in the RA-2 rain mode retrieval algorithms.

Table 9.II: Range sidelobe reduction techniques performance comparison

	<i>minimum detectable rate</i>	<i>minimum detectable height</i>	<i>relative detection region</i>
Full Deramp	13 mm/h	1.0 km	39 %
Hamming	5 mm/h	1.2 km	52 %
AGC (Hamming)	8 mm/h	0.8 km	52 %
AGC (Exponential)	8 mm/h	1.2 km	47 %
Amplitude & Phase	7 mm/h	0.8 km	58 %

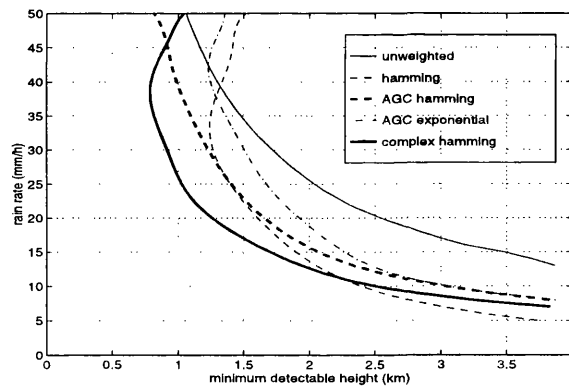


Figure 9.3. Minimum detectable height as a function of rain rate for different sidelobe suppression techniques.

Unfortunately, in spite of the obvious benefits of the presented altimeter rainfall measurement system design, it was decided not to include the rain mode to the RA-2 in order not to delay the construction and launching tight schedules of the ENVISAT Mission.

9.5 MACSIM Design Discussion

Several waveform selection alternatives have been considered for ESA's Millimetre wave Active Cloud Structure Imaging Mission Pre Phase A Study. The two most common system waveform configurations for spaceborne meteorological radars have been investigated in detail and their performance analysis shows that both alternatives are compliant with the system specifications in terms of range sidelobe level requirement and radiometric resolution accuracy.

In the unmodulated pulse alternative, the signal width is determined by the specified range resolution. Severe constraints on the transmitter peak power on board the satellite do not allow an increase of the pulse energy by employing longer signal widths, thus limiting the attainable signal-to-noise ratio. Frequency agility may be considered in order to increase the number of independent samples for a given pulse repetition frequency.

The specified minimum detectable cloud reflectivity of -30 dBZ imposes stringent requirements on both the antenna sidelobe pattern (-35 dB [Riegger et al., 1996]) and the compressed pulse range sidelobe level (-80 dB). Several pulse compression range sidelobe reduction techniques have been analysed in order to attain such specification, including:

- Linear FM matched and mismatched systems (Hamming, Dolph-Chebyshev, Blackman-Harris)
- Non linear FM matched and mismatched systems (Blackman-Harris)
- Predistorted linear FM mismatched system (Dolph-Chebyshev, Blackman-Harris)
- Asymmetric FM matched and mismatched systems (Blackman-Harris)
- Amplitude modulated linear FM matched system (ARMAR function)

The range sidelobe level specifications have ruled out most FM signal design techniques since their point target responses do not comply with the minimum detectable cloud reflectivity. The amplitude modulated linear FM waveform (ARMAR) is the most suitable candidate for the pulse compression alternative, due to the monotonically decreasing range sidelobe pattern of its compressed pulse. Amplitude modulated waveforms force the transmitter to work in the linear region instead of the normal

saturation region of operation. The ARMAR amplitude modulation function is designed to minimise the signal-to-noise ratio loss to a figure of -2.3 dB.

Unfortunately, very high time-bandwidth products are needed in order to reduce the range sidelobe level at the sufficient level of -80 dB, thus obtaining lower range resolutions than required with a further associated signal-to-noise ratio loss. Therefore, multiple look averaging processing must be carried out to deliver cloud reflectivity estimations within the specified user range resolution cell of 500 m. The fact that a blind layer of 250 m is allowed above the Earth's surface allows to convert (and relax) the peak range sidelobe level requirement into the average of the range sidelobe pattern level in the most critical first range resolution cell. It has been established that a minimum bandwidth of 8 MHz is required to avoid the range sidelobe pattern of the surface return to interfere cloud measurements.

The performance of both waveform alternatives has been analysed and compared in terms of single pulse sensitivity (cloud reflectivity whose return power is equivalent to the system noise power level) and the measurement radiometric resolution. The single pulse sensitivity of the unmodulated pulse ($T = 3.33 \mu\text{s}$) is of -14.1 dBZ [Girard et al., 1996]. Cloud reflectivities are estimated through a short term average of the output of a square law detector after the reception filter. The minimum detectable reflectivity of -30 dBZ can be achieved through the 30 km allowed integration length.

In order to determine the pulse compression alternative single pulse sensitivity, a detailed loss balance has been evaluated. Since the amplitude modulated linear FM signal is filtered with a matched filter which maximises the peak signal-to-noise ratio, no mismatching losses are considered by amplitude weighting other than the reported signal-to-noise ratio loss of 2.3 dB.

It has been found that signal decorrelation is not critical for linear FM signals even when the signal width is longer than the decorrelation time imposed by the system geometry and target return fluctuation. Signal decorrelation is analysed through the ensemble average of the signal instantaneous returned power. A decrease in the response level and a smeared range sidelobe pattern are effects associated with decorrelation. However, the energy of the compressed pulse remains constant as a function of signal width (while its peak level is subject to severe degradation for pulse widths above the decorrelation time). The decorrelation loss for the ARMAR compressed pulse has been found to be of 2.4 dB.

The shape of the amplitude modulated transmitted waveform constitutes a range

weighting function which reduces the pulse volume scatterer contributions. The equivalent finite bandwidth loss due to the amplitude modulation has been determined to be of 7.3 dB, which gives a negative balance of 5.1 dB with respect the unmodulated pulse option. It is unfortunate that such loss cannot be corroborated with experimental data from the ARMAR mission.

Finally, the incoherent multiple averaging processing produces a gain between 5.5 and 6 dB (depending on how the range resolution within the user range resolution cell is defined), which helps to alleviate the signal-to-noise ratio decrease associated with the selected bandwidth. The final amplitude modulated pulse compression loss balance ($TB = 1200$) matches the performance of the unmodulated pulse alternative in terms of single pulse sensitivity, with yet the signal width magnitude to be selected. ④

An optimum radiometric resolution for the range of detectable reflectivities cannot be obtained. Therefore, the cloud reflectivity measurement radiometric resolution needs to be optimised in order to attain the best possible accuracy for the lowest detectable reflectivities, since the waveform parameter selection has relatively little impact in the measurement accuracy of higher cloud reflectivities. Since the signal width decorrelation time limit restriction has been lifted for linear FM signals, it is possible to select a sufficiently long pulse duration in order to maximise the accuracy of the measurement for low cloud reflectivities. It has been found that better measurement accuracy can be obtained with the pulse compression alternative than with the unmodulated pulse option. The signal width selection ^{fully determined} ~~lies~~ in the range between 200 and 500 μ s, where radiometric resolutions below 20% can be achieved. The final value must be determined by the available signal generator capability. ⑤

A particular problem in the MACSIM system arises from the fact that small waveform generation distortion errors may degrade the compressed pulse range sidelobe pattern. The evaluation of amplitude and phase distortion errors has been extended for the MACSIM case. In order to guarantee the range sidelobe level of -80 dB amplitude and phase distortions must be kept at a very low level during the waveform generation (amplitude deviation below 0.002 dB and phase deviation below 0.001 degrees).

Further investigation needs to be carried out in order to determine whether more severe amplitude modulation functions could trade off a lower time-bandwidth product (and thus better signal-to-noise ratios inside the range resolution of 500 m) at the expense of a further signal-to-noise ratio loss.

Another possibility to reduce ground clutter interference is to implement an off-nadir pointing antenna (the optimum tilt angle needs to be determined). The increase of the blind layer region for off-nadir pointing combined with the relaxation of the range sidelobe level specification may also reduce the time bandwidth product of the pulse compression waveform. Research into ground clutter cancellation or subtraction may also be considered. It is obvious that the entire surface return cannot be completely coherently subtracted from previous measurements of surface reflectivity. However, even if incoherent cancellation allows the reduction of the compressed pulse range sidelobe specification by a few dB, such an option would have a valuable contribution in reducing the selected time-bandwidth product and improving the system loss balance.

APPENDIX A

Doppler Frequency Due to Satellite Motion Formulation

The Doppler frequency offset f_d is defined as the difference between the received and transmitted frequencies and given by:

$$f_d = -\frac{2}{\lambda} \frac{dr(t)}{dt} \hat{r} \quad (1)$$

where λ is the wavelength, $r(t)$ a function describing the satellite motion trajectory and \hat{r} a unit vector in the scanning direction.

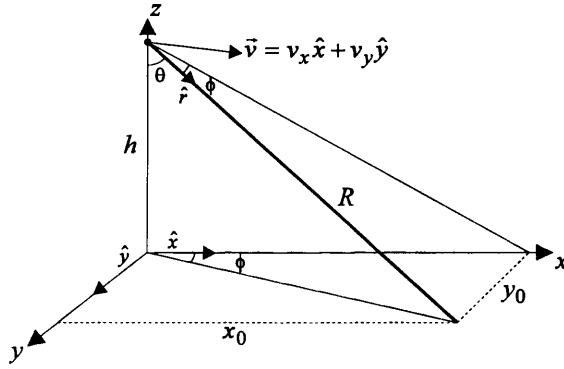


Figure A.1. Spaceborne rain radar system geometry.

The system geometry is displayed in Figure A.1 (assuming a flat Earth geometry). Without loss of generality, it is assumed that the satellite moves along the xy plane at a constant speed $|\vec{v}_{sat}|$, described by the following vector:

$$\vec{v}_{sat}(t) = v_x \hat{x} + v_y \hat{y} \quad (2)$$

where \hat{x} and \hat{y} are unit vectors in the x and y directions, and $|\vec{v}_{sat}| = \sqrt{v_x^2 + v_y^2}$. Thus, the satellite trajectory $r(t)$ is given by:

$$r(t) = \sqrt{(v_x t)^2 + (v_y t)^2 + h^2} \quad (3)$$

where h is the satellite altitude.

The Doppler frequency shift can now be expressed as:

$$f_d = -\frac{2}{\lambda} \frac{v_x^2 t + v_y^2 t}{\sqrt{(v_x t)^2 + (v_y t)^2 + h^2}} = -\frac{2}{\lambda} \frac{v_x x + v_y y}{\sqrt{x^2 + y^2 + h^2}} \quad (4)$$

The cartesian coordinates of a ground scatterer of a differential area at slant range R from the satellite are given by:

$$x_0 = R \sin \theta \cos \phi \quad (5)$$

$$y_0 = R \sin \theta \sin \phi \quad (6)$$

Thus, the Doppler offset introduced into the backscattered signal corresponding to that particular section of the ground (x_0, y_0) is then given by:

$$f_d = -\frac{2}{\lambda} \sin \theta \frac{v_x R \cos \phi + v_y R \sin \phi}{R} = -\frac{2}{\lambda} \sin \theta (v_x \cos \phi + v_y \sin \phi) \quad (7)$$

Applying the following trigonometric transformation:

$$v_x = |\vec{v}_{sat}| \cos \phi \quad (8)$$

$$v_y = |\vec{v}_{sat}| \sin \phi \quad (9)$$

the final expression for the Doppler frequency offset is given by:

$$f_d = -\frac{2}{\lambda} |\vec{v}_{sat}| \sin \theta \quad (10)$$

It must be pointed out that the Doppler offset due to the radar platform motion is independent of slant range. Thus, the return at a given direction determined by the scanning angles θ and ϕ will have a constant main Doppler component which could easily be compensated¹.

¹ The previous calculation does not consider the Doppler frequency spread due to hydrometeor motion or at the edges of the antenna footprint.

APPENDIX B

B.1 Linear FM Compressed Pulse Calculation

The linear FM signal complex envelope is defined as:

$$\tilde{s}(t) = \frac{1}{\sqrt{T}} \text{rect}\left(\frac{t}{T}\right) e^{j\pi \frac{B}{T} t^2} \quad (1)$$

where T is the pulse width and B the signal bandwidth. The compressed pulse is given by the convolution between the linear FM signal and a conjugated replica of the signal itself (matched filter):

$$s_0(\tau) = \int_{-\infty}^{\infty} \tilde{s}(t) \tilde{s}^*(t - \tau) dt \quad (2)$$

Inserting Eq.1 into Eq.2 the compressed pulse is given by:

$$s_0(\tau) = \frac{1}{T} \int_{-\infty}^{\infty} \text{rect}\left(\frac{t}{T}\right) \text{rect}\left(\frac{t - \tau}{T}\right) e^{j\pi K t^2} e^{-j\pi K (t - \tau)^2} dt \quad (3)$$

and expanding the exponential terms, the compressed pulse can be rewritten as:

$$s_0(\tau) = \frac{e^{-j\pi K \tau^2}}{T} \int_{-\infty}^{\infty} \text{rect}\left(\frac{t}{T}\right) \text{rect}\left(\frac{t - \tau}{T}\right) e^{j2\pi K t \tau} dt \quad (4)$$

As it was described in section 3.3.3 (Figure 3.4), $s_0(\tau)$ needs to be integrated separately for positive and negative values of τ . Thus, for $\tau > 0$, the 'positive' compressed pulse is given by:

$$s_0(\tau)|_{\tau > 0} = \frac{e^{-j\pi K \tau^2}}{T} \int_{\tau - \frac{T}{2}}^{\frac{T}{2}} e^{j2\pi K t \tau} dt \quad (5)$$

The exponential integral in Eq. 5 can be directly expressed as:

$$s_0(\tau)|_{\tau>0} = \frac{1}{j2\pi K\tau T} \left(e^{j\pi K\tau(T-\tau)} - e^{-j\pi K\tau(T-\tau)} \right) \quad (6)$$

The exponential terms in Eq. 6 can be transformed through a trigonometric identity into:

$$s_0(\tau)|_{\tau>0} = \frac{(T-\tau)}{\pi K\tau T} \sin(\pi K\tau(T-\tau)) \quad (7)$$

The final expression for the compressed pulse ($\tau > 0$) is then given as a $\sin(x)/x$ function:

$$s_0(\tau)|_{\tau>0} = \left(1 - \frac{\tau}{T} \right) \text{sinc} \left(B\tau \left(1 - \frac{\tau}{T} \right) \right) \quad (8)$$

For $\tau < 0$, the 'negative' compressed pulse is given by:

$$s_0(\tau)|_{\tau<0} = \frac{e^{-j\pi K\tau^2 \frac{T}{2} + \tau}}{T} \int_{-\frac{T}{2}}^{\frac{T}{2} + \tau} e^{j2\pi K\tau t} dt \quad (9)$$

The same procedure is applied to attain the following final expression:

$$s_0(\tau)|_{\tau<0} = \left(1 + \frac{\tau}{T} \right) \text{sinc} \left(B\tau \left(1 + \frac{\tau}{T} \right) \right) \quad (10)$$

Thus, combining Eq. 8 and Eq. 10, the linear FM compressed pulse is given by:

$$s_0(\tau) = \left(1 - \frac{|\tau|}{T} \right) \text{sinc} \left(B\tau \left(1 - \frac{|\tau|}{T} \right) \right) \quad (11)$$

B.2 Linear FM Ambiguity Function Calculation

The linear FM signal ambiguity function is defined as:

$$\chi(\tau, \nu) = \int_{-\infty}^{\infty} \tilde{s}(t) \tilde{s}^*(t - \tau) e^{j2\pi\nu t} dt \quad (12)$$

Inserting the linear FM signal expression Eq. 1 into Eq. 12, the ambiguity function is given by:

$$\chi(\tau, \nu) = \frac{1}{T} \int_{-\infty}^{\infty} \text{rect}\left(\frac{t}{T}\right) \text{rect}\left(\frac{t - \tau}{T}\right) e^{j\pi K t^2} e^{-j\pi K (t - \tau)^2} e^{j2\pi\nu t} dt \quad (13)$$

and expanding the exponential terms, Eq. 13 can be expressed as:

$$\chi(\tau, \nu) = \frac{e^{-j\pi K \tau^2}}{T} \int_{-\infty}^{\infty} \text{rect}\left(\frac{t}{T}\right) \text{rect}\left(\frac{t - \tau}{T}\right) e^{j2\pi(K\tau + \nu)t} dt \quad (14)$$

In the same way as $s_0(\tau)$, $\chi(\tau, \nu)$ needs to be integrated separately for positive and negative values of τ . Thus, for $\tau > 0$, the ‘time-positive’ ambiguity function is given by:

$$\chi(\tau, \nu)|_{\tau > 0} = \frac{e^{-j\pi K \tau^2}}{T} \int_{\tau - \frac{T}{2}}^{\frac{T}{2}} e^{j2\pi(K\tau + \nu)t} dt \quad (15)$$

The exponential integral in Eq. 15 can be directly expressed as:

$$\chi(\tau, \nu)|_{\tau > 0} = \frac{e^{j\pi\nu\tau}}{j2\pi(K\tau + \nu)T} \left(e^{j\pi(K\tau + \nu)(T - \tau)} - e^{-j\pi(K\tau + \nu)(T - \tau)} \right) \quad (16)$$

The exponential terms are transformed through a trigonometric identity into:

$$\chi(\tau, \nu)|_{\tau > 0} = \frac{(T - \tau)}{\pi(K\tau + \nu)T} \sin(\pi(K\tau + \nu)(T - \tau)) e^{j\pi\nu\tau} \quad (17)$$

The final expression for the ambiguity function ($\tau > 0$) is then given by a $\sin(x)/x$ function:

$$\chi(\tau, \nu)|_{\tau > 0} = \left(1 - \frac{\tau}{T}\right) \text{sinc}\left((B\tau + T\nu)\left(1 - \frac{\tau}{T}\right)\right) e^{j\pi\nu\tau} \quad (18)$$

For $\tau < 0$, the 'time-negative' ambiguity function is given by:

$$\chi(\tau, \nu)|_{\tau < 0} = \frac{e^{-j\pi K\tau^2}}{T} \int_{-\frac{T}{2}}^{\frac{T}{2} + \tau} e^{j2\pi(K\tau + \nu)t} dt \quad (19)$$

The same procedure is applied to attain the following final expression:

$$\chi(\tau, \nu)|_{\tau < 0} = \left(1 + \frac{\tau}{T}\right) \text{sinc}\left((B\tau + T\nu)\left(1 + \frac{\tau}{T}\right)\right) e^{j\pi\nu\tau} \quad (20)$$

Thus, combining Eq. 18 and Eq. 20, the linear FM ambiguity function is given by:

$$\chi(\tau, \nu) = \left(1 - \frac{|\tau|}{T}\right) \text{sinc}\left((B\tau + T\nu)\left(1 + \frac{|\tau|}{T}\right)\right) e^{j\pi\nu\tau} \quad (21)$$

B.3 Linear FM Ambiguity Function Calculation (Amplitude Mismatch)

The linear FM signal ambiguity function (matched filter mismatched in amplitude) is defined as:

$$\chi(\tau, \nu) = \int_{-\infty}^{\infty} \tilde{s}(t) \tilde{s}^*(t - \tau) w(t - \tau) e^{j2\pi\nu t} dt \quad (22)$$

where $w(t)$ is given by:

$$w(t) = \text{rect}\left(\frac{t}{T}\right) \sum_{n=0}^N a_n \cos(2\pi n f_T t) \quad (23)$$

where $f_T = 1/T$.

Inserting the linear FM signal expression Eq. 1 into Eq. 22, the ambiguity function is given by:

$$\chi(\tau, \nu) = \frac{1}{T} \int_{-\infty}^{\infty} \text{rect}\left(\frac{t}{T}\right) \text{rect}\left(\frac{t - \tau}{T}\right) w(t - \tau) e^{j\pi K t^2} e^{j\pi K (t - \tau)^2} e^{j2\pi\nu t} dt \quad (24)$$

and expanding the exponential terms, Eq. 24 can be expressed as:

$$\chi(\tau, \nu) = \frac{1}{T} e^{-j\pi K \tau^2} \int_{-\infty}^{\infty} \text{rect}\left(\frac{t}{T}\right) \text{rect}\left(\frac{t - \tau}{T}\right) w(t - \tau) e^{j2\pi(K\tau + \nu)t} dt \quad (25)$$

which can be formulated as the following sum:

$$\chi(\tau, \nu) = \sum_{n=0}^2 A_n(\tau, \nu) \quad (26)$$

where the generic term $A_n(\tau, \nu)$ is given by:

$$A_n(\tau, \nu) = \frac{a_n}{T} e^{-j\pi K \tau^2} \int_{-\infty}^{\infty} \text{rect}\left(\frac{t}{T}\right) \text{rect}\left(\frac{t - \tau}{T}\right) \cos(2\pi n f_T (t - \tau)) e^{j2\pi(K\tau + \nu)t} dt \quad (27)$$

The first term $A_0(\tau, \nu)$ is equivalent to the linear FM ‘matched’ ambiguity function (Eq. 21) scaled by the factor a_0 :

$$A_0(\tau, \nu) = a_0 \left(1 - \frac{|\tau|}{T}\right) \text{sinc} \left((B\tau + \nu T) \left(1 - \frac{|\tau|}{T}\right) \right) e^{j\pi\nu\tau} \quad (28)$$

The following terms can be developed generically as:

$$A_n(\tau, \nu) = \frac{a_n}{T} \left(\cos(2\pi n f_T \tau) B_{1n}(\tau, \nu) + \sin(2\pi n f_T \tau) B_{2n}(\tau, \nu) \right) \quad (29)$$

where:

$$B_{1n}(\tau, \nu) = e^{-j\pi K \tau^2} \int_{-\infty}^{\infty} \text{rect} \left(\frac{t}{T} \right) \text{rect} \left(\frac{t - \tau}{T} \right) \cos(2\pi n f_T t) e^{j2\pi(K\tau + \nu)t} dt \quad (30)$$

$$B_{2n}(\tau, \nu) = e^{-j\pi K \tau^2} \int_{-\infty}^{\infty} \text{rect} \left(\frac{t}{T} \right) \text{rect} \left(\frac{t - \tau}{T} \right) \sin(2\pi n f_T t) e^{j2\pi(K\tau + \nu)t} dt \quad (31)$$

$A_n(\tau, \nu)$ can then be rewritten as:

$$A_n(\tau, \nu) = \frac{a_n}{2T} \left(B'_{1n}(\tau, \nu) (\cos(2\pi n f_T \tau) - j \sin(2\pi n f_T \tau)) + B'_{2n}(\tau, \nu) (\cos(2\pi n f_T \tau) + j \sin(2\pi n f_T \tau)) \right) \quad (32)$$

where:

$$B'_{1n}(\tau, \nu) = e^{-j\pi K \tau^2} \int_{-\infty}^{\infty} \text{rect} \left(\frac{t}{T} \right) \text{rect} \left(\frac{t - \tau}{T} \right) e^{j2\pi(K\tau + \nu + n f_T)t} dt \quad (33)$$

$$B'_{2n}(\tau, \nu) = e^{-j\pi K \tau^2} \int_{-\infty}^{\infty} \text{rect} \left(\frac{t}{T} \right) \text{rect} \left(\frac{t - \tau}{T} \right) e^{j2\pi(K\tau + \nu - n f_T)t} dt \quad (34)$$

$A_n(\tau, \nu)$ can be finally formulated as:

$$A_n(\tau, \nu) = \frac{a_n}{T} \left(B''_{1n}(\tau, \nu) + B''_{2n}(\tau, \nu) \right) \quad (35)$$

where:

$$B''_{1n}(\tau, \nu) = e^{-j2\pi n f_T \tau} B'_{1n}(\tau, \nu) \quad (36)$$

$$B''_{2n}(\tau, \nu) = e^{+j2\pi n f_T \tau} B'_{2n}(\tau, \nu) \quad (37)$$

$B''_{1n}(\tau, \nu)$ and $B''_{2n}(\tau, \nu)$ need to be integrated separately for their positive and negative values of τ . For positive values of τ , $B''_{1n}(\tau, \nu)$ is given by:

$$B''_{1n}(\tau, \nu)|_{\tau>0} = e^{-j\pi(K\tau+2nf_T)\tau} \int_{\tau-\frac{T}{2}}^{\frac{T}{2}} e^{j2\pi(K\tau+\nu+nf_T)t} dt \quad (38)$$

The exponential integral in Eq. 38 can be directly expressed as:

$$B''_{1n}(\tau, \nu)|_{\tau>0} = \frac{e^{-j\pi(K\tau+2nf_T)\tau}}{j2\pi(K\tau+\nu+nf_T)} \cdot \left(e^{j2\pi(K\tau+\nu+nf_T)\frac{T}{2}} - e^{j2\pi(K\tau+\nu+nf_T)\left(\tau-\frac{T}{2}\right)} \right) \quad (39)$$

Modifying the exponential terms, Eq. 39 can be rewritten as:

$$B''_{1n}(\tau, \nu)|_{\tau>0} = \frac{e^{-j\pi(K\tau+2nf_T)\tau} e^{j\pi(K\tau+\nu+nf_T)}}{j2\pi(K\tau+\nu+nf_T)} \cdot \left(e^{j\pi(K\tau+\nu+nf_T)(T-\tau)} - e^{-j\pi(K\tau+\nu+nf_T)(T-\tau)} \right) \quad (40)$$

and applying a trigonometric identity, Eq. 40 is then given by:

$$B''_{1n}(\tau, \nu)|_{\tau>0} = \frac{e^{j\pi(\nu-nf_T)\tau}}{\pi(K\tau+\nu+nf_T)} \cdot \sin\left(\pi(K\tau+\nu+nf_T)(T-\tau)\right) \quad (41)$$

which can be finally expressed as:

$$B''_{1n}(\tau, \nu)|_{\tau>0} = T \left(1 - \frac{\tau}{T}\right) \text{sinc}\left((B\tau + \nu T + n) \left(1 - \frac{\tau}{T}\right)\right) e^{j\pi(\nu-nf_T)\tau} \quad (42)$$

For negative values of τ , $B''_{1n}(\tau, \nu)$ is given by:

$$B''_{1n}(\tau, \nu)|_{\tau < 0} = e^{-j\pi(K\tau + 2nf_T)\tau} \int_{-\frac{T}{2}}^{\frac{T}{2} + \tau} e^{j2\pi(K\tau + \nu + nf_T)t} dt \quad (43)$$

The exponential integral in Eq. 43 can be directly expressed as:

$$B''_{1n}(\tau, \nu)|_{\tau < 0} = \frac{e^{-j\pi(K\tau + 2nf_T)\tau}}{j2\pi(K\tau + \nu + nf_T)} \cdot \left(e^{j2\pi(K\tau + \nu + nf_T)\left(\frac{T}{2} + \tau\right)} - e^{-j2\pi(K\tau + \nu + nf_T)\frac{T}{2}} \right) \quad (44)$$

Modifying the exponential terms, Eq. 44 can be rewritten as:

$$B''_{1n}(\tau, \nu)|_{\tau < 0} = \frac{e^{-j\pi(K\tau + 2nf_T)\tau} e^{j\pi(K\tau + \nu + nf_T)}}{j2\pi(K\tau + \nu + nf_T)} \cdot \left(e^{j\pi(K\tau + \nu + nf_T)(T + \tau)} - e^{-j\pi(K\tau + \nu + nf_T)(T + \tau)} \right) \quad (45)$$

and applying a trigonometric identity, Eq. 45 is then given by:

$$B''_{1n}(\tau, \nu)|_{\tau < 0} = \frac{e^{j\pi(\nu - nf_T)\tau}}{\pi(K\tau + \nu + nf_T)} \cdot \sin(\pi(K\tau + \nu + nf_T)(T + \tau)) \quad (46)$$

which can be finally expressed as:

$$B''_{1n}(\tau, \nu)|_{\tau < 0} = T \left(1 + \frac{\tau}{T} \right) \text{sinc} \left((B\tau + \nu T + n) \left(1 + \frac{\tau}{T} \right) \right) e^{j\pi(\nu - nf_T)\tau} \quad (47)$$

Combining Eq. 42 and Eq.47, the generic term $B''_{1n}(\tau, \nu)$ is given by:

$$B''_{1n}(\tau, \nu) = T \left(1 - \frac{|\tau|}{T} \right) \text{sinc} \left((B\tau + \nu T + n) \left(1 - \frac{|\tau|}{T} \right) \right) e^{j\pi(\nu - nf_T)\tau} \quad (48)$$

$B''_{2n}(\tau, \nu)$ is integrated in the same way to give:

$$B''_{2n}(\tau, \nu) = T \left(1 - \frac{|\tau|}{T}\right) \text{sinc} \left((B\tau + \nu T - n) \left(1 - \frac{|\tau|}{T}\right) \right) e^{j\pi(\nu + n/T)\tau} \quad (49)$$

Therefore, the ambiguity function for the weighted linear FM signal can be finally expressed as:

$$\chi(\tau, \nu) = \frac{1}{2} \left(1 - \frac{|\tau|}{T}\right) e^{j\pi\nu\tau} \sum_{n=-N}^N a'_n \text{sinc} \left((B\tau + \nu T + n) \left(1 - \frac{|\tau|}{T}\right) \right) e^{-j\pi\frac{n}{T}\tau} \quad (50)$$

where the new coefficients are defined as:

$$a'_0 = 2a_0 \quad (51)$$

$$a'_n = a'_{-n} = a_n \quad (52)$$

APPENDIX C

Predistorted linear FM Crosscorrelation Formulation

The complex envelope of a predistorted linear FM signal is defined as:

$$\tilde{s}(t) = \frac{1}{\sqrt{T+2\delta}} \text{rect}\left(\frac{t}{T+2\delta}\right) e^{j2\pi \int_{T+2\delta} f_i(\tau) d\tau} \quad (1)$$

The instantaneous frequency of the predistorted linear FM signal $f_i(t)$ is given by:

$$f_i(t) = \begin{cases} K_{pf} \left(t - \frac{T+\delta}{2} \right) + \frac{B+\Delta f}{2} & \frac{T}{2} \geq t \geq \frac{T}{2} + \delta \\ K_{lfm} t & |t| \leq \frac{T}{2} \\ K_{pf} \left(t + \frac{T+\delta}{2} \right) - \frac{B+\Delta f}{2} & -\left(\frac{T}{2} + \delta\right) \leq t \leq -\frac{T}{2} \end{cases} \quad (2)$$

where according to Figure C.1, $K_{lfm} = \frac{B}{T}$ and $K_{pf} = \frac{\Delta f}{\delta}$.

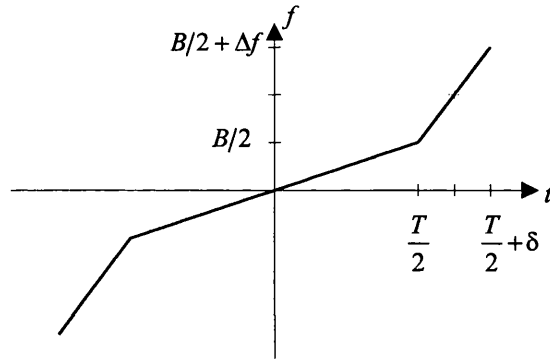


Figure C.1. Predistorted linear FM instantaneous frequency.

The predistorted linear FM signal phase is obtained through direct integration of its instantaneous frequency (Eq. 2), given by:

$$\theta_{lfm}(t) \Big|_{|t| \leq \frac{T}{2}} = 2\pi \int K_{lfm} \tau d\tau = \pi K_{lfm} t^2 \quad (3)$$

The signal predistortion function phase is given by:

$$\theta_{pf}(t) = \begin{cases} \pi K_{pf} t^2 + 2\pi \left(\frac{B + \Delta f}{2} - K_{pf} \frac{T + \delta}{2} \right) t + c_0 & \frac{T}{2} \geq t \geq \frac{T}{2} + \delta \\ 0 & |t| \leq \frac{T}{2} \\ \pi K_{pf} t^2 - 2\pi \left(\frac{B + \Delta f}{2} - K_{pf} \frac{T + \delta}{2} \right) t + c_0 & -\left(\frac{T}{2} + \delta \right) \leq t \leq -\frac{T}{2} \end{cases} \quad (4)$$

where the integration constant c_0 is calculated applying phase continuity between both phase functions $\theta_{lfm}\left(\frac{T}{2}\right) = \theta_{pf}\left(\frac{T}{2}\right)$, given by:

$$c_0 = \pi \frac{T^2}{4} (K_{lfm} - K_{pf}) - \pi \left(\frac{B + \Delta f}{2} - K_{pf} \frac{T + \delta}{2} \right) T \quad (5)$$

The predistorted linear FM compressed pulse (when the matched filter is mismatched in amplitude with a function of the form of a sum of sinusoidal terms) can be expressed as:

$$R_{\bar{s}, \bar{s}w}(\tau) = \frac{1}{T + 2\delta} \int_{-\infty}^{\infty} \text{rect}\left(\frac{t}{T + 2\delta}\right) \text{rect}\left(\frac{t - \tau}{T + 2\delta}\right) w(t - \tau) \cdot e^{j(\theta_{lfm}(t) + \theta_{pf}(t))} e^{-j(\theta_{lfm}(t - \tau) + \theta_{pf}(t - \tau))} dt \quad (6)$$

where:

$$w(t) = \text{rect}\left(\frac{t}{T + 2\delta}\right) \sum_{n=0}^N a_n \cos\left(\frac{2\pi n t}{T + 2\delta}\right) = \text{rect}\left(\frac{t}{T + 2\delta}\right) \sum_{n=0}^N a_n \cos(2\pi n f_T t) \quad (7)$$

As described in Section 5.2.2, $R_{\bar{s}, \bar{s}w}(\tau)$ is approximated by the sum of 2 terms:

$$R_{\bar{s}, \bar{s}w}(\tau) \approx R_1(t) + R_3(t) \quad (8)$$

where $R_1(\tau)$ is equivalent to the compressed central linear FM signal:

$$R_1(\tau) = \frac{1}{T + 2\delta} \int_{-\infty}^{\infty} \text{rect}\left(\frac{t}{T}\right) \text{rect}\left(\frac{t - \tau}{T + 2\delta}\right) w(t - \tau) e^{j\theta_{lfm}(t)} e^{-j\theta_{lfm}(t - \tau)} dt \quad (9)$$

and $R_3(\tau)$ is given by the crosscorrelation between the central linear FM signal and its predistortion function:

$$R_3(\tau) = \frac{1}{T+2\delta} \int_{-\infty}^{\infty} \text{rect}\left(\frac{t}{T+2\delta}\right) \text{rect}\left(\frac{t-\tau}{T}\right) w(t-\tau) e^{j\theta_{pf}(t)} e^{-j\theta_{lfm}(t-\tau)} dt \quad (10)$$

$R_3(\tau)$ (for positive values of time) can be expressed as:

$$R_3(\tau)|_{\tau>0} = \frac{1}{T+2\delta} \int_0^{\infty} \text{rect}\left(\frac{t-\frac{T+\delta}{2}}{\delta}\right) \text{rect}\left(\frac{t-\tau}{T}\right) w(t-\tau) \cdot e^{j\left(\pi K_{pf} t^2 + 2\pi\left(\frac{B+\Delta f}{2} - K_{pf} \frac{T+\delta}{2}\right)t + c_0\right)} e^{-j\pi K_{lfm}(t-\tau)^2} dt \quad (11)$$

Rearranging terms, $R_3(\tau)$ (for $\tau \geq \delta$) can be written as:

$$R_3(\tau)|_{\tau \geq \delta} = \frac{e^{-j(\pi K_{lfm} \tau^2 - c_0)}}{T+2\delta} \cdot \int_{\frac{T}{2}}^{\frac{T}{2}+\delta} e^{j\pi(K_{pf} - K_{lfm})t^2} e^{j2\pi\left(K_{lfm}\tau - \left(\frac{B+\Delta f}{2} - K_{pf} \frac{T+\delta}{2}\right)t\right)} w(t-\tau) dt \quad (12)$$

Making the following variable changes:

$$b = \sqrt{\pi(K_{pf} - K_{lfm})} \quad (13)$$

$$\lambda(\tau) = \frac{\pi\left(K_{lfm}\tau + \frac{B+\Delta f}{2} - K_{pf} \frac{T+\delta}{2}\right)}{\sqrt{\pi(K_{pf} - K_{lfm})}} \quad (14)$$

$R_3(\tau)$ is then given by:

$$R_3(\tau)|_{\tau \geq \delta} = \frac{e^{-j(\pi K_{lfm} \tau^2 + \lambda^2(\tau) - c_0)}}{T+2\delta} \int_{\frac{T}{2}}^{\frac{T}{2}+\delta} e^{j(bt + \lambda(\tau))^2} w(t-\tau) dt \quad (15)$$

Expanding the weighting function, $R_3(\tau)$ can be expressed as a sum given by:

$$R_3(\tau)|_{\tau \geq \delta} = \frac{e^{-j(\pi K_{lfn} \tau^2 + \lambda^2(\tau) - c_0)}}{T + 2\delta} \sum_{n=0}^N A_n(\tau) \quad (16)$$

where:

$$A_n(\tau) = \int_{\frac{T}{2}}^{\frac{T}{2} + \delta} a_n \cos(2\pi n f_T (t - \tau)) e^{j(b t + \lambda(\tau))^2} dt \quad (17)$$

Through the following change of variables:

$$\sqrt{\frac{\pi}{2}} z = b t + \lambda(\tau) \quad (18)$$

the first term of the sum $A_0(\tau)$ can be rewritten as:

$$A_0(\tau) = \sqrt{\frac{\pi}{2}} \frac{a_0}{b} (F(z_2) - F(z_1)) \quad (19)$$

where $F(z)$ is the complex Fresnel integral:

$$F(z) = \int e^{j \frac{\pi z^2}{2}} dz = C(z) + jS(z) \quad (20)$$

with the following integration limits:

$$z_1 = \sqrt{\frac{2}{\pi}} \left(b \frac{T}{2} + \lambda(\tau) \right) \quad (21)$$

$$z_2 = \sqrt{\frac{2}{\pi}} \left(b \left(\frac{T}{2} + \delta \right) + \lambda(\tau) \right) \quad (22)$$

The generic term $A_n(\tau)$ can be written as:

$$A_n(\tau) = \frac{a_1 \cos(2\pi n f_T \tau)}{2} (B_1(\tau) + B_2(\tau)) + \frac{a_1 \sin(2\pi n f_T \tau)}{2j} (B_1(\tau) - B_2(\tau)) \quad (23)$$

where:

$$B_1(\tau) = \int_{\frac{T}{2}}^{\frac{T}{2}+\delta} e^{j2\pi f_T t} e^{j(bt+\lambda(\tau))^2} dt \quad (24)$$

$$B_2(\tau) = \int_{\frac{T}{2}}^{\frac{T}{2}+\delta} e^{-j2\pi f_T t} e^{j(bt+\lambda(\tau))^2} dt \quad (25)$$

$B_1(\tau)$ and $B_2(\tau)$ can be rewritten as:

$$B_1(\tau) = e^{-j\left(\frac{(\pi f_T)^2}{b^2} + \frac{2\pi f_T \lambda(\tau)}{b}\right) \frac{T}{2}} \int_{\frac{T}{2}}^{\frac{T}{2}+\delta} e^{j\left(bt+\lambda(\tau) + \frac{\pi f_T}{b}\right)^2} dt \quad (26)$$

$$B_2(\tau) = e^{-j\left(\frac{(\pi f_T)^2}{b^2} - \frac{\pi f_T \lambda(\tau)}{b}\right) \frac{T}{2}} \int_{\frac{T}{2}}^{\frac{T}{2}+\delta} e^{j\left(bt+\lambda(\tau) - \frac{\pi f_T}{b}\right)^2} dt \quad (27)$$

Making the following change of variables in Eq.26 and Eq.27:

$$\sqrt{\frac{\pi}{2}}z = bt + \lambda(\tau) + \frac{\pi f_T}{b} \quad (28)$$

$$\sqrt{\frac{\pi}{2}}z = bt + \lambda(\tau) - \frac{\pi f_T}{b} \quad (29)$$

Eq. 26 and Eq. 28 can also be transformed into Fresnel integrals and be expressed as:

$$B_1(\tau) = \sqrt{\frac{\pi}{2}} \frac{1}{b} e^{-j\left(\frac{(\pi f_T)^2}{b^2} + \frac{2\pi f_T \lambda(\tau)}{b}\right)} \left(F(z_2 + nz_0) - F(z_1 + nz_0)\right) \quad (30)$$

$$B_2(\tau) = \sqrt{\frac{\pi}{2}} \frac{1}{b} e^{-j\left(\frac{(\pi f_T)^2}{b^2} - \frac{2\pi f_T \lambda(\tau)}{b}\right)} \left(F(z_2 - nz_0) - F(z_1 - nz_0)\right) \quad (31)$$

where:

$$z_0 = \sqrt{\frac{2}{\pi}} \frac{\pi f_T}{b} \quad (32)$$

Therefore, $A_n(\tau)$ is now given by:

$$\begin{aligned} A_n(\tau) = & \sqrt{\frac{\pi}{2}} \frac{a_n}{2b} e^{-j \frac{(\pi f_T)^2}{b^2}} \left(\cos(2\pi f_T \tau) \left(e^{-j \frac{2\pi f_T \lambda(\tau)}{b}} (F(z_2 + nz_0) - F(z_1 + nz_0)) \right) + \right. \\ & \left. + e^{j \frac{2\pi f_T \lambda(\tau)}{b}} + (F(z_2 - nz_0) - F(z_1 - nz_0)) \right) + \\ & + \frac{1}{j} \sin(2\pi f_T \tau) \left(e^{-j \frac{2\pi f_T \lambda(\tau)}{b}} (F(z_2 + nz_0) - F(z_1 + nz_0)) - \right. \\ & \left. - e^{j \frac{2\pi f_T \lambda(\tau)}{b}} + (F(z_2 - nz_0) - F(z_1 - nz_0)) \right) \Bigg) \end{aligned} \quad (33)$$

Rearranging terms, Eq. 33 can be rewritten as:

$$\begin{aligned} A_n(\tau) = & \sqrt{\frac{\pi}{2}} \frac{a_n}{2b} e^{-j \frac{(\pi f_T)^2}{b^2}} \\ & \left(e^{-j \frac{2\pi f_T \lambda(\tau)}{b}} (F(z_2 + nz_0) - F(z_1 + nz_0)) (\cos(2\pi f_T \tau) - j \sin(2\pi f_T \tau)) + \right. \\ & \left. + e^{j \frac{2\pi f_T \lambda(\tau)}{b}} (F(z_2 - nz_0) - F(z_1 - nz_0)) (\cos(2\pi f_T \tau) + j \sin(2\pi f_T \tau)) \right) \end{aligned} \quad (34)$$

which leads to the following final expression:

$$\begin{aligned} A_n(\tau) = & \sqrt{\frac{\pi}{2}} \frac{a_n}{2b} e^{-j \frac{(\pi f_T)^2}{b^2}} \left(e^{-j 2\pi f_T \left(\frac{\lambda(\tau)}{b} + \tau \right)} (F(z_2 + nz_0) - F(z_1 + nz_0)) + \right. \\ & \left. + e^{j 2\pi f_T \left(\frac{\lambda(\tau)}{b} + \tau \right)} (F(z_2 - nz_0) - F(z_1 - nz_0)) \right) \end{aligned} \quad (35)$$

The predistorted linear FM compressed pulse, mismatched in amplitude with a function of the form of a sum of sinusoidal terms (for $\tau \geq \delta$) is given by:

$$R_3(\tau)|_{\tau \geq \delta} = \sqrt{\frac{\pi}{2}} \frac{1}{2b(T+2\delta)} e^{-j(\pi K_{f_m} \tau^2 + \lambda^2(\tau) - c_0)} \cdot \sum_{n=-N}^N a'_n e^{-j \frac{(\pi n f_T)^2}{b^2}} e^{-j 2\pi n f_T \left(\frac{\lambda(\tau)}{b} + \tau \right)} \int_{z_1 + n z_0}^{z_2 + n z_0} e^{j \frac{\pi z^2}{2}} dz \quad (36)$$

where $a'_0 = 2a_0$ and $a'_n = a'_{-n} = a_n$. Applying symmetry properties of the crosscorrelation function, $R_3(\tau)$ can be obtained for the interval $|\tau| \geq \delta$.

APPENDIX D

D.1 Full-Deramp Formulation of Linear FM Signals of Equal Lengths

The transmitted linear FM signal (pulse width T s and bandwidth B Hz) can be formulated as:

$$s_t(t) = \frac{1}{\sqrt{T}} \text{rect}\left(\frac{t}{T}\right) \cos\left(2\pi f_0 t + \pi \frac{B}{T} t^2\right) \quad (1)$$

The returned echo can be considered to be a replica of the transmitted signal with a time delay $2r/c$ corresponding to the position of the target:

$$s_r(t) = \frac{1}{\sqrt{T}} \text{rect}\left(\frac{t-t_d}{T}\right) \cos\left(2\pi f_0(t-t_d) + \pi \frac{B}{T}(t-t_d)^2\right) \quad (2)$$

Successive returns corresponding to adjacent range bins are separated by constant factors $2\Delta r/c$ in time and Δf in frequency (Figure D.1(a)). The frequency difference between two adjacent range bins is given by:

$$\Delta f = \frac{B}{T} \frac{2\Delta r}{c} \quad (3)$$

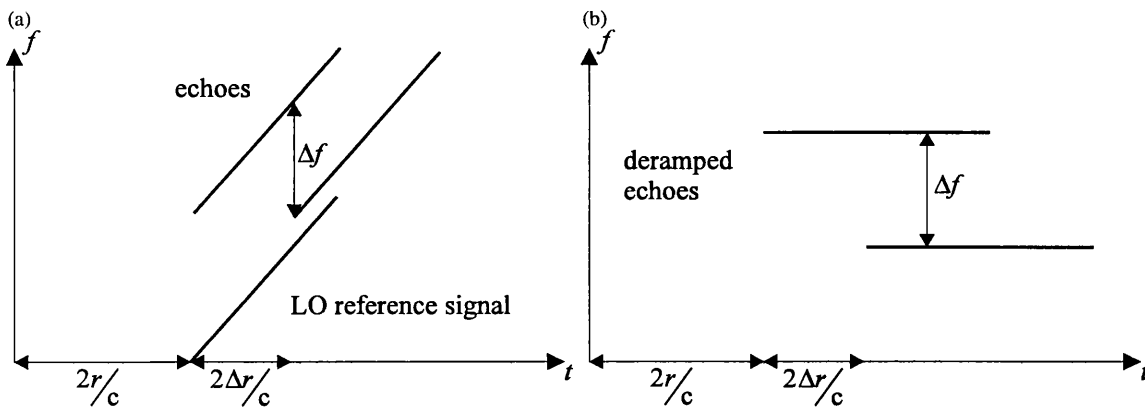


Figure D.1. Time vs. frequency characteristic: (a) Point target return; (b) Point target deramped return.

A diagram of the receiver is shown in Figure D.2. The returned linear FM signal is mixed with a first Local Oscillator reference signal at an intermediate frequency and subsequently band pass filtered. The resulting signal is downconverted to base band by a

coherent demodulator and digitised in order to perform a Fast Fourier Transform operation. A final stage square law detector provides the power spectrum of the full deramped signal which will constitute the system point target response.

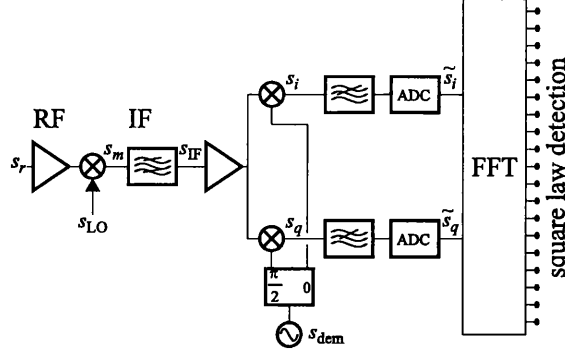


Figure D.2. Altimeter receiver diagram.

The intermediate frequency Local Oscillator reference signal is given by:

$$s_{LO}(t) = \frac{1}{\sqrt{T}} \text{rect}\left(\frac{t-t_h}{T}\right) \cos\left(2\pi(f_0 - f_{IF})(t-t_h) + \pi\frac{B}{T}(t-t_h)^2\right) \quad (4)$$

where $f_0 - f_{IF}$ is the intermediate frequency and the trigger instant t_h is determined by the altimeter tracker. The resulting beat signal $s_m(t) = s_r(t)s_{LO}(t)$ can be expressed as

$$s_m(t) = \frac{1}{2T} \text{rect}\left(\frac{t \pm \frac{t_h - t_d}{2}}{T \pm (t_h - t_d)}\right) \left(\cos\left(2\pi\left(f_{IF} + \frac{B}{T}(t_h - t_d)\right)t + \theta_1\right) + \cos\left(2\pi\left(2f_0 - f_{IF} - \frac{B}{T}(t_h + t_d)\right)t + \theta_2\right) \right) \quad (5)$$

where:

$$\theta_1 = 2\pi f_0(t_h - t_d) - 2\pi f_{IF}t_h + \pi\frac{B}{T}(t_d^2 - t_h^2) \quad (6)$$

$$\theta_2 = 2\pi f_{IF}t_h - 2\pi f_0(t_h + t_d) + \pi\frac{B}{T}(t_d^2 + t_h^2) \quad (7)$$

The term centred at $2f_0 - f_{IF}$ falls outside the intermediate frequency band pass filter. Therefore, $s_{IF}(t)$ is a tone centred at the intermediate frequency whose frequency is proportional to the time difference between the returned linear FM signal and the LO reference signal, given by:

$$s_{\text{IF}}(t) = \frac{1}{2T} \text{rect} \left(\frac{t \pm \frac{t_h - t_d}{2}}{T \pm (t_h - t_d)} \right) \cos \left(2\pi \left(f_{\text{IF}} + \frac{B}{T}(t_h - t_d) \right) t + \theta_1 \right) \quad (8)$$

The second LO demodulating signal can be expressed as:

$$s_{\text{dem}}(t) = 2 \text{rect} \left(\frac{t - t_h}{T} \right) \cos \left(2\pi f_{\text{IF}}(t - t_h) + \varphi \right) \quad (9)$$

where φ is equal to 0 in the in-phase branch and to $\pi/2$ in the quadrature branch. The signals in each branch of the coherent demodulator are given by:

$$s_i(t) = \frac{1}{T} \text{rect} \left(\frac{t \pm \frac{t_h - t_d}{2}}{T \pm (t_h - t_d)} \right) \left(\cos \left(2\pi \frac{B}{T}(t_h - t_d)t + \phi_1 \right) + \cos \left(2\pi \left(2f_{\text{IF}} + \frac{B}{T}(t_h - t_d) \right) t + \phi_2 \right) \right) \quad (10)$$

$$s_q(t) = \frac{1}{T} \text{rect} \left(\frac{t \pm \frac{t_h - t_d}{2}}{T \pm (t_h - t_d)} \right) \left(\sin \left(2\pi \frac{B}{T}(t_h - t_d)t + \phi_1 \right) + \cos \left(2\pi \left(2f_{\text{IF}} + \frac{B}{T}(t_h - t_d) \right) t + \phi_2 \right) \right) \quad (11)$$

where:

$$\phi_1 = 2\pi f_0(t_h - t_d) + \pi \frac{B}{T}(t_d^2 - t_h^2) \quad (12)$$

$$\phi_2 = -2\pi f_0(t_h + t_d) + \pi \frac{B}{T}(t_d^2 + t_h^2) \quad (13)$$

The terms centred at $2f_{\text{IF}}$ are eliminated by the demodulator low pass filters. Finally, the complex envelope of the full-deramped signal $\tilde{s}_d(t) = \tilde{s}_i(t) + j\tilde{s}_q(t)$, is a baseband tone whose frequency is proportional to the time difference between the returned linear FM signal and the LO reference signal (Figure D.1(b)). Assuming without loss of generality that $t_h > t_d$, $\tilde{s}_d(t)$ can be expressed in the form of the following phasor:

$$\tilde{s}_d(t) = \frac{1}{T} \operatorname{rect} \left(\frac{t - \frac{t_h - t_d}{2}}{T - (t_h - t_d)} \right) e^{j2\pi \frac{B}{T} (t_h - t_d)t + j\phi_1} \quad (14)$$

The Fourier transform of the deramped signal complex envelope is formulated as:

$$\tilde{S}_d(f) = \frac{1}{T} e^{j\phi_1} \int_{t_h - \frac{T}{2}}^{t_d + \frac{T}{2}} e^{j2\pi \frac{B}{T} (t_h - t_d)t} e^{-j2\pi ft} dt \quad (15)$$

which can be directly integrated to give:

$$\tilde{S}_d(f) = \frac{1}{T} \frac{e^{j\phi_1}}{j2\pi \left(\frac{B}{T} (t_h - t_d) - f \right)} \cdot \left(e^{j2\pi \left(\frac{B}{T} (t_h - t_d) - f \right) \left(t_d + \frac{T}{2} \right)} - e^{j2\pi \left(\frac{B}{T} (t_h - t_d) - f \right) \left(t_h - \frac{T}{2} \right)} \right) \quad (16)$$

Rearranging the exponential terms, Eq. 16 can be rewritten into:

$$\tilde{S}_d(f) = \frac{1}{T} \frac{e^{j\phi_1} e^{j\pi \left(\frac{B}{T} (t_h - t_d) - f \right) (t_h + t_d)}}{j2\pi \left(\frac{B}{T} (t_h - t_d) - f \right)} \cdot \left(e^{j\pi \left(\frac{B}{T} (t_h - t_d) - f \right) (T - (t_h - t_d))} - e^{-j\pi \left(\frac{B}{T} (t_h - t_d) - f \right) (T - (t_h - t_d))} \right) \quad (17)$$

The final expression for the deramped signal spectrum is given by:

$$\tilde{S}_d(f) = \left(1 - \frac{t_h - t_d}{T} \right) \operatorname{sinc} \left(\left(B(t_h - t_d) - fT \right) \left(1 - \frac{t_h - t_d}{T} \right) \right) e^{j\phi_1} e^{j\pi \left(\frac{B}{T} (t_h - t_d) - f \right) (t_h + t_d)} \quad (18)$$

After the square law detector, the frequency point target power spectrum can be expressed as:

$$|\tilde{S}_d(f)|^2 = \left(1 - \frac{t_h - t_d}{T}\right)^2 \left| \text{sinc}\left(\left(B(t_h - t_d) - fT\right)\left(1 - \frac{t_h - t_d}{T}\right)\right) \right|^2 \quad (19)$$

The factor $\left(1 - \frac{t_h - t_d}{T}\right)^2$ accounts for the point target mainlobe degradation. If the LO reference signal is perfectly aligned in time with the returned echo ($t_d = t_h$), the power spectrum is then given by:

$$|\tilde{S}_d(f)|^2 = |\text{sinc}(fT)|^2 \quad (20)$$

D.2 Full-Deramp Formulation of Linear FM Signals of Different Lengths

The number of range bins that can be deramped with a single triggered LO reference signal (T_{LO} width) is given by:

$$n_{rb} = \frac{T_{LO} - T_p}{t_d} \quad (21)$$

where T_p is the transmitted signal duration and t_d is the delay between two consecutive range bins determined by the range resolution Δr :

$$t_d = \frac{2\Delta r}{c} \quad (22)$$

Therefore, the returned echo is now formulated as:

$$s_r(t) = \frac{1}{\sqrt{T_p}} \text{rect} \left(\frac{t - \left(kt_d + \frac{T_p}{2} \right)}{T_p} \right) \cdot \cos \left(2\pi f_0 \left(t - \left(kt_d + \frac{T_p}{2} \right) \right) + \pi \frac{B}{T_p} \left(t - \left(kt_d + \frac{T_p}{2} \right) \right)^2 \right) \quad (23)$$

with $0 \leq k \leq n_{rb}$, which determines the position of the deramped echo inside the range window. Without loss of generality, the down conversion from the carrier frequency f_0 to base band is carried out with only one LO reference signal, given by:

$$s_{LO}(t) = \frac{1}{\sqrt{T_{LO}}} \text{rect} \left(\frac{t - \frac{T_{LO}}{2}}{T_{LO}} \right) \cos \left(2\pi f_0 (t - T_{LO}) + \pi \frac{B}{T_p} (t - T_{LO})^2 \right) \quad (24)$$

The in-phase component of the deramped signal complex envelope is then given by

$$\tilde{s}_i(t) = \frac{1}{\sqrt{T_{LO}T_p}} \text{rect} \left(\frac{t - \left(kt_d + \frac{T_p}{2} \right)}{T_p} \right) \cos \left(2\pi \frac{B}{T_p} \left(k - \frac{n_{rb}}{2} \right) t_d t + \phi \right) \quad (25)$$

where:

$$\phi = 2\pi f_0 \left(k - \frac{n_{\text{rb}}}{2} \right) t_d + \pi \frac{B}{T_p} \left(T_{\text{LO}}^2 - \left(kt_d + \frac{T_p}{2} \right)^2 \right) \quad (26)$$

The Fourier transform of the deramped echo complex envelope is formulated as:

$$\tilde{S}_d(f) = \frac{1}{\sqrt{T_{\text{LO}} T_p}} e^{j\phi} \int_{kt_d}^{kt_d + T_p} e^{j2\pi \frac{B}{T_p} \left(k - \frac{n_{\text{rb}}}{2} \right) t_d} e^{-j2\pi f t} dt \quad (27)$$

which is solved in the same way as the previous section to give:

$$\tilde{S}_d(f) = \sqrt{\frac{T_p}{T_{\text{LO}}}} \text{sinc} \left(B \left(k - \frac{n_{\text{rb}}}{2} \right) t_d - f T_p \right) e^{j\phi} e^{j2\pi \left(\frac{B}{T_p} \left(k - \frac{n_{\text{rb}}}{2} \right) t_d - f \right) \left(kt_d - \frac{T_p}{2} \right)} \quad (28)$$

After the square law detector, the power spectrum can be expressed as:

$$|\tilde{S}_d(f)|^2 = \frac{T_p}{T_{\text{LO}}} \left| \text{sinc} \left(B \left(k - \frac{n_{\text{rb}}}{2} \right) t_d - f T_p \right) \right|^2 \quad (29)$$

which is coherent with the full-deramp formulation of signals of equal width derived in the previous section. Assuming that $k = 0$ (1st range bin in the range window) and making $T_p = T_{\text{LO}}$ so that $n_{\text{rb}} = 1$, then the power spectrum is again given by:

$$|\tilde{S}_d(f)|^2 = \left| \text{sinc}(f T_p) \right|^2 \quad (30)$$

which is equivalent to the perfectly aligned deramped signal of Eq.20.

D.3 Full-Deramp Formulation of Weighted Linear FM Signals

For simplicity, the full deramp complex envelope in-phase component is considered to be:

$$\tilde{s}_d(t) = \frac{1}{T} \text{rect}\left(\frac{t-t_d}{T}\right) \left(\cos\left(2\pi \frac{B}{T} t_d t + \phi\right) + j \sin\left(2\pi \frac{B}{T} t_d t + \phi\right) \right) \quad (31)$$

The Hamming weighting function is defined as:

$$w_h(t) = \text{rect}\left(\frac{t-t_d}{T}\right) \left(0.54 + 0.46 \cos\left(\frac{2\pi(t-t_d)}{T}\right) \right) \quad (32)$$

Therefore, Fourier transform of the Hamming weighted deramped signal is given by:

$$\tilde{S}_{dw}(f) = \int_{-\infty}^{\infty} \tilde{s}_d(t) \left(0.54 + 0.46 \frac{e^{j2\pi \frac{t-t_d}{T}} + e^{-j2\pi \frac{t-t_d}{T}}}{2} \right) e^{-j2\pi f t} dt \quad (33)$$

which can be rewritten into:

$$\begin{aligned} \tilde{S}_{dw}(f) &= 0.54 \tilde{S}_d(f) + \\ &+ 0.23 \left(e^{-j2\pi \frac{t_d}{T}} \int_{-\infty}^{\infty} \tilde{s}_d(t) e^{-j2\pi \left(f + \frac{1}{T}\right) t} dt + e^{j2\pi \frac{t_d}{T}} \int_{-\infty}^{\infty} \tilde{s}_d(t) e^{-j2\pi \left(f - \frac{1}{T}\right) t} dt \right) \end{aligned} \quad (34)$$

The final expression for the weighted deramped signal is then given by:

$$\tilde{S}_{dw}(f) = 0.54 \tilde{S}_d(f) + 0.23 \left(\tilde{S}_d\left(f + \frac{1}{T}\right) e^{-j2\pi \frac{t_d}{T}} + \tilde{S}_d\left(f - \frac{1}{T}\right) e^{j2\pi \frac{t_d}{T}} \right) \quad (35)$$